



# Nonlinear photonics in silicon germanium waveguides for mid-infrared supercontinuum generation

A thesis submitted in fulfilment of the requirements for the degree of Doctor of Philosophy

**MILAN SINOBAD**

Dipl. Ing. University of Belgrade  
M. Sci. University of Lyon

School of Engineering  
College of Science, Engineering and Health  
RMIT University

November, 2019



# Declaration

I certify that except where due acknowledgement has been made, the work is that of the author alone; the work has not been submitted previously, in whole or in part, to qualify for any other academic award; the content of the thesis is the result of work which has been carried out since the official commencement date of the approved research program; any editorial work, paid or unpaid, carried out by a third party is acknowledged; and, ethics procedures and guidelines have been followed.

Milan Sinobad  
November 9<sup>th</sup>, 2019

# Acknowledgments

First of all, I would like to thank Arnan Mitchell, Distinguished Professor and Director of the Micro Nano Research Facility, for welcoming me to the laboratory and for having accepted to be my thesis advisor. I am grateful to him for his encouragement and valuable advice.

I am deeply grateful to my principal supervisor, Christian Grillet, for his constant enthusiasm, support, and guidance throughout the four years of my thesis. I am especially thankful to him for introducing me to this field of research. My appreciation and thanks also go to Christelle Monat, Professor at Ecole Centrale Lyon, for a valuable contribution to my work. I will be forever grateful to her for everything she has taught me.

I am grateful to Thach Nguyen for his help and for co-supervising my thesis. I also thank David Moss, Professor at the Swinburne University of Technology and Director of the Centre for Micro Photonics, for many discussions we had and his assistance in writing and editing articles.

Special thanks to Delphine Marris-Morini and Alfredo De Rossi for accepting the invitation to examine this thesis manuscript.

Thanks must go to Jean-Marc Fedeli, Jean-Michel Hartmann, and Salim Boutami at the micro and nanotechnology research center CEA-Leti in Grenoble, France, for the manufacturing silicon-germanium waveguides. I am grateful for the excellent cooperation we had. I want to thank Professor Barry-Luther Davies, Steve Madden, Pan Ma, and their entire team for welcoming me to their laboratory at Australian National University and for their contribution to the experimental part of my work.

I thank all my colleagues, especially to David Allieux, Alberto Della-Torre, and Remi Armand, for their help and discussions about numerous topics. I appreciate all of them for the pleasant moments we spent together. I also thank the staff and administration at RMIT University and Ecole Centrale de Lyon.

I want to thank my family and friend for their support. I thank Jelena for always believing in me and for being with me since the beginning of this thesis.

# Abstract

Mid-infrared light (2.5 – 15 $\mu\text{m}$ ) can be advantageously used for high-sensitivity molecular detection in environment, healthcare, industry and security applications. Various molecules can be detected at trace levels by measuring their strong absorption that is several orders of magnitude stronger in the mid-infrared than in the near-infrared. In recent years, there has been a high demand for compact mid-infrared sensors that can be equipped within cars, drones or even smartphones. These sensors could be realized by relying on a technology that is used in a cost-effective micro-electronics industry. The field of photonics utilizing the complementary metal-oxide-semiconductor technology is referred to as silicon photonics. The envisioned compact (on-chip) mid-infrared sensor consists of a light source, sensing area, and photo-detector. The scope of this thesis has been to develop the first building block of this sensor, which is the mid-infrared supercontinuum light source on a silicon-based chip.

Supercontinuum (SC) light is particularly interesting for molecular spectroscopy as it allows for accessing multiple absorption wavelengths at once, enabling the reliable and simultaneous detection of many molecules. Mid-infrared supercontinua on a silicon-based chip have been reported in several platforms on insulating substrates, i.e. silica and sapphire. However, the operation wavelength ranges in these platforms are limited to 3.7 and 5.5  $\mu\text{m}$  due to the absorption in silica and sapphire, respectively. The main goals of this thesis have been to explore a silicon-based platform with extended wavelength range deeper in the mid-infrared and to demonstrate a spectrally bright supercontinuum beyond 5.5 $\mu\text{m}$ . Such a supercontinuum would cover the entire mid-infrared atmospheric absorption band from 4 to 8  $\mu\text{m}$ . In addition to high brightness, ultra-fast and high-precision molecular spectroscopy requires high coherence of a supercontinuum. In this context, an additional objective has been to achieve a coherent supercontinuum generation.

Germanium is a well-known material in the microelectronics industry which has been suggested for silicon photonics in the mid-infrared owing to its wide transparency window. However, the lattice mismatch between germanium and silicon eventually leads to a large density of threading dislocations at the germanium/silicon interface, which limits the performance of nonlinear optical devices. Our solution to this issue has been to use a silicon germanium-on-silicon platform with 40% of germanium in the alloy. Silicon germanium waveguides buried in silicon, which were not dispersion engineered for supercontinuum, were explored in our group. In these waveguides, L. Carletti demonstrated a promising low loss operation and identified an optimal operation wavelength at around 4 $\mu\text{m}$ . Based on these initial results; I designed air clad waveguides and optimized their dispersion for supercontinuum generation.

The waveguides used in this thesis were fabricated using a technological process developed over the last two decades by our collaborators at the micro and nanotechnology research center CEA-Leti in Grenoble, France. The experiments were then performed at the Laser Physics Centre at Australian National University (ANU) in Canberra, Australia. There, we performed linear and nonlinear measurements using a picosecond and sub-picosecond pump at 4 $\mu\text{m}$  in wavelength. The experimental results were analyzed using an in-house developed software. The measured supercontinuum spectra/transmission fits and coherence properties have been analyzed using a generalized nonlinear Schrodinger equation solver. Dispersion trimming presented in the fourth chapter has been investigated using a custom-built mode solver. The theory of nonlinear optics used in this thesis is introduced in the first chapter.

The second chapter reports a spectrally bright supercontinuum spanning to  $8.5\mu\text{m}$  from a dispersion-engineered silicon germanium-on-silicon waveguide. This is a milestone in the mid-infrared silicon photonics since the supercontinuum reached the onset of silicon absorption at  $8.5\mu\text{m}$ . In this waveguide, we measured a propagation loss as low as  $0.2\text{ dB/cm}$  and more than  $10\text{mW}$  on chip supercontinuum power. This is the lowest measured loss and the largest supercontinuum power reported in any silicon-based waveguide in the mid-infrared.

The third chapter discusses the coherence of an octave-spanning supercontinuum. Coherence has been numerically analyzed for an experimentally measured supercontinuum. This chapter shows that a high coherence can be achieved in a long waveguide pumped in the anomalous dispersion regime with  $200\text{fs}$  pulses. This is possible thanks to the specific dispersion profile with a relatively narrow anomalous dispersion band.

In the last chapter, we demonstrate a simple post-fabrication dispersion trimming technique that can be used to optimize dispersion or to shift dispersion from anomalous to all normal.

The mid-infrared possesses the fundamental barrier for standard silicon-based platforms including silicon-on-insulator, silicon nitride-on-insulator, and silicon-on-sapphire. The results reported in this thesis clearly establish silicon germanium-on-silicon as a relevant platform for nonlinear silicon photonics in the mid-infrared. The octave-spanning coherent supercontinuum that has been demonstrated paves the way for future mid-infrared molecule sensor on a silicon chip.

# Table of contents

Declaration.....	i
Acknowledgments.....	ii
Abstract .....	iii
Table of contents.....	v
List of figures.....	vii
List of tables.....	ix
List of abbreviations.....	ix
List of publications and presentations .....	x
Chapter 1. Introduction.....	1
1.1 Theory of nonlinear optics .....	4
1.1.1 Optical response of bulk materials.....	6
1.1.1.1 Overview of the nonlinear effects associated with nonlinear bulk materials .....	6
1.1.1.2 The wave equation in bulk materials .....	10
1.1.1.3 Phase matching condition.....	18
1.1.2 Optical response in waveguides.....	19
1.1.2.1 Contribution of the waveguide to dispersion .....	20
1.1.2.2 Modification of the nonlinearity – waveguide effective nonlinearity.....	23
1.1.2.3 Phase-matching in the four-wave mixing process .....	26
1.1.3 Third-order nonlinear pulse propagation in waveguides .....	28
1.1.3.1 Model for pulse propagation in waveguides .....	28
1.1.3.2 Solitons.....	30
1.1.3.3 Supercontinuum generation dynamics .....	33
1.1.3.4 Phase-matching in the dispersive-wave generation process .....	36
1.2 Silicon photonics .....	38
1.2.1 Silicon photonics in the near-infrared.....	39
1.2.2 Silicon photonics in the mid-infrared .....	42
1.2.2.1 Group IV materials .....	44
1.2.2.2 Germanium.....	45
1.2.2.3 Silicon-Germanium .....	48
1.2.3 Supercontinuum generation on a silicon chip.....	51
1.2.3.1 An octave span.....	52
1.2.3.2 Coherence .....	53

1.2.3.3	Brightness.....	54
1.3	Conclusion.....	56
Chapter 2.	Mid-infrared octave-spanning supercontinuum generation to 8.5 $\mu\text{m}$ in silicon-germanium waveguides.....	58
	Dispersion engineering.....	59
	Conclusion.....	71
Chapter 3.	High coherence at $f$ and $2f$ of mid-infrared supercontinuum generation in silicon germanium waveguides.....	72
	Conclusion.....	81
Chapter 4.	Dispersion trimming for mid-infrared supercontinuum generation in a hybrid chalcogenide/silicon-germanium waveguide .....	82
	Conclusion.....	90
Chapter 5.	Conclusion and perspectives .....	91
References	.....	95



# List of figures

Figure 1: (a) Scanning electron microscope image of the core and inner cladding of a photonic crystal fiber, (b) supercontinuum generated in a PCF (solid curve) with 100fs input pulse (dashed curve), image – J.K. Ranka [5] .....1

Figure 2: The molecular spectroscopy scheme on a silicon chip using mid-infrared supercontinuum light generated along an integrated waveguide.....3

Figure 3: (a) shows an experimental setup that was used to report second harmonic generation in 1960s. The red light enters the nonlinear crystal and the blue light – the second harmonic – exits the crystal, image – R. W. Terhune, (b) shows the visible supercontinuum generation in an optical fiber. Infrared light enters the fiber at right and spectrum from visible to infrared is generated, image – J. M. Dudley [30].....4

Figure 4: Energy diagrams for the main third-order nonlinear processes: self-phase modulation (SPM), two-photon absorption (TPA), cross-phase modulation (XPM), third-harmonic generation (THG), four-wave mixing (FWM) and stimulated (and coherent anti-Stokes) Raman scattering (SRS and CRS) .....9

Figure 5: measured wavelength dependence of Kerr index  $n_2$  (left) and TPA coefficient (right), image – Q.Lin [43]..15

Figure 6: Schematics of the self-phase modulation induced frequency-shift for an optical pulse propagating in a nonlinear Kerr medium. Figure on the left shows the calculated instantaneous frequency shift (with respect to the  $\omega_0$  carrier frequency of the input pulse) for a Gaussian shaped pulse. Figure on the right shows schematics of the pulse carrier wave before and after the SPM effect occurs.....16

Figure 7: The energy diagram of the degenerate four-wave mixing process (left) and the collinear matching of the propagation constants (right).....18

Figure 8: shows different light guiding platforms (a) single-mode fiber, (b) solid-core photonic crystal fiber and (c) on-chip ridge waveguide. Core cross-section is smaller in on-chip waveguides compared to the fibers.....19

Figure 9: Schematics of a ridge waveguide. The waveguide is oriented along the z-axis and does not have here a top cladding .....21

Figure 10: (a) FWM gain coefficient ( $g$ ) calculated with respect to the pump frequency (at 64 THz) for 1, 2 and 4 kW peak pump power associated with the dispersion profile of the  $6.0 \mu\text{m} \times 4.2 \mu\text{m}$  cross-section SiGe-on-Si waveguide presented in Figure 13, (b) FWM gain coefficient in a fiber operating in a strong anomalous dispersion regime where  $\Delta\beta \gg \gamma P_p$  – image Agrawal [10].....27

Figure 11 : schematics of the pulse carrier-wave affected by the self-phase modulation effect (SPM – top right) and by the anomalous group velocity dispersion (GVD – bottom right).....31

Figure 12: Calculated time (top) and spectral evolution (bottom) of (a) a fundamental, (b) a second order and (c) a third order soliton. Simulations are performed taking into account  $\beta_2 = -5.14 \times 10^{-24} \text{ s}^2/\text{m}$ , and 1, 4 and 9 kW pump peak power, 210 fs hyperbolic secant pulse centered at  $4.71 \mu\text{m}$  (64 THz). Dispersion length ( $L_D$ ) is equal to 0.28 cm while nonlinear lengths ( $L_{NL}$ ) are equal to 0.28, 0.07 and 0.03 cm, respectively. ....32

Figure 13: Calculated group velocity  $v_g$  (a) and group velocity dispersion  $D$  versus wavelength, (b) Calculated evolution of the pulse envelope (normalized power in dB scale) over time (c) and wavelength (d) along the propagation distance L The simulations parameters used here are summarized in Table 1.....34

Figure 14 : (a) Group-velocity dispersion (black) with the superimposed spectrum from Figure 13 calculated at 2cm distance (blue), DW is generated at a wavelength around  $10 \mu\text{m}$ , (b) calculated phase-matched dispersive wave wavelength for different soliton wavelengths ( $\lambda$ -label) and 1, 2 and 4 kW soliton peak-powers. ....37

Figure 15: (left) Intel’s concept of a terabit optical transmitter integrated on a silicon chip, image – Intel, (right) hybrid integration of the indium phosphide (InP) laser on a silicon photonics chip, image – B. Song et al. [74] .....40

Figure 16: shows transparency of Earth’s atmosphere. Molecules have strong absorption in windows located around  $3 \mu\text{m}$ ,  $4 \mu\text{m}$  and from  $5$  to  $8 \mu\text{m}$ . Atmospheric windows from  $3$  to  $5 \mu\text{m}$  can be used for the secure free-space communications. ....42

Figure 17: Transparency window of several CMOS compatible semiconductor materials that are listed on the left [64, 66, 108]. The related bandgap and the wavelength limit beyond which two-photon absorption disappears are

indicated by the first and second vertical line from the left, respectively. The transparency window (denoted by the white areas) is defined as the bend where the absorption loss is below 2dB/cm. ....44

Figure 18: Experimentally extracted  $\chi^{(3)}$  nonlinearity in silicon (a) and germanium (b), *img.* – N. K. Hon et al. [108]46

Figure 19: a pulse train with an evolving carrier-envelope phase (bottom) and corresponding spectrum (top). The carrier wave is presented by the solid blue curve, the pulse envelope by the dotted blue curve .....52

Figure 20: A survey of the reported supercontinuum demonstrations on a silicon chip in the near- and mid-IR range. Each result is represented by a horizontal bar that indicates the SC spectral span and whether it was coherent (dashed line) or not (solid line). The colors refer to the different platforms that were exploited, while the pump wavelength and pulse regime is denoted by a (full, for picosecond, or empty, for femtosecond) circle. ....55

Figure 21: Group-velocity dispersion (GVD in units ps/nm/km) calculated for top air-clad  $\text{Si}_{0.6}\text{Ge}_{0.4}$ -on-Si waveguides (see cross-section in the inset) at  $4.5\mu\text{m}$  for TE (left) and TM (right) modes for different waveguide widths (x-axis) and heights (y-axis). The green dashed lines indicate the mode effective area calculated as per equation (72) in  $\mu\text{m}^2$ . The white solid line highlights the achievement of a zero-GVD.....60

Figure 22: Calculated group-velocity dispersion (solid curves) and mode confinement in the core (dashed curves) versus wavelength for quasi-TE (blue) and quasi-TM modes (blue) for the top air-clad  $\text{Si}_{0.6}\text{Ge}_{0.4}/\text{Si}$  waveguide 1 (left) and waveguide 2 (right).....61

## List of tables

<i>Table 1: Summary of parameters used in the simulation of supercontinuum generation of Figure 13</i> .....	33
<i>Table 2: a survey of demonstrators achieved in Germanium based integrated platforms. SiGe<sup>1</sup> and SiGe<sup>2</sup> refer to high and low germanium content silicon-germanium alloys, respectively. The schematics of these platforms are shown on Table 3.</i> .....	47
<i>Table 3: A comparison of Germanium based integrated platforms with the main material parameters. Schematics of the different waveguide geometry are presented for each platform. SiGe<sup>1</sup> and SiGe<sup>2</sup> refer to high and low germanium content silicon-germanium alloys, respectively.</i> .....	48

## List of abbreviations

CMOS	Complementary-Metal-Oxide-Semiconductor
CARS	Stimulated Coherent Anti-Stokes Raman Scattering
DFWM	Degenerate Four-Wave Mixing
FCA	Free-Carrier Absorption
FCD	Free-Carrier Dispersion
FWM	Four-Wave Mixing
GNLSE	Generalized Nonlinear Schrodinger Equation
GOS	Germanium-On-Silicon
GVD	Group Velocity Dispersion
OCT	Optical Coherence Tomography
PCF	Photonic-Crystal Fiber
PDM	Polarization Division Multiplexing
QAM	Quadrature Amplitude Modulation
QCL	Quantum Cascade Laser
RIN	Relative Intensity Noise
SC	Supercontinuum
SHG	Second-Harmonic Generation
SOI	Silicon-On-Insulator
SPM	Self-Phase Modulation
SRS	Stimulated Raman Scattering
SSFM	Split-Step Fourier Method
THG	Third-Harmonic Generation
TPA	Two-Photon Absorption
WDM	Wavelength Division Multiplexing
XPM	Cross-Phase Modulation

# List of publications and presentations

## Publications

1. L. Carletti, M. Sinobad, P. Ma, Y. Yu, D. Allieux, R. Orobtcchouk, M. Brun, S. Ortiz, P. Labeye, J.-M. Hartmann, S. Nicoletti, S. Madden, B. Luther-Davies, D. J. Moss, C. Monat and C. Grillet, “*Mid-infrared nonlinear optical response of Si-Ge waveguides with ultra-short optical pulses*”, Opt. Express 23 (25), 32202-14 (2015)
2. M. Sinobad, C. Monat, B. Luther-Davies, P. Ma, S. Madden, D. J. Moss, A. Mitchell, D. Allieux, R. Orobtcchouk, S. Boutami, J.-M. Hartmann, J.-M. Fedeli and C. Grillet, “*Mid-infrared octave spanning supercontinuum generation to 8.5 $\mu$ m in silicon-germanium waveguides*”, Optica 5 (4), 360-366 (2018)
3. D. Allieux, A. Belarouci, D. Hudson, E. Magi, M. Sinobad, G. Beaudin, A. Michon, N. Singh, R. Orobtcchouk and C. Grillet, “*Toward mid-infrared nonlinear optics applications of silicon carbide microdisks engineered by lateral under-etching*” (invited), Photonics Research (6) 5, B74-B81 (2018)
4. M. Sinobad, A. Della Torre, B. Luther-Davis, P. Ma, S. Madden, S. Debbarma, K. Vu, D. J. Moss, A. Mitchell, J.-M. Hartmann, J.-M. Fedeli, C. Monat, and C. Grillet, “*Dispersion trimming for mid-infrared supercontinuum generation in a hybrid chalcogenide/silicon-germanium waveguide*”, J. Opt. Soc. Am. B 36 (2), A98-A104 (2019)
5. M. Sinobad, A. Della Torre, R. Armand, B. Luther-Davies, P. Ma, S. Madden, A. Mitchell, D. J. Moss, J.-M. Hartmann, J.-M. Fédéli, C. Monat and C. Grillet “*High coherence at  $f$  and  $2f$  of mid-infrared supercontinuum generation in silicon germanium waveguides*”, IEEE J. Sel. Top. Quantum Electron 26 (2), 1-8 (2020).

## Presentations

1. M. Sinobad, P. Ma, B. Luther-Davies, D. Allieux, R. Orobtcchouk, D. J. Moss, S. Madden, S. Boutami, J.-M. Fedeli, C. Monat and C. Grillet, “*Dispersion engineered air-clad SiGe waveguides with low propagation loss in the mid-infrared*”, CLEO/Europe-EQEC 2017, 25 - 29 June 2017, Munich, Germany
2. M. Sinobad, P. Ma, B. Luther-Davies, D. Allieux, R. Orobtcchouk, D. J. Moss, S. Madden, S. Boutami, J.-M. Fedeli, C. Monat and C. Grillet, “*Broadband mid-infrared supercontinuum generation in low loss dispersion engineered silicon-germanium waveguide*”, CLEO/Europe-EQEC 2017, 25 - 29 June 2017, Munich, Germany (post-deadline session)
3. M. Sinobad, P. Ma, B. Luther-Davies, S. Madden, D. Moss, R. Orobtcchouk, S. Boutami, J.-M. Hartmann, J.-M. Fedeli, C. Monat, C. Grillet, “*Experimental Demonstration of Mid-IR Octave Spanning Supercontinuum Generation in Low Loss Silicon-Germanium Waveguide Waveguide*”, 2018 Optical Fiber Communication Conference (OFC), 11 - 15 March 2018, San Diego, California, USA
4. M. Sinobad, C. Monat, B. Luther-Davies, P. Ma, S. Madden, D. Moss, A. Mitchell, R. Orobtcchouk, A. Della Torre, S. Boutami, J.-M. Hartmann, J.-M. Fedeli, C. Grillet, “*Coherent Supercontinuum Generation in a Silicon-Germanium Waveguide in the Mid Infrared*”, OSA 2018 High-brightness Congress, 26 - 28 March 2018, Strasbourg, France
5. M. Sinobad, C. Monat, P. Ma, B. Luther-Davies, S. Madden, D. J. Moss, A. Mitchell, A. Della Torre, R. Orobtcchouk, S. Boutami, J.-M. Hartmann, J.-M. Fedeli, C. Grillet, “*Mid-IR octave spanning supercontinuum generation in an air clad silicon germanium waveguide*”, EPE18-EPE116-30. Photonics Europe 2018, 22 - 26 April 2018, Strasbourg, France
6. M. Sinobad, C. Monat, B. Luther-Davies, P. Ma, S. Madden, D. J. Moss, A. Mitchell, R. Orobtcchouk, S. Boutami, J.-M. Hartmann, J.-M. Fedeli, C. Grillet, “*Mid-wavelength Infrared Supercontinuum Generation Spanning 1.4 Octaves in a Silicon-Germanium Waveguide*”, 2018 Conference on Lasers and Electro-Optics (CLEO), 13 - 18 May 2018, San Jose, California, USA

# Chapter 1.

## Introduction

Supercontinuum (SC) generation might be the most compelling signature of nonlinear optics. This is a nonlinear process that manifests as a large spectral broadening of a narrowband input light signal in a nonlinear and dispersive optical medium. A supercontinuum source can be simply described as “white-light laser”, since the generated broadband light can maintain the intensity, collimation, focus and coherence properties of the laser probe [1]. The spectral brightness of the supercontinuum light can be several orders of magnitude (a million times) brighter than sunlight [2].

The year 2019 marks three significant anniversaries related to supercontinuum generation. The first is the 50<sup>th</sup> anniversary of the discovery of supercontinuum generation [1]. Supercontinuum light spanning over an octave has been first observed by R. Alfano and S. Shapiro in 1969, as a large frequency broadening – from violet to red light (400 – 700nm) – in bulk glass under picosecond pulse excitation [3, 4]. The second is the 20<sup>th</sup> anniversary of the first demonstration of supercontinuum generation in photonic-crystal fibers [5, 6]. This achievement led to the so called “supercontinuum revolution” – the development of this technology by industries and the subsequent deployment to end-users. More recently, supercontinuum has been investigated in integrated waveguides. The third anniversary marks the 5 years of the first octave-spanning supercontinuum generated on a chip [7, 8].

The supercontinuum revolution [6] is referred to as a radical change in the supercontinuum generation technology enabled by the technological development of ultra-fast laser sources and fiber optics – particularly by the invention of photonic-crystal fibers (PCF) [9]. PCFs provide a platform for engineering dispersion by changing the position and diameter of the micro-structured air-holes that surround the fiber core (see Figure 1a). Engineering the dispersion in PCFs enabled the achievement of supercontinuum using femtosecond titanium-sapphire laser operating around 800nm. Moreover, the strong field confinement in a solid core PCF led to the supercontinuum generation at low power level. In 1999 J. Ranka et al reported the first supercontinuum in PCFs spanning from violet to telecom wavelengths (400 – 1500nm) with nano-joule energy 100fs pulses [5] (Figure 1b).

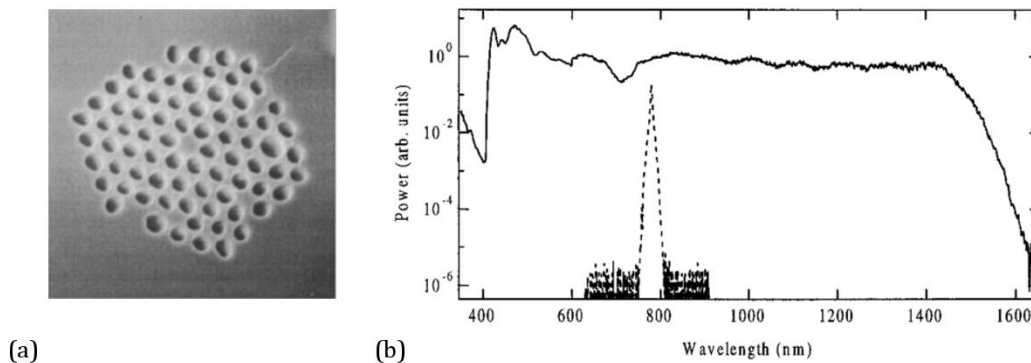


Figure 1: (a) Scanning electron microscope image of the core and inner cladding of a photonic crystal fiber, (b) supercontinuum generated in a PCF (solid curve) with 100fs input pulse (dashed curve), image – J.K. Ranka [5]

Supercontinuum light enabled broadband and ultra-fast applications. The optical signal associated with a bright and broad supercontinuum improved broadband molecular spectroscopy, while ultra-short supercontinuum pulses enabled resolving ultra-fast bio-chemical processes. Supercontinuum sources have been used for the fundamental research in chemistry, biology and medicine. They also found numerous applications in optical communications [10] and frequency metrology [11]. This eventually resulted in the demonstration of an optical atomic clock that was awarded the Nobel prize in 2005 [11, 12].

Over the last decade, significant progress has been made in achieving supercontinuum generation on a chip [7, 8, 13, 14]. Small cross-section waveguides (with a core area below  $1\mu\text{m}^2$ ) realized in a planar geometry on a chip can have strong field confinement and well-defined polarization states lowering the threshold for supercontinuum generation [15]. Integrated waveguides can provide an efficient supercontinuum generation at low power levels – e.g. with pico-joule energy 100fs pulses [16]. Reliable and cost effective waveguide fabrication is possible relying on the complementary-metal-oxide-semiconductor (CMOS) technology from the microelectronics industry. Moreover, CMOS is the enabling technology for integration of many photonics components on the same chip and/or for integration of photonics with electronics components. The ultimate goal is to achieve compact and fully integrated supercontinuum sources. Such sources could be used in widespread and everyday applications.

For a long time, SC sources have been bound to the visible and short infrared part of the spectrum, due, in particular to the dominant use of silica based materials. Recently, significant attention has been paid on extending the emission wavelength of SC sources up to the mid-infrared (2.5 –  $15\mu\text{m}$ ), as relevant for molecular spectroscopy applications. Many molecules have fundamental absorption lines in the mid-infrared, allowing for high-sensitivity optical gas detection. In the mid-infrared, gas molecules can be detected at trace levels measured in parts per billion. The mid-infrared absorption spectroscopy can be used for numerous important applications such as gas sensing for environment monitoring, water quality control and toxic molecules detection for security applications. It can be used in health for non-invasive blood glucose monitoring and the early cancer diagnosis using exhaled breath analysis. In this context, generating a mid-infrared supercontinuum on a silicon chip is a first step toward the development of compact point sensors such as the lab-on-a-chip that can be used at the point of care (see Figure 2).

Nonlinear optical materials other than silica are required for the supercontinuum generation in the mid-infrared. Two material groups are particularly suitable: chalcogenides and group IV materials (e.g. silicon and germanium). Chalcogenides are non-oxide amorphous (glass) materials containing one or more chalcogen elements. These elements are sulfur, selenium and tellurium. Sulphide glasses can be used up to  $12\mu\text{m}$ ; selenides to around  $16\mu\text{m}$ ; and tellurides to beyond  $20\mu\text{m}$  [8]. Beyond these wavelengths, the materials are not transparent. Supercontinuum up to  $10\mu\text{m}$  [17] and  $13.3\mu\text{m}$  [18] were reported in chalcogenide step index fibers, and more recently on a chalcogenide chip [8, 15]. For more information about mid-infrared supercontinuum in chalcogenide glass fibers, the readers are referred to the review article [19]. In this thesis I focused, instead, on the use of group IV materials and silicon chips, so as to take advantage of the CMOS technology involving CMOS compatible fabrication processes. In a standard CMOS platform – silicon-on-insulator – the operation wavelength is limited to  $3.7\mu\text{m}$  and in the silicon-on-sapphire platform, up to  $5.5\mu\text{m}$ , due to the absorption in the silica and sapphire substrates respectively. In order to extend the operation wavelength range, the use of other group IV materials has been

proposed. Supercontinuum in alternative group IV materials has the potential to extend the operation wavelength up to  $15\mu\text{m}$ .

In this thesis the silicon germanium-on-silicon (SiGe-on-Si) platform has been chosen. The technological process to realize efficient devices out of this platform has been developed by our collaborators at Leti's Center for Research in Grenoble, France. Based on this technology, waveguides have been designed, optimized and realized for enabling on chip supercontinuum generation in the mid-infrared. One key aspect has been to achieve coherent supercontinuum generation.

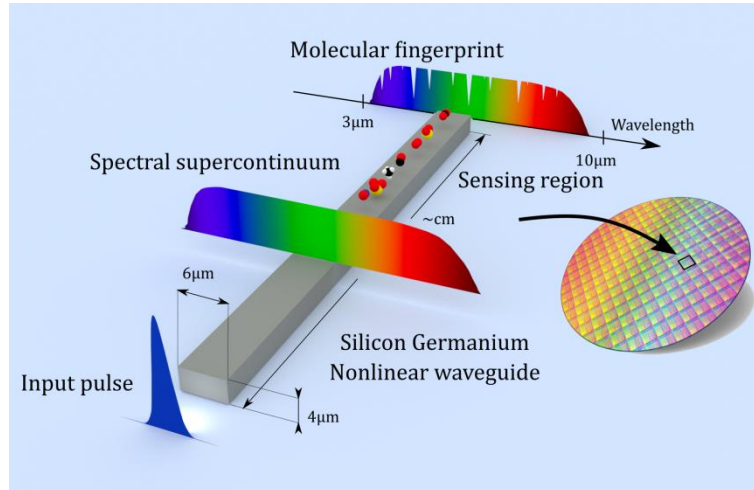


**Figure 2: The molecular spectroscopy scheme on a silicon chip using mid-infrared supercontinuum light generated along an integrated waveguide**

The first chapter introduces the underlying notions and concepts behind this thesis. I will first remind some theoretical aspects of nonlinear optics, as well as some background related to nonlinear silicon photonics in the mid-infrared. I will also provide some overview of supercontinuum generation and its related dynamics. The second chapter presents our results on mid-IR supercontinuum generation in silicon germanium waveguides and focuses on achieving a wide bandwidth. The third chapter discusses the coherence properties of the generated supercontinuum, by means of simulations. The fourth chapter shows how it is possible to use post-processing techniques to trim the waveguide dispersion, which is key to generate on chip supercontinuum. This tool allows us to tailor the supercontinuum so that it is best suited for the intended application.

Considering the significant results achieved in this thesis – supercontinuum from 3 to  $8.5\mu\text{m}$  – we established silicon germanium as a relevant platform for chip-based nonlinear applications in the mid-IR.

## 1.1 Theory of nonlinear optics

This section introduces the electromagnetic theory of nonlinear optics used in this thesis.

The theory of nonlinear optics is very rich as it covers various materials, platforms and effects achieved under different types of light excitation. Depending on the material crystalline symmetry, either second order nonlinear effects such as the electro-optic effect and second harmonic generation (see Figure 3a) can be observed or third-order nonlinear effects such as self-phase modulation, four-wave mixing and supercontinuum generation (see Figure 3b). Second harmonic generation (SHG) is the first nonlinear optical effect that was experimentally demonstrated. It was first observed in a bulk material in 1961, just one year after the invention of lasers [20]. Since then, nonlinear effects have been explored in different platforms such as fibers in the 1970's [21-24], photonic-crystal fibers in the 1990's [5, 6, 9, 25] and more recently in waveguides on a chip [26, 27]. Nonlinear optics evolved together with the laser technology. Ultra-short pulse lasers (duration less than 100fs) have been developed in the 1990's [28, 29].

In this chapter I summarize the theory related to the specific aspects (material, platform and applications) that are directly relevant to this thesis, namely the generation of mid-infrared supercontinuum in silicon-based waveguides using ultra-short optical pulses.

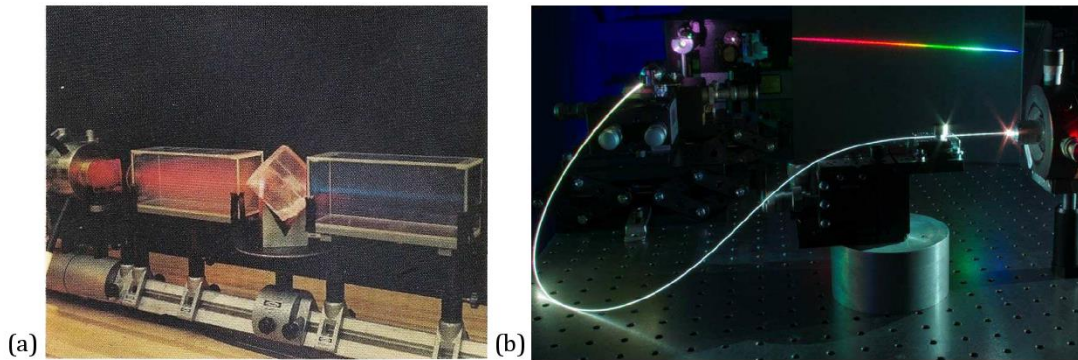


**Figure 3: (a) shows an experimental setup that was used to report second harmonic generation in 1960s. The red light enters the nonlinear crystal and the blue light – the second harmonic – exits the crystal, image – R. W. Terhune, (b) shows the visible supercontinuum generation in an optical fiber. Infrared light enters the fiber at right and spectrum from visible to infrared is generated, image – J. M. Dudley [30]**

Supercontinuum can be characterized by its bandwidth, brightness, spectral flatness and coherence. These parameters are affected by the choice of material, waveguide geometry and pulse duration. In this chapter, each of these items will be discussed. The section “theory of nonlinear photonics” is therefore divided into three parts:

1. Optical response of bulk materials
2. Optical response in waveguides
3. Modeling of pulse propagation in waveguides

The first part – Optical response of bulk materials – explains the way a bulk material responds to light (typically a plane-wave), inducing both linear and nonlinear effects. The second part – Optical response in waveguides – introduces the waveguide contribution to light propagation, which manifests in the waveguide dispersion and modifies the nonlinear response. This calls for the need to define effective parameters, which characterize light propagation in nonlinear waveguides. The



third part – Modeling of pulse propagation in waveguides – introduces the pulse propagation equation, known as the Generalized Nonlinear Schrodinger Equation (GNLSE). This equation has been extensively used for simulating the generation of SC in waveguide based platforms, and has been the main simulation tool in this thesis. Here will be discussed the dynamics of supercontinuum generation in more details, with the main aspects highlighted.

Optical pulse propagation in waveguides can be accurately modeled using Maxwell's equations. These equations consist of three sets of coupled equations, which will be developed in the next three sub-sections (1.1.1, 1.1.2 and 1.1.3): constitutive relations, divergence equations and curl equations. *Constitutive relations* model the material response to the applied optical field. *Divergence equations* express constraints such as those imposed by the waveguide cross-section geometry in the plane perpendicular to the propagation direction. *Curl equations*, the third set of Maxwell's equations, provide the nonlinear wave equation. A more detailed theoretical background can be found in textbooks [10, 31-34]. Readers are also referred to review articles describing the theory of optical pulse propagation [35], nonlinear phenomena in silicon waveguides [36] and supercontinuum generation [37].

### 1.1.1 Optical response of bulk materials

In this section, we will discuss the linear and nonlinear response of the material to the optical field. We will briefly explain the microscopic origin of these effects, and introduce some related macroscopic description that can be readily included in Maxwell's equations. This allows us to infer a wave equation, from which the different linear and nonlinear mechanisms arising in a bulk material can be reviewed. The third-order nonlinear response will be discussed in more details as this is at the origin of supercontinuum generation, while dominating the nonlinear response in silicon and silica, which are the main materials used in CMOS technology.

#### 1.1.1.1 Overview of the nonlinear effects associated with nonlinear bulk materials

Upon propagation in a material, light can interact with nuclei in atoms, charges in atoms or with free charges in the material. The interaction with nuclei, which can result in Raman and Brillouin effects, can be described using the light scattering theory. Through interacting with charges in atoms, light induces and drives the motion of electric dipoles. The response of matter to the electromagnetic field can thus be macroscopically described through the density of induced dipole momenta represented by the polarization vector  $P$ . Through interacting with free charges, which are electrons and holes that are not bound to nuclei, light induces a current. This is represented with the free charge current density  $J_f$ . Light-matter interaction can be described using quantum mechanics. However, light propagation through a medium can be accurately modeled using Maxwell's equations. The polarization vector and the free charge current density, i.e. the material response, are introduced via the constitutive relations, which are written below in the frequency domain:

$$\mathbf{D}(\mathbf{r}, \omega) = \varepsilon_0 \mathbf{E}(\mathbf{r}, \omega) + \mathbf{P}(\mathbf{r}, \omega) \quad (1)$$

$$\mathbf{B}(\mathbf{r}, \omega) = \mu_0 (\mathbf{H}(\mathbf{r}, \omega) + \mathbf{M}(\mathbf{r}, \omega)) \approx \mu_0 \mathbf{H}(\mathbf{r}, \omega) \quad (2)$$

$$\mathbf{J}_f(\mathbf{r}, \omega) = \sigma \mathbf{E}(\mathbf{r}, \omega) \quad (3)$$

The first equation introduces the relation between the electric displacement  $D$  and the electric field  $E$ . The response of atoms to the electric field is represented by the polarization vector  $P$ . The response to the magnetic field is introduced by the magnetic polarization  $M$  in the second equation, which assumes here, a non-magnetic material ( $M \approx 0$ ). The third equation relates the current density associated with the motion of free-charges in the medium  $J_f$  to the electric field through the conductivity  $\sigma$ . The electric properties of the material subjected to an electric field are therefore included in the polarization vector  $P$  and the free charge current density  $J_f$ . The nature of the material's response is determined by their relation with the electric field,  $P(E)$  and  $J_f(E)$ . This relation can be, like the material response, either linear or nonlinear. In particular, the  $J_f(E)$  relation is linear under the assumption that the electric conductivity is constant. However, the electric conductivity may depend on the electric field, resulting in an effective nonlinear response.

The polarization vector defines the response of the atoms (bound electrons and nuclei) to the applied electric field. It can be divided into a linear polarization term  $P_L$  and the nonlinear polarization term  $P_{NL}$ . The polarization terms can be defined in the frequency domain as [31]:

$$\mathbf{P}(\mathbf{r}, \omega) = \mathbf{P}_L(\mathbf{r}, \omega) + \mathbf{P}_{NL}(\mathbf{r}, \omega) \quad (4)$$

$$\mathbf{P}_L(\mathbf{r}, \omega) = \varepsilon_0 \chi^{(1)} \mathbf{E}(\mathbf{r}, \omega) \quad (5)$$

$$\mathbf{P}_{NL}(\mathbf{r}, \omega) = \varepsilon_0 \chi^{(2)} : \mathbf{E}_a(\mathbf{r}, \omega_a) \mathbf{E}_b(\mathbf{r}, \omega_b) + \varepsilon_0 \chi^{(3)} : \mathbf{E}_a(\mathbf{r}, \omega_a) \mathbf{E}_b(\mathbf{r}, \omega_b) \mathbf{E}_c(\mathbf{r}, \omega_c) + \dots \quad (6)$$

The susceptibility coefficients  $\chi$  model the optical properties of the material subjected to an electric field. The linear relation between the electric field vector and the polarization vector (i.e. linear response) involves the vacuum permittivity  $\varepsilon_0$  and *the linear susceptibility*  $\chi^{(1)}$ . In this case, the induced dipoles oscillate at the same frequency  $\omega$  as that of the optical field. The nonlinear response (associated with the  $\mathbf{P}_{NL}$  polarization vector) can allow for the interaction between multiple waves propagating at different frequencies. As a result, unlike linear interactions, nonlinear ones can induce the generation of optical fields at new frequencies. More generally, the frequency of the input field can be changed upon its propagation in a nonlinear medium while new frequency components can be generated. The nonlinear properties are modeled via *the nonlinear susceptibility coefficients*  $\chi^{(2)}$  and  $\chi^{(3)}$ . In isotropic materials, the susceptibility is a scalar quantity, while in anisotropic crystals; the susceptibility takes the form of a tensor that relates the induced polarization in a particular direction to the different components of the electric field in all three directions. Here, the second- and third-order susceptibilities  $\chi^{(2)}$  and  $\chi^{(3)}$  are third and fourth rank tensors, respectively. Symbols “:” and “::” in the equation represent the products between tensors and electric field vectors. Since all materials become nonlinear when subjected to intense input electric fields, they all possess a priori both a linear and nonlinear response. However, we will use the term “nonlinear material” for a material with a strong nonlinearity.

The linear response related to bound electrons can be classically described using the Lorentz model and that of free (conduction) electrons using the Drude model. Consequences of these interactions are light dispersion and absorption. Interactions with free charge carriers (electrons and holes) are important in semiconductors, giving rise to the free-carrier dispersion and absorption effects. In transparent materials, free-carriers are generated through nonlinear absorption in a process where a bound electron is excited by absorbing multiple photons simultaneously.

In contrast with the linear response of the material, the nonlinear optical response enables the interaction between multiple waves, as mediated by the material. A strong nonlinear response can arise from the interactions between photons and (free or bound) electrons – “photon-electron” interactions. A nonlinear response contribution can be also due to the “photon-phonon” interaction (i.e. interaction between photons and atom vibrations in a crystal) resulting in nonlinear scattering effects (such as Brillouin or Raman processes). We review these different mechanisms in details below.

In nonlinear interactions, energy and momentum conservation laws must be satisfied (see section 1.1.1.3 for further details). The nonlinear interactions with bound electrons are elastic. The sum of annihilated photon energies/momenta is equal to the sum of the generated photon energies/momenta. The nonlinear interactions with nuclei (such as stimulated Raman scattering) are inelastic. In these inelastic scattering processes, the energy of the photons is partially transferred to the nonlinear medium. The annihilated photon generally creates a lower frequency photon (called Stokes wave) and a phonon with the right energy and momentum so the conservation laws are satisfied [10].

The time-scale of the nonlinear interactions associated with bound electrons is ultra-short in the order of few femtoseconds. This has enabled the demultiplexing of optical signals at Tb/s data rate [38]. The nonlinear interactions with nuclei are characterized with two time constants. The first is an ultra-fast response time ( $\sim 10$ fs) and the second one is the phonon lifetime, which is, in silicon, in the order of a few picoseconds ( $\sim 3$ ps)[36]. Regarding the interaction of light with free carriers, the latter are generated almost instantaneously through multi-photon absorption. The generated free carriers then affect the propagation of the pulse that created them. By contrast, the radiative recombination of the free carriers is a slow process in the order of 10s of nano-seconds. The long free carrier life-time generally limits the performance of nonlinear and electro-optic applications.

The dominant nonlinear material response is determined by the material structure and crystalline symmetry [32]. In this context, materials can be divided into two groups 1) materials with inversion symmetry – centrosymmetric materials and 2) materials with no inversion symmetry – non-centrosymmetric materials. Semiconducting III-V compounds,  $\text{LiNbO}_3$  are examples of non-centrosymmetric materials, allowing for second-order nonlinear effects. By contrast, gas, liquids and amorphous materials (glass) can be considered as centrosymmetric materials. Moreover, the main materials used for on-chip silicon photonics such as silicon (its oxide and nitride), silicon germanium alloys and germanium are centrosymmetric materials [26, 27]. In centrosymmetric materials, the response to positive and negative optical fields is symmetrical. Therefore the even order nonlinear response is forbidden. The first non-zero nonlinear term is the third-order susceptibility  $\chi^{(3)}$  and these materials are often named  $\chi^{(3)}$  materials [33]. We will here discuss in more details the nonlinear response of  $\chi^{(3)}$  materials.

The third-order nonlinear response is the result of the interaction between three waves in the material that manifests as the generation of a fourth wave. This is represented by the equation:

$$\mathbf{P}_{NL}(\omega) = \varepsilon_0 \chi^{(3)} : \mathbf{E}_a(\omega_a) \mathbf{E}_b(\omega_b) \mathbf{E}_c(\omega_c) \quad (7)$$

In the literature [26, 27], third-order nonlinear effects are introduced considering the general response to three waves at distinct frequencies. Here, the same approach is used. The superimposed monochromatic waves are given by:

$$\mathbf{E}(\mathbf{r}, \omega; \omega_{abc}) = \text{Re} \left\{ \sum_{n=abc} \mathbf{E}_n(\mathbf{r}) e^{-i\omega_n t} \right\} = \sum_{n=abc} \frac{1}{2} (\mathbf{E}_n(\mathbf{r}) e^{-i\omega_n t} + c.c.) \quad (8)$$

When energy and momentum conservation laws are satisfied, the interaction between the three waves and the associated generation of the fourth wave can become very efficient. The general polarization response upon the interaction of three waves at distinct frequencies contains  $6^3$  terms (including complex conjugate c.c.) that are not distinct in frequencies though and can be gathered as follows:

$$\begin{aligned}
\mathbf{P}_{NL}(\mathbf{r}, \omega; \omega_{abc}) = 1/8 \varepsilon_0 \chi^{(3)} : [ & (\mathbf{E}_a^3(\mathbf{r}, \omega_a) e^{-j3\omega_a t} && \text{THG} && (9) \\
& + 3\mathbf{E}_a^2(\mathbf{r}, \omega_a) \mathbf{E}_b(\mathbf{r}, \omega_b) e^{-j(2\omega_a + \omega_b)t} && \text{FWM} \\
& + 3\mathbf{E}_a^2(\mathbf{r}, \omega_a) \mathbf{E}_b^*(\mathbf{r}, \omega_b) e^{-j(2\omega_a - \omega_b)t} && \text{FWM} \\
& + 6\mathbf{E}_a(\mathbf{r}, \omega_a) \mathbf{E}_b(\mathbf{r}, \omega_b) \mathbf{E}_c(\mathbf{r}, \omega_c) e^{-j(\omega_a + \omega_b + \omega_c)t} && \text{FWM} \\
& + 6\mathbf{E}_a(\mathbf{r}, \omega_a) \mathbf{E}_b(\mathbf{r}, \omega_b) \mathbf{E}_c^*(\mathbf{r}, \omega_c) e^{-j(\omega_a + \omega_b - \omega_c)t} && \text{FWM} \\
& + 6|\mathbf{E}_b(\mathbf{r}, \omega_b)|^2 \mathbf{E}_a(\mathbf{r}, \omega_a) e^{-j\omega_a t} && \text{XPM} \\
& + 3|\mathbf{E}_a(\mathbf{r}, \omega_a)|^2 \mathbf{E}_a(\mathbf{r}, \omega_a) e^{-j\omega_a t} + c. c. ] + \Pi && \text{SPM}
\end{aligned}$$

Here, symbol “ $\Pi$ ” at the end of this formula adds all possible permutations. The third-order nonlinear response results in third-harmonic generation (THG), four-wave mixing (FWM), self-phase modulation (SPM) and cross-phase modulation (XPM) nonlinear effects [10]. Figure 4 shows the related energy diagrams that schematically present the interactions involved in the various third-order nonlinear effects.

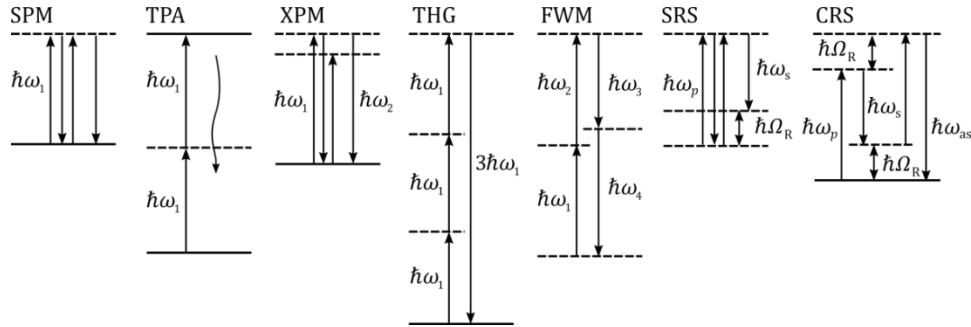


**Figure 4: Energy diagrams for the main third-order nonlinear processes: self-phase modulation (SPM), two-photon absorption (TPA), cross-phase modulation (XPM), third-harmonic generation (THG), four-wave mixing (FWM) and stimulated (and coherent anti-Stokes) Raman scattering (SRS and CRS)**

*Third-harmonic generation* is the fundamental third-order phenomenon where three incident waves at frequency  $\omega$  generate a wave at frequency  $3\omega$ .

*Four-wave mixing* is the third-order nonlinear phenomenon involving four waves. The first two FWM terms in the equation refer to the degenerate FWM case, where two incident photons have the same frequency. In this parametric process, a degenerate pump mixes with a probe signal at a distinct frequency to generate a signal at a symmetric frequency from the pump (relative to the probe), while amplifying the probe signal. The third and fourth FWM terms refer to non-degenerate FWM where the two pump waves are not at the same frequency.

*Cross-phase modulation* and *self-phase modulation* are related to the index change induced by a pump signal and that affects the propagation of the third wave. The third wave is either at a different frequency (cross phase modulation) or at the same frequency (self-phases modulation). An optically induced index change as in the form of the self-phase modulation process will be discussed in more details in section 1.1.1.2 c).

*Stimulated Raman scattering* and *stimulated Brillouin scattering* are two important third-order nonlinear processes related to the vibration response of the crystal atoms. In Raman scattering, optical phonons are excited while in Brillouin scattering, these are acoustic phonons. In this work, Brillouin scattering has not been taken into account as the relative strength of Brillouin scattering, in our structures, is around two orders of magnitude smaller than that of Raman scattering [39]. Therefore, we assume in this thesis that the third-order susceptibility has two dominant contributions, one from bound electrons and the other – the Raman contribution – from nuclei:

$$\chi^{(3)} = \chi_e^{(3)} + \chi_n^{(3)} \quad (10)$$

The Raman response in silicon will be discussed in more details in sections 1.1.3.1.

Now that the bulk material response and the third-order nonlinear effects have been introduced, we will show next how the material response affects an incident electromagnetic-wave.

#### 1.1.1.2 *The wave equation in bulk materials*

This section discusses how the linear and the nonlinear material response affect the electromagnetic wave propagation. This will be discussed in a simple scenario, where a monochromatic plane-wave propagates in a homogenous bulk material (i.e. the response does not depend on the spatial coordinate axis). The free carriers and the nonlinear response are considered in the first approximation as small perturbations to the linear response. Under these assumptions the general wave equation can be simplified and analytically solved. Although this scenario is simple, it allows us to introduce dispersion and absorption, and to understand the origin of these effects.

In addition to the constitutive relations accounting for the material response and introduced in the previous section, Maxwell's equations include divergence and curl equations. These equations can be written in the frequency domain:

$$\nabla \cdot \mathbf{D}(\mathbf{r}, \omega) = \rho_f \approx 0 \quad (11)$$

$$\nabla \cdot \mathbf{B}(\mathbf{r}, \omega) = 0 \quad (12)$$

$$\nabla \times \mathbf{E}(\mathbf{r}, \omega) = -j\omega \mathbf{B}(\mathbf{r}, \omega) \quad (13)$$

$$\nabla \times \mathbf{H}(\mathbf{r}, \omega) = \mathbf{J}_f(\mathbf{r}, \omega) + j\omega \mathbf{D}(\mathbf{r}, \omega) \quad (14)$$

The first equation introduces the free charge carrier density  $\rho_f$  as the source of the electric displacement field  $D$ . Taking into consideration that the free carriers are generated via multi-photon absorption, electrons and holes are created (and later on annihilated) by pairs and have equal densities. Therefore, we can assume, as a first approximation (neglecting the distinct diffusion processes of electrons and holes for instance) that the total density of free charge carriers is equal to zero and that they do not act as sources of the electric field. However, the optical wave drives the motion of free electrons and holes that give rise to the free charge current density  $J_f$ . The latter cannot be neglected and thus can modify the propagating optical wave as per equations (3) and (14).

The exact way the material linear and nonlinear response affect the propagation of an optical wave can be understood when turning to the wave equation that is derived from Maxwell's

equations while taking into account the constitutive relations of the material above. The wave equation includes the material response and the geometry constraints such as those imposed by the waveguide (as will be described in the next part). The wave equation in its most general form can be written as [35]:

$$\begin{aligned} \Delta \mathbf{E}(\mathbf{r}, \omega) - \nabla(\nabla \cdot \mathbf{E}(\mathbf{r}, \omega)) + k_0^2 \left(1 + \chi^{(1)}(\mathbf{r}, \omega)\right) \mathbf{E}(\mathbf{r}, \omega) \\ = -\mu_0 \left(j\omega \mathbf{J}_f(\mathbf{r}, \omega) + \omega^2 \mathbf{P}_{NL}(\mathbf{r}, \omega)\right) \end{aligned} \quad (15)$$

In this equation, the polarization has been split between its linear and nonlinear parts. The left-hand side of the equation contains the linear susceptibility, while the right-hand side contains the free carriers and the nonlinear terms.

In the first approximation the free carriers and the nonlinear terms can be considered as small perturbation to the linear response. The perturbation due to the nonlinear response is then described by the nonlinear polarization vector  $P_{NL}$  while the perturbation due to the free carriers can be defined as:

$$\delta \mathbf{P}_L = (j/\omega) \mathbf{J}_f \quad (16)$$

The wave equation can be now analytically solved assuming a homogenous bulk material. Solving the equation involves two steps: the equation is solved in the case of a linear response and then the solution is modified including the perturbation. When considering only the linear response from bound electrons, the right hand side of the general wave equation can be neglected. The wave equation can be further simplified assuming a homogenous bulk material:

$$\Delta \mathbf{E}(\mathbf{r}, \omega) + k_0^2 \left(1 + \chi^{(1)}(\omega)\right) \mathbf{E}(\mathbf{r}, \omega) = 0 \quad (17)$$

For a monochromatic plane-wave of electric field

$$\mathbf{E}(\mathbf{r}, \omega) = \text{Re}\{\mathbf{E}_0 e^{-i(\omega t - \mathbf{k}\mathbf{r})}\} \quad (18)$$

to be solution of the wave equation, its wave number  $k$  (defined as the magnitude of the wave vector  $\mathbf{k}$ ) needs to satisfy the condition:

$$k(\omega) = k_0 \left(1 + \chi^{(1)}(\omega)\right)^{1/2} \quad (19)$$

Here, the wave number in the bulk material is proportional to the wave number in free-space that is multiplied with the term containing the first order susceptibility  $\chi^{(1)}$ .

The solutions in the presence of free charge carriers and the nonlinear response are waves where the linear susceptibility term is modified by the perturbation. These modifications are all present in our SiGe-on-Si platform. We will present them in more details in the remaining parts of this section. The first part discusses how the linear response affects the wave propagation through material dispersion and absorption effects. The second part discusses how the free-carrier response affects the wave propagation through free-carrier dispersion and absorption. The third part discusses the nonlinear response. Here will be introduced the Kerr index and two-photon absorption (TPA) as well as the self-phase modulation (SPM) effect. The fourth part introduces

high-order nonlinear absorption. Finally, we will discuss the phase matching condition, which is critical for nonlinear processes to occur efficiently.

### a) Material dispersion and absorption

The linear response from bound electrons results in dispersion and absorption processes. The macroscopic parameters used to describe these effects are a frequency dependent refractive index  $n$  and extinction coefficient  $\kappa$ . These coefficients are calculated from the relation between the complex index and the linear susceptibility:

$$\tilde{n}^2(\omega) = 1 + \chi^{(1)}(\omega) \quad (20)$$

$$\tilde{n}(\omega) = n(\omega) + j\kappa(\omega) \quad (21)$$

In a weakly absorbing medium, for instance in spectral bands where semiconductor materials are almost transparent, the real and imaginary parts of the complex index can be calculated using a binomial approximation:

$$n(\omega) \approx \left(1 + \text{Re}\{\chi^{(1)}(\omega)\}\right)^{1/2} \quad (22)$$

$$\kappa(\omega) \approx \left(2n(\omega)\right)^{-1} \text{Im}\{\chi^{(1)}(\omega)\} \quad (23)$$

The refractive index and extinction coefficient can be measured in bulk materials e.g. using ellipsometry. The real part of the complex index depends on the wave frequency according to the material dispersion that can be accounted for by a Sellmeier equation for transparent dielectric materials. Material dispersion data are available for many materials such as silicon and silica [40]. The imaginary part of the optical index, the extinction coefficient  $\kappa$ , is directly related to material absorption. The real and imaginary parts of the complex index are related through the Kramers–Kronig relations [32]. This relation is often used to calculate one component when the other one is known.

Following the relation between the wave number  $k$  and the first order susceptibility given by the equation (19), the monochromatic plane-wave experiences a propagation constant  $\beta$  and an absorption coefficient  $\alpha$ :

$$k(\omega) = k_0 \tilde{n}(\omega) = \beta + j\alpha/2 \quad (24)$$

These simple relations are valid for plane-waves propagating across bulk materials, and should be modified when considering wave propagation in waveguides, as will be discussed in more details in the section “Optical response in waveguides” (1.1.2).

### b) Free charge carrier dispersion and absorption

The free-carrier response that is induced by the interaction between photon and free charge carriers (electrons and holes) generally modifies the refractive index and the absorption coefficient. In semiconductors such as silicon this complex index change must be taken into account.

In the wave equation, the free carrier response originates from the free charge current density  $J_f$  vector. Upon the assumption that the free charge current density is linearly related to the



electric field (constant  $\sigma$  in the equation (3)) this response acts as an effective linear polarization vector:

$$\delta \mathbf{P}_L = (j/\omega) \mathbf{J}_f = \varepsilon_0 \delta \chi^{(1)} \mathbf{E}(\mathbf{r}, \omega) \quad (25)$$

The contribution of free carriers can be then included as a modification of the linear susceptibility:

$$\chi^{(1)} \approx \chi_0^{(1)} + \delta \chi^{(1)} \quad (26)$$

This is equivalent to the modification of the complex index:

$$\tilde{n}(\omega) \approx \tilde{n}_0(\omega) + \delta \tilde{n}(\omega) \quad (27)$$

$$\delta \tilde{n}(\omega) = n_{fc}(\omega) + j\kappa_{fc}(\omega) \quad (28)$$

Free carriers induce a modification in both the real and the imaginary part of the refractive index. This modification can be related to the free-carrier contribution to the susceptibility as:

$$n_{fc}(\omega) \approx (2n(\omega))^{-1} \text{Re}\{\delta \chi^{(1)}(\omega)\} \quad (29)$$

$$\kappa_{fc}(\omega) \approx (2n(\omega))^{-1} \text{Im}\{\delta \chi^{(1)}(\omega)\} \quad (30)$$

Here, the free carrier induced index change is negative ( $n_{fc} < 0$ ). Its relation to the wave number gives free-carrier dispersion (FCD) and free-carrier absorption (FCA) coefficients,  $\beta_{fc}$  and  $\alpha_{fc}$ , respectively:

$$k_{fc}(\omega) = k_0 \delta \tilde{n}(\omega) = \beta_{fc} + j\alpha_{fc}/2 \quad (31)$$

Both coefficients depend on the free carrier (electrons and holes) densities  $N_e$  and  $N_h$  that are typically small in semiconductors at room temperature. However, considerable densities can be accumulated under intense pulse excitation. When operating at longer wavelengths than that associated with the semiconductor band-gap energy (e.g. 1.1 $\mu\text{m}$  in silicon at room temperature [40]), one photon does not have enough energy to excite electrons from the valence band to the conduction band. In this transparent band, free carriers can nevertheless be created in equal densities of electrons and holes through multi-photon absorption i.e.  $N_e = N_h = N_{fc}$ . Relations between free-carrier coefficients and carrier densities are generally non-trivial and in practice empirical expressions are used [41, 42]. Simplified relations are often used in the literature through introducing free-carrier dispersion and free-carrier absorption coefficients  $\sigma_c$  and  $k_c$  (or  $\mu$ ) that linearly relate the real and imaginary index to the free carrier density in the material. These coefficients are related to the coefficients ( $\beta_{fc}$  and  $\alpha_{fc}$ ) introduced above as follows:

$$k_{fc}(\omega) = k_0(k_c(\omega) + j\sigma_c(\omega)/2) \times N_{fc} \quad (32)$$

$$k_{fc}(\omega) = j\sigma_c(\omega)/2 (1 + \mu(\omega)) \times N_{fc} \quad (33)$$

Here,  $\mu$  is a dimensionless parameter calculated as  $\mu = 2k_0(\omega)/\sigma_c(\omega)$ .

The free-carrier response appears here as linear considering the linear relation between the current density and the electric field. This is valid under the assumption that the electric conductivity does not depend on the electric field. However, this is no longer correct in transparent

dielectrics under intense optical excitation, where electrons and holes are generated via multi-photon absorption (see next sub-section). In this case, the electric conductivity, which varies with electron and hole densities, depends on the electric field. Therefore, the free-carrier response is effectively nonlinear.

### c) Kerr index and two-photon absorption

This section discusses in more details the index change that is induced by the material third-order (or Kerr) nonlinear response associated with bound electrons. Indeed, the self-phase modulation (SPM) and the cross-phase modulation (XPM) effects introduced earlier cause an intensity dependent index change.

Similarly to the free carrier effects, the index change induced by the nonlinear response is related to a modification of the linear susceptibility, which becomes the effective susceptibility  $\chi_{eff}$ :

$$\chi_{eff}^{(1)} \approx \chi^{(1)} + \chi_{NL} \quad (34)$$

This is equivalent to a modification of the complex index as per:

$$\tilde{n}(\omega) \approx \tilde{n}_0(\omega) + \tilde{n}_{NL}(\omega) \quad (35)$$

$$\tilde{n}_{NL}(\omega) = n_{NL}(\omega) + j\kappa_{NL}(\omega) \quad (36)$$

The SPM induced nonlinear polarization is related to the electric field through:

$$\mathbf{P}_{NL}(\mathbf{r}, \omega) = \frac{3}{4} \epsilon_0 \chi^{(3)} : |\mathbf{E}(\mathbf{r}, \omega)|^2 \mathbf{E}(\mathbf{r}, \omega) \quad (37)$$

The effective nonlinear contribution to the susceptibility can be defined as:

$$\chi_{NL} = \frac{3}{4} \chi^{(3)} : |\mathbf{E}(\mathbf{r}, \omega)|^2 \quad (38)$$

By assuming that the nonlinear susceptibility is small compared to the linear susceptibility, the index change due the third-order nonlinearity can be calculated as:

$$n_{NL}(\omega) \approx \frac{3}{8n(\omega)} \text{Re}\{\chi^{(3)}(\omega)\} |\mathbf{E}(\mathbf{r}, \omega)|^2 \quad (39)$$

$$\kappa_{NL}(\omega) \approx \frac{3}{8n(\omega)} \text{Im}\{\chi^{(3)}(\omega)\} |\mathbf{E}(\mathbf{r}, \omega)|^2 \quad (40)$$

The index change is proportional to the square of the applied electric field, i.e. to the optical field intensity  $I$ , defined by:

$$I = \frac{1}{2} \epsilon_0 n(\omega) c |\mathbf{E}(\mathbf{r}, \omega)|^2 \quad (41)$$

The third-order nonlinear response contributes to the phase change of the propagating wave by affecting the wave number. By introducing the complex index change to the wave number, while substituting the electric field term with the intensity, we obtain two key nonlinear coefficients: the Kerr coefficient  $n_2$  and the two-photon absorption coefficient  $\alpha_2$ :

$$k_{NL}(\omega) = k_0 \tilde{n}_{NL}(\omega) = (k_0 n_2 + j \alpha_2 / 2) I \quad (42)$$

These two nonlinear coefficients are related to the third-order susceptibility as per [26]:

$$n_2 = 3 / (4 \epsilon_0 n^2(\omega) c) \operatorname{Re}\{\chi^{(3)}(\omega)\} \quad (43)$$

$$\alpha_2 = -3 \omega / (2 \epsilon_0 n^2(\omega) c^2) \operatorname{Im}\{\chi^{(3)}(\omega)\} \quad (44)$$

The imaginary part of the complex index thus depends on the optical field intensity via the two-photon absorption coefficient and the real part via the Kerr coefficient, which drives self-phase modulation. The latter is the optical equivalent of the electro-optic Kerr effect that was observed in the late 19th century. Here, the index change is induced by light, so that this effect is referred to as *the optical Kerr effect*. The Kerr coefficient value of a material can be measured e.g. using the z-scan technique.

The  $\alpha_2$  coefficient (i.e. related to the imaginary part of  $\chi^{(3)}$ ) is responsible for two-photon absorption (TPA), which involves simultaneous absorption of two photons<sup>1</sup>. Note that all multi-photon absorption effects (e.g. three- or four-photon absorption) are odd order nonlinear processes. They exist in all materials, including centrosymmetric ones.

The figure below shows the experimentally measured Kerr index and two-photon absorption coefficients in silicon [43]. The two-photon absorption coefficient becomes equal to zero for photons with energy that is less than half the silicon band-gap. In silicon this corresponds to wavelengths that are longer than 2.2  $\mu\text{m}$ .

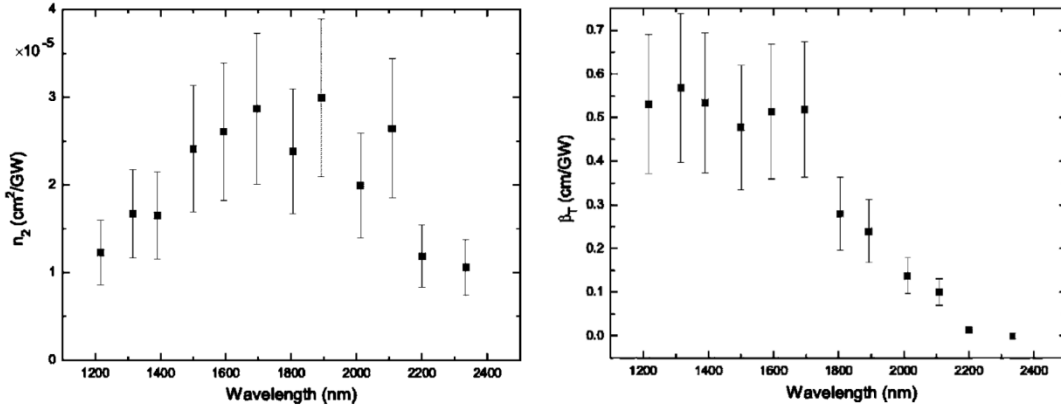


Figure 5: measured wavelength dependence of Kerr index  $n_2$  (left) and TPA coefficient (right), image – Q.Lin [43]

A critical metric to assess the performance of third-order nonlinear materials is given by the ratio between  $n_2$  and  $\alpha_2$  coefficient. This ratio is considered as a nonlinear figure of merit (FOM), which sets the efficiency of the  $\chi^{(3)}$  based nonlinear optical devices [26]:

$$FOM = \frac{1}{2\pi} \frac{k_0 n_2}{\alpha_2} \quad (45)$$

A large FOM is preferable as it corresponds to a large nonlinearity and low nonlinear loss. In crystalline silicon, for telecom wavelengths (around 1.55  $\mu\text{m}$ ) values of FOM are low, around 0.3.

<sup>1</sup> photon energy is proportional to the square of the electric field, so it effectively implies four waves

However, for wavelength that reaches half the band-gap, at  $2.2\mu\text{m}$ , the FOM increases to 4.4 [43], which considerably increases the performance of the associated nonlinear devices.

By taking into account the intensity dependent index change due to the Kerr effect, we get the following modified refractive index for the material:

$$n = n_0 + n_2 I \quad (46)$$

As a result of this, self-phase modulation occurs and effectively generates photons at frequencies that lie on either side of the input signal frequency. This can be best understood through considering an optical pulse propagating in the medium along the  $z$  axis. Such a pulse induces an instantaneous change in the refractive index according to the variation of its electric field envelope.

The instantaneous phase of this pulse at time  $t$  and position  $z$  in the medium is given by:

$$\varphi(z, t) = \omega_0 t - k_0 n z + \varphi_0 \quad (47)$$

The instantaneous frequency can then be calculated by taking the time derivative of the instantaneous phase:

$$\omega(z, t) = \frac{\partial \varphi(z, t)}{\partial t} = \omega_0 - k_0 z n_2 (\partial I / \partial t) \quad (48)$$

This equation shows that the spectral component at each time  $t$  is shifted in frequency according to the time derivative of the pulse intensity, which is proportional to the square of the electric field pulse envelope. This is illustrated in the Figure 6 below.

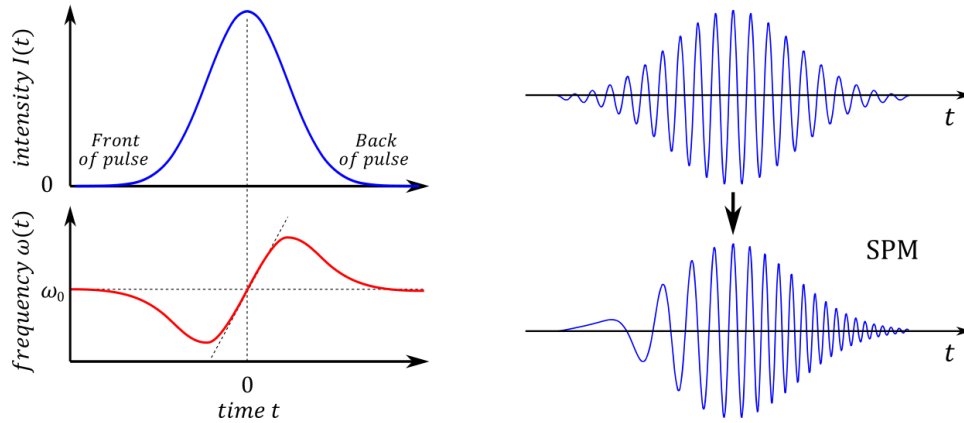


**Figure 6: Schematics of the self-phase modulation induced frequency-shift for an optical pulse propagating in a nonlinear Kerr medium. Figure on the left shows the calculated instantaneous frequency shift (with respect to the  $\omega_0$  carrier frequency of the input pulse) for a Gaussian shaped pulse. Figure on the right shows schematics of the pulse carrier wave before and after the SPM effect occurs**

#### d) High order nonlinear absorption

Higher odd order nonlinear responses result in multi-photon absorption processes. These processes are weak but may be dominant in semiconductors excited at long wavelengths. Two-photon absorption is the dominant nonlinear absorption process for photon energies lower than the bandgap but higher than the half-bandgap, three-photon absorption for energies less than half and larger than the third of the bandgap and so on. Three and four-photon absorption are fifth and seventh-order processes, respectively. As for the two-photon absorption, three- and four-photon absorption coefficients can be related to the fifth- ( $\chi^{(5)}$ ) and seventh-order ( $\chi^{(7)}$ ) susceptibilities, respectively, through:

$$\alpha_{3PA} = k_0 \frac{10}{4^2 n(\omega)} \text{Im}\{\chi^{(5)}(\omega)\} \quad (49)$$

$$\alpha_{4PA} = k_0 \frac{35}{4^3 n(\omega)} \text{Im}\{\chi^{(7)}(\omega)\} \quad (50)$$

The operation in the mid-infrared wavelength range, as in this thesis, led us to take into account multiphoton absorption up to the 4<sup>th</sup> order for our silicon germanium-on-silicon platform.

### 1.1.1.3 Phase matching condition

As already alluded to, the efficiency of nonlinear effects is conditioned by the fulfillment of two conservation laws, namely the energy conservation and the momentum conservation or phase matching condition. Below, we will use degenerate four-wave mixing (DFWM) as an example to illustrate how the energy and momentum conservation laws translate in practice.

Considering that DFWM involves elastic interactions between optical waves, their energy and momentum must be conserved. The momentum of the optical wave (or photon) is related to the propagation constant and phase of the wave, while the energy of the wave (assumed here to be monochromatic as per equation (18)) is related to the wave frequency  $\omega$  through:

$$E = \hbar\omega \quad (51)$$

$$\mathbf{p} = \hbar\mathbf{k} = \hbar\beta \quad (52)$$

The degenerate four-wave mixing is the third-order nonlinear process where two photons from the pump (at frequency  $\omega_p$ ) are absorbed and one idler photon (at  $\omega_i$ ) and one signal photon (at  $\omega_s$ ) are created. The process is efficient if the momentum and energy of the interacting waves are conserved. This is illustrated in the energy diagram in the figure below.



Figure 7: The energy diagram of the degenerate four-wave mixing process (left) and the collinear matching of the propagation constants (right)

The energy conservation simply writes in this case:

$$2\omega_p = \omega_s + \omega_i \quad (53)$$

The momentum conservation condition takes the following form for this DFWM process:

$$\Delta\beta = 2\beta(\omega_p) - \beta(\omega_s) - \beta(\omega_i) = 0 \quad (54)$$

This is illustrated in the Figure 7 right for collinear propagating waves.

If the nonlinear contribution is not taken into account, the wave number  $\beta$  at each frequency simply depends on the material dispersion. Phase matching in bulk material is then possible relying on non-collinear wave propagation or can be achieved using material birefringence. In waveguides, phase-matching can be achieved thanks to the additional contribution of the waveguide dispersion. Careful dispersion engineering, which is achievable in waveguides, is thus critical to reach the phase matching condition. This will be discussed in more detail in the section 1.1.2. Similarly, the nonlinear contribution to the phase matching condition will be effectively taken into account in the context of nonlinear waveguides, 1.1.2.3.

## 1.1.2 Optical response in waveguides

This section discusses how waveguides affect the linear and the nonlinear response. This is important as waveguides can be used to change the dispersion and thus enhance the nonlinear interactions, through enabling phase matching between the different waves. In general, the nonlinear interactions of waves with matter can be enhanced if light is spatially and temporally confined. Spatial confinement can be readily achieved using small cross-section fibers or integrated waveguides. Temporal confinement is afforded by the use of short optical pulses. Waveguides can maintain or enhance the temporal confinement in some conditions, for example, by engineering the waveguide geometry so that it presents a very low or anomalous dispersion.

In standard fibers or waveguides, light is guided in a “high” index core material with a small cross-section surrounded by a lower index cladding. Confinement and guiding is based on the total internal reflection effect i.e. light is reflected back to the core from the core-cladding interface. Standard single-mode silica fibers (see Figure 8a) confine light at telecom wavelengths to the  $8\mu\text{m}$  diameter core. However, the relatively small core-cladding index contrast in silica fibers (around 0.02) limits the degree of light confinement [10]. Improvements can be achieved using a larger index contrast, as, for example in photonic crystal fibers (PCFs – see Figure 8b) where the solid core is surrounded with a cladding formed of air holes. PCFs with a solid core smaller than  $2\mu\text{m}$  in diameter enabled the achievement of anomalous chromatic dispersion and high effective nonlinearities [9]. This in turn, led to the demonstration of the first supercontinuum covering the entire visible wavelength range [5]. In silicon-on-insulator (SOI) waveguides (Figure 8c), the spatial light confinement is further increased thanks to the large index contrast between the refractive index of the silicon (3.5 at  $1.55\mu\text{m}$ ) core and the surrounding silica material (1.4 at  $1.55\mu\text{m}$ ). Low-loss waveguides with cross-section down to around  $0.1\mu\text{m}^2$  can thus be achieved [44].

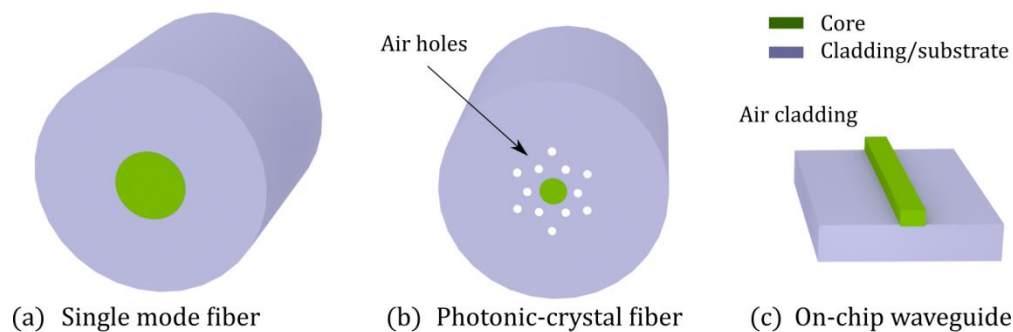


**Figure 8:** shows different light guiding platforms (a) single-mode fiber, (b) solid-core photonic crystal fiber and (c) on-chip ridge waveguide. Core cross-section is smaller in on-chip waveguides compared to the fibers.

In a dispersive medium, waves at different frequencies propagate at different velocities. Strong dispersion results in pulse temporal broadening that is induced by the walk-off between the distinct pulse frequency components. The temporal confinement of the pulse is maintained when operating in the low dispersion regime. Operating in the anomalous dispersion regime can enhance the nonlinear interactions between pulse components. Indeed, in combination with the nonlinear Kerr response, it can induce temporal pulse compression, i.e. an increase of the pulse peak power that drives the nonlinear effects. Therefore, the control of dispersion – *dispersion engineering* – is necessary to achieve efficient nonlinear interactions and provides an essential tool in nonlinear photonics to optimize nonlinear effects. In a bulk material, dispersion is determined by the material linear response, which is typically set, unless the material itself is engineered (e.g. changing the

content of the compound). Light guiding structures offer a more convenient and practical way to control dispersion. The waveguide dispersion depends on the core and cladding material dispersion, as well as on the distribution of light in the waveguide cross-section, i.e. on the waveguide geometry. Engineering the waveguide dispersion is thus possible by changing the material platform (core and/or cladding) but also by changing the waveguide shape and cross-section dimensions. Photonic crystal fibers revolutionized the field of nonlinear optics due to the strong spatial confinement and high degree of freedom for engineering the dispersion [6]. Photonic crystal waveguides have been realized on a chip, showing a great potential for on-chip dispersion engineering that has not been yet fully explored for nonlinear optics [45]. Regarding supercontinuum generation, dispersion engineering enables the creation of zero dispersion wavelengths that can be controlled by the design, as well as the achievement of broadband anomalous dispersion regimes, which contribute to increasing the bandwidth of the supercontinuum sources.

The waveguide geometry affects both the overall linear and nonlinear response experienced by the optical wave upon propagation. This section is divided into three parts. The first part discusses the waveguide contribution to the linear response. The linear response is mainly affected by the waveguide dispersion. The second part discusses the waveguide contribution to the nonlinear response. The nonlinear response is predominantly affected by the effective area of the mode. The waveguide dispersion and the effective nonlinear parameters will be introduced. The third part shows how tailoring the dispersion in waveguides can be used to enhance the four-wave mixing process.

#### 1.1.2.1 Contribution of the waveguide to dispersion

The waveguide affects both the linear dispersion and attenuation experienced by the optical signal. These effects are described by introducing effective waveguide dispersion and an additional optical propagation loss, respectively.

The impact of the waveguide geometry can be accounted for in the wave equation. The starting point to calculate the waveguide contribution is the wave equation (15) in the absence of the nonlinear and free carrier effects. In the previous section where the material response has been discussed, we have assumed a homogenous material. In waveguides, the material is different in the core and the cladding, so that the material response now depends on the spatial coordinate. Following equation (15) the wave equation can be written as:

$$\Delta \mathbf{E}(\mathbf{r}, \omega) - \nabla(\nabla \cdot \mathbf{E}(\mathbf{r}, \omega)) + k_0^2 \varepsilon_r(\mathbf{r}, \omega) \mathbf{E}(\mathbf{r}, \omega) = 0 \quad (55)$$

$$\varepsilon_r(\mathbf{r}, \omega) = \left(1 + \chi^{(1)}(\mathbf{r}, \omega)\right) \quad (56)$$

Here,  $\varepsilon_r$  is the relative permittivity that is defined in the equation (56). In the waveguide (see Figure 9) the relative permittivity depends on the coordinate in the transverse plane  $\varepsilon_r(\mathbf{r}, \omega) = \varepsilon_r(r_\perp, \omega)$  where  $r_\perp = (x, y)$ .

Solving the wave equation in this case becomes the known boundary value problem. This type of mathematical problem assumes that the solution must satisfy the boundary conditions, which are usually simple, e.g. it can be assumed that the electric field is well confined in the waveguide core and is negligible in the cladding far from the waveguide. Solutions of the wave equation are monochromatic waves expressed as:



$$\mathbf{E}(\mathbf{r}_\perp, \omega, z) = \text{Re}\{\mathbf{E}_t(\mathbf{r}_\perp, \omega)e^{-i(\omega t - \beta z)}\} \quad (57)$$

$$\mathbf{E}_t(\mathbf{r}_\perp, \omega) = E_x(\mathbf{r}_\perp, \omega)\mathbf{i}_x + E_y(\mathbf{r}_\perp, \omega)\mathbf{i}_y \quad (58)$$

with the propagation constant  $\beta$  and the field profile  $E_t$  in the transverse plane. Here, the wave propagates along a defined direction ( $z$  axis) and we assume that the electric field vector belongs to the transverse plane ( $x, y$ ) and that its amplitude does not vary long the  $z$  direction (i.e. no loss). The mode is either TE ( $E_t = E_y$ ) or TM ( $E_t = E_x$ ) polarized, which is strictly valid for a waveguide symmetric with respect to the ( $y, z$ ) plane crossing the mid-height of the waveguide core.

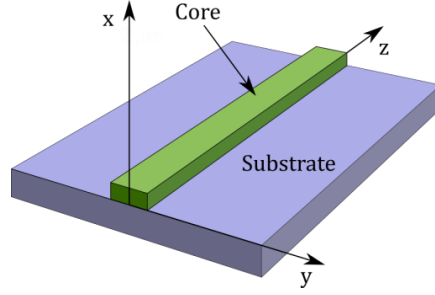


**Figure 9: Schematics of a ridge waveguide. The waveguide is oriented along the  $z$ -axis and does not have here a top cladding**

This problem is usually numerically solved using mode solver software. The wave equation can be simplified and decomposed into the longitudinal and transverse wave components:

$$(\nabla_t^2 + k_0^2 \epsilon_r) \mathbf{E}_t + \nabla_t (\epsilon_r^{-1} \nabla_t \epsilon_r \cdot \mathbf{E}_t) = \beta^2 \mathbf{E}_t \quad (59)$$

In the software, it is written in such a way that the field profile in the transverse direction corresponds to the eigenvector and the complex propagation constant as the eigenvalue of the problem. This determines a finite number of solutions, each corresponding to a distinct mode, with a specific electric field distribution, that can be sustained by the waveguide.

The waveguide modes define all the possible ways in which an optical wave can propagate across the waveguide. Here we focus on the fundamental mode which has the largest effective index. The mode propagation constant can be related to the field profile by multiplying the wave equation (59) by  $E^*$  and integrating it across the transverse plane:

$$\beta^2 = \iint (\nabla_t^2 + k_0^2 \epsilon_r) \mathbf{E}_t \mathbf{E}_t^* + \mathbf{E}_t^* \nabla_t (\epsilon_r^{-1} \nabla_t \epsilon_r \cdot \mathbf{E}_t) dx dy / \iint \mathbf{E}_t \mathbf{E}_t^* dx dy \quad (60)$$

The effective index  $n_{eff}$  corresponding to the mode above can be defined via:

$$\beta = k_0 n_{eff} \quad (61)$$

Dispersion in the waveguide is imposed by the frequency dependence of the mode propagation constant  $\beta$ . The mode propagation constant in the waveguide is smaller than that of light propagating in the core material and larger than that in the cladding material. Generally, due to the variation in the electric field distribution in the waveguide cross-section (or confinement in the core) with wavelength, the mode propagation constant is close to that in the core material at short wavelength and to the propagation constant in the cladding material at long wavelengths.

Dispersion is often described by developing the mode propagation constant in a Taylor series around the input signal angular frequency:

$$\beta(\omega) = \beta_0 + \beta_1(\omega - \omega_0) + \frac{\beta_2}{2!}(\omega - \omega_0)^2 + \frac{\beta_3}{3!}(\omega - \omega_0)^3 + \dots \quad (62)$$

In the literature, the role of the first four dispersion orders is often analyzed in cases such as pulse spreading [46], four-wave mixing [47] or the generation of dispersive waves [48].

*The first dispersion order* ( $\beta_1$ ) is the first derivative of the propagation constant  $\beta$  with respect to the angular frequency. It is, by definition, proportional to the inverse of the group velocity ( $v_g$ ):

$$\beta_1 = \frac{\partial\beta}{\partial\omega} = \frac{1}{v_g} \quad (63)$$

This parameter will be used when pulse propagation in the waveguide is considered, since the group velocity is the speed at which the envelope of a pulse propagates.

*The second dispersion order* ( $\beta_2$ ) is referred to as group velocity dispersion (GVD). This parameter gives some information about the relative velocities of distinct spectral components contained in an optical pulse. If the GVD is positive ( $\beta_2 > 0$ ), red components (longer wavelengths) travel faster than blue components (shorter wavelengths). This is called the normal dispersion regime, as it normally occurs in transparent bulk materials. If the GVD is negative ( $\beta_2 < 0$ ), blue components travel faster than red components, and this is called the anomalous dispersion regime. The second dispersion order is often represented by the dispersion parameter  $D$  (in units of ps/nm/km) that is calculated as the derivative of the first dispersion order  $\beta_1$  with respect to wavelength. Its sign is opposite to that of  $\beta_2$ , and they are related as follows:

$$D = -\frac{2\pi c}{\lambda^2} \beta_2 \quad (64)$$

*The third dispersion order* ( $\beta_3$ ) gives the slope of the group velocity dispersion and consequently information about the peak of the group velocity dispersion. The third order dispersion is the dominant dispersion term in the vicinity of a zero group velocity dispersion [46]. The role of the third-order dispersion in the supercontinuum generation has been explored in [48].

Since the waveguide affects both the real and imaginary part of the effective index, the dispersion and loss can be engineered by changing the waveguide platform or geometry.

Loss engineering is a critical task. Telecom and Datacom applications require minimizing the propagation losses, while sensing applications require a strong interaction between the optical field and the sensing medium, which typically induces light attenuation. For nonlinear optics it is essential to reduce the loss, since the nonlinear interactions accumulate across the propagation. Hence the longer the distance, the larger is the overall nonlinear effect. In principle, waveguide loss can be lowered down to the bulk material absorption loss. In this work, one of the objectives was to minimize the waveguide propagation losses, allowing for efficient supercontinuum generation. Quantitatively, the waveguide loss modifies the electric field intensity of a given mode upon its propagation along the waveguide, in the  $z$  direction, through the following expression:

$$I = I_0 e^{-\alpha z} \quad (65)$$

This equation is known as the Beer–Lambert law. Here the optical field intensity  $I$  (defined in equation (41)) of the signal that propagates in an optical medium with a linear attenuation coefficient  $\alpha$  (defined in equation (24)), experiences an exponential decay along the propagation direction  $z$ . The linear attenuation coefficient  $\alpha$  (in units of 1/cm) can be related to the propagation loss  $\alpha_{dB}$  (in units of dB/cm) as per:

$$\alpha_{dB} = \alpha \cdot 10 / \ln 10 \quad (66)$$

Dispersion engineering is referred to as designing the waveguide (e.g. by changing the waveguide dimensions) with the objective to obtain the desired dispersion profile for the intended nonlinear application. For example, low and anomalous dispersion is required to preserve the pulse duration of an optical pulse and to enhance nonlinear processes such as four-wave mixing. This will be discussed in more details in the section 1.1.2.3.

### 1.1.2.2 Modification of the nonlinearity – waveguide effective nonlinearity

In this section, the contribution of the waveguide to the nonlinear parameters will be discussed. The waveguide contribution to the nonlinear response is accounted for by defining effective nonlinear parameters.

Calculating the waveguide contribution to the nonlinear parameters requires introducing the nonlinear polarization response to the wave equation (55) in the waveguide, which gives:

$$\Delta \mathbf{E}(\mathbf{r}, \omega) - \nabla(\nabla \cdot \mathbf{E}(\mathbf{r}, \omega)) + k_0^2 \varepsilon_r(\mathbf{r}_\perp, \omega) \mathbf{E}(\mathbf{r}, \omega) = -\mu_0 \omega^2 \mathbf{P}_{NL}(\mathbf{r}, \omega) \quad (67)$$

As for bulk materials, the nonlinearity induces an index change in the waveguide. It therefore affects the propagation constant of the waveguide modes. Here, we assume that the nonlinear polarization can be, as a first approximation, considered as a small perturbation, which does not affect the waveguide mode profile. The waveguide mode profile is defined by the normalized electric field distribution of the mode in the plane perpendicular to the propagation direction. Yet, the waveguide mode intensity can be affected upon propagation, e.g. by multi-photon absorption. To describe this phenomenon, we include the wave component that evolves along the propagation direction ( $z$ ). This field component may present some additional slower variation (referred to as an envelope  $A$ ), as for a light pulse with limited duration. This can be described by the following expression, which is solution of the wave equation:

$$\mathbf{E}(\mathbf{r}_\perp, \omega, z) \approx A(\omega, z) \bar{\mathbf{E}}_t(\mathbf{r}_\perp, \omega) e^{-i(\omega t - \beta z)} \quad (68)$$

The frequency-domain pulse envelope  $A(\omega, z)$  is defined as the Fourier transform of the pulse envelope in the time-domain. The mode field profile and the propagation constant can be calculated as in the previous section. Here, the field cross-section profile  $\bar{\mathbf{E}}_t$  is normalized according to the intensity integrated along the transverse plane:

$$\bar{\mathbf{E}}_t(x, y, \omega) = \mathbf{E}_t(x, y, \omega) / \left( \iint \mathbf{E}_t(x, y, \omega) \mathbf{E}_t^*(x, y, \omega) dx dy \right)^{1/2} \quad (69)$$

The time-domain envelope  $A(t, z)$  of the electric field thus represents the square root of the electric field intensity (in units of W/m<sup>2</sup>).

The effective values of the third-order nonlinear parameters can be calculated from the nonlinear polarization term:

$$\mathbf{P}_{NL}(\mathbf{r}_\perp, \omega, z) = \frac{3}{4} \varepsilon_0 \chi^{(3)}(\mathbf{r}_\perp, \omega) : |\mathbf{E}(\mathbf{r}_\perp, \omega, z)|^2 \mathbf{E}(\mathbf{r}_\perp, \omega, z) \quad (70)$$

After introducing the expression for the electric field into this wave equation, then removing the carrier wave factor and integrating the field in the transverse plane, the nonlinear polarization becomes:

$$\mathbf{P}_{NL}(\omega, z) \approx \frac{3}{4} \varepsilon_0 \chi^{(3)}(\omega) : |A(\omega, z)|^2 A(\omega, z) \frac{\iint |\mathbf{E}_t(x, y, \omega)|^4 dx dy}{(\iint |\mathbf{E}_t(x, y, \omega)|^2 dx dy)^2} \quad (71)$$

The factor associated with the integrals defines a third-order nonlinear effective area:

$$A_{eff3}(\omega) = \left( \iint |\mathbf{E}_t(x, y, \omega)|^2 dx dy \right)^2 / \iint |\mathbf{E}_t(x, y, \omega)|^4 dx dy \quad (72)$$

The mode field confinement in the core material is defined as the fraction of the electric field intensity in the (nonlinear) core material through:

$$\Gamma = \frac{\iint_{core} |\mathbf{E}_t(x, y, \omega)|^2 dx dy}{\iint_{tot} |\mathbf{E}_t(x, y, \omega)|^2 dx dy} \quad (73)$$

This gives the following effective nonlinearity (in units of  $W^{-1}m^{-1}$ ) for the related mode propagating along the nonlinear waveguide:

$$\gamma = \frac{\omega}{c} \frac{\bar{n}_2}{A_{eff3}} \quad (74)$$

Here  $\bar{n}_2$  is the effective nonlinear index averaged across the waveguide cross-section according to the field distribution in the core/ cladding material. The waveguide contribution to the  $\gamma$  nonlinear parameter thus comes from the Kerr response of the core material and that of the cladding material. The latter has generally a much lower nonlinear index and can be neglected. Under this assumption, the effective nonlinear index can be calculated as [49, 50]:

$$\bar{n}_2 \approx \Gamma \cdot n_2 \quad (75)$$

where  $n_2$  is the Kerr index of the core material and  $\Gamma$  is associated to the mode confinement in the core and is given in equation (73).

In a large waveguide, most of the pulse intensity is confined in the core and the nonlinear parameter  $\gamma$  (or  $\bar{n}_2$ ) approaches that of the core material. In a small waveguide, the nonlinear parameter  $\gamma$  is enhanced as the effective area is decreased. However, there are optimal core dimensions that induce a minimal effective area [50]. In a waveguide that is smaller than this optimum, the mode field is less confined in the core, resulting in an increased effective area as well as a decreased effective Kerr index of the waveguide, both effectively reducing  $\gamma$ .

The waveguide nonlinear parameter  $\gamma$  is frequency dependent. This is referred to as the dispersion of nonlinearity. The waveguide contributes to the dispersion of nonlinearity through a

frequency dependent effective area given by the equation (72). The effective area can significantly vary with frequency close the mode cutoff, so the dispersion of nonlinearity must be taken into account accordingly. The dispersion of the nonlinearity is included via the shock term that will be introduced in the section 1.1.3.1.

Similarly to the third-order nonlinear effective area, effective areas corresponding to the higher odd orders of the susceptibility can be also derived as:

$$A_{eff\ 5}^2(\omega) = \left( \iint |\mathbf{E}_t(x, y, \omega)|^2 dx dy \right)^3 / \iint |\mathbf{E}_t(x, y, \omega)|^6 dx dy \quad (76)$$

$$A_{eff\ 7}^3(\omega) = \left( \iint |\mathbf{E}_t(x, y, \omega)|^2 dx dy \right)^4 / \iint |\mathbf{E}_t(x, y, \omega)|^8 dx dy \quad (77)$$

The higher-order effective nonlinearities associated to calculated effective areas can now be simply calculated by dividing the higher-order nonlinearity of the core material by the associated effective area term – see equations (49) and (50) in the section 1.1.1.2 d).

### 1.1.2.3 Phase-matching in the four-wave mixing process

In section 1.1.1.3, we have discussed the energy and momentum conservation laws in the four-wave mixing process in bulk materials. Here will be discussed how dispersion engineering in waveguides can be used to tailor the dispersion to satisfy the phase-matching condition and the consequence on the efficiency and spectral dependence of this nonlinear process.

The equation (54) was derived without taking into account the nonlinear contribution to the propagation constant. To include the nonlinear contribution it is necessary to consider how the phases of the waves are affected by the nonlinear response of the waveguide.

The phase of the degenerate pump (at frequency  $\omega_p$ ), signal ( $\omega_s$ ) and idler ( $\omega_i$ ) at distance  $z$  and after a delay  $t = z/v_g$  can be written as:

$$\varphi_p = (\beta(\omega_p) - \omega_p v_g^{-1}(\omega_p) + \gamma P_p)z \quad (78)$$

$$\varphi_s = (\beta(\omega_s) - \omega_s v_g^{-1}(\omega_s) + 2\gamma P_p)z \quad (79)$$

$$\varphi_i = (\beta(\omega_i) - \omega_i v_g^{-1}(\omega_i) + 2\gamma P_p)z \quad (80)$$

Here  $P_p$  is the peak power of the pump, and the effective nonlinearity is taken into account through the terms associated with  $\gamma$ . As a result, the pump wave experiences self-phase modulation (SPM) and induces cross-phase modulation (XPM) on the signal and the idler waves, which is twice as large as the pump SPM – see equation (9) [44]. Under the assumption that the waves propagate with almost the same group velocities, which is correct around the zero group velocity dispersion wavelength, the phase matching condition becomes [44, 47]:

$$\Delta\varphi = 2\varphi_p - \varphi_s - \varphi_i = 0 \quad (81)$$

$$\Delta\varphi/z \approx 2\gamma P_p - (2\beta(\omega_p) - \beta(\omega_s) - \beta(\omega_i)) = 0 \quad (82)$$

Since,  $\omega_p$ ,  $\omega_s$  and  $\omega_i$  are related to one another through the energy conservation law, the first term in the equation (82) is a phase mismatch due to the nonlinearity  $\gamma$ , while the second term is the linear or dispersive phase-mismatch ( $\Delta\beta$ ) given by the equation (54). The dispersion terms are often developed into a Taylor series around the pump angular frequency (see equation (62)). This allows us to express the phase matching condition as:

$$\Delta\varphi/z \approx \gamma P_p + \sum_{n=2m} \frac{\beta_n(\omega_p)}{n!} (\omega_i - \omega_p)^n = 0 \quad (83)$$

The equation shows that the phase-matching condition depends only on the even order dispersion parameters evaluated at the pump frequency [47]. Since the nonlinear term is positive, in order for the phase-matching condition to be satisfied the dispersion term must be negative. Far from the zero-GVD wavelength, the  $\beta_2$  dispersion term is dominant, and the dispersion term will be negative if the  $\beta_2$  coefficient is negative. For the phase-matching condition to be satisfied, the pump must then experience low anomalous dispersion. Near the zero-GVD wavelength, where  $\beta_2$  is close to zero, the higher-order dispersion terms (such as  $\beta_4$ ) can be dominant. The phase-matching condition can then be satisfied in the normal dispersion regime if the  $\beta_4$  dispersion term is negative and its absolute value is stronger than the  $\beta_2$  dispersion term.

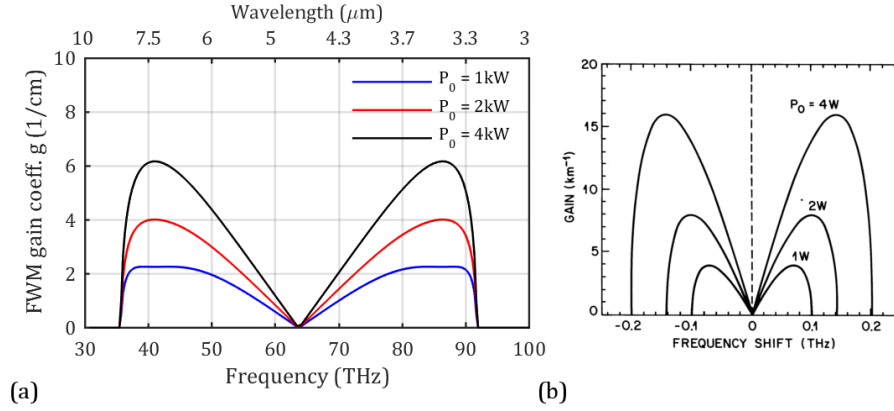


**Figure 10: (a) FWM gain coefficient ( $g$ ) calculated with respect to the pump frequency (at 64 THz) for 1, 2 and 4 kW peak pump power associated with the dispersion profile of the  $6.0\ \mu\text{m} \times 4.2\ \mu\text{m}$  cross-section SiGe-on-Si waveguide presented in Figure 13, (b) FWM gain coefficient in a fiber operating in a strong anomalous dispersion regime where  $\Delta\beta \gg \gamma P_p$  - image Agrawal [10]**

To illustrate how critical the phase matching condition can be, we show how it impacts the spectral dependence of the FWM efficiency below.

The signal gain ( $G_s$ ) in a four-wave mixing process can be defined by the ratio between the output and input signal power ( $P_s$ ) through [44, 47]:

$$G_s = P_s^{out}/P_s^{in} = 1 + (\gamma P_p/g)^2 \sinh^2(gl) \quad (84)$$

here  $l$  is the waveguide length,  $P_p$  is the pump power,  $\Delta\beta$  is the linear dispersive phase-mismatch (given in equation (54)) and  $g$  is the exponential gain coefficient defined as [44, 47]:

$$g^2 = (\gamma P_p)^2 - (\gamma P_p - \Delta\beta/2)^2 \quad (85)$$

Figure 10 (a) shows the calculated gain coefficient  $g$  for the dispersion profile presented in Figure 13 (a) and (b), which is close to the dispersion of the SiGe/Si waveguides studied in this PhD. It is calculated for a pump in the anomalous dispersion at the  $4.7\ \mu\text{m}$  ( $\sim 64\ \text{THz}$ ) pump at different pump power levels (1, 2 and 4 kW). For a pump in the anomalous dispersion ( $\beta_2 < 0$ ) the gain coefficient has two maxima symmetrically positioned in frequency on either side of the pump. The maxima are set to the frequencies with the maximum linear phase-mismatch ( $\Delta\beta/2$  equal to  $3.3\ \text{cm}^{-1}$ ), which partially compensates for the nonlinear phase contribution beyond 2kW ( $\gamma P_p$  equal to 2.25, 4.5 and  $9\ \text{cm}^{-1}$  to at 1, 2 and 4kW, respectively). By contrast, for a pump in the normal dispersion ( $\beta_2 > 0$ ) the gain coefficient  $g$  is generally equal to zero unless the  $\beta_4$  dispersion term is negative and its contribution is stronger than of the  $\beta_2$  dispersion term.

In the previous case, the group velocity dispersion at the pump wavelength is low ( $\beta_2 \approx -3 \times 10^{-26}\ \text{s}^2/\text{m}$ ) giving a relatively small linear contribution to the phase mismatch, with respect to the nonlinear contribution. Therefore, the nonlinear phase mismatch can be fully compensated for by the (weak) linear phase mismatch only at very low pump power ( $P_p < 1\text{ kW}$ ). By contrast, when operating in a strong anomalous dispersion regime, the linear contribution can be stronger, so as to overcome the nonlinear phase shift for a wide range of pump power. In this case, the spectral positions of the gain maxima continuously shift in frequency further and further from the pump for increasing peak pump power (see an example of this case in Figure 10 b).

### 1.1.3 Third-order nonlinear pulse propagation in waveguides

This section presents a model for the propagation of optical pulses in nonlinear waveguides. This model will be used to describe the supercontinuum generation dynamics. To extend the bandwidth of the supercontinuum, the generation of dispersive waves is often exploited [7]. The last section discusses the phase-matching in the dispersive-wave generation process.

#### 1.1.3.1 Model for pulse propagation in waveguides

The evolution of the pulse envelope along the propagation distance in the nonlinear waveguide can be numerically calculated. The model accurately describes how the pulse propagation is affected by nonlinear effects, giving insight into the underlying physics of the pulse propagation in the nonlinear waveguide. This section presents the theory of pulse propagation in nonlinear optical waveguides, which is based on the Generalized Nonlinear Schrodinger Equation (GNLSE). The GNLSE includes all effects presented above, i.e. dispersion, loss, free-carrier and third-order nonlinear effects including stimulated Raman scattering. This equation has been widely used by the optical fiber community [10] and can be applied to on-chip waveguides [36]. The modeling of pulse propagation was used to support experimental nonlinear measurements and largely contributed to better understanding nonlinear phenomena in waveguide structures. It is also a useful engineering tool, providing design guidelines for specific applications.

The starting point to derive the GNLSE is the wave equation with the free-carrier and nonlinear effects included. The wave equation (15) can be written in a compact form as:

$$\Delta \mathbf{E}(\mathbf{r}, \omega) - \nabla(\nabla \cdot \mathbf{E}(\mathbf{r}, \omega)) + k_0^2 \varepsilon_r(\mathbf{r}, \omega) \mathbf{E}(\mathbf{r}, \omega) = -\mu_0 \omega^2 (\delta \mathbf{P}^{(1)} + \mathbf{P}_{NL}(\mathbf{r}, \omega)) \quad (86)$$

Here, the free-carriers and nonlinear effects are introduced via the polarization terms in the right-hand side of the equation. The wave equation can describe the temporal and spatial evolution of the unidirectional forward-propagating pulse along the waveguide. This light pulse can be defined as in the previous section by equation (68):

$$\mathbf{E}(\mathbf{r}_\perp, \omega, z) \approx A(\omega, z) \bar{\mathbf{E}}_t(\mathbf{r}_\perp, \omega) e^{-i(\omega t - \beta z)} \quad (87)$$

The pulse is modeled as a carrier wave of frequency  $\omega$  propagating along the  $z$  direction with a linear polarization of the electric field  $E_t(\mathbf{r}_\perp, \omega)$  in the transverse plane (associated here with the fundamental waveguide mode) and modulated by the pulse envelope  $A(\omega, z)$ . The pulse and field profile are normalized in such a way that the absolute square value of the envelope  $A(t, z)$  corresponds to the pulse intensity ( $\text{W}/\text{m}^2$ ), while the field profile, normalized in the transverse plane (see section 1.1.2.2), contains information about the pulse polarization and mode area.

The GNLSE is derived for the input pulses starting from the wave equation above. The pulse model and the polarization terms are substituted in the wave equation. We chose as a reference the local pulse frame moving along with the pulse (at a speed equal to its group velocity) and remove the carrier wave from the equation. Considering the effective parameters originating from the presence of the waveguide, the evolution of the pulse envelope along the propagation direction can be calculated in the local frame. The Generalized Nonlinear Schrodinger Equation can be then developed under the slowly varying envelope approximation [35]. It describes the evolution of the electric field envelope in the presence of free-carriers and third-order nonlinear effects as per:



$$\frac{\partial A}{\partial z} = -\frac{\alpha}{2}A + \sum j^{m+1} \frac{\beta_m}{m!} \frac{\partial^m A}{\partial t^m} - \frac{\sigma}{2}(1 + j\mu)N_c A + j \left( \frac{\omega_0}{c} \frac{n_2}{A_{eff_3}} + j \frac{\alpha_{2PA}}{2A_{eff_3}} \right) \left( 1 + j\tau_{sh} \frac{\partial}{\partial t} \right) \left( A \int_{-\infty}^t R(t') |A(t-t')|^2 dt' \right) \quad (88)$$

Most of the parameters in this equation have been already introduced. The terms on the right hand side are related to absorption, dispersion, free-carrier (absorption and refraction) effects and third-order nonlinear effects, respectively. The third-order nonlinear effects include the response from bound electrons and the Raman response from the material. The response function  $(t)$  models the response from the bound electrons as instantaneous and the response related to the nuclei vibrations as delayed. Raman effects are accounted for by the Raman response function  $h(t)$  that contributes to the overall third-order nonlinear response as dictated by the fraction  $f_R$  through:

$$R(t) = (1 - f_R)\delta(t) + f_R h_R(t) \quad (89)$$

The analytical form of the Raman response function derives from the Raman gain spectrum that can be experimentally measured. The Raman gain spectrum is usually fitted by a Lorentzian shape function characterized by the full-width at half maximum  $\Gamma_R$  and the frequency shift from the pump  $\Omega_R$ . These parameters are well known for silica [51] and silicon [52]. The Raman response function derives from the Raman gain spectrum in two steps. In the first step, the Raman spectral response  $H_R(\Omega)$  is calculated from the Raman gain spectrum. The imaginary part of  $H_R(\Omega)$  is proportional to the Raman gain. The real part of  $H_R(\Omega)$  is related to the Raman-induced refractive index change and can be obtained from the imaginary part by using the Kramers–Kronig relations. In the second step, the Raman response function  $h_R(t)$  is calculated as the inverse Fourier transform of  $H_R(\Omega)$ . The Raman response function for silicon can be written in the form [10]:

$$\begin{aligned} h_R(t) &= 0 & t < 0 \\ h_R(t) &= (\tau_1^{-2} + \tau_2^{-2})\tau_1 e^{-t/\tau_2} \sin(t/\tau_1) & t > 0 \end{aligned} \quad (90)$$

Here, the time constants, the Raman response time  $\tau_1$  and the phonon lifetime  $\tau_2$  are reciprocal to the Raman frequency shift  $\Omega_R$  and the Raman gain bandwidth  $\Gamma_R$  (i.e.  $\tau_1 \approx 1/\Omega_R$  and  $\tau_2 = 1/\Gamma_R$ ). The values of the constants  $\tau_1$ ,  $\Omega_R$ ,  $\tau_2$  and  $\Gamma_R$  in silicon are 12.2 fs,  $2\pi \times 15.6$  THz, 3 ps and  $\pi \times 105$  GHz respectively [36]. The fractional contribution of the Raman response to the third-order nonlinearity  $f_R$  is found to be 0.043 [52]. The Raman gain spectrum in silicon is narrowband and 1000 times stronger at its maximum than the very broad gain spectrum in silica [36]. The relatively narrow and strong Raman gain of silicon has been used to demonstrate light amplification and laser operation [53-55]. However, considering pulse propagation in silicon waveguides and the spectral content around the input pulse spectrum, the Raman effect impact is generally low due to the large Raman frequency shift and the relatively short on-chip waveguide lengths (around the cm scale).

The parameter  $\tau_{sh}$  in the GNLS equation (88) is related to the shock term that accounts for the dispersion of the nonlinearity and thus allows for modeling ultra-short pulses (i.e. with sub picosecond duration). The nonlinear parameters of the optical waveguide take effective values that are governed by the effective mode areas defined as per equations (72), (76) and (77). Both the nonlinear index  $n_2$  and the effective area  $A_{eff}$  (see equation (72)) are frequency dependent. Some additional dispersion of the nonlinearity comes from the frequency dependence of the effective area  $A_{eff}$  [37]. This can be included as an additional correction to the shock term:

$$\tau_{sh} = \tau_0 - \left( n_{eff}^{-1} \frac{\partial n_{eff}}{\partial \omega} \right) - \left( A_{eff}^{-1} \frac{\partial A_{eff}}{\partial \omega} \right) \quad (91)$$

with the derivatives of the effective index and effective area calculated at the carrier frequency  $\omega_0$ .

Multi-photon absorption has to be included when operating at long wavelengths, like in the mid-infrared. Three- and four-photon absorption terms can be included in the right-hand side of the equation as additional terms respectively given by:

$$T_{3PA} = -\frac{\alpha_{3PA}}{2A_{eff5}^3} |A|^6 A \quad (92)$$

$$T_{4PA} = -\frac{\alpha_{4PA}}{2A_{eff7}^4} |A|^8 A \quad (93)$$

The GNSLE is coupled with an additional rate equation that governs the dynamics of free-carrier generation/recombination. This equation is derived starting from the continuity equation, assuming (in our case) that free-carriers are generated as electron/hole pairs, through multi-photon absorption only [36]. Taking into account two-, three- and four-photon absorption effects, this equation can be written as:

$$\frac{\partial N_c}{\partial t} = \frac{\alpha_{2PA}}{2\hbar\omega_0} \left( \frac{|A(t)|^2}{A_{eff3}} \right)^2 + \frac{\alpha_{3PA}}{3\hbar\omega_0} \left( \frac{|A(t)|^2}{A_{eff5}} \right)^3 + \frac{\alpha_{4PA}}{4\hbar\omega_0} \left( \frac{|A(t)|^2}{A_{eff7}} \right)^4 - \frac{N_c}{\tau} \quad (94)$$

The choice of the multi-photon absorption terms to be included depends on the operation wavelength. Two-photon absorption vanishes at long wavelengths when photon energy is less than half the bandgap. In this thesis, only four-photon absorption was considered as the pump wavelength (around  $4\mu\text{m}$ ) corresponds to photon energy larger than the quarter bandgap but less than the third of the bandgap energy (e.g.  $1.1\mu\text{m}$  in silicon). The last term in this equation stands for free-carrier recombination with  $\tau$  the free-carrier lifetime that is usually in the nanosecond range.

The GNLSE equation is usually numerically solved using the split-step Fourier method (SSFM). In this method as the first step (at distance  $z$ ) the linear response is taken into account in the frequency domain and in the second step (at distance  $z + dz$ ) the free-carrier and nonlinear response is calculated in the time domain. This method is efficient as it relies on the Fast Fourier transform calculations of the envelope between two steps. However, the accuracy of the approximation used here depends on the step size  $dz$  [56], so there is a trade-off between the speed of this numerical method and the accuracy achieved. In order to have both accurate and fast calculations adaptive step-size techniques have been developed. In this thesis we used the version of the split-step Fourier method from J. M. Dudley and J. R. Taylor [34].

The solution obtained from the SSFM gives the pulse envelope in both the time-domain and the spectral domain calculated at each distance step along the propagation. A result example will be shown in the section 1.1.3.3 where the supercontinuum generation dynamics will be discussed.

### 1.1.3.2 Solitons

As will be discussed in the next section, solitons have played a major role in the driving mechanisms at the origin of the generation of supercontinuum. Solitons are pulses that maintain their shape while propagating in a dispersive medium. They appear as analytical solutions of a

simplified version of the GNLS (88) that includes only the second-order dispersion and the nonlinear Kerr optical response  $\gamma$ . These particular solutions occur as a consequence of the interplay between self-phase modulation and second order dispersion. Self-phase modulation generates a positive chirp in the pulse as in Figure 6. Blue-shifted components are generated near the trailing edge and red-shifted components near the leading edge of the pulse [10]. In the anomalous dispersion regime, blue-shifted components are faster, i.e. anomalous dispersion introduces a negative chirp in the pulse. Therefore, the SPM induced chirp counteracts the chirp due to anomalous dispersion (see Figure 11). If the two effects balance each other, a fundamental soliton is formed, i.e. a pulse that propagates without temporal and spectral distortion. If the nonlinearity is stronger, a high-order soliton can be formed and eventually lead to temporal pulse compression.

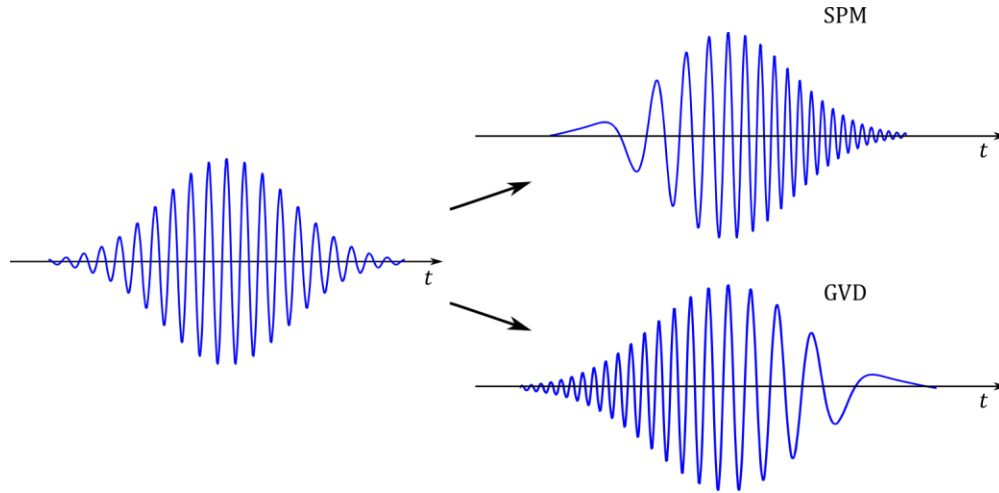


**Figure 11 : schematics of the pulse carrier-wave affected by the self-phase modulation effect (SPM - top right) and by the anomalous group velocity dispersion (GVD - bottom right).**

The soliton order is dictated by the relative importance of dispersion and nonlinearity in a specific nonlinear waveguide and for given input pulse characteristics. To quantify this, typical length scales are generally defined, associated with the dispersion and nonlinearity, respectively. The second-order dispersion length is defined by the equation:

$$L_D = \frac{T_0^2}{|\beta_2|} \quad (95)$$

where  $T_0$  is the full-width at maximum of the temporal envelope of the pulse. It corresponds to the propagation distance over which the accumulated dispersive phase reaches  $2\pi$ . This roughly corresponds to the distance where the pulse is broadened in time by a factor 2 (depending on the pulse shape).

The nonlinear length is defined by the equation:

$$L_{NL} = \frac{1}{\gamma P_0} \quad (96)$$

where  $P_0$  is the peak power at the entrance of the waveguide.

The nonlinear length is the propagation distance over which the accumulated nonlinear phase reaches  $2\pi$  (assuming there is no loss). When either the dispersion or nonlinear length is much shorter than the waveguide length, the related (dispersion or nonlinear) effect plays a significant role during pulse propagation. The shorter the characteristic length, the stronger is the associated effect. The relative values of dispersion and nonlinear lengths define the soliton order  $N$  via:

$$N^2 = \frac{L_D}{L_{NL}} \quad (97)$$

A fundamental soliton corresponds to the situation where  $L_d$  is equal to  $L_{NL}$ , both being close to the physical length of the waveguide. Figure 12 (a) shows the evolution of the pulse in the time and spectral domain under these conditions, as it propagates along the  $z$  direction: the pulse remains undistorted upon propagation.

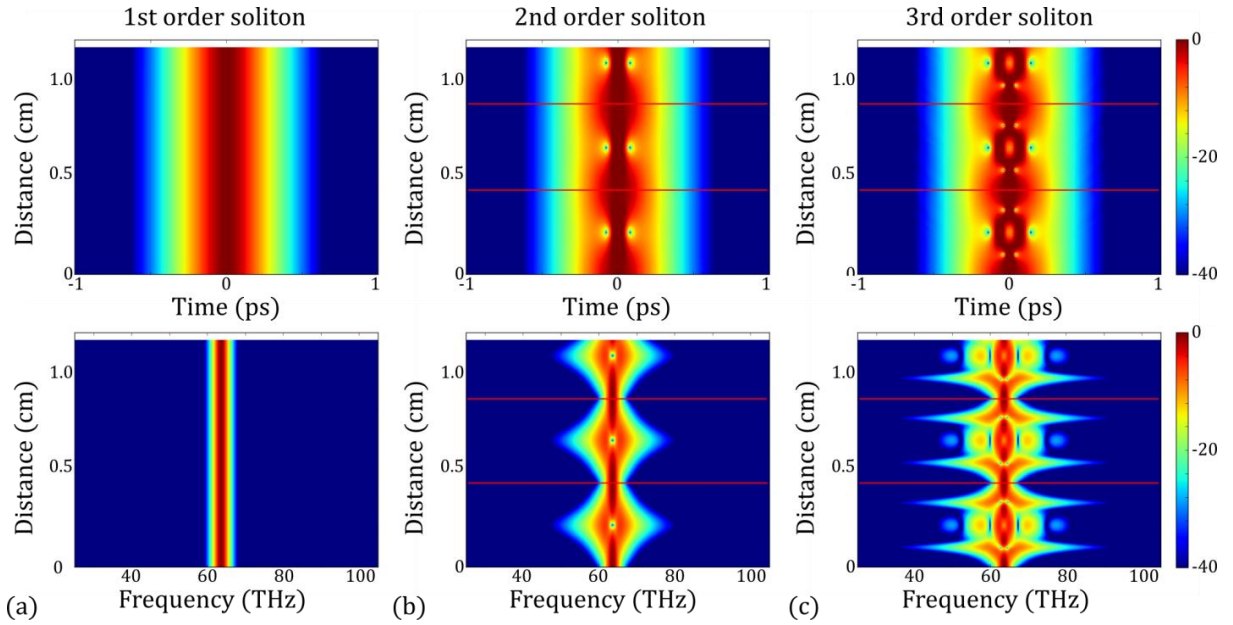


Figure 12: Calculated time (top) and spectral evolution (bottom) of (a) a fundamental, (b) a second order and (c) a third order soliton. Simulations are performed taking into account  $\beta_2 = -5.14 \times 10^{-24} \text{ s}^2/\text{m}$ , and 1, 4 and 9 kW pump peak power, 210 fs hyperbolic secant pulse centered at  $4.71 \mu\text{m}$  (64 THz). Dispersion length ( $L_D$ ) is equal to 0.28 cm while nonlinear lengths ( $L_{NL}$ ) are equal to 0.28, 0.07 and 0.03 cm, respectively.

Figure 12 (b) and (c) show the evolution for a soliton of orders 2 and 3. A periodic beating in the time and spectral domain can be observed along the  $z$  direction in these cases. The spatial period can be calculated as per [10]:

$$z_0 = \frac{\pi}{2} L_D \quad (98)$$

The Figures 12 (b) and (c) are plotted for more than two periods ( $2z_0 = 0.87 \text{ cm}$ ). The propagation of the high-order solitons (2<sup>nd</sup> and 3<sup>rd</sup> order) shows how the pulse is periodically compressed in time, which is accompanied by the pulse spectral broadening. At the length equal to the half of the soliton period we can observe the pulse splitting to spectral components after which the pulse recovers its initial pulse shape.

We show in the next section how this has been used to generate supercontinuum.

### 1.1.3.3 Supercontinuum generation dynamics

This section will present key concepts and parameters necessary to understand the dynamics of supercontinuum generation relying on soliton fission and dispersive wave generation processes. For more details about the supercontinuum generation dynamics, the readers are referred to J.M. Dudley et al. [37].

To illustrate the dynamics of supercontinuum generation, we will follow how an intense mid-infrared 210 fs ultra-short pulse evolves temporally and spectrally as it propagates in a silicon germanium (SiGe) dispersion-engineered waveguide on a silicon substrate. We chose this platform and this wavelength range since this case is close to the experiments that will be reported in this manuscript. However, this example might not exhibit all the typical features associated with supercontinuum generation in standard silica fibers (such as Raman self-frequency shift). We will describe the different physical processes as they arise and the associated key parameters and length scales.

The waveguide dispersion presented in the Figure 13 (a) and (b) is calculated for a  $6.0 \times 4.2 \mu\text{m}^2$  cross-section  $\text{Si}_{0.6}\text{Ge}_{0.4}/\text{Si}$  ridge waveguide. The SiGe/Si waveguide of nonlinearity  $\gamma = 0.36$  ( $\text{W}^{-1}\text{m}^{-1}$ ) is pumped at  $4.7 \mu\text{m}$  wavelength in the anomalous dispersion regime close to the first zero dispersion wavelength located at  $4.6 \mu\text{m}$  (see Figure 13b). High-order dispersion coefficients at the pump wavelength are calculated to be  $\beta_2 = -2.93 \times 10^{-26}$   $\text{s}^2/\text{m}$  and  $\beta_3 = 3.02 \times 10^{-39}$   $\text{s}^3/\text{m}$ . The input pulse is a Fourier-transform limited 210 fs ultra-short optical Gaussian pulse with 2 kW peak power. The numerical model includes the Raman effect and takes it as equal to that of crystalline silicon.

**Table 1: Summary of parameters used in the simulation of supercontinuum generation of Figure 13**

Parameter	Value	Dispersion	Value calc. at $\lambda_0 = 4.7 \mu\text{m}$ (TM)
$\lambda_0$ ( $\mu\text{m}$ )	4.7	$\beta$ (1/m)	$4.70 \times 10^6$
$T_{\text{FWHM}}$ (fs)	210	$\beta_1$ (s/m)	$1.21 \times 10^{-8}$
$P_p$ (W)	2000	$\beta_2$ ( $\text{s}^2/\text{m}$ )	$-2.93 \times 10^{-26}$
		$\beta_3$ ( $\text{s}^3/\text{m}$ )	$3.02 \times 10^{-39}$
$A_{\text{eff}}$ ( $\mu\text{m}^2$ )	14.74	$\beta_4$ ( $\text{s}^4/\text{m}$ )	$-3.24 \times 10^{-54}$
$L$ (cm)	5	$\beta_5$ ( $\text{s}^5/\text{m}$ )	$2.14 \times 10^{-68}$
$\alpha$ (dB/cm)	0.38	$\beta_6$ ( $\text{s}^6/\text{m}$ )	$1.99 \times 10^{-81}$
$n_2$ ( $\text{cm}^2/\text{W}$ )	$4.0 \times 10^{-14}$	$\beta_7$ ( $\text{s}^7/\text{m}$ )	$-3.56 \times 10^{-94}$
		$\beta_8$ ( $\text{s}^8/\text{m}$ )	$1.83 \times 10^{-107}$
		$\beta_9$ ( $\text{s}^9/\text{m}$ )	$-5.14 \times 10^{-121}$
		$\beta_{10}$ ( $\text{s}^{10}/\text{m}$ )	$8.67 \times 10^{-135}$
		$\beta_{11}$ ( $\text{s}^{11}/\text{m}$ )	$-8.41 \times 10^{-149}$
		$\beta_{12}$ ( $\text{s}^{12}/\text{m}$ )	$3.66 \times 10^{-163}$

In this example, multi-photon absorption and free-carrier effects are neglected, and the long wavelength loss and cutoff have not been taken into account. Under these assumptions, and starting from the equation (88), the GNLSE used in our simulations takes the following form:

$$\frac{\partial A}{\partial z} = -\frac{\alpha}{2}A + \sum_{j^{m+1}} \frac{\beta_m}{m!} \frac{\partial^m A}{\partial t^m} + j \left( \frac{\omega_0}{c} \frac{n_2}{A_{eff_3}} \right) \left( 1 + j\tau_{sh} \frac{\partial}{\partial t} \right) \left( A \int_{-\infty}^t R(t') |A(t-t')|^2 dt' \right) \quad (99)$$

The values of the parameters used in the simulations are summarized in Table 1. The pulse evolution (temporally and spectrally) along the 5cm long waveguide is shown in Figure 13 (c) and (d) respectively.

In addition to the dispersion length and nonlinear length defined as per equations (95) and (96) in the previous section, the dispersion length associated with the third-order dispersion term is often used to compare the relative importance of the  $\beta_2$  and  $\beta_3$  terms [10]. It is defined by:

$$L'_D = \frac{T_0^3}{|\beta_3|} \quad (100)$$

The additional terms in the GNLSE (e.g. the higher order dispersion, SRS or even noise) with respect to those included in the simplified version of the NLSE (section 1.1.3.2) perturb the ideal soliton evolution that was described in the previous section. In particular, the periodic beating is typically not observed and soliton fission occurs after a characteristic soliton fission length equals to:

$$L_{fiss} = \frac{L_D}{N} \quad (101)$$

Soliton fission manifests as a breakup of the higher-order soliton into its constituent fundamental solitons due to perturbations by the higher-order effects [10].

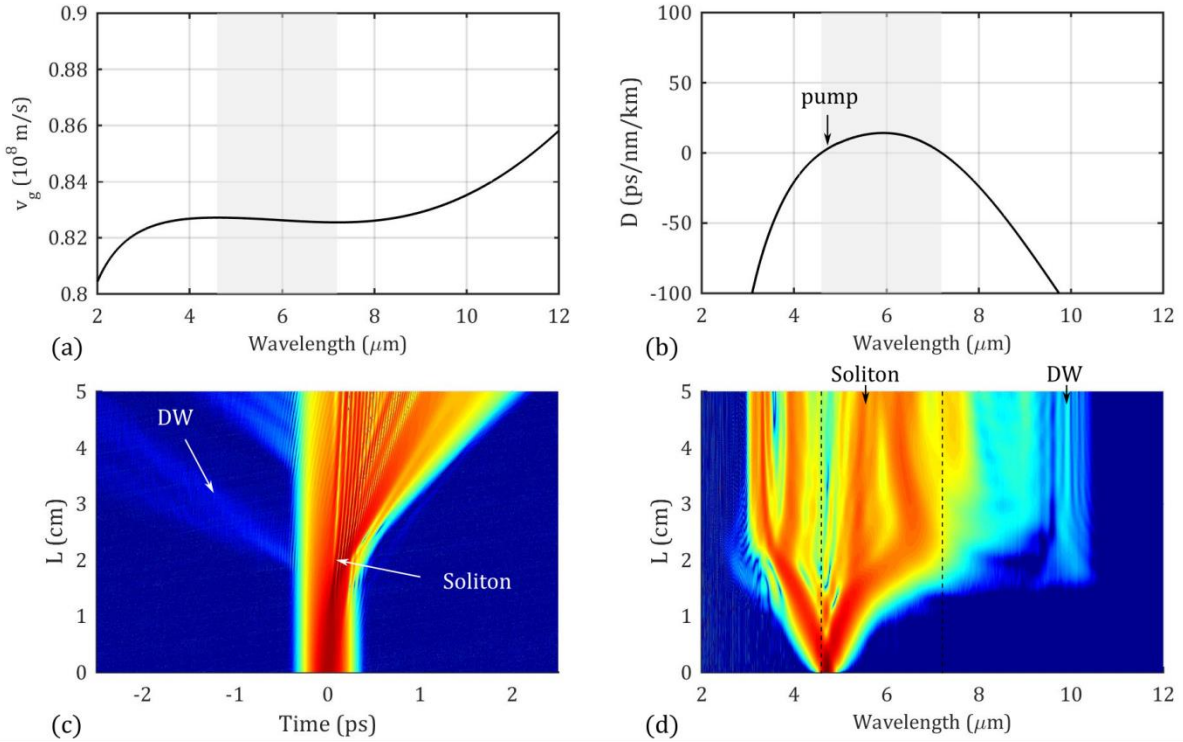


**Figure 13:** Calculated group velocity  $v_g$  (a) and group velocity dispersion  $D$  versus wavelength, (b) Calculated evolution of the pulse envelope (normalized power in dB scale) over time (c) and wavelength (d) along the propagation distance  $L$ . The simulations parameters used here are summarized in Table 1

The soliton fission length corresponds to the distance at which the higher order soliton (of order  $N$ ) attains its maximum bandwidth and its maximum temporal pulse compression. For our waveguide example above, the characteristic lengths are:  $L_D = 55$  cm,  $L'_D = 67$  cm,  $L_{NL} = 0.14$  cm and  $L_{fiss} = 2.74$  cm and the soliton order  $N = 19$ .

The supercontinuum generation dynamics can thus be divided into several stages. The first stage can be characterized by the pulse compression triggered by the higher-order soliton formation. This is followed by the soliton fission and dispersive wave generation. In the third stage, four-wave mixing and scattering effects (such as SRS) define the final spectrum shape.

The initial pulse compression stage occurs at a distance shorter than the fission length. The time-domain pulse compression is driven by self-phase modulation (SPM) over-balancing anomalous group velocity dispersion (GVD). SPM manifests in the initial symmetric spectral broadening (see spectrum in Figure 13d at 1cm distance). The pulse compression can be generally seen in the time-domain, however in our case it is not significant due to the low dispersion that is associated with a nearly flat group velocity curve and long dispersion lengths (the dispersion length is much longer than the waveguide length).

Soliton fission occurs here at around 2 cm, which is slightly shorter than the soliton fission length given by equation (101). This difference can be attributed to the strong third-order dispersion.

The soliton fission process is followed by subsequent dispersive wave radiation, which will be explained in the next section. The Figure 13 (c) shows, in the time domain, the dispersive wave radiation at around 2 cm propagation distances. It manifests here (considering the group velocity curve) as a radiation at long wavelengths ( $\lambda \sim 10$   $\mu\text{m}$ ) which is thus faster than the solitons in the central region of the spectrum (around  $\lambda = 6$   $\mu\text{m}$ ) according to the group velocity curve. The dispersive wave wavelength can be obtained from the phase-matching conditions that will be introduced below and depends on the soliton peak power and frequency.

In the last stage, four-wave mixing and scattering effects (such as SRS) determine the final spectrum shape. After a propagating distance long enough, the pulse components disperse and do not overlap in time so the supercontinuum generation spectrum no longer evolves and is only affected by the linear loss.

We detail in the next section the underlying mechanisms associated with dispersive wave generation, which has been extensively exploited as a way to extend the bandwidth of supercontinuum. Specific conditions, governed by phase matching, allow us to accurately predict the wavelength associated with this useful radiation.

### 1.1.3.4 Phase-matching in the dispersive-wave generation process

Dispersive waves (DWs) are closely related to supercontinuum generation and they provide a way to extend the supercontinuum bandwidth at the extreme parts of the spectrum. Dispersive waves have been exploited to achieve an octave-spanning supercontinuum generation in the silicon-on-insulator platform [7, 13, 14]. This section discusses the phase matching condition required for the dispersive-wave generation process, which typically appears as a radiation leakage associated with a soliton [57].

The phase of the soliton at frequency ( $\omega_s$ ) and of a dispersive-wave at frequency ( $\omega_d$ ) can be written as:

$$\varphi_s = \left( \beta(\omega_s) - \omega_s v_g^{-1}(\omega_s) + \frac{1}{2} \gamma P_s \right) z \quad (102)$$

$$\varphi_d = \left( \beta(\omega_d) - \omega_d v_g^{-1}(\omega_d) \right) z \quad (103)$$

Here, the nonlinear contribution to the phase of the soliton is calculated for the fundamental soliton assuming the condition  $L_D = L_{NL}$  [10]. Under the assumption that the waves propagate with the same group velocity, the phase-matching condition between the soliton and dispersive wave becomes:

$$\Delta\varphi = \varphi_s - \varphi_d = 0 \quad (104)$$

$$\Delta\varphi/z \approx \beta(\omega_s) + \beta_1(\omega_s)(\omega_d - \omega_s) + \frac{1}{2} \gamma P_s - \beta(\omega_d) = 0 \quad (105)$$

The dispersion terms in the equation are often developed into a Taylor series around the soliton frequency ( $\omega_s$ ) giving:

$$\Delta\varphi/z \approx \frac{1}{2} \gamma P_s - \sum_{n \geq 2} \frac{\beta_n(\omega_s)}{n!} (\omega_d - \omega_s)^n = 0 \quad (106)$$

The resulting phase-matching condition in the dispersive wave generation process is quite different from the one associated with four-wave mixing processes given by the equation (83). The equation above shows that the phase-matching is affected by all dispersion orders (even and odd). Here the second-order dispersion term  $\beta_2$  calculated at the frequency  $\omega_s$  must be negative assuming that the soliton can be maintained only in the anomalous dispersion regime. Therefore, the phase-matching condition cannot be satisfied by taking into account only the  $\beta_2$  dispersion term, making it necessary to consider higher-order dispersion terms.

The third-order dispersion term  $\beta_3$  is the most important term when considering the DW generation process. In the case when only the second and third-order dispersion terms are taken into account, to satisfy the phase-matching condition between a soliton and a blue-side dispersive wave (where  $\omega_d > \omega_s$ ) the  $\beta_3$  term must be positive, and between a soliton and a red-side dispersive wave the  $\beta_3$  term must be negative. Roy S. et al. showed that the dispersion strength of the dispersive wave depends on the third-order dispersion [48].



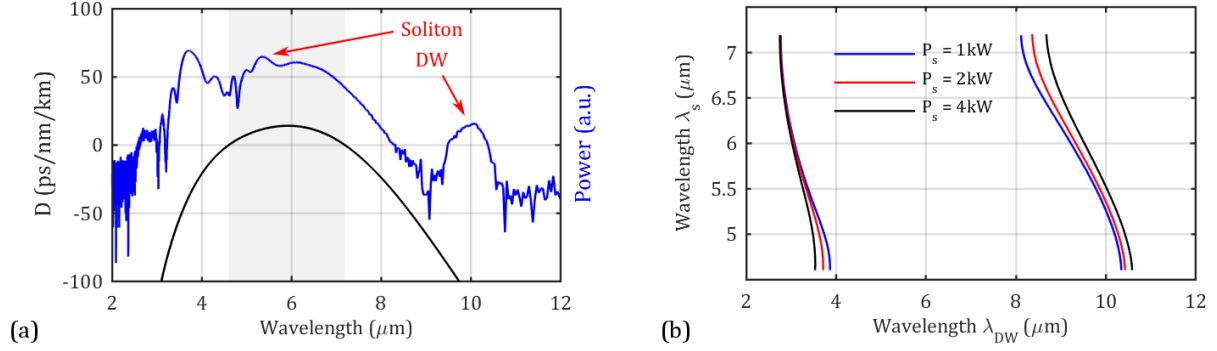


**Figure 14 : (a) Group-velocity dispersion (black) with the superimposed spectrum from Figure 13 calculated at 2cm distance (blue), DW is generated at a wavelength around 10 $\mu$ m, (b) calculated phase-matched dispersive wave wavelength for different soliton wavelengths (y-label) and 1, 2 and 4 kW soliton peak-powers.**

In the case when the dispersion terms up to the fourth-order are taken into account, dispersive-waves can be generated at both sides of the pulse spectrum. Figure 14a) shows the dispersive-wave at around 10 $\mu$ m wavelength that is generated in the normal dispersion region on the other side of the second zero-GVD wavelength ( $\lambda > 7\mu$ m) with respect to a soliton in the anomalous dispersion region. Figure 14b) shows phase-matching calculated using the equation (106) for different soliton wavelengths and peak-powers. The phase-matching is satisfied for the soliton positioned at a wavelength between 5 and 5.5 $\mu$ m. Regarding dispersive-waves at the blue side of the spectrum, in this particular case, it is difficult to identify them as they overlap with the part of the spectrum that is transferred to the normal dispersion due to SPM and FWM in the initial phase of the pulse propagation (see Figure 13). The phase-matching condition shows that dispersive-waves at the blue-side should be generated, in principle, in a band between 3 and 4  $\mu$ m, i.e. on the short wavelength side of the first zero-GVD wavelength.

The generation of the blue-shifted components associated with the short wavelength dispersive wave creates photons that carry more energy than the photons associated with the initial soliton at longer wavelengths. This indicates that the dispersive wave generation process must be a nonlinear process that most likely involves the interaction of multiple photons. Dispersive waves were initially interpreted as the FWM process between the Stokes and anti-Stokes waves, but their frequencies do not satisfy the FWM condition. Besides, this seems to be contradicted by the fact that dispersive waves can be observed in numerical simulations when neglecting the Raman effect [10]. More recently, significant effort has been done to interpret the dispersive wave generation as FWM or cascaded FWM process between SPM generated components and/or solitons [58, 59].

After having presented the theoretical background and simulation tools that will be used to analyze and understand our experimental results on the generation of supercontinuum in SiGe/Si waveguides in the mid-IR, we present next the state of the art of supercontinuum in chip-based platforms.

## 1.2 Silicon photonics

CMOS (complementary metal-oxide-semiconductor) technology is one of the most sophisticated technologies today. Several generations of researchers and engineers contributed in achieving a density of 100 million transistors per square millimeter on a chip [60]. The integration of high transistor density is possible in a mature and fully automated fabrication process. This process is highly reliable, as it results in a very small number of defects per number of produced devices. The CMOS technology relies on an abundant and cheap material – silicon – and this is one of the key factors enabling large scale “mass” production resulting in compact, cheap and abundant electronic devices. Initially exclusively used by the electronics industry, CMOS technologies have been feeding for more than 15 years the field of integrated photonics leading to the recent development of silicon photonics [61, 62].

Over the last decade, silicon photonics has attracted significant attention for sensing and spectroscopy applications in the mid-infrared wavelength range [63-66]. In this context, achieving mid-infrared supercontinuum generation in a silicon chip is highly desirable. The main objective of this thesis is to explore silicon-based platform – silicon germanium-on-silicon – for mid-infrared supercontinuum generation on a silicon chip. We give here an introductory overview on the recent development aspects that are relevant to this topic, and organized in three parts:

1. Silicon photonics in the near-infrared
2. Silicon photonics in the mid-infrared
3. Supercontinuum generation on silicon chip

The first part – silicon photonics in the near-infrared – briefly introduces the fields of silicon photonics and nonlinear silicon photonics that have been primarily explored in the near-infrared around telecom wavelengths. The second part – silicon photonics in the mid-infrared – discusses applications in the mid-infrared wavelength range and germanium based CMOS compatible platforms for the mid-IR. The silicon germanium-on-silicon platform and associated advantages for the envisaged applications will be introduced. The third part – supercontinuum generation on a silicon chip – reviews the literature on supercontinuum in silicon based waveguides and discusses the objectives of this thesis in more details.

### 1.2.1 Silicon photonics in the near-infrared

Silicon and its native oxide, silica – the two main materials in the CMOS technology – are good photonics materials for optical data transmission. Silica fibers are one of the key elements in the photonics industry. They are used in fiber lasers and amplifiers, fiber-optic sensors, and thanks to their extremely low loss (a fraction of a dB/km) at telecom wavelengths in transmission links for long-distance optical communications. Fiber optics has played a major role in the information and communication revolution enabling the rapid growth of the Internet. Very high aggregated data rates can be achieved by multiplexing information over multiple wavelengths (WDM). In addition, optical fibers allow for techniques such as polarization division multiplexing (PDM) and quadrature amplitude modulation (QAM) to increase the data throughput even further. In 2018, a record of ~160Tb/s total data-rate over a single, 1000km long, fiber has been reported [67].

Photonics technologies could play also a major role in interconnects. In electronics, data are processed and transferred electrically. Transistors are very efficient in performing logic operations. However, electrons carry information with significant losses and heat dissipation even across short distance metallic wires. These losses are the main source of high power consumption in modern data-centers. Counter intuitively, high power dissipation in data-centers comes from transmitting data and not from high-performance computing. In addition, these losses are significantly limiting the clock rate, i.e. the computing performance, leading to the so called “interconnect bottleneck” [68]. A solution envisioned to this problem is to develop chip-to-chip optical data transfer, i.e. to replace, at least partially, electrical wires by optical interconnects (see Figure 15 left). Introducing photonics on a silicon chip (silicon photonics) could have a tremendous impact in reducing the huge power consumption of modern data centers.

While fiber optics relies on silica, silicon photonics uses silicon to guide light. The large refractive index of silicon (around 3.5 at 1.55  $\mu\text{m}$ ) compared to silica (around 1.4) provides a large core – cladding index contrast. This, in turn, results in strong light confinement and an order of magnitude smaller waveguide cross-section than in silica fibers (see the section 1.1.2). Nanotechnology used for photonics allows for advanced photonics device engineering in the form of photonic crystal or nanoscale slot waveguides that can improve the degree of light confinement and the control of light properties [66]. Silicon photonics holds therefore a great potential for integrating various photonic components such as waveguides, grating-couplers, splitters, interferometers, rings and race-track resonators on a single chip [69] and the possibility of developing hybrid photonics/electronics platform [69]. However, fully integrated photonic systems require an integrated laser which still remains a challenge on a silicon chip [70]. Silicon is a good material to transfer light, but due to its indirect bandgap, the silicon radiative efficiency is very low, forbidding the realization of lasers from this material [71]. Nevertheless, until an efficient monolithic solution (e.g. Ge-on-Si [72] or GeSn [73]) is reached, the hybrid integration of III-V lasers (e.g. indium phosphide) on a silicon chip shows promising results (Figure 15 right) [74].

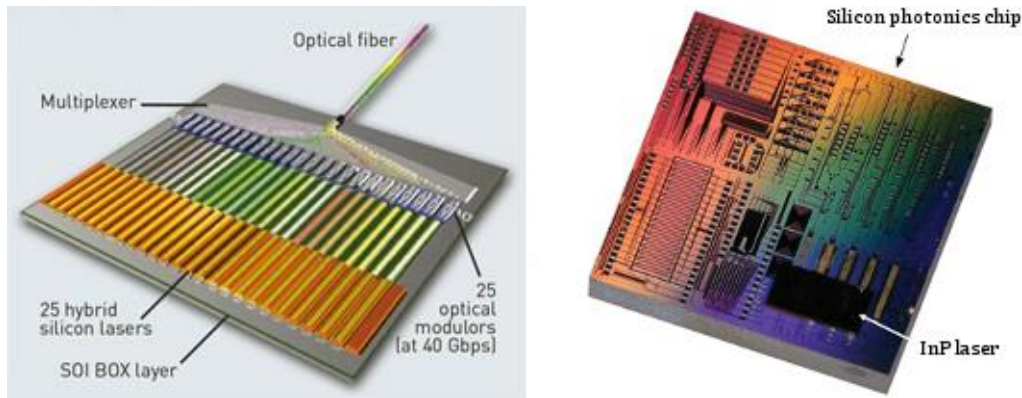


**Figure 15: (left) Intel's concept of a terabit optical transmitter integrated on a silicon chip, image - Intel, (right) hybrid integration of the indium phosphide (InP) laser on a silicon photonics chip, image - B. Song et al. [74]**

Nonlinear silicon photonics [26], allowing for frequency conversion as well as the generation of new frequencies, has emerged with the main objective to process ultra-fast optical data signals and to bridge the gap between optics and electronics [68]. Silicon has a 2 to 3 orders of magnitude stronger nonlinearity than silica. The third-order nonlinear response in silicon is ultra-fast, of the order of few femtoseconds, allowing for Tb/s applications. Broadband and ultra-fast nonlinear applications are possible due to the strong silicon nonlinearity enhanced in a small cross-section silicon waveguide [27]. Several critical nonlinear photonic functions for ultrafast optical signal processing have been reported, such as modulators, multiplexers/demultiplexers and wavelength convertors among others [38].

Electro-optical modulators in silicon are based on free-carrier effects. The phase of an optical signal can be changed by injecting free carriers using metal-oxide-semiconductor transistors, PN or PIN diodes. Figure 15 left shows Intel's approach to achieve 1Tb/s optical communication between optical chips. Here, the signals emitted, in parallel, by a series of on-chip lasers are electro-optically modulated before multiplexing to a single optical fiber. In 2015, an optical communication link between a memory unit on one chip and a processing unit on the other chip has been demonstrated by a US consortium involving IBM [75]. This demonstration relied on the co-integration of photonics and microelectronic devices using fully CMOS manufacturing approaches. In this work an optical modulator based on a PN junction has been used to modulate light from an external laser. The on-off keying modulation speed relying on the fast free carrier effects in PIN diodes can be as high as 70Gb/s [38]. Data throughput can be further increased using PDM-16-QAM modulation scheme up to 320 Gb/s [76].

Four-wave mixing in silicon waveguide has been exploited to all-optically de-multiplex 10 Gb/s signal, that can be processed in the electrical domain, from high data rate signal at 160 Gb/s [77] and 1.28 Tb/s [78]. In this scenario sub-picosecond pulses at 10 GHz repetition rate, used as a pump, have been synchronized with 1.28 Tb/s signal to generate de-multiplexed 10 Gb/s idler data. In principle, using this method, 1.28 Tb/s signal can be de-multiplexed to 128 channels at 10 Gb/s.

These promising results led to the concept of all-optical signal processing on a chip that could be used in all-optical networks to transfer data "on the fly" without conversion to the electronic domain [79]. Together with these advances, significant results such as third harmonic generation [45], ultra-fast optical monitoring [80] and efficient correlated photon pair generation [81] have been achieved, expanding the opportunities offered by nonlinear integrated optics.

However, the significant two-photon absorption (TPA) of crystalline silicon (c-Si) at telecom wavelengths is such that its nonlinear figure of merit (see equation (45)) is in the range of  $FOM = 0.3$  to  $0.5$  (see section 1.1.1.2 c) – much less than what is ideal for nonlinear optics applications. This has significantly limited the efficiency of the reported nonlinear devices [82]. This low FOM of c-Si in the telecom band is a fundamental material property that cannot be improved. If we want to operate in the telecom band, which has now become a standard in the telecommunications field, the search for a new platform with a better FOM is necessary to overcome the limits of c-Si. Some of the proposed solutions include silicon nitride ( $Si_3N_4$ ) [83] and hydrogenated amorphous silicon (a-Si:H) [84] and even silicon carbide (SiC). On the other hand, if we allow ourselves to change the operation wavelength, crystalline silicon and its derived alloys (such as SiGe) remain relevant because they have a higher FOM at longer wavelength (typically at short mid-infrared wavelengths around  $2.5 \mu m$ ). In the context of this thesis, we have explored the non-linear properties of silicon germanium in the mid-infrared range.

## 1.2.2 Silicon photonics in the mid-infrared

Nonlinear silicon devices operating beyond the TPA absorption limit in silicon at  $2.2\mu\text{m}$  shows a great potential for communications applications. In this wavelength range, compact and efficient silicon modulators have been demonstrated [85, 86]. However, as optical communication applications are mainly conducted at telecom wavelengths where silica fibers have low transmission loss, the main interest in the mid-infrared lies in the possibility to perform high-sensitivity molecule sensing and, more generally, in spectroscopy applications. It is well acknowledged that silicon photonics applications in the mid-infrared will be different from data and telecom applications in the near-infrared [64].

Mid-infrared radiation is important for numerous applications in fundamental research, life-science [87], healthcare, industry, environment and security [88]. The boundary between the near-infrared and mid-infrared can vary in the scientific literature depending on the field of research [66]. Throughout this manuscript, I consider that near-infrared (near-IR) spans from  $0.7$  to  $2.5\mu\text{m}$ , mid-infrared (mid-IR) from  $2.5$  to  $15\mu\text{m}$  and far-infrared (far-IR) from  $15\mu\text{m}$  to  $1\text{mm}$ . A simple distinction can be made between near- and mid-IR radiations. Earth atmosphere is transmitting near-IR and absorbing mid-IR radiation. Therefore, the main photonics applications in the near-IR are related to optical communications – free space and fiber optic – while the main applications in the mid-IR are based on molecular sensing and spectroscopy.

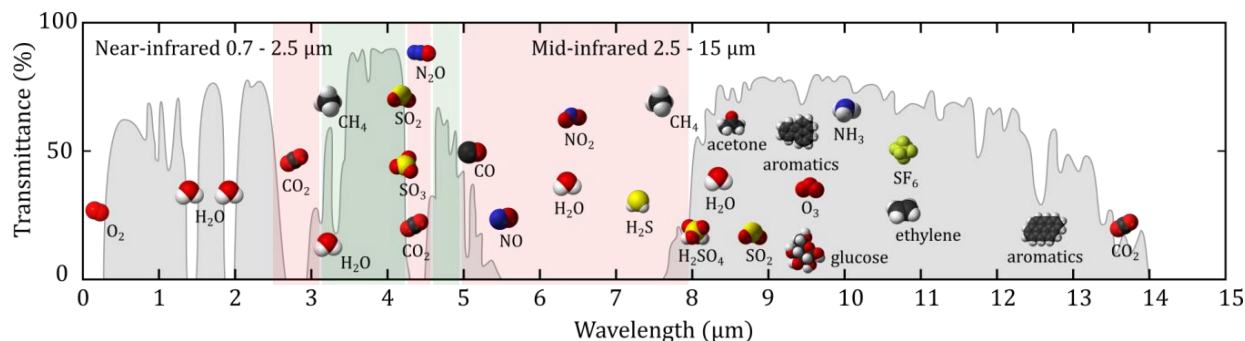


**Figure 16:** shows transparency of Earth's atmosphere. Molecules have strong absorption in windows located around  $3\mu\text{m}$ ,  $4\mu\text{m}$  and from  $5$  to  $8\mu\text{m}$ . Atmospheric windows from  $3$  to  $5\mu\text{m}$  can be used for the secure free-space communications.

Each molecule has distinct spectral absorption lines corresponding to its rotational and vibrational transitions. Most of the molecules have their fundamental lines called “molecular fingerprints” in the mid-infrared (Figure 16). These spectral lines are narrow and strong compared to broad and weak overtones in the near-infrared. Detecting molecules and their concentration in a low volume sample is possible by measuring the absorption spectrum of a relatively broad light. This method is termed as the molecular absorption spectroscopy.

Molecules can be detected in a gas or liquid phase. Sensing of greenhouse gasses (e.g. carbon-dioxide or methane) and toxic gasses at trace levels can be utilized for environmental monitoring and security applications. Detecting carbon-dioxide can be also useful for the control of industrial processes as the carbon-dioxide is commonly a byproduct. In healthcare, analyzing the molecular content of exhaled breath has been explored for early cancer detection. The absorption spectroscopy of molecules in liquid phase is important for water quality control, biological and

chemical sensing. An important application is the non-invasive monitoring of the glucose level in blood, considering the increasing population with diagnosed diabetes [89, 90].

One of the main objectives of silicon photonics in the mid-infrared is to develop low cost sensing devices. This point sensor (or lab-on-a-chip) consists of a light source, a sensing area such as an evanescent waveguide and a detector.

This thesis is focused on the development of a broadband mid-IR source, which is an important building block to realize the on-a-chip mid-infrared sensing system (see schematics in Figure 2) [90]. A pulsed pump laser is required to achieve a supercontinuum source. In this work, as a pump, we used a state-of-the-art turnkey mid-infrared femtosecond source. Such pump lasers are generally high-priced and bulky. For commercial use, low-cost and compact pulsed lasers are required. Until a suitable pulsed laser is achieved on-a-chip, all-fiber mode-locked lasers, which are operating around 3  $\mu\text{m}$ , are the best solution in terms of price and size. In 2016, researchers had developed holmium doped ZBLAN fiber laser emitting 180 fs pulses at 2.9  $\mu\text{m}$  wavelength outside the water vapor absorption band [91, 92]. More recently, emission of 80 fs pulses has been reported at 2.9  $\mu\text{m}$  from a Germania glass ( $\text{GeO}_2$ ) fiber laser [93].

Molecules can be detected on-a-chip by measuring the attenuation transmission through the interaction of the evanescent field of a waveguide mode with its surrounding environment. This method is referred to as evanescent field spectroscopy [94]. The attenuation caused by absorption then depends on the waveguide length as well as on the field extension into the surrounding analytes. In order to increase the interaction length across a small footprint, compact spiral waveguides can be used [90]. To increase the evanescent field interaction with the sample, slot waveguides where the significant part of the mode is confined in a central air-gap containing some bio-molecules to detect might be a good solution [69, 95]. How much the field extends into the surrounding environment depends on the waveguide geometry but also on the mode polarization. The interaction with molecules in a liquid phase can be controlled with microfluidic systems on a chip.

The spectra altered by the molecular resonances can be analyzed using a spectrometer. Two schemes for the detection of the mid-infrared spectra are the most significant: Fourier transform-based and dual-comb spectroscopy [96]. Significant and promising results have recently been achieved in this field. In 2018 Qiankun L. et al. realized an integrated multi-aperture spatial heterodyne Fourier-transform spectrometer (SHFTS) for operation beyond 5  $\mu\text{m}$  wavelength [97]. At the same time, on-chip supercontinuum has been used in a dual-comb spectroscopy scheme for carbonyl sulfide detection [98].

Most of the mid-infrared was inaccessible to conventional lasers until the invention of quantum-cascade lasers (QCLs) in 1990s [99-101]. At the same time, mid-IR fiber lasers have been developed [102]. The gain medium in fiber lasers is a mid-IR transparent fiber doped with rare-earth elements such as thulium, erbium, ytterbium or dysprosium. In this technology, the dopant choice determines the laser emission wavelength [88]. In the context of accessing a broad part of the mid-infrared spectrum at once, for molecule sensing, nonlinear photonics is particularly relevant as it enables frequency conversion and parametric amplification. This allows for achieving tunable or broadband sources operating in the mid-IR.

On-chip broadband sources such as those enabled by supercontinuum generation are particularly important for spectroscopy, owing to their large bandwidth and high brightness. The supercontinuum source allows for accessing multiple wavelengths altogether. This permits reliable and parallel detection of multiple molecules. High spectral brightness when operating in the mid-IR can enable high sensitivity molecule detection. Molecules can be detected at trace levels measured as ppb (parts per billion) [103]. The coherence of the supercontinuum can further improve sensitivity, enabling label-free and ultra-fast molecular detection [104].

Optical materials for mid-IR spectroscopy on silicon-based chips should exhibit a wider transparency spectral window as compared to traditional silicon photonic materials used for telecom applications. Silicon-on-insulator is the dominant CMOS compatible platform for both electronics and silicon photonics in the near-IR. However, the transmission window of this platform is limited up to around  $3.5\mu\text{m}$  due to the absorption in the silica substrate [65]. Several material platforms have been proposed for on-chip operation in the mid-IR (see the transparency of materials in Figure 17). The first solution is to use advanced designs such as suspended or pillar silicon waveguides in the SOI platform so as to remove silica [105, 106]. The second option is to use amorphous materials such as chalcogenide glasses [15, 107]. The third solution is to explore on other CMOS compatible materials (group IV materials). We discuss below these group IV materials and their applications for mid-IR nonlinear integrated photonics.

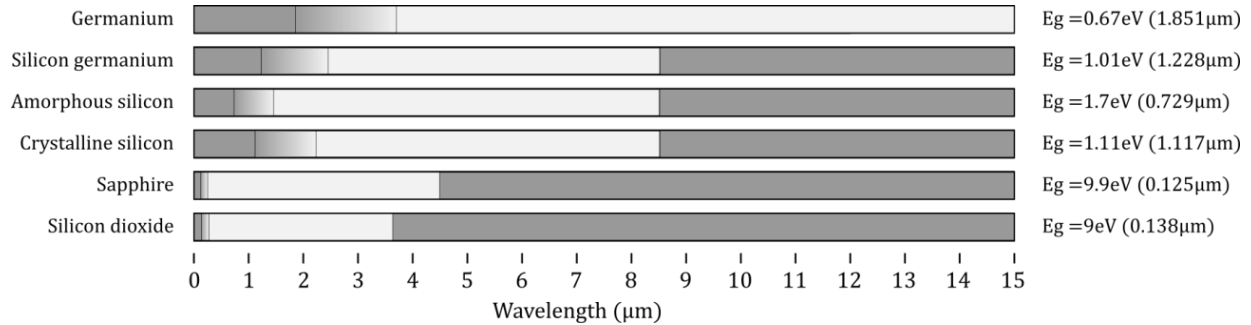


Figure 17: Transparency window of several CMOS compatible semiconductor materials that are listed on the left [64, 66, 108]. The related bandgap and the wavelength limit beyond which two-photon absorption disappears are indicated by the first and second vertical line from the left, respectively. The transparency window (denoted by the white areas) is defined as the bend where the absorption loss is below  $2\text{dB/cm}$ .

### 1.2.2.1 Group IV materials

The detrimental effects of TPA in silicon can be mitigated when operating at wavelengths longer than  $2.2\mu\text{m}$  – beyond the two-photon absorption limit. In addition to low nonlinear loss, silicon has a wide transparency band up to  $9\mu\text{m}$ . However, when employed in standard CMOS platforms – silicon-on-insulator (SOI) [109] – transmission is limited to  $3.7\mu\text{m}$  [108] due to the onset of absorption in the silica substrate (Figure 17). To address this issue, the use of group IV (group 14 in the periodic table of elements) elements and especially germanium has been proposed. Germanium has been long considered as an important photonic material due to its strong nonlinearity and its wide mid-IR transparency [110]. The use of germanium for nonlinear applications is closely related to the development of mid-infrared photonics, since germanium is not transparent in the near-infrared at telecom wavelengths [111, 112].



Mid-infrared operation brings to silicon photonics several important technological advantages. The scaling of the waveguide size with wavelength improves the coupling efficiency from fibers as compared with that related to (small cross-section) waveguides operating in the near-infrared. Conventional CMOS mass manufacturing processes, in particular ultraviolet lithography, are compatible with typical mid-IR device dimensions. Finally, scattering loss is intrinsically less at longer wavelengths, resulting in a reduced impact of the surface roughness [66]. The larger cross section typically improves the field confinement in the nonlinear core material, but this comes to the detriment of the mode effective area, which equally increases. The latter reduces, in turn, the nonlinear parameter  $\gamma$ . In this thesis I will study the potential trade-off related to the pros and cons of this platform for nonlinear optics.

Optical properties of silicon [113], germanium [114] and silicon-germanium compounds [115] have been studied in the 1950s. The refractive index of silicon and germanium over the entire transparency windows has been accurately measured as early as 1957 [116]. Raman scattering in silicon and germanium have been reported in 1967 [117]. The refractive index of germanium is larger than that of silicon (4.02 of germanium compared to 3.42 of silicon at 4  $\mu\text{m}$  wavelength), allowing for the realization of germanium waveguides on silicon substrates.

#### 1.2.2.2 Germanium

Before germanium was discovered, its existence was predicted and this element was labeled as “eka-Silicon”. Germanium is the first element below silicon in the same group of the periodic table. While silicon is one of the most abundant elements in Earth's crust, germanium is a fairly rare element. Like silicon, germanium is a semiconductor that conducts electricity when doped with phosphorus (n type semiconductor) or with boron (p type semiconductor). In the form of p – n junctions, germanium can be used as diodes or photodetectors. The first transistor was made of germanium [118]. It is therefore a part of the microelectronics industry since its beginnings. Germanium photodetectors are sensitive to light at near-infrared wavelengths. Germanium is used also in scintillators to detect gamma radiation. Today, it is mostly used in fiber-optics, where the fiber core is doped with Germanium ( $\text{GeO}_2$ ) to increase the core-cladding index contrast. Due to the germanium's transparency in the mid-infrared, it is used to create bulk optics for mid-IR lenses [119].

In the context of integrated photonics, germanium is used for integrated photodetectors that is now a mature technology. Germanium photodetectors are indeed a key technology in receivers for Datacom applications [120]. The small energy difference between the direct and indirect bandgap transitions makes germanium a suitable candidate for integrated lasers. Germanium alloys such as silicon-germanium-tin ( $\text{SiGeSn}$ ) and germanium-tin ( $\text{GeSn}$ ) are good candidates for hetero-structure lasers [64]. More recently, germanium has been envisioned as the material of choice for mid-infrared nonlinear photonics on-a-chip owing to its wide transparency up to 15 $\mu\text{m}$ , large refractive index and strong nonlinearity [111]. The third-order nonlinearity  $\chi^{(3)}$  in germanium [121] is stronger than that of crystalline silicon (see Figure 18) [43, 108, 122].

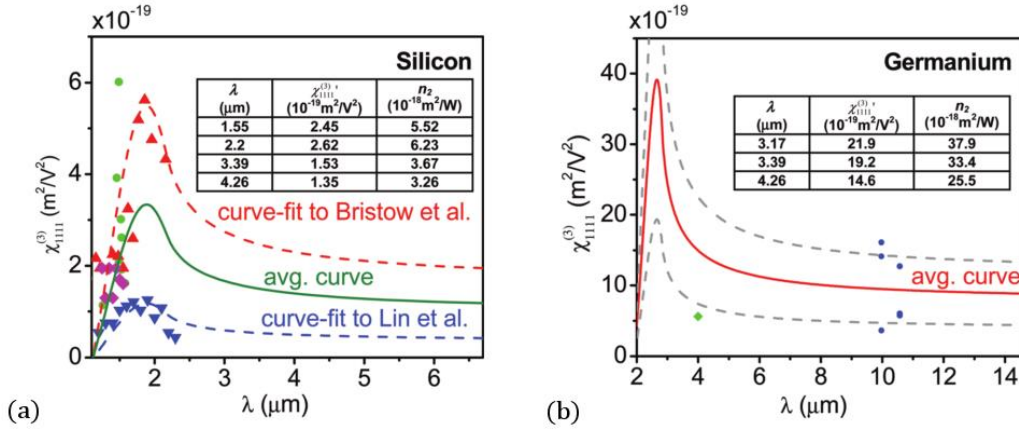


Figure 18: Experimentally extracted  $\chi^{(3)}$  nonlinearity in silicon (a) and germanium (b), img. – N. K. Hon et al. [108]

Figure 18 presents an overview of the different nonlinear  $\chi^{(3)}$  values that have been reported in silicon and germanium. Based on experimentally measured values, Hon N. K. [108] et al. plotted an average curve predicting the silicon and germanium nonlinearities over a wide wavelength ranges, i.e. from 1 to 7  $\mu\text{m}$  in silicon (green curve) and from 2 to 15  $\mu\text{m}$  in germanium (red solid curve). The Kerr index ( $n_2$ ) in the mid-IR (at 4.26  $\mu\text{m}$ ) for germanium is 25.5 ( $\text{m}^2/\text{V}^2$ ), which is much stronger than the maximum 3.26 ( $\text{m}^2/\text{V}^2$ ) value for silicon at 2  $\mu\text{m}$ .

The germanium-on-silicon (Ge-on-Si or GOS) platform has attracted significant research interest as it has the potential to operate well beyond the silica absorption limit [112]. In this platform, the propagation loss has been characterized over a wide wavelength range. Starting from the germanium bandgap (around 2 $\mu\text{m}$ ), a constant loss around 3dB/cm has been measured in (1.2  $\mu\text{m} \times 2.25 \mu\text{m}$  cross-section) Ge-on-Si rib waveguides in the range from 2 to 4 $\mu\text{m}$  [112]. A low record loss of 0.6dB/cm has been reported at 3.8 $\mu\text{m}$  wavelength (1.7  $\mu\text{m} \times 2.7 \mu\text{m}$  cross-section) [123, 124]. In the wavelength region where the silicon substrate starts to absorb, from 7 $\mu\text{m}$ , low 2.5 dB/cm losses have been reported around 7.5  $\mu\text{m}$  [125]. In addition to loss characterization, free-carrier electro-absorption [42] and two-photon absorption have been investigated in this platform [112, 126]. Although the GOS platform had been anticipated to be of interest for nonlinear applications in the mid-IR at the beginning of this PhD, nonlinear applications based on third-order nonlinear effects in this platform had been only theoretically investigated [127-130].

The germanium-on-SOI platform enables the use of standard CMOS manufacturing processes for realizing germanium components. As in electronics, where silica is used to electrically isolate electric components and as a thermal conductor, in photonics the underlying silica layer can be also used to efficiently remove heat from components. Hence, thermo-optic phase-shifters have been realized in germanium-on-SOI [131]. However, as already mentioned, silica absorbs light beyond 3.7 $\mu\text{m}$ , which limits the operation range of potential nonlinear photonic devices. Despite this fact, efficient fiber-to-chip grating couplers and Vernier tunable racetrack resonator filters operating at 5 $\mu\text{m}$  have been reported [132, 133]. Table 2 shows summarized the results reported in Ge-on-Si and Ge-on-SOI platforms.

For more details about germanium waveguide platforms, the readers are referred to the review article [111].

**Table 2: a survey of demonstrators achieved in Germanium based integrated platforms.  $SiGe^1$  and  $SiGe^2$  refer to high and low germanium content silicon-germanium alloys, respectively. The schematics of these platforms are shown on Table 3.**

<i>Platforms and references</i>	<i>Loss (dB/cm)</i>	<i>Wavelength (<math>\mu\text{m}</math>)</i>	<i>Devices demonstrated</i>
<i>Ge-on-Si platform</i>			
Chang, Y.-C. et al. (2012) [134]	2.5	5.8	ridge waveguide (WG)
Malik, A. et al. (2013) [135]	2.5 – 3.5	5.1 – 5.4	arrayed waveguide grating
Roelkens, G. et al (2013) [136]	$\sim 2$	2.6	Mach-Zehnder interferometer
Malik, A. et al. (2014) [131]	-	$\sim 5$	thermo-optic modulator (phase shifter)
Nedeljković, M. et al. (2015) [123]	0.6	3.8	multimode interferometers (MMI)
Shen, L. et al. (2015) [126]	-	$\sim 2$	cross-absorption modulator
Alonso-Ramos, C. et al. (2016) [124]	-	3.8	grating coupler
Mašanović, G. Z. et al (2017) [112]	3/3 $\pm$ 0.8	2 – 4/7.5	MMI and grating coupler
Nedeljković, M. et al. (2017) [125]	$\geq 2.5$	7.5 – 8.5	multimode interferometers
Gallacher, K. et al. (2018) [137]	1 – 5	7.5 – 11	rib waveguide
<i>Ge-on-SOI platform</i>			
Malik, A. et al. (2014) [131]	-	$\sim 5$	thermo-optic modulator
Radosavljević, S. et al. (2017) [132]	-	$\sim 5$	grating couplers
Radosavljević, S. et al. (2018) [133]	-	$\sim 5$	Vernier racetrack resonator tunable filter
<i>SiGe<sup>1</sup>-on-Si platform</i>			
Ramirez, J. M. et al. (2016) [138]	1.5 $\pm$ 0.5	4.6	rib waveguide on graded index substrate
Ramirez, J. M. et al. (2018) [139]	2 – 3	5.5 – 8.5	graded index rib straight/spiral waveguide
Serna, S. et al. (2017) [140]	6 $\pm$ 1.5	1.58	rib waveguide ( $n_2$ and $\alpha_2$ at 1.58 $\mu\text{m}$ )
Vakarin, V. et al. (2017) [141]	< 5	5.5 – 8.5	Mach-Zehnder interferometer and MMI
Liu, Q. et al. (2018) [97]	< 2.5	5.5 – 8.5	Fourier-transform-based spectrometer
<i>SiGe<sup>2</sup>-on-SOI platform</i>			
Hammani, K. et al. (2014) [142]	$\sim 2$	2.12	FWM-based wavelength conversion
Ettabib, M. A. et al. (2015) [143, 144]	2	2.4	supercontinuum generation
<i>SiGe<sup>2</sup>-on-Si platform</i>			
Brun, M. et al. (2014) [145, 146]	1/2	4.5/7.4	waveguides, Y-junctions, crossings, couplers
Hammani, K. et al. (2013) [147, 148]	0.43 – 4.77	1.55	SiGe buried-in Si WGs ( $n_2$ and $\alpha_2$ at 1.55 $\mu\text{m}$ )
Ettabib, M. A. et al. (2013) [149]	1.4	1.55	FWM-based wavelength conversion
Ettabib, M. A. et al. (2016) [150]	-	1.56	FWM-based wavelength conversion
Carletti, L. et al. (2015) [151, 152]	0.5 – 1.5	3.25 – 4.75	SiGe buried-in Si WGs ( $n_2$ and $\alpha_2$ at $\sim 4$ $\mu\text{m}$ )
Sinobad, M. et al. (2018) [153]	0.23	4.15	supercontinuum generation

**Table 3: A comparison of Germanium based integrated platforms with the main material parameters. Schematics of the different waveguide geometry are presented for each platform.  $SiGe^1$  and  $SiGe^2$  refer to high and low germanium content silicon-germanium alloys, respectively.**

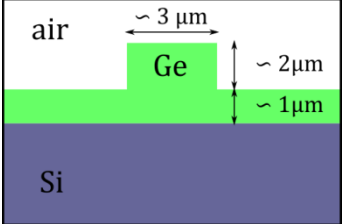
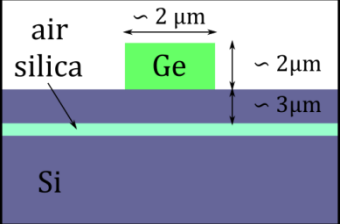
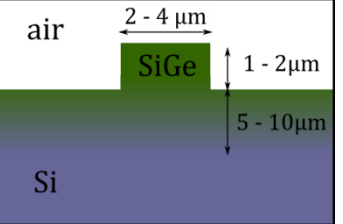
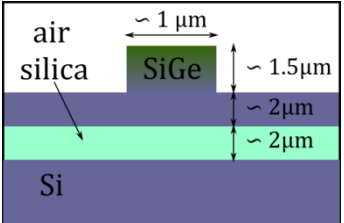
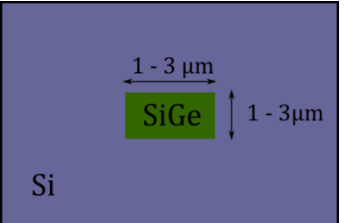
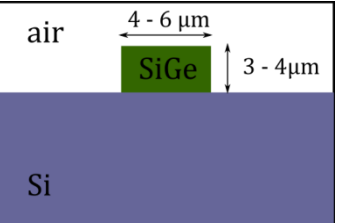
Platform	<i>Ge-on-Si</i>	<i>Ge-on-SOI</i>	<i>SiGe<sup>1</sup>-on-Si</i>
$\alpha$ (dB/cm)	0.6 (at 3.8 $\mu\text{m}$ ) [123]	N/A	$1.5 \pm 0.5$ (at 4.6 $\mu\text{m}$ ) [138]
$n_2$ (cm <sup>2</sup> /W)	N/A	N/A	$23 \pm 2.3 \times 10^{-14}$ (at 1.58 $\mu\text{m}$ ) [140]
$\gamma$ (W $\cdot$ m) <sup>-1</sup>	N/A	N/A	0.36 (at 1.58 $\mu\text{m}$ )
			
Platform	<i>SiGe<sup>2</sup>-on-SOI</i>	<i>SiGe<sup>2</sup>-on-Si</i>	<i>SiGe<sup>2</sup>-on-Si</i>
$\alpha$ (dB/cm)	2.0 (at 2.4 $\mu\text{m}$ ) [143]	0.5 – 1.5 (3.25 – 4.75 $\mu\text{m}$ ) [151]	0.23 (at 4.15 $\mu\text{m}$ ) [153]
$n_2$ (cm <sup>2</sup> /W)	$11 \times 10^{-14}$ (at 2.4 $\mu\text{m}$ ) [143]	$0.7 - 2 \times 10^{-14}$ (3.25 – 4.75 $\mu\text{m}$ )	$2.55 \times 10^{-14}$ (at 4 $\mu\text{m}$ )
$\gamma$ (W $\cdot$ m) <sup>-1</sup>	24.2	0.3 – 0.2 (3.25 – 4.75 $\mu\text{m}$ )	0.63 (at 4 $\mu\text{m}$ )
			

Table 3 shows the typical cross-section schematics of waveguides realized in the different platforms that have been included in Table 2. The main material parameters are indicated for comparison.

Although germanium based platforms have been foreseen as platforms of choice for nonlinear mid-IR photonics, germanium has not been yet successfully applied for nonlinear applications in the mid-infrared. This is mainly due to the high losses that originate from defects at the germanium-silicon interface [64, 154]. This is however thought to be a technical issue that can be addressed. One approach to minimize these defects is to use silicon-germanium alloys on silicon, as will be discussed in the next section.

### 1.2.2.3 Silicon-Germanium

Silicon germanium is an alloy of silicon and germanium noted as  $Si_{1-x}Ge_x$  where  $x$  is the germanium content. The content of germanium can be varied to tune the refractive index and the third order nonlinearity in a range between that of bulk silicon and that of germanium (larger values). This additional degree of freedom can be exploited in dispersion engineering. It has been theoretically predicted that SiGe alloys behave as “silicon-like” when the germanium content is less than 80% and as “germanium-like” when the content is more than 80% [108]. For “silicon-like”, silicon germanium  $\chi^{(3)}$  nonlinearity is comparable to that of silicon, while for “germanium-like”, the  $\chi^{(3)}$  nonlinearity is expected to be comparable to that of germanium.

### **a) High germanium content silicon-germanium alloys ( SiGe<sup>1</sup>)**

Germanium-rich silicon germanium is a “germanium-like” alloy with a small energy difference between direct and indirect bandgap transitions. Waveguides realized on the germanium-rich silicon germanium-on-silicon platform have the potential to extend the operation wavelength range up to 15 $\mu$ m. More than this, this platform can enable the realization of the long desired lasers on a silicon chip. In this purpose, silicon germanium with different germanium contents can be realized in the form of multiple quantum well hetero-structures. Silicon germanium hetero-structures can be also used within a photodetector [155].

As already alluded to, in the germanium-on-silicon (GOS) platform, the loss induced by the interaction of the optical field with the interface dislocations has been recognized as one of the main issues [125]. These threading dislocations are the consequence of the large lattice mismatch between silicon and germanium (lattice constants of Ge and Si are 5.7 and 5.4 Å, respectively). To address this issue “the interface-free waveguide” solution has been proposed. Such graded index waveguides are formed by gradually changing the germanium content in the Si<sub>1-x</sub>Ge<sub>x</sub> from 0% (silicon) to 100% (germanium). Significant progress has been achieved on this platform [138-141].

Results have been recently reported in the Ge-rich SiGe-on-Si platform demonstrating low loss, strong nonlinearity and the realization of devices that can potentially be used in future on-chip spectrometers. A low measured loss of 1.5 $\pm$ 0.5 dB/cm has been reported in a Si<sub>0.2</sub>Ge<sub>0.8</sub>/Si waveguide at 4.6  $\mu$ m wavelength [138]. At longer wavelengths, from 5.5 to 8.5  $\mu$ m, the reported loss is nearly constant loss between 2 and 3 dB/cm [139]. The Kerr index and two-photon absorption have been measured in the proximity of the band edge at 1.58  $\mu$ m using a novel single beam technique referred to as “D-scan”. Values have been reported for 70, 80 and 90% germanium content SiGe alloys. Results showed that the measured Kerr index agrees well with theory around 1.6 $\mu$ m wavelength [140].

Toward the objective of achieving photonic integrated circuits operating in the mid-infrared, several photonics devices have been demonstrated. In the last few years, multimode interference couplers, broadband Mach-Zehnder interferometers [141] and integrated Fourier-transform spectrometer [97] have been realized (see an overview of key results in Table 2).

### **b) Low germanium content silicon-germanium alloys (SiGe<sup>2</sup>)**

Low germanium content silicon germanium-on-silicon emerged as an alternative to silicon-on-insulator and silicon-on-sapphire platforms to extend the operation wavelength range deeper in the mid-infrared. At the same time this platform addresses the issue of threading dislocations existing in germanium-on-silicon platform caused by the lattice mismatch between silicon and germanium. Initially, graded index profile has been used providing “the interface-free waveguide”. The reported results showed silicon germanium core with graded index from 0% in the cladding to 40% in the middle of the core. The refractive index of the alloy has been measured at 2.15 $\mu$ m for different germanium content [146]. This was followed by the work reporting low measured losses of 1dB/cm at 4.5 $\mu$ m and 2dB/cm at 7.4 $\mu$ m in these waveguides [145]. In addition to this, the same article reported the demonstration of several basic wave-guiding devices such as Y-junctions, S-bend waveguides, X-crossings and evanescent couplers.

Low germanium content silicon-germanium waveguides have been first explored for nonlinear applications in the near-infrared at telecom wavelengths. The linear and nonlinear responses of silicon germanium waveguides buried in silicon have been studied [147, 148]. The Kerr index extracted in 1.4 $\mu\text{m}$  thick waveguides showed an enhancement of nonlinearity when increasing germanium content from 10 to 30% [147, 148]. The articles reported an increase of FOM from 0.3 of silicon to 0.5 in silicon germanium [43] at 1.55 $\mu\text{m}$  wavelength. The same group then used silicon germanium waveguides for wavelength conversion via four-wave mixing process. First, wavelength conversions of 40 Gb/s high-data rate signal have been demonstrated at telecom wavelengths [149, 150]. Second, signal from the short-wave infrared has been converted to the near-infrared [142]. This was followed by broadband supercontinuum generation covering wavelength range from 1.5 to almost 3.0 $\mu\text{m}$  [143, 144] (see an overview of the associated results in Table 2).

In our group, we have studied  $\text{Si}_{0.6}\text{Ge}_{0.4}$  alloys in the actual mid-infrared extending up to 8.5 $\mu\text{m}$  where absorption in silicon starts to be significant. Luca Carletti during his PhD at INL explored the linear and nonlinear response of such silicon germanium waveguides. Low propagation losses of only 0.5 dB/cm at 4.75  $\mu\text{m}$  wavelength were measured [151] although these waveguides were not optimized to achieve low losses as in Ge/Si waveguides, for instance [123]. The optical field confinement in the core of these waveguides is calculated to be around 60% at 4  $\mu\text{m}$ , therefore, resulting in a strong interaction between the field and SiGe/Si interfaces. The nonlinear response has been explored in the picosecond [151] and femto-second regime in the 3 – 5  $\mu\text{m}$  and 3 – 4  $\mu\text{m}$  bands, respectively [152]. The extracted nonlinear parameters were in line with the theoretical predictions and comparable to those in silicon.

In this thesis, I built on these preliminary and promising results to exploit  $\text{Si}_{0.6}\text{Ge}_{0.4}$ /Si waveguides for achieving broadband and coherent mid-IR supercontinuum generation. With respect to the prior results achieved during L. Carletti's PhD, one key aspect to reach this goal has been have been to engineer the waveguide geometry so as to achieve low loss and anomalous dispersion regimes.

### 1.2.3 Supercontinuum generation on a silicon chip

This section presents the state of the art of mid-infrared supercontinuum generation on a silicon-based chip, which has been the primary focus of this PhD. The specific objectives pursued in this work, related to the intended operation wavelength, bandwidth (octave span) and coherence of the supercontinuum will be then clarified. For more details and a comprehensive study of supercontinuum generation in different pulse regimes, detailed numerical modeling studies and a full discussion on the supercontinuum coherence properties, readers are referred to [37] from J. M. Dudley et al.

Following astonishing results achieved in PCFs, supercontinuum technologies have been commercialized at least for use in academia and laboratory environments. Recent work has focused on achieving supercontinuum on a compact, reliable and low-cost chip-based platform. This could significantly expand the commercial use of supercontinuum and potentially impact our everyday life.

Supercontinuum generation on a silicon chip has been theoretically investigated in 2007 [52]. The same year, the experimental demonstration of supercontinuum in a silicon-on-insulator waveguide spanning 350 nm in the near-infrared has been reported [156]. In [157] a silicon waveguide was pumped with 100 fs pulses at telecom wavelengths in the normal dispersion regime and a limited bandwidth was achieved despite the use of high pump intensities. This was attributed to two-photon absorption and the subsequently generated free carriers [157]. In contrast to [157], a supercontinuum spanning from 1.5 to 2.5 $\mu\text{m}$  could be achieved [13] by pumping silicon waveguides with picosecond pulses in the anomalous dispersion regime close to the two-photon absorption limit in silicon (around 2.2 $\mu\text{m}$ ). An octave-spanning supercontinuum in the short wavelength infrared (from 1.5 to 3.6 $\mu\text{m}$ ) on a silicon chip was reported a few years later in 2014 [7]. In this paper, the Si nanowire was pumped in the anomalous dispersion regime near 2.5  $\mu\text{m}$  with 300 fs pulses. Dispersive waves at the extreme parts of the spectrum were exploited to extend the continuum span. Shortly after, supercontinuum from 1.45 to 2.8 $\mu\text{m}$  was reported in the silicon germanium-on-SOI platform [143, 144].

The first supercontinuum generation on a silicon-based chip in the actual mid-infrared range (up to 5.5  $\mu\text{m}$ ) was reported in 2015 [14, 158]. To extend the operation wavelength range to the mid-infrared, beyond the absorption limit of silica at 3.7 $\mu\text{m}$ , silicon-on-sapphire waveguides were used. Relatively small cross-section waveguides (2.40  $\mu\text{m} \times 0.48 \mu\text{m}$ ) were pumped at 3.75 $\mu\text{m}$  with 320fs pulses and supercontinuum from 1.9 to 5.5 $\mu\text{m}$  was achieved. The reported supercontinuum was limited by the absorption in the sapphire substrate though (see the transparency of CMOS materials in the Figure 17). More recently, mid-IR supercontinuum has been reported in suspended silicon waveguides in the SOI platform [106, 159]. Despite the 4 $\mu\text{m}$  long-wavelength pump used in this case, the supercontinuum only extended up to 5 $\mu\text{m}$  [106].

The main objective of this thesis was to exploit the silicon germanium-on-silicon platform for generating mid-infrared supercontinuum beyond 5 $\mu\text{m}$ . Such a supercontinuum source should span at least up to the silicon absorption limit at 8.5 $\mu\text{m}$ , so as to cover the entire mid-infrared absorption window that includes the main absorption lines of relevant molecules. Beyond this bandwidth requirement, we detail below the different characteristics (brightness, spectral span and coherence properties) that are targeted for this source to be used for future on-chip spectroscopy applications. We also provide some benchmarks for these properties extracted from the literature.

### 1.2.3.1 An octave span

Reaching an octave span (the interval between two frequencies having a ratio of 2 to 1) for the supercontinuum is important because it enables the measurement of comb-line frequencies using the  $f$  and  $2f$  waves in the supercontinuum [1]. A supercontinuum spectrum consists of many discrete spectral lines (comb lines) separated by the repetition frequency ( $f_{rep}$ ) of the pump laser. If the comb line frequencies are known, supercontinuum can be used as an “optical frequency ruler” to measure the absolute optical frequency of an optical source.

If the carrier and envelope in a pulse train are in phase, e.g. the peak of the envelope coincides in the time-domain with a maximum of the carrier, then the frequency of the  $n$ -th comb line is simply  $n f_{rep}$ . Both  $n$  and  $f_{rep}$  are relatively easy to determine. However, in real situations, in a laser delivering identical pulses, there is a constant phase-shift between the peak of the envelope and the closest peak of the carrier wave, named the carrier-envelope offset phase ( $\varphi_{ceo}$ ), see Figure 19. In the frequency domain, the accumulated phase shift between subsequent pulses, translates into the carrier-envelope offset frequency ( $f_{ceo}$ ). The resulting frequency of a comb line is then shifted by this frequency offset and trying to measure absolute optical frequencies ends up in measuring the carrier-envelope offset frequency. This offset can be detected using heterodyne beating between the doubled low-frequency component and the high-frequency component that are separated by an octave. The offset frequency is the difference between the two signals:

$$f_{ceo} = 2(nf + f_{ceo}) - (2nf + f_{ceo}) \quad (107)$$

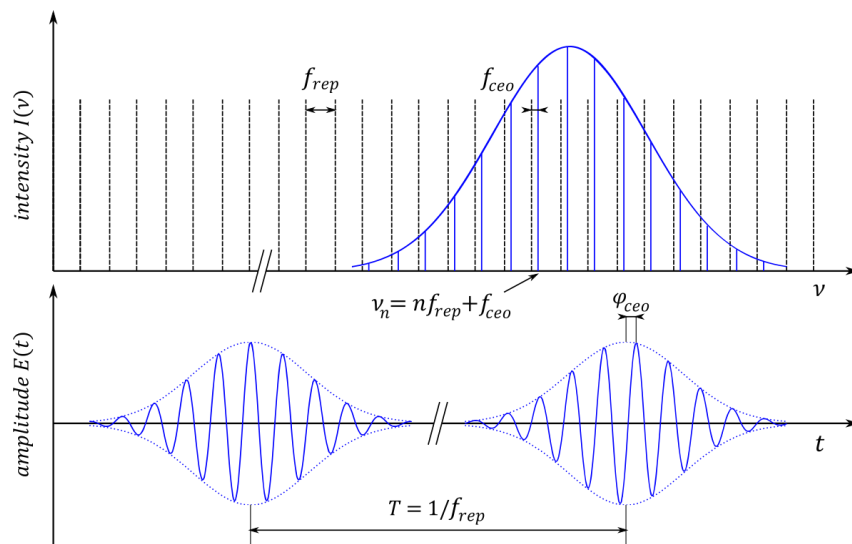


Figure 19: a pulse train with an evolving carrier-envelope phase (bottom) and corresponding spectrum (top). The carrier wave is presented by the solid blue curve, the pulse envelope by the dotted blue curve

This method, which is referred to as the interferometric  $f$  to  $2f$  self-referencing scheme, is quite practical since the frequency components belong to the same signal [160]. Furthermore, the detection of the carrier envelope offset frequency can be used to control the phase of the carrier wave in order to stabilize the supercontinuum source. This can be used to improve the spectral coherence of the supercontinuum, which is important for maintaining the accuracy of frequency combs for an optical atomic clock and metrology applications.



### 1.2.3.2 Coherence

In the context of a supercontinuum, coherence is related to spectrum fluctuations (amplitude and phase of its spectral components) from pulse to pulse. A coherent supercontinuum thus exhibits high shot-to-shot spectrum stability. This is very important from a practical standpoint as a coherent supercontinuum allows for ultra-fast (single-shot) time-resolved measurements. Low spectral fluctuations enable high-precision measurements that are useful for frequency metrology, high-precision spectroscopy or optical communications. Coherence and flatness of the supercontinuum are more desirable for wavelength-division multiplexing (WDM) than an ultra-large bandwidth [10]. Recently, coherence has become increasingly important in optical communications as advanced modulation formats combined with coherent detection have been employed to increase the data-rate. Furthermore, a coherent supercontinuum can be used for measurements where coherence is directly used as in optical coherence tomography (OCT) and coherent anti-stokes Raman spectroscopy (CARS).

Fluctuations of the SC spectra are consequences of noise and nonlinear dynamics. In practical situations, there are many sources of noise. However, most of them are technical and in principle they could be avoided [161, 162]. When numerically investigating the coherence of a supercontinuum, only the fundamental (intrinsic) noise sources are generally taken into account. These include the quantum limited shot-noise of an input pulse and the noise due to spontaneous Raman fluctuations in a waveguide [37]. These may affect the resulting supercontinuum coherence.

Superimposed coherent supercontinuum pulses exhibit interference effects, which can be exploited for applications. Actually, interference techniques have been used to experimentally measure the coherence of a supercontinuum. The demonstration of an interference pattern from two independently generated supercontinua, in a modified Young's double-slit experiment, provided the experimental proof of the supercontinuum coherence [163]. An improved experimental setup to demonstrate the supercontinuum coherence uses an asymmetric Michelson interferometer where one supercontinuum pulse is delayed in a longer arm so as to interfere with subsequent pulses from the same pulse train. The interference creates a pattern with distinct fringes across the spectrum, and coherence has been linked to the visibility of the fringes [37]. In addition to this method, another technique can be used to measure the intensity fluctuations in a spectrum. Relative intensity noise (RIN) can be measured in the radio-frequency domain (MHz range). The information about coherence can be then extracted by comparing the RIN of the pump with that of the narrow-band part of the SC spectra centered at a defined frequency/wavelength. The optical signal is coherent if the measured intensity noise (RIN) of the signal closely follows that of the pump [98].

In addition to a direct measurement of the supercontinuum coherence, the latter can be numerically modeled so as to theoretically investigate the coherence properties of an experimentally measured supercontinuum. This is particularly useful in the mid-IR where the technical difficulties of coherence measurements are strongly increased with respect to that in the near-IR, having made it impossible to date. Coherence is calculated as the absolute value of the complex degree of the first-order coherence, defined as:

$$|g_{12}^{(1)}(\lambda)| = \left| \frac{\langle E_1(\lambda)E_2^*(\lambda) \rangle}{\sqrt{\langle |E_1(\lambda)|^2 \rangle \langle |E_2(\lambda)|^2 \rangle}} \right| \quad (108)$$

It has been shown that this mathematical expression corresponds to the maximal fringe visibility in the previously mentioned interference experiment [37]. Angle brackets here denote an averaging over an ensemble of independently simulated spectra associated with different (and randomly defined) noise scenarios. In contrast to experiments where only subsequent pulses interfere, in simulations averaging can be performed over all simulated pairs. In this case, each simulation is performed with different noise seeds. Quantum shot noise is included by adding one photon per mode (comb-line) with random phase to the input pulse. This is done in the frequency domain. Practically, since the spectral discretization bin does not necessarily correspond to the separation between comb-lines, several photons might be added per bin to model one noise photon per mode. To more fairly reproduce the result of an experiment, noise related to intensity fluctuations of the pump pulse can be also included by randomly varying the input pulse intensity for each supercontinuum simulation scenario.

It has been experimentally demonstrated that the pump coherence can be transferred to the supercontinuum when pumping with short pulses in low all-normal dispersion regimes [164, 165]. By contrast, an incoherent supercontinuum would be almost certainly generated by pumping a nonlinear waveguide with long pulses in the anomalous dispersion. Mechanisms responsible for de-coherence have been studied in intermediate regimes, for short pump pulses launched in the anomalous dispersion [37] as well as for long pump pulses launched in the all normal dispersion regime [166]. Supercontinuum is coherent in these two cases within certain limitations. The main source for de-coherence in the supercontinuum dynamics associated with anomalous dispersion is modulation instability (MI). Through amplifying noise, this process tends to produce large fluctuations in power of the solitons formed after the soliton fission process [37].

Coherent supercontinuum generation has been reported in CMOS-compatible platforms. Leo *et al.* have reported the generation of a coherent SC spanning 500 nm around a pump at 1.55  $\mu\text{m}$  in a silicon-on-insulator (SOI) waveguide, showing that coherence is preserved if the effective soliton fission length is short enough to suppress modulation instability [167]. More than an octave-spanning coherent SC has been reported in a 7.5 mm silicon nitride-on-insulator waveguide when pumping waveguide in the anomalous dispersion at 1  $\mu\text{m}$  with sub-100 fs pulses [16]. In subsequent works, the trend was to shift the generated spectrum toward the mid-IR. First, an octave-spanning coherent SC has been reported in a silicon-on-insulator waveguide, designed to be pumped at 1.9  $\mu\text{m}$  aiming to generate dispersive waves close to the silicon edge ( $\approx 1.1 \mu\text{m}$ ) [168]. More recently, coherent SC has been reported in the actual mid-IR in silicon-on-sapphire waveguides [98].

### 1.2.3.3 Brightness

Supercontinuum source can be simply defined as a high brightness broadband light source [169]. While having a spectrum as broad as that of lamps and thermal sources, it possesses a high brightness, for laser sources.

Brightness (or more precisely radiance) of a light source, is a radiometric quantity defined as an optical power emitted from the source per unit of surface area per unit of solid angle (in units  $\text{W}/\text{m}^2/\text{sr}$ ) [170]. Thanks to the high directionality of a laser beam, they typically produce several orders of magnitude brighter light than that of the brightest conventional sources, which is a useful characteristics for many applications [170]. In the context of supercontinuum, it is also useful to define the spectral brightness (or spectral radiance) either as the radiance per unit of frequency (Hz) or per unit of wavelength (nm). Provided that high directivity of the laser beam with a small

diameter can be achieved (as in a small cross section waveguide), achieving high brightness ends up in achieving high output-power of a supercontinuum.

Record high output-power levels, greater than 10W, from the supercontinuum operating in the mid-infrared (limited up to 4.5  $\mu\text{m}$ ) were reported in a heavy metal fluoride glass (ZBLAN) optical fibers [171-173]. The power level in this platform is limited by the damage threshold due to the low thermal stability at the glass transition temperature. More recently, fluorotellurite glass fibers, with higher transition temperature, were developed, providing  $\sim 16$  W output power for 0.9 – 3.9  $\mu\text{m}$  spanning supercontinuum [174].

On a silicon based chip, the largest output power reported to date, was achieved in the silicon-on-sapphire platform reaching around 1 mW for a supercontinuum covering the 1.9 – 5.5  $\mu\text{m}$  band [14]. The power reported there was limited by the multi-photon absorption, which reduced the power conversion efficiency. In this PhD thesis, our approach was to design a low-loss waveguide, while operating beyond the three-photon absorption limit of silicon, so as to reach large optical power conversion efficiency.

Figure 20 presents a summary of the reported supercontinuum demonstrations on a silicon chip in different platforms and across different wavelength ranges in the near- and mid-IR. These provide some benchmarks in terms of the achieved bandwidth and spectral span covered by the different demonstrations of supercontinuum. To anticipate on our results that will be presented in the next chapter, we can note that the supercontinuum achieved in our SiGe on Si platform (red solid line at the bottom) compares favorably. It exhibits a very broad spectrum, shifted up to longer wavelengths than what has been achieved so far on chip-based supercontinuum in Group IV materials.

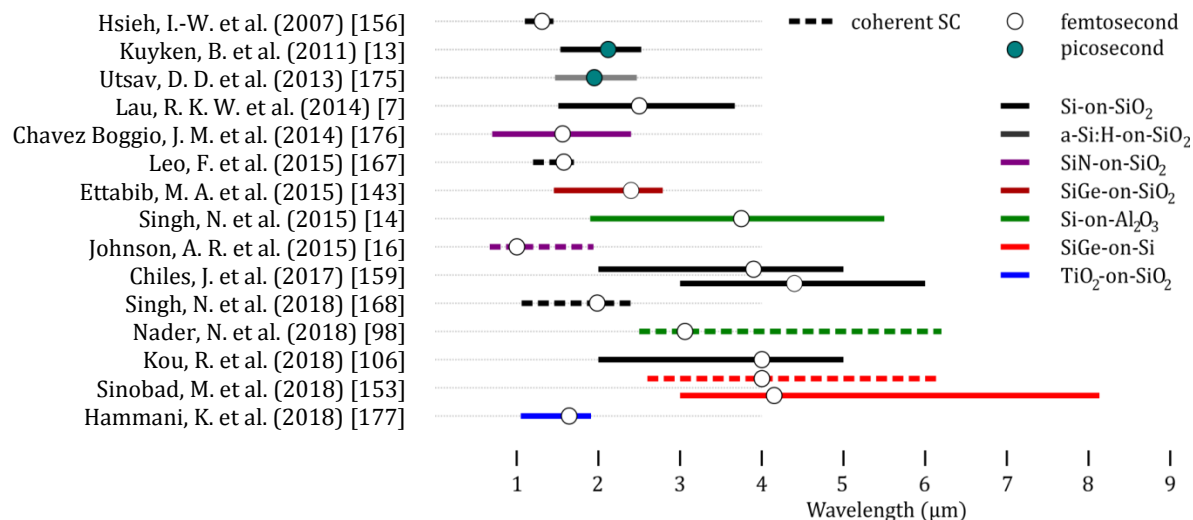


Figure 20: A survey of the reported supercontinuum demonstrations on a silicon chip in the near- and mid-IR range. Each result is represented by a horizontal bar that indicates the SC spectral span and whether it was coherent (dashed line) or not (solid line). The colors refer to the different platforms that were exploited, while the pump wavelength and pulse regime is denoted by a (full, for picosecond, or empty, for femtosecond) circle.

## 1.3 Conclusion

This chapter introduced some theoretical background related to third-order nonlinear effects and described the state of the art of relevant nonlinear integrated platforms, with a primary focus on supercontinuum generation and nonlinear applications of silicon photonics in the mid-infrared.

Among the nonlinear integrated platform candidates that were presented in this chapter for mid-infrared photonics based on Group IV materials, we chose the silicon germanium-on-silicon (SiGe-on-Si) platform. Silicon germanium alloys with 40% germanium content ( $\text{Si}_{0.6}\text{Ge}_{0.4}$ ) have a larger refractive index than silicon (Si), allowing for efficient light guiding in SiGe core waveguides on a Si substrate. Moreover, the previous work in our group in collaboration with Leti's Center for Research showed that low loss waveguides could be realized in the SiGe-on-Si platform. In particular, the lattice mismatch between  $\text{Si}_{0.6}\text{Ge}_{0.4}$  and Si is sufficiently low as well as the density of threading dislocations at the core/cladding interface, which were recognized as the main loss contribution in Ge-on-Si waveguides. The operation wavelength in the SiGe-on-Si platform is bound to silicon absorption at long wavelengths ( $\sim 8.5\mu\text{m}$ ); beyond which silicon becomes opaque (absorption is more than 2dB/cm). However, this limit is related to any Si based platform unless sophisticated designs (e.g. suspended waveguides) are used. Hence, this platform allows, in principle, for harnessing the full potential of silicon photonics in the mid-infrared. The  $\text{Si}_{0.6}\text{Ge}_{0.4}$  material was discussed, in this chapter, to be a relevant nonlinear material: its nonlinearity is theoretically anticipated to be stronger than that of Si [108], while its low nonlinear loss is expected to be low when operating beyond the two-photon absorption limit (in Si at  $2.2\mu\text{m}$ ).

The main objective of this thesis has been to generate a supercontinuum in the mid-infrared using this platform. In this context, this chapter introduced the main aspects of the dynamics of supercontinuum generation as well as the model and simulation tools to numerically investigate them. SiGe and Si materials are third-order ( $\chi^{(3)}$ ) nonlinear optical materials. All kinds of third-order nonlinear effects such as self-phase modulation (SPM), cross-phase modulation (XPM), four-wave mixing (FWM) and stimulated Raman scattering (SRS) play a significant role in the dynamics of supercontinuum generation. Higher odd-order nonlinear absorption effects also have a non-negligible impact. Multi-photon absorption causes nonlinear losses while generating free charge carriers, which potentially limit the related nonlinear device performance. Our model takes into account all these different effects, accordingly.

Following a state of the art review of chip-based supercontinuum, I clarified our objectives in terms of the targeted supercontinuum bandwidth, coherence and brightness. I also showed how waveguides could be used to enhance the underlying material nonlinearity and the associated nonlinear processes that lead to supercontinuum generation. In particular, tight light confinement and dispersion engineering provide useful tools for the design of waveguides that are capable of generating supercontinuum with the intended characteristics.

After presenting our platform, objectives and simulation tools, the next chapter deals with the experimental demonstration of a bright and broadband mid-IR supercontinuum using SiGe-on-Si waveguides. Thanks to a careful optimization of the waveguide design, and dispersion engineering, we reported a supercontinuum that spans up to the onset of the silicon absorption at  $8.5\mu\text{m}$ . The third chapter discusses the coherence properties of such a supercontinuum, which is generated in a waveguide with a relatively narrow anomalous dispersion band enclosed by two

zero dispersion wavelengths. We use simulations to clarify these coherence properties as well as their origin. The fourth chapter shows how all-normal dispersion regime can be reached using a post-processing step that consists of depositing a chalcogenide top cladding on top of SiGe-on-Si waveguides. Because dispersion engineering lies at the core of the supercontinuum characteristics, this tool provides us with an additional and flexible degree of freedom that can be used to adapt the waveguide for the intended application.

## **Chapter 2.**

# **Mid-infrared octave-spanning supercontinuum generation to 8.5 $\mu\text{m}$ in silicon-germanium waveguides**

This chapter deals with the experimental demonstration of a mid-IR bright and broadband supercontinuum out of our SiGe-on-Si waveguide platform. This supercontinuum spans up to the onset of the silicon absorption at 8.5 $\mu\text{m}$ .

As discussed in Chapter 1, silicon-based platforms such as silicon-on-insulator, silicon nitride-on-insulator, and silicon germanium-on-insulator are restricted to 3.7 $\mu\text{m}$  due to the absorption in a silica substrate. This limit was extended to 5.5 $\mu\text{m}$  by exploiting the wider transparency of sapphire in the silicon-on-sapphire platform [14]. As reported in this chapter, we investigated the silicon germanium-on-silicon platform with the potential to cover the entire mid-IR atmospheric absorption band (4 – 8 $\mu\text{m}$ ).

In order to show the full potential of the silicon germanium-on-silicon platform for the mid-infrared silicon photonics, we present and discuss here our results on supercontinuum generation, which intended to achieve a very large bandwidth. We study two engineered waveguide devices: 1) a small cross-section waveguide with a relatively high nonlinearity that was designed for providing single-mode operation and an anomalous dispersion regime at 4 $\mu\text{m}$  and 2) a large cross-section waveguide designed for extending the supercontinuum span up to the silicon absorption limit at 8.5 $\mu\text{m}$ .

This chapter corresponds to the article entitled “Mid-infrared octave-spanning supercontinuum generation to 8.5 $\mu\text{m}$  in silicon-germanium waveguides” published in “Optica” in mid-2018. The article is organized into five sections, which present the device design/fabrication, the linear and nonlinear experimental results, and the numerical analysis using the modeling tools introduced in Chapter 1. Additional technical details are included in the supplementary material. To expand on the results published in this paper, we start by presenting our design work that allowed us to harness the full potential of the SiGe/ Si waveguide platform. In particular, we had to take into account several factors so as to increase the nonlinear response through tight mode confinement, while reaching a suitable dispersion profile for supercontinuum generation. This background dispersion engineering prior to the device fabrication was key in achieving the results presented in the paper.

## Dispersion engineering

Both the linear and nonlinear response of the waveguide are intrinsically related to the linear and nonlinear parameters of the core and cladding materials. Yet, in section 1.1.2.1 we showed that by changing the waveguide geometry (i.e. the cross-section dimensions), we could impact the optical mode field distribution and therefore the waveguide dispersion as per equation (60). This is referred to as dispersion engineering. As already alluded to in chapter 1, dispersion engineering is necessary to achieve efficient nonlinear interactions. In particular, the efficient generation of broadband supercontinuum generally requires a low anomalous dispersion spanning across a large bandwidth.

In this thesis, we exploited the  $\text{Si}_{0.6}\text{Ge}_{0.4}$  on Si platform, which was developed at Leti's Center for Research in Grenoble, France [178]. This platform takes advantage of the low lattice mismatch between  $\text{Si}_{0.6}\text{Ge}_{0.4}$  and Si to resolve the issue of treading dislocations existing in the germanium-on-silicon (GOS) platform. In addition, in this platform the operation wavelength range can be, in principle, extended deeper into the mid-infrared, compared to the silicon-on-insulator and silicon-on-sapphire platforms.

In our group, Luca Carletti, during his Ph.D. (2011-2015), explored buried-in waveguides fabricated in this platform, where the silicon germanium core was buried in a silicon cladding [179]. In his work, he measured linear loss in the 3 – 5  $\mu\text{m}$  band, achieving values as low as 0.5 dB/cm at 4.75  $\mu\text{m}$  [151]. At the same time, he determined the optimal operational wavelength to be around 4  $\mu\text{m}$  wavelength, due to some trade-off between the material nonlinear response and low values of the three- and four-photon absorption [152]. The buried in waveguides he used exhibited 1.9  $\mu\text{m} \times 1.4 \mu\text{m}$ , 2.0  $\mu\text{m} \times 1.4 \mu\text{m}$  and 3.0  $\mu\text{m} \times 2.7 \mu\text{m}$  cross-section dimensions, so that they presented a strong normal dispersion. At the beginning of my PhD, I showed, by simulations, that it was actually not possible to design a buried-in SiGe-on-Si waveguide operating in a single-mode anomalous dispersion regime around 4  $\mu\text{m}$ .

Based on these initial results, I designed top air cladding waveguides, which were dispersion engineered for supercontinuum generation. Figure 21 shows the group-velocity dispersion calculated at 4.5  $\mu\text{m}$  for different air clad  $\text{Si}_{0.6}\text{Ge}_{0.4}$ / Si waveguide widths and heights. This figure shows that waveguides of height greater than 2.5  $\mu\text{m}$  can operate in the anomalous dispersion regime (see the zero GVD white solid line), both in the TE and TM polarization. However, a top air cladding geometry breaks the symmetry of the waveguide with respect to the vertical plane, which induces a mode cutoff at long wavelengths, eventually precluding light propagation beyond a certain wavelength. In addition, the top air cladding enables the mode field to interact with its (top) environment, thereby potentially increasing the waveguide loss and, degrading, in turn, its performance, especially when operating in the mid-infrared. We therefore took all these aspects into account for our waveguide design optimization work.

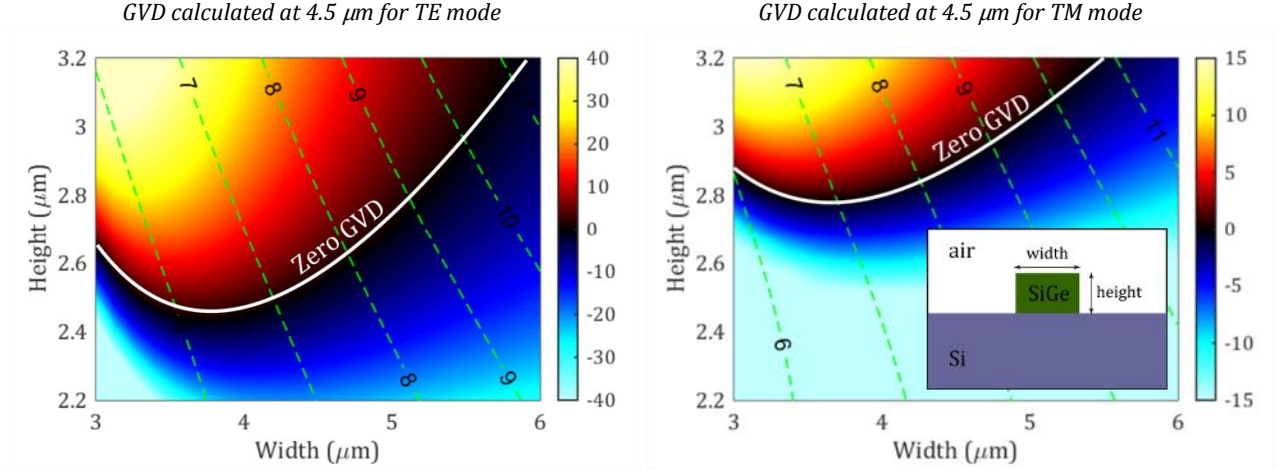


Figure 21: Group-velocity dispersion (GVD in units ps/nm/km) calculated for top air-clad  $\text{Si}_{0.6}\text{Ge}_{0.4}$ -on-Si waveguides (see cross-section in the inset) at  $4.5\mu\text{m}$  for TE (left) and TM (right) modes for different waveguide widths (x-axis) and heights (y-axis). The green dashed lines indicate the mode effective area calculated as per equation (72) in  $\mu\text{m}^2$ . The white solid line highlights the achievement of a zero-GVD.

Our main objective was to achieve waveguides with a low anomalous dispersion while maintaining a low propagation loss. In order to achieve this objective, waveguide should be designed so that the optical mode field is well confined into the waveguide core. The degree of confinement (factor  $\Gamma$  in equation (73)) increases with the waveguide height, being more than 0.9 for a waveguide height greater than  $2.5\mu\text{m}$ , calculated for waveguide widths between  $3$  and  $6\mu\text{m}$ . However, increasing the waveguide thickness increases the effective area, which potentially reduces the nonlinear parameter  $\gamma$  (see equation (74)).

In the Optica paper, we decided to explore two dispersion engineered waveguide designs, one with an optimized nonlinear  $\gamma$  parameter, which presents a small mode cross-section and operates in the single-mode regime at  $4\mu\text{m}$  and another one with an optimized bandwidth due to the shift of the cutoff wavelength beyond the silicon absorption limit at  $8.5\mu\text{m}$ . The second one turns out to present a larger cross-section and operates in the multi-mode regime around the  $4\mu\text{m}$  wavelength.

*The waveguide 1* of cross-section  $3.75\mu\text{m} \times 2.70\mu\text{m}$  satisfies our conditions for a single-mode operation in a low anomalous dispersion at  $4\mu\text{m}$  with a minimized effective area ( $\sim 6.5\mu\text{m}^2$ ). However, this waveguide has a cutoff wavelength at around  $6\mu\text{m}$  (see Figure 22). In order to shift the cutoff wavelength beyond  $8.5\mu\text{m}$  the larger waveguide cross-section is required. This is achieved in *the waveguide 2* of cross-section  $6.0\mu\text{m} \times 4.2\mu\text{m}$ . This waveguide is operating in the multi-mode regime at a low normal dispersion at  $4\mu\text{m}$  wavelength that is close to the first zero-GVD wavelength at around  $4.5\mu\text{m}$  (see Figure 22). We note that an anomalous dispersion regime exists in this waveguide and covers large bandwidth from  $4.5$  to  $7.7\mu\text{m}$  enabling us to fully exploit this platform.



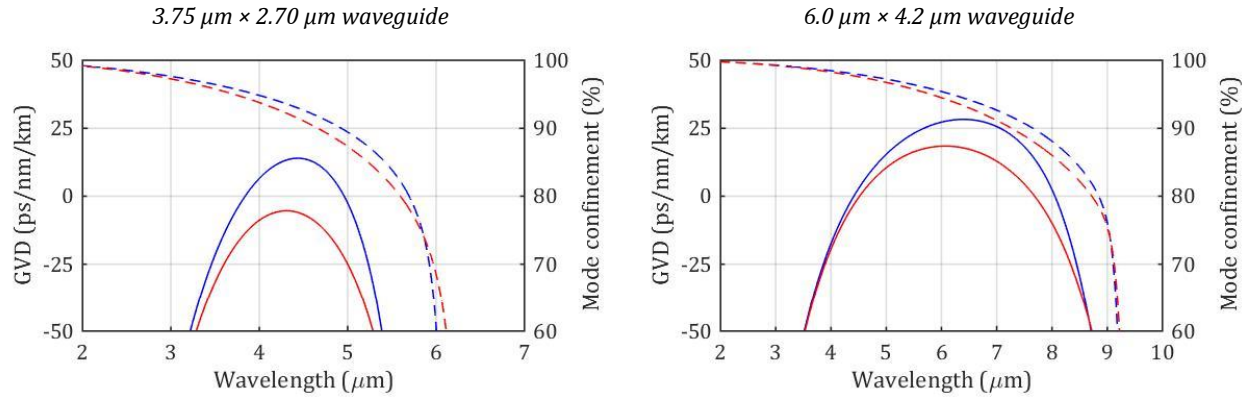



**Figure 22:** Calculated group-velocity dispersion (solid curves) and mode confinement in the core (dashed curves) versus wavelength for quasi-TE (blue) and quasi-TM modes (red) for the top air-clad  $\text{Si}_{0.6}\text{Ge}_{0.4}/\text{Si}$  waveguide 1 (left) and waveguide 2 (right)

These designed waveguides proved to be relatively robust against deviations from the nominal dimensions, allowing for high fabrication tolerance. In the article [153] (see the supplementary material) we showed that changes in the waveguide thickness and width do not have a large impact on dispersion parameters. By changing the width of the waveguide 1 by  $\pm 100\text{nm}$ , we calculated a shift in the zero-GVD wavelength of less than  $50\text{nm}$ . Changes in the thickness by  $\pm 100\text{nm}$  increased the first zero-GVD wavelength by only  $20\text{ nm}$  and the second zero-GVD by less than  $100\text{nm}$ .

In the following of the chapter, we present the experimental results achieved on these two waveguide designs.



# Mid-infrared octave spanning supercontinuum generation to 8.5 $\mu\text{m}$ in silicon-germanium waveguides

MILAN SINOBAD,<sup>1,2,7</sup>  CHRISTELLE MONAT,<sup>1</sup> BARRY LUTHER-DAVIES,<sup>3</sup> PAN MA,<sup>3</sup> STEPHEN MADDEN,<sup>3</sup> DAVID J. MOSS,<sup>4</sup> ARNAN MITCHELL,<sup>2</sup> DAVID ALLIOUX,<sup>1</sup> REGIS OROBTCHOUK,<sup>1</sup> SALIM BOUTAMI,<sup>5</sup> JEAN-MICHEL HARTMANN,<sup>5</sup> JEAN-MARC FEDELI,<sup>5</sup> AND CHRISTIAN GRILLET<sup>1,6</sup>

<sup>1</sup>Université de Lyon, Institut des Nanotechnologies de Lyon (INL, UMR-CNRS 5270), Ecole Centrale de Lyon, 69130 Ecully, France

<sup>2</sup>CUDOS and School of Engineering, RMIT University, Melbourne, VIC 3001, Australia

<sup>3</sup>CUDOS, Laser Physics Centre, Australian National University, Canberra, ACT 0100, Australia

<sup>4</sup>Centre for Microphotonics, Swinburne University of Technology, Hawthorn, VIC 3122, Australia

<sup>5</sup>CEA-Leti, MINATEC Campus, 17 rue des Martyrs, 38054 Grenoble Cedex 9, France

<sup>6</sup>e-mail: christian.grillet@ec-lyon.fr

<sup>7</sup>e-mail: milan.sinobad@student.rmit.edu.au

Received 30 October 2017; revised 13 February 2018; accepted 14 February 2018 (Doc. ID 310213); published 27 March 2018

**Efficient on-chip molecule and bio-agent detection can be achieved by accessing strong molecular absorption lines in the mid-infrared, but it requires high output power broadband mid-IR sources. Here, we report supercontinuum generation in an air-clad  $\text{Si}_{0.6}\text{Ge}_{0.4}/\text{Si}$  waveguide that emits a broad spectrum spanning from 3.0  $\mu\text{m}$  to 8.5  $\mu\text{m}$ . These waveguides have anomalous dispersion and low propagation loss ( $<0.4$  dB/cm) in the mid-IR, which leads to a supercontinuum output with a high average power of more than 10 mW on-chip. The realization of broadband mid-IR sources with high spectral brightness makes the SiGe-on-Si platform promising for a wide range of applications.** © 2018 Optical Society of America under the terms of the [OSA Open Access Publishing Agreement](#)

**OCIS codes:** (320.6629) Supercontinuum generation; (190.4390) Nonlinear optics, integrated optics; (140.3070) Infrared and far-infrared lasers.

<https://doi.org/10.1364/OPTICA.5.000360>

## 1. INTRODUCTION

Molecule or bio-agent detection has a large number of applications in medicine, the food industry, environmental monitoring, and security [1,2]. If implemented in the form of low-cost, disposable on-chip sensors, it could lead to applications in early cancer diagnosis, real-time pollution detection, and food quality control [3]. To achieve high sensitivity, the molecules must be identified by measuring their fundamental rotational and vibration transitions that have strong characteristic “fingerprints” in the mid-infrared (mid-IR, between 3  $\mu\text{m}$  and 20  $\mu\text{m}$ ) [4]. Mid-IR light sources with high spectral brightness are key enablers for such technologies. Various approaches have been used to achieve spectrally bright mid-IR sources, such as stand-alone quantum cascade lasers (QCLs) or tunable optical parametric amplifiers (OPAs) [5,6]. In this context, supercontinuum generation (SCG) operating via the nonlinear Kerr effect is particularly important. Indeed, this type of broad spectrum enables reliable molecule detection with high throughput by measuring, in parallel, the multiple and spectrally distinct absorption lines of a given molecule [7]. Demonstrations of such supercontinua with wide mid-IR bandwidth and high-power spectral density have already

been reported in fibers [8–13] and recently in compact chalcogenide chip-based platforms [14]. The challenge is, however, to obtain an efficient and broadband mid-IR light source on a CMOS-compatible platform to leverage a mature and reliable fabrication technology and provide a path toward mass production.

High-performance linear and nonlinear photonic devices have been developed for telecom wavelengths, i.e., in the near-infrared, on the silicon-on-insulator (SOI) standard CMOS platform. A 350 nm spanning supercontinuum was achieved by pumping a low-loss SOI waveguide at 1.3  $\mu\text{m}$  [15]. Despite the relatively large nonlinear gamma parameter ( $\gamma$ ) in silicon at this wavelength, enabled by the combination of a large Kerr nonlinearity and small effective area, the nonlinear loss caused by two-photon absorption (TPA) significantly limited the bandwidth of the generated light [16]. By pumping at 2.1  $\mu\text{m}$ , near the 2.2  $\mu\text{m}$  TPA cutoff in silicon, a broader spectrum exceeding 990 nm in bandwidth could be generated [17], followed more recently by the demonstration of SCG up to 3.6  $\mu\text{m}$  [18]. As an alternative to silicon, another group IV alloy,  $\text{Si}_x\text{Ge}_{1-x}$ , which is also CMOS compatible, has proven to be an attractive nonlinear material for mid-IR applications [19–21]. The transparency window of SiGe expands more

deeply into the mid-IR (potentially up to 15  $\mu\text{m}$ —well beyond the Si absorption limit—by employing Ge [22] or Ge-rich SiGe waveguides [23]), as compared to other CMOS-compatible platforms considered for operation in this wavelength region, such as silicon nitride [24] and Hydex [25,26]. In particular, a supercontinuum covering almost an octave (1.45–2.79  $\mu\text{m}$ ) in the short-wave infrared (SWIR) band was achieved in the SiGe-on-silica platform [27]. However, in addition to the nonlinear loss of the pump in the waveguide core, the silica cladding transparency eventually limits the SCG bandwidth up to 3.5  $\mu\text{m}$ . Therefore, the SCG bandwidth generated on a SOI platform or its kin (SiGe/SiO<sub>2</sub>) is bound at the short wavelength end by absorption and nonlinear loss in the core material and, at long wavelengths, by substrate absorption. Sophisticated SOI waveguide designs were proposed to overcome the latter limit [28]. By replacing silica with sapphire in the silicon-on-sapphire (SOS) platform, a supercontinuum covering more than an octave in the mid-infrared was demonstrated for the first time on any CMOS-compatible platform [29]. The spectrum was then limited to 6  $\mu\text{m}$  by absorption in the sapphire substrate. This result represents the longest wavelength generated in a CMOS-compatible chip to date. Finally, the highest average power that has been generated via supercontinuum in the mid-IR to date is still less than 1 mW [29], largely because of linear and nonlinear losses in the waveguides.

Here, we demonstrate an octave-spanning, CMOS-compatible supercontinuum source in the mid-IR with high spectral brightness. We believe this is the first CMOS-compatible chip to exceed 6  $\mu\text{m}$ , in fact reaching an unprecedented 8.5  $\mu\text{m}$ . Our low-loss (<0.4 dB/cm) SiGe-on-Si waveguide platform enables high on-chip power of more than 10 mW—almost two orders of magnitude greater than previous demonstrations in SiGe [20]. By choosing a geometry for the SiGe waveguides patterned on a Si substrate with air as the upper cladding, we are able to appropriately engineer the waveguide dispersion while achieving a suitable trade-off between tight mode confinement and low effective area. The transparency of the silicon substrate from 1.1 to 8.5  $\mu\text{m}$  [2,30] enables us to achieve a supercontinuum spectrum covering the entire 4 to 8  $\mu\text{m}$  spectral band, where many atmospheric molecules have strong “fingerprints.”

## 2. DEVICE DESIGN AND FABRICATION

Supercontinuum generated through soliton fission requires waveguides operating in a low and relatively flat anomalous dispersion regime [31,32]. Achieving low anomalous dispersion in waveguides with a low index contrast, such as those with a Si<sub>0.6</sub>Ge<sub>0.4</sub> core and Si cladding ( $\sim 0.16$ ) [21], is challenging. Thus, we investigated SiGe/Si waveguides with a top air-cladding (see Fig. 1 inset). However, this vertically asymmetric waveguide geometry introduces additional constraints. First, it introduces a cutoff for the fundamental mode at long wavelengths. Second, the interaction between the evanescent field of the mode and the air cladding makes it more sensitive to the ambient environment and surface contamination, which might induce additional propagation losses. The main objectives of our design were to achieve low anomalous dispersion over a large bandwidth while strongly confining light in the waveguide core to minimize propagation losses. We also targeted a low effective area ( $A_{\text{eff}}$ ) to achieve as high a nonlinear parameter ( $\gamma = \omega_0 n_2 / c A_{\text{eff}}$ ) as possible. Our waveguides were designed to be pumped around 4  $\mu\text{m}$ , which we previously identified as providing a good trade-off between

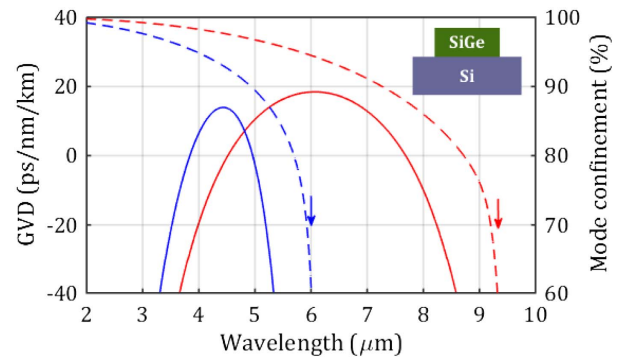


**Fig. 1.** Calculated group velocity dispersion (GVD) (solid lines) and mode confinement (dashed lines) of waveguide (1) in the TE mode (blue) and waveguide (2) in the TM mode (red). The arrows indicate the related cutoff wavelengths.

high nonlinearity and low nonlinear losses (figure of merit—FOM) [21].

Here, we used air/SiGe/Si ridge waveguides with a slightly larger cross-sectional area than previously employed [21]. Because of the trade-off between effective area minimization (single-mode operation and maximized nonlinear parameter  $\gamma$ ) and cutoff wavelength extension (low loss and strong mode confinement), we studied two designs: waveguide (1) with a 3.75  $\mu\text{m} \times 2.70 \mu\text{m}$  cross-section and waveguide (2) with a 6.0  $\mu\text{m} \times 4.2 \mu\text{m}$  cross-section. The key parameters of the two waveguides were calculated by a finite difference mode solver and are summarized in Table 1.

In essence, waveguide (1) yielded transverse-electric (TE) single-mode operation in the low anomalous dispersion regime, with a minimal effective area at 4  $\mu\text{m}$ . Despite its relatively small effective area, we reached a mode confinement greater than 95% in the highly nonlinear SiGe core (Fig. 1). This, in turn, should improve the nonlinear parameter, and hence the conversion efficiency for SCG. The drawback of this design is the relatively short ( $\sim 6 \mu\text{m}$ ) cutoff wavelength for the fundamental TE waveguide mode that intrinsically limits the SC spectrum at long wavelengths. In contrast, waveguide (2) had a larger cross-sectional area and was designed to shift the cutoff wavelength of the fundamental transverse-magnetic (TM) mode beyond 8.5  $\mu\text{m}$  (9.3  $\mu\text{m}$ ), enabling us to exploit, in principle, the full transparency window of the

**Table 1. Summary of the Waveguide Parameters for the Two Designs<sup>a</sup>**

Parameter	Waveguide (1) at 4 $\mu\text{m}$ in TE	Waveguide (2) at 4.15 $\mu\text{m}$ in TM
w ( $\mu\text{m}$ ) $\times$ h ( $\mu\text{m}$ )	3.75 $\times$ 2.70	6.0 $\times$ 4.2
$\gamma$ ( $\text{W}^{-1} \text{m}^{-1}$ )	0.63	0.30
$\beta_2$ ( $\text{ps}/\text{m}^2$ )	$-5.1 \times 10^{-2}$	$1.1 \times 10^{-1}$
$A_{\text{eff}}$ ( $\mu\text{m}^2$ )	6.25	14.0
Mode conf. (%)	95	98
1st ZDW ( $\mu\text{m}$ )	3.84	4.5
2nd ZDW ( $\mu\text{m}$ )	4.96	7.7
Cutoff $\lambda$ ( $\mu\text{m}$ )	6.0	9.3

<sup>a</sup>From top to bottom: waveguide cross section, nonlinear parameter  $\gamma$ , second-order dispersion  $\beta_2$ , mode effective area  $A_{\text{eff}}$ , ratio of the mode energy in the waveguide core, 1st and 2nd zero dispersion wavelength (ZDW), and mode cutoff wavelength.

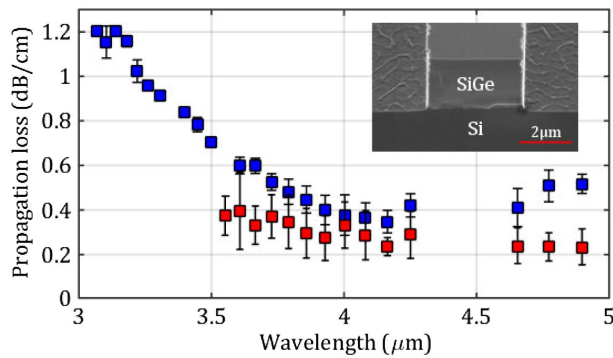


**Fig. 2.** Measured propagation loss for the TE mode of waveguide (1) (blue) and the TM mode of waveguide (2) (red). Inset: 3D scanning electron microscopy image of a cleaved SiGe 40%/Si waveguide.

SiGe/Si platform. However, we note that this larger waveguide is multimode at the pump wavelength (4.15  $\mu\text{m}$ ), and the effective area is double that of waveguide (1), which is expected to decrease the nonlinear conversion efficiency. The light confinement in the waveguide core was 98% and, most importantly, the dispersion of the TM fundamental mode was low and anomalous across a wider spectral range than for waveguide (1) (Fig. 1), which helped to maximize the bandwidth of the SC.

The two waveguides were fabricated on a 200 mm CMOS pilot line, using regular processes. First, 2.7  $\mu\text{m}$  and 4.2  $\mu\text{m}$  thick SiGe (40% Ge) layers were grown by epitaxy on top of Si substrates and encapsulated by 550 nm thick Si layers. Chemical-mechanical polishing was performed to remove the so-called surface cross-hatch, leaving a 50 nm thick Si layer. The waveguides were then patterned using deep ultraviolet photolithography followed by a deep reactive ion etching process (see Fig. 2 inset). More details about the fabrication procedure are included in Supplement 1.

### 3. EXPERIMENTAL RESULTS

We performed linear and nonlinear measurements on these two types of waveguides. By probing waveguides with three different lengths each (from 2 to 7 cm) under relatively low average powers ( $<1$  mW), we measured the propagation losses using the cutback method. Measurements were performed using a tunable OPA delivering 7.5 ps long pulses at a 1.5 MHz repetition rate across a tunable wavelength range between approximately 3–5  $\mu\text{m}$ . For waveguide (1), the propagation loss (Fig. 2) decreased from 1.2 to 0.5 dB/cm between 3 and 3.8  $\mu\text{m}$ . We attribute the larger loss in the short wavelength range to absorption by the O–H bonds adsorbed on the waveguide surface and to the interaction of the higher-order modes with the waveguide sidewalls. Beyond 3.8  $\mu\text{m}$ , where waveguide (1) was single mode, the measured propagation loss was relatively constant at 0.35–0.5 dB/cm. For waveguide (2), the measured propagation loss was equally flat versus wavelength (independent of the polarization, and not shown here), and reached a value as low as 0.23 dB/cm around 4.75  $\mu\text{m}$  consistent with the larger cross-section area and tighter mode confinement (Fig. 2). To the best of our knowledge, this is the lowest propagation loss measured to date in any Si-based waveguides on a chip in the mid-IR. It is comparable to the recently inferred loss propagation in an Si microring [28].

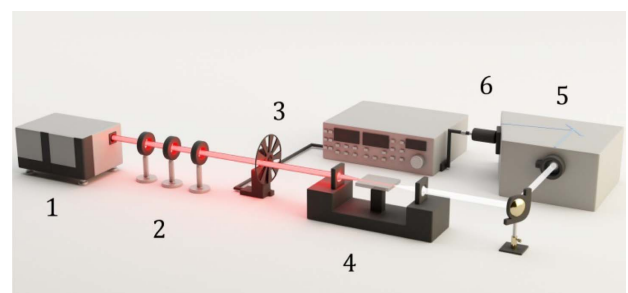
Next, we probed the waveguides in the nonlinear regime by pumping them with sub-picosecond pulses using the experimental setup illustrated in Fig. 3. The 200 mW tunable OPA laser source (MIROPA-fs, Hotlight Systems) delivered  $\sim 200$  fs pulses centered at either 4  $\mu\text{m}$  [for waveguide (1)] or 4.15  $\mu\text{m}$  [for waveguide (2)] at a 63 MHz repetition rate. We selected two different pump wavelengths to slightly adjust the pump to the two waveguide dispersions to operate as close as possible to the zero-dispersion wavelength (ZDW) for each waveguide, while avoiding the 4.15–4.30  $\mu\text{m}$  CO<sub>2</sub> absorption wavelength band. Power and polarization-controlled optical pulses were coupled to the waveguide using a set of chalcogenide lenses. The generated SC spectrum was recorded using a liquid-nitrogen-cooled MCT (HgCdTe) photodetector positioned at the output of the spectrometer. In our setup, the impact of thermal noise was minimized using a lock-in detection technique. This setup was used in [14,20,21,29].

By pumping waveguide (1) with a 7 cm length at 4  $\mu\text{m}$  in the anomalous dispersion regime close to the ZDW, more than an octave-spanning supercontinuum was achieved through the soliton fission process.

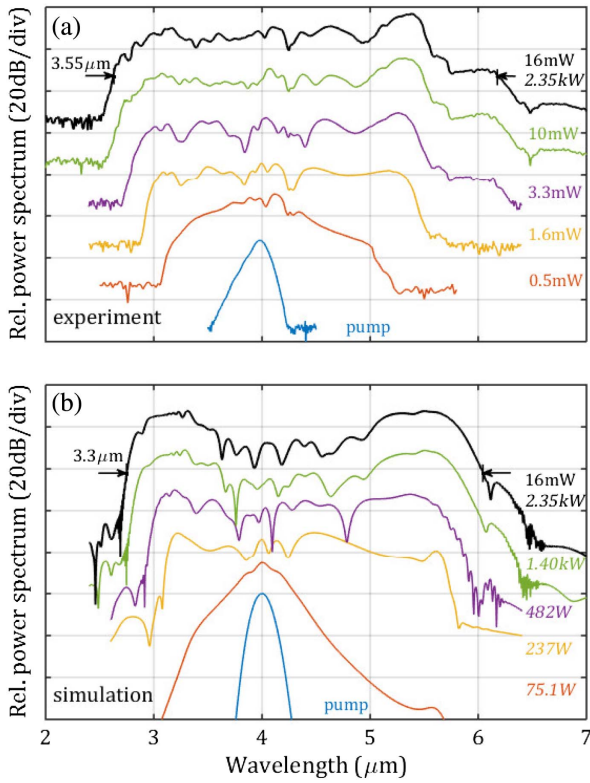
As illustrated in Fig. 4(a), which shows the different spectra measured for increasing coupled average power up to 16 mW, the SC extends between 2.63 and 6.18  $\mu\text{m}$ , with a 3.55  $\mu\text{m}$  bandwidth at  $-30$  dB. The coupled power was estimated from the total chip transmission of  $-12.5$  dB measured at low power, taking into account the chip propagation loss of  $-2.7$  dB and assuming that the coupling loss was the same ( $-4.9$  dB) at the input and output end facet of the waveguide.

Figure 5 shows the power contained in this broad supercontinuum (blue squares) at the end of our SiGe waveguides (which we refer to as “on-chip” SC power). It reached a value greater than 8 mW for 32 mW of coupled average power.

As can be seen in Fig. 4(a), the SC bandwidth achieved for waveguide (1) was limited by the fundamental mode cutoff at 6  $\mu\text{m}$ . Next, we performed measurements on waveguide (2), which was designed to shift the cutoff wavelength up to 9.3  $\mu\text{m}$  [i.e., beyond the silicon absorption limit at 8.5  $\mu\text{m}$  (see Fig. 6—dashed red curve)]. Waveguide (2) was pumped at 4.15  $\mu\text{m}$ , which is close to the first ZDW. We achieved a 1.4 octave-wide supercontinuum from 3 up to 8.3  $\mu\text{m}$  (see Fig. 6), fully covering the 4–8  $\mu\text{m}$  molecular fingerprint band. The generated spectrum was relatively flat across the whole wavelength range, as evidenced by the large  $-10$  dB bandwidth of 4.9  $\mu\text{m}$  (covering the 3.1–8  $\mu\text{m}$  band), a value almost as wide



**Fig. 3.** Experimental setup used in SCG measurements. Elements are (1) tunable OPA, (2) optical waveplate and polarizers, (3) chopper connected to the lock-in amplifier, (4) sample and ChG lenses, (5) an optical spectrum analyzer (OSA), and (6) the MCT photodetector.



**Fig. 4.** (a) Spectra measured out of the 7 cm long waveguide (1) for increasing the coupled average power (quoted in regular font) and corresponding peak power (italic font). (b) Related spectra simulated by the split-step Fourier method for this waveguide geometry using the same peak power (italic font) as in (a). The arrows indicate the -30 dB bandwidth of the SC.

as the -30 dB bandwidth of 5.3 μm. The long wavelength boundary at -35 dB lies at 8.56 μm, limited by absorption in Si substrate, with an associated signal well above the noise level. The role of Si absorption is clearly seen with a drop of the generated SC spectrum intensity starting at ~7 μm (see the green curve in Fig. 6).

As for waveguide (1), the SC signal is also spectrally bright, with a 3.85 mW power measured on the detector for 25 mW

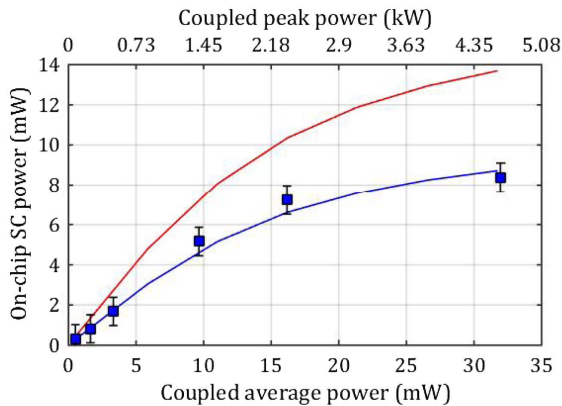


**Fig. 5.** On-chip SC power versus coupled average power measured for the 7 cm long waveguide (1) in TE at 4.0 μm (blue squares), simulated results for the 7 cm waveguide (blue line) and simulated results for a 2 cm long similar waveguide (red line).

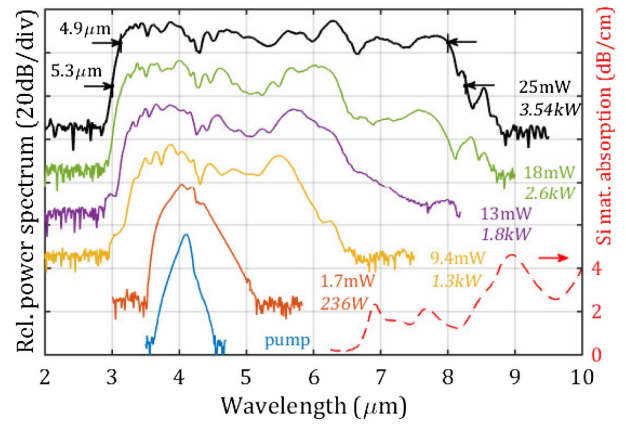


**Fig. 6.** Spectra measured out of the 7 cm long waveguide (2) pumped in TM at 4.15 μm for increasing coupled average power (indicated in regular font on the right side of each spectrum) and corresponding peak power (italic font). The dashed red curve highlights the absorption of crystalline silicon extracted from [30]. The two black arrows on the left highlight the -10 dB bandwidth and -30 dB bandwidth of 4.9 μm and 5.3 μm, respectively.

coupled average power, corresponding to 12.5 mW SC on-chip power (taking into account the ~ -5 dB coupling loss at the input/output facet).

#### 4. NUMERICAL MODELING AND DISCUSSION

To better understand our findings and clarify the enabling and limiting factors in these SCG results, we compared our experimental results to numerical modeling. Sub-picosecond pulse propagation in a SiGe waveguide can be described by the nonlinear Schrödinger equation (NLSE), which was solved numerically using the split-step Fourier method (SSFM). In our model, we included the linear loss, high-order dispersion (up to  $\beta_8$ ), the nonlinear effect (Kerr and four-photon absorption), free-carrier absorption and dispersion, self-steepening, and Raman effects (see Supplement 1). Our model reproduced the experimental SC spectral signatures relatively well, as illustrated by the good agreement between the simulated [Fig. 4(b)] and measured [Fig. 4(a)] spectra of waveguide (1).

For waveguide (1), a 45% power conversion efficiency was achieved at 16 mW coupled average power. We similarly achieved reasonably good agreement between the simulated SC on-chip power generated at the end of the waveguide and the experimental data of Fig. 5. The best fit to the spectrum and SC on-chip power measurements of waveguide (1) were obtained for a  $\gamma$  of  $0.63 \text{ W}^{-1} \text{ m}^{-1}$  and a four-photon absorption coefficient  $\alpha_{4\text{PA}}$  of  $1.16 \times 10^{-6} \text{ cm}^5/\text{GW}^3$ . The inferred effective nonlinearity  $n_2 = 2.5 \times 10^{-14} \text{ cm}^2/\text{W}$  is in good agreement with the value reported earlier by our group [20]. Note that our estimate for the effective nonlinear absorption coefficient is more than an order of magnitude lower than that reported in c-Si [33]. This reemphasizes the potential of the SiGe platform for nonlinear optics in the mid-IR.

We simulated the propagation of 205 fs long, 2.35 kW coupled peak power (16 mW coupled average power) input pulses at a wavelength of 4 μm across the 7 cm long propagation distance (Fig. 7).

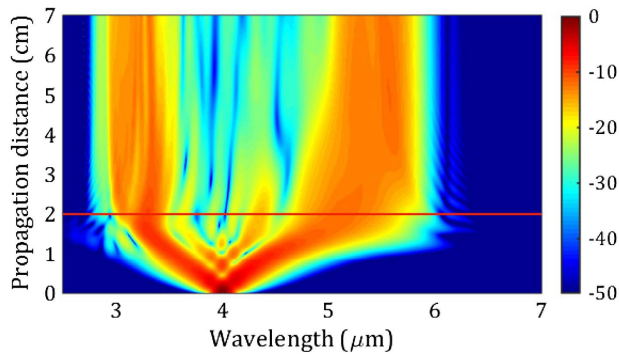


**Fig. 7.** Simulation of the pulse propagation along the 7 cm long waveguide (1) under 16 mW (2.35 kW) coupled (peak) average power at 4  $\mu\text{m}$ .

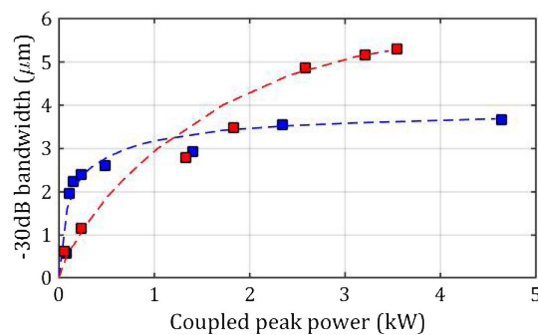


**Fig. 8.** Bandwidth at  $-30$  dB versus coupled peak power experimentally measured for the waveguide (1) (blue) and waveguide (2) (red). The dashed curves are guides for the eye.

As described in [29], the spectral broadening shown in Fig. 7 is governed by higher-order soliton propagation in waveguide (1) pumped in the anomalous dispersion regime. This effect broadens the spectrum around the pump wavelength via the soliton fission process [31], while at the same time generating phase-matched dispersive waves in the normal dispersion region below  $3.8 \mu\text{m}$  and beyond  $5.0 \mu\text{m}$ . The calculated soliton number is 20 at a peak power of 2.35 kW giving a soliton fission length of 1.39 cm, which is in good agreement with Fig. 7. From these simulations, the spectrum appears completely broadened after

a propagation distance of only 2 cm. The associated on-chip SC power calculated for a 2 cm long waveguide is plotted in Fig. 5, showing that we should be able to achieve an even higher 14 mW SC power (at 30 mW) with a high power conversion efficiency of 67% at 15 mW pump power in a shorter waveguide.

When comparing the results achieved in waveguides (1) and (2), we can see the impact of the  $\gamma$  parameter being twice as large in waveguide (1), as shown in Table 2. This effect is illustrated in Fig. 8, which shows the  $-30$  dB bandwidth of the supercontinuum generated by the two waveguides versus coupled peak power. The SC bandwidth is higher for waveguide (1) at low pump power ( $<1$  kW) while waveguide (2) performs better for higher pump powers, allowing us to achieve a much wider SC spectrum. This highlights the trade-offs of each design, depending on whether power consumption or bandwidth (particularly for applications requiring an octave span for self-referencing [34]) is most critical. We also found our design to be highly fabrication tolerant, with the dispersion remaining relatively constant when changing the waveguide width by 50 nm (see Supplement 1). This is well within the fabrication tolerance of the 200 nm pilot line and is significantly more robust than the previously reported silicon-on-sapphire approach [29].

When comparing with other Si based platforms used for the mid-IR (Table 2), the combination of dispersion engineering and low (linear and nonlinear) losses in our SiGe waveguides allowed us to achieve spectrally brighter SC signal.

The SC on-chip power of 12.5 mW at the end of our waveguide is indeed almost two orders of magnitude larger than that reported in previous work on SiGe waveguides [27] and an order of magnitude higher than for silicon-on-sapphire waveguides [29]. In particular, the low nonlinear loss allowed us to maintain high power conversion efficiency (the ratio of on-chip SC power  $P_{\text{out}}$  to coupled average power  $P_{\text{in}}$  was estimated at 0.5 compared to approximately 0.1 and 0.16 for silicon-on-sapphire and SiGe on silica, respectively [27,29]), even with high peak pump power, resulting in a spectrally bright SC signal.

Although we used slightly longer waveguides, our simulations pointed out that an even spectrally brighter (and similarly broad) SC on-chip signal could be achieved in a 2 cm long waveguide (i.e., a length comparable to previous work). We also achieved what we believe is the longest wavelength— $8.56 \mu\text{m}$ —generated by any Si-based platform. Our results are competitive even with ChG waveguides, where spectrally bright (power conversion efficiency  $\sim 0.6$ ) and broad mid-IR SC were generated. However,

**Table 2. Comparison of Current Results with Literature Data on Si-based Platforms Used for the Mid-IR and Results Achieved with the On-chip ChG Platform<sup>a</sup>**

Platform	$\alpha$ (dB/cm)	l (cm)	$\gamma$ (Wm) <sup>-1</sup>	$P_0/P_{\text{out}}$	SCG Bandwidth
<i>Our waveguides</i>					
SiGe/Si (wg 1)	0.377 (4 $\mu\text{m}$ )	7	0.63	2.35 kW/7.25 mW	2.6–6.2 $\mu\text{m}$
SiGe/Si (wg 2)	0.275 (4.15 $\mu\text{m}$ )	7	0.30	3.5 kW/12.5 mW	3.0–8.3 $\mu\text{m}$
<i>CMOS Compatible Platforms</i>					
Si/Al <sub>2</sub> O <sub>3</sub> [29]	$1 \pm 0.3$ (3.7 $\mu\text{m}$ )	1.6	8.2	1.82 kW/ $\sim 1$ mW	1.9–5.5 $\mu\text{m}$
SiGe/SiO <sub>2</sub> [27]	2 (2.4 $\mu\text{m}$ )	3	24.7	120 W/0.15 mW	1.4–2.8 $\mu\text{m}$
Si/SiO <sub>2</sub> [18]	N/A	2	$\sim 50$	15 W/N/A	1.5–3.7 $\mu\text{m}$
Si/SiO <sub>2</sub> [17]	2.5 (2.12 $\mu\text{m}$ )	2	150	12.7 W/N/A	1.5–2.5 $\mu\text{m}$
<i>On-Chip Chalcogenide Glass Platform</i>					
GeAsSe/GeAsS [14]	0.6 (4.2 $\mu\text{m}$ )	1.8	0.2	4.5 kW/20 mW	2.2–10.2 $\mu\text{m}$

<sup>a</sup>From left to right: propagation loss, waveguide length, extracted gamma parameter, coupled peak power ( $P_0$ )/on-chip SC power ( $P_{\text{out}}$ ), and SC-generated  $-30$  dB bandwidth. N/A stands for not available.

SiGe waveguides are fully CMOS compatible in terms of fabrication and yield a higher gamma parameter. Finally, in terms of power consumption, all of our results were achieved using a coupled peak power ( $P_0$ ) comparable to that used to generate SC in the mid-IR (pumped around 4  $\mu\text{m}$ ) with SOS [29] and ChG [14], while being lower than in ChG fibers with similar cross sections [9,13].

## 5. CONCLUSION

We have demonstrated, in a CMOS-compatible waveguide platform, supercontinuum generation across a broad mid-IR wavelength range, spanning the entire 4–8  $\mu\text{m}$  molecular fingerprint range. We used SiGe/Si dispersion engineered waveguides in the mid-IR to achieve a 1.4 octave wide spectrum, thanks to a careful design and tight mode confinement in the waveguide core, which yielded a propagation loss as low as 0.23 dB/cm. The low propagation loss combined with a low nonlinear loss allowed us to harness nonlinear effects in longer waveguides, resulting in a spectrally bright SC signal with more than 10 mW on-chip power corresponding to  $\sim 50\%$  power conversion efficiency. The broad anomalous dispersion profile of our waveguides yielded supercontinuum spectra extending to what we believe is the longest wavelength reported to date in any Si-based platform, reaching the c-Si absorption limit at 8.5  $\mu\text{m}$ . Our results clearly establish silicon germanium-on-silicon as a promising platform for integrated nonlinear photonics in the mid-IR with the ability to operate at least up to 8.5  $\mu\text{m}$ .

**Funding.** H2020 Marie Skłodowska-Curie Actions (MSCA) (631543); H2020 European Research Council (ERC) (GRAPHICS, 648546); Australian Research Council (ARC) (150104327, CE1101018); Agence Nationale de la Recherche (ANR) (MIRSICOMB, ANR-17-CE24-0028).

**Acknowledgment.** We acknowledge the support of the International Associated Laboratory in Photonics between France and Australia (LIA ALPhFA), and author Christelle Monat acknowledges the support of the Institut Universitaire de France.

See [Supplement 1](#) for supporting content.

## REFERENCES

- R. Soref, "Mid-infrared photonics in silicon and germanium," *Nat. Photonics* **4**, 495–497 (2010).
- L. Zhang, A. M. Agarwal, L. C. Kimerling, and J. Michel, "Nonlinear group IV photonics based on silicon and germanium: from near-infrared to mid-infrared," *Nanophotonics* **3**, 247–268 (2014).
- B. Mizaikoff, "Waveguide-enhanced mid-infrared chem/bio sensors," *Chem. Soc. Rev.* **42**, 8683–8699 (2013).
- Y.-C. Chang, "Design, fabrication and characterization of mid-infrared strip waveguide for laser spectroscopy in liquid environments" Ph.D. thesis (EPFL, 2012).
- Y. Yao, A. J. Hoffman, and C. F. Gmachl, "Mid-infrared quantum cascade lasers," *Nat. Photonics* **6**, 432–439 (2012).
- X. Liu, R. M. Osgood, Y. A. Vlasov, and W. M. J. Green, "Mid-infrared optical parametric amplifier using silicon nanophotonic waveguides," *Nat. Photonics* **4**, 557–560 (2010).
- H. Pires, M. Baudisch, D. Sanchez, M. Hemmer, and J. Biegert, "Ultrashort pulse generation in the mid-IR," *Prog. Quantum Electron.* **43**, 1–30 (2015).
- R. R. Gattass, L. B. Shaw, V. Q. Nguyen, P. C. Pureza, I. D. Aggarwal, and J. S. Sanghera, "All-fiber chalcogenide-based mid-infrared supercontinuum source," *Opt. Fiber Technol.* **18**, 345–348 (2012).
- C. R. Petersen, U. Möller, I. Kubat, B. Zhou, S. Dupont, J. Ramsay, T. Benson, S. Sujecki, N. Abdel-Moneim, Z. Tang, D. Furniss, A. Seddon, and O. Bang, "Mid-infrared supercontinuum covering the 1.4–13.3  $\mu\text{m}$  molecular fingerprint region using ultra-high NA chalcogenide step-index fibre," *Nat. Photonics* **8**, 830–834 (2014).
- Y. Yu, B. Zhang, X. Gai, C. Zhai, S. Qi, W. Guo, Z. Yang, R. Wang, D.-Y. Choi, S. Madden, and B. Luther-Davies, "1.8–10  $\mu\text{m}$  mid-infrared supercontinuum generated in a step-index chalcogenide fiber using low peak pump power," *Opt. Lett.* **40**, 1081–1084 (2015).
- T. Cheng, K. Nagasaka, T. H. Tuan, X. Xue, M. Matsumoto, H. Tezuka, T. Suzuki, and Y. Ohishi, "Mid-infrared supercontinuum generation spanning 2.0 to 15.1  $\mu\text{m}$  in a chalcogenide step-index fiber," *Opt. Lett.* **41**, 2117–2120 (2016).
- C. R. Petersen, R. D. Engelsholm, C. Markos, L. Brilland, C. Caillaud, J. Trolès, and O. Bang, "Increased mid-infrared supercontinuum bandwidth and average power by tapering large-mode-area chalcogenide photonic crystal fibers," *Opt. Express* **25**, 15336–15348 (2017).
- D. D. Hudson, S. Antipov, L. Li, I. Alamgir, T. Hu, M. El Amraoui, Y. Messaddeq, M. Rochette, S. D. Jackson, and A. Fuerbach, "Toward all-fiber supercontinuum spanning the mid-infrared," *Optica* **4**, 1163–1166 (2017).
- Y. Yu, X. Gai, P. Ma, K. Vu, Z. Yang, R. Wang, D.-Y. Choi, S. Madden, and B. Luther-Davies, "Experimental demonstration of linearly polarized 2–10  $\mu\text{m}$  supercontinuum generation in a chalcogenide rib waveguide," *Opt. Lett.* **41**, 958–961 (2016).
- I.-W. Hsieh, X. Chen, X. Liu, J. I. Dadap, N. C. Panoui, C.-Y. Chou, F. Xia, W. M. Green, Y. A. Vlasov, and R. M. Osgood, "Supercontinuum generation in silicon photonic wires," *Opt. Express* **15**, 15242–15249 (2007).
- P. Koonath, D. R. Solli, and B. Jalali, "Limiting nature of continuum generation in silicon," *Appl. Phys. Lett.* **93**, 091114 (2008).
- B. Kuyken, X. Liu, R. M. Osgood, R. Baets, G. Roelkens, and W. M. J. Green, "Mid-infrared to telecom-band supercontinuum generation in highly nonlinear silicon-on-insulator wire waveguides," *Opt. Express* **19**, 20172–20181 (2011).
- R. K. W. Lau, M. R. E. Lamont, A. G. Griffith, Y. Okawachi, M. Lipson, and A. L. Gaeta, "Octave-spanning mid-infrared supercontinuum generation in silicon nanowaveguides," *Opt. Lett.* **39**, 4518–4521 (2014).
- M. Brun, P. Labeye, G. Grand, J.-M. Hartmann, F. Boullia, M. Carras, and S. Nicoletti, "Low loss SiGe graded index waveguides for mid-IR applications," *Opt. Express* **22**, 508–518 (2014).
- L. Carletti, P. Ma, Y. Yu, B. Luther-Davies, D. Hudson, C. Monat, R. Orobtschouk, S. Madden, D. J. Moss, M. Brun, S. Ortiz, P. Labeye, S. Nicoletti, and C. Grillet, "Nonlinear optical response of low loss silicon germanium waveguides in the mid-infrared," *Opt. Express* **23**, 8261–8271 (2015).
- L. Carletti, M. Sinobad, P. Ma, Y. Yu, D. Allieux, R. Orobtschouk, M. Brun, S. Ortiz, P. Labeye, J. M. Hartmann, S. Nicoletti, S. Madden, B. Luther-Davies, D. J. Moss, C. Monat, and C. Grillet, "Mid-infrared nonlinear optical response of Si-Ge waveguides with ultra-short optical pulses," *Opt. Express* **23**, 32202–32214 (2015).
- G. Z. Mashanovich, C. J. Mitchell, J. S. Penades, A. Z. Khokhar, C. G. Littlejohns, W. Cao, Z. Qu, S. Stanković, F. Y. Gardes, T. B. Masaud, H. M. H. Chong, V. Mittal, G. S. Murugan, J. S. Wilkinson, A. C. Peacock, and M. Nedeljkovic, "Germanium mid-infrared photonic devices," *J. Lightwave Technol.* **35**, 624–630 (2017).
- J. M. Ramirez, V. Vakarín, C. Gilles, J. Frigerio, A. Ballabio, P. Chaisakul, X. Le Roux, C. Alonso-Ramos, G. Maisons, L. Vivien, M. Carras, G. Isella, and D. Marris-Morini, "Low-loss Ge-rich  $\text{Si}_{0.2}\text{Ge}_{0.8}$  waveguides for mid-infrared photonics," *Opt. Lett.* **42**, 105–108 (2017).
- R. Halir, Y. Okawachi, J. S. Levy, M. A. Foster, M. Lipson, and A. L. Gaeta, "Ultrabroadband supercontinuum generation in a CMOS-compatible platform," *Opt. Lett.* **37**, 1685–1687 (2012).
- D. J. Moss, R. Morandotti, A. L. Gaeta, and M. Lipson, "New CMOS-compatible platforms based on silicon nitride and Hydex for nonlinear optics," *Nat. Photonics* **7**, 597–607 (2013).
- D. Duchesne, M. Peccianti, M. R. E. Lamont, M. Ferrera, L. Razzari, F. Légaré, R. Morandotti, S. Chu, B. E. Little, and D. J. Moss, "Supercontinuum generation in a high index doped silica glass spiral waveguide," *Opt. Express* **18**, 923–930 (2010).

27. M. A. Ezzabib, L. Xu, A. Bogris, A. Kapsalis, M. Belal, E. Lorent, P. Labeye, S. Nicoletti, K. Hammani, D. Syvridis, D. P. Shepherd, J. H. V. Price, D. J. Richardson, and P. Petropoulos, "Broadband telecom to mid-infrared supercontinuum generation in a dispersion-engineered silicon germanium waveguide," *Opt. Lett.* **40**, 4118–4121 (2015).
28. S. A. Miller, M. Yu, X. Ji, A. G. Griffith, J. Cardenas, A. L. Gaeta, and M. Lipson, "Low-loss silicon platform for broadband mid-infrared photonics," *Optica* **4**, 707–712 (2017).
29. N. Singh, D. D. Hudson, Y. Yu, C. Grillet, S. D. Jackson, A. Casas-Bedoya, A. Read, P. Atanackovic, S. G. Duvall, S. Palomba, B. Luther-Davies, S. Madden, D. J. Moss, and B. J. Eggleton, "Midinfrared supercontinuum generation from 2 to 6  $\mu\text{m}$  in a silicon nanowire," *Optica* **2**, 797–802 (2015).
30. D. Chandler-Horowitz and P. M. Amiratharaj, "High-accuracy, midinfrared ( $450\text{ cm}^{-1} \leq \omega \leq 4000\text{ cm}^{-1}$ ) refractive index values of silicon," *J. Appl. Phys.* **97**, 123526 (2005).
31. J. M. Dudley, G. Genty, and S. Coen, "Supercontinuum generation in photonic crystal fiber," *Rev. Mod. Phys.* **78**, 1135–1184 (2006).
32. J. M. Dudley and J. R. Taylor, *Supercontinuum Generation in Optical Fibers*, 1st ed. (Cambridge University, 2010), p. 418.
33. X. Gai, Y. Yu, B. Kuyken, P. Ma, S. J. Madden, J. Van Campenhout, P. Verheyen, G. Roelkens, R. Baets, and B. Luther-Davies, "Nonlinear absorption and refraction in crystalline silicon in the mid-infrared," *Laser Photon. Rev.* **7**, 1054–1064 (2013).
34. S. A. Diddams, "The evolving optical frequency comb," *J. Opt. Soc. Am. B* **27**, B51–B62 (2010).



# Mid-infrared octave spanning supercontinuum generation to 8.5 $\mu\text{m}$ in silicon-germanium waveguides: supplementary material

MILAN SINOBAD,<sup>1,2,\*</sup> CHRISTELLE MONAT,<sup>1</sup> BARRY LUTHER-DAVIES,<sup>3</sup> PAN MA,<sup>3</sup> STEPHEN MADDEN,<sup>3</sup> DAVID J. MOSS,<sup>4</sup> ARNAN MITCHELL,<sup>2</sup> DAVID ALLIOUX,<sup>1</sup> REGIS OROBTCHOUK,<sup>1</sup> SALIM BOUTAMI,<sup>5</sup> JEAN-MICHEL HARTMANN,<sup>5</sup> JEAN-MARC FEDELI,<sup>5</sup> AND CHRISTIAN GRILLET<sup>1,\*</sup>

<sup>1</sup>Université de Lyon, Institut des Nanotechnologies de Lyon (INL), 69131 Ecully, France

<sup>2</sup>CUDOS and School of Engineering, RMIT University, Melbourne, VIC 3001, Australia

<sup>3</sup>CUDOS, Laser Physics Centre, Australian National University, Canberra, ACT 0100, Australia

<sup>4</sup>Centre for Microphotonics, Swinburne University of Technology, Hawthorn, VIC 3122, Australia

<sup>5</sup>CEA-Leti, MINATEC Campus, 17 rue des Martyrs, 38054 Grenoble Cedex 9, France

\*Corresponding author: [milan.sinobad@student.rmit.edu.au](mailto:milan.sinobad@student.rmit.edu.au), [christian.grillet@ec-lyon.fr](mailto:christian.grillet@ec-lyon.fr)

Published 27 March 2018

---

This document provides supplementary information to “Mid-infrared octave spanning supercontinuum generation to 8.5  $\mu\text{m}$  in silicon-germanium waveguides,” <https://doi.org/10.1364/OPTICA.5.000360>.

---

## 1. Waveguide fabrication

A  $\text{Si}_{0.6}\text{Ge}_{0.4}$  alloy concentration was chosen as it provides a suitable trade-off between high nonlinear properties [1], transparency window and low propagation loss when grown on Si (low misfit dislocation) [2].  $\text{Si}_{0.6}\text{Ge}_{0.4}$  material refractive index (real and imaginary part) was obtained by ellipsometry measurement between 1700 nm and 9000 nm.

The  $\text{Si}_{0.6}\text{Ge}_{0.4}$  layers and the Si caps were grown at 850°C, 20 Torr in a 200mm Applied Materials Epi Centura 5200 tool. Given the large thicknesses targeted, a chlorinated chemistry, with a mixture of  $\text{SiH}_2\text{Cl}_2 + \text{GeH}_4$  (pure  $\text{SiH}_2\text{Cl}_2$ ) in high purity  $\text{H}_2$  was used to grow the SiGe layers (the Si caps) and avoid chamber quartz wall clogging (and flaking). Ref. [3] data points were called upon to select the right  $\text{SiH}_2\text{Cl}_2$  and  $\text{GeH}_4$  mass-flow to have 40% of Ge inside the SiGe layers. Most of the sacrificial Si cap was removed during the CMP steps used to get rid of the surface cross-hatch (i.e. undulations along the  $\langle 110 \rangle$  directions) inherent to such thick, nearly 100% plastically relaxed layers. A smooth, featureless surface was recovered (i.e. with a root mean square roughness typically around 1-2 Å in Atomic Force Microscopy) [4]. The threading dislocations density inside such high Ge content SiGe layers grown directly on Si(001) is typically around  $10^9 \text{ cm}^{-2}$ , as detailed in Ref. [5].

## 2. Tolerance in waveguide fabrication

We studied the fabrication tolerance of our dispersion engineered air-clad SiGe/ Si waveguides, taking the example of the  $3.75\mu\text{m} \times 2.70\mu\text{m}$  cross-section waveguide 1). The deviations we consider for the waveguide width and thickness were  $\pm 100\text{nm}$  and  $\pm 50\text{nm}$ , respectively, which are well above the accuracy of the lithography and epitaxy processes used during fabrication. Figure S 1 shows the dispersion of the waveguide fundamental TE mode when varying either the width (a) for a fixed thickness or the thickness (b) for a fixed waveguide width. When the waveguide width increases, we observe an increase of the mode effective area ( $A_{\text{eff}}$ ) and a slight red-shift of the two zero dispersion wavelengths (ZDW) along with the cut-off wavelength (Fig S1a). We also observe a slight decrease in the maximum group velocity dispersion (max GVD). In contrast, an increase of the waveguide thickness leads to a slight increase of both the second ZDW and of the max GVD. These variations (ZDW, cut-off wavelength) are low, in the 1% to 3% range, typically. Our design is thus robust against waveguide width or thickness changes, as summarized in Table S 1.

We note that the impact on the maximum GVD value is larger. We can however take advantage of the opposite effects of

increasing the waveguide width and thickness with regards to this parameter to maintain a low GVD value across a wide band, while shifting the mode cut-off towards longer wavelengths, through an increase of both geometrical parameters simultaneously. By increasing the waveguide size (thickness and width), the difference between the two ZDW increases, resulting in a wider band in the anomalous dispersion regime.

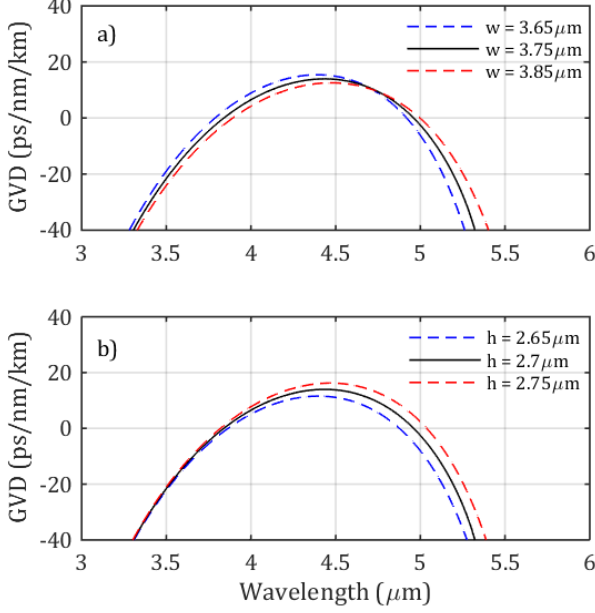


**Figure S 1** Calculated group velocity dispersion (GVD) of the 2.7μm thick waveguide when varying the waveguide width (top) and GVD of the 3.75μm width waveguide when varying the thickness (bottom)

**Table S 1 Comparison of the waveguide parameters when changing the width and height of the waveguide**

Waveguide cross-section	1 <sup>st</sup> ZDW (μm)	2 <sup>nd</sup> ZDW (μm)	λ cutoff (μm)	max GVD (ps/nm/km)	A <sub>eff</sub> at 4μm (μm <sup>2</sup> )
Increasing width for a fixed thickness a)					
3.65x2.70μm <sup>2</sup>	3.79	4.92	5.87	15.4	6.09
3.75x2.70μm <sup>2</sup>	3.84	4.96	5.97	14.0	6.25
3.85x2.70μm <sup>2</sup>	3.89	5.0	6.06	12.6	6.40
Increasing thickness for a fixed width b)					
3.75x2.65μm <sup>2</sup>	3.86	4.88	5.93	11.5	6.17
3.75x2.70μm <sup>2</sup>	3.84	4.96	5.97	14.0	6.25
3.75x2.75μm <sup>2</sup>	3.82	5.04	6.00	16.2	6.33

### 3. Extraction of the propagation loss

The method used to extract the waveguide propagation loss is based on a linear fit of the total loss (insertion loss) versus waveguide length. We estimate the propagation loss as the slope of this linear dependence, as fitted by the method of least squares. The error bars were then estimated as the standard deviation (i.e. uncertainty) of the slope value using this linear regression.

### 4. Numerical modeling and simulations

We simulate the propagation of 4μm femtosecond pulses across the air/SiGe/Si waveguides by using the nonlinear Schrödinger

equation (NLSE), which is numerically solved using the split-step Fourier method (SSFM) [6, 7]. Basically, the electric field amplitude of the pulse envelope  $A(z,t)$  spatially varies along the propagation direction ( $z$ ) according to the following NLSE equation:

$$\frac{\partial A}{\partial z} = -\frac{\alpha}{2}A + \sum j^{m+1} \frac{\beta_m}{m!} \frac{\partial^m A}{\partial t^m} + j\gamma(\omega_0) \left(1 + \frac{j}{\omega} \frac{\partial}{\partial t}\right) A \times \int_{-\infty}^t R(t-t')|A|^2 dt' - \frac{\alpha_{4PA}}{2A_{eff}^3} |A|^6 A - \frac{\sigma}{2} (1 + j\mu) N_c A$$

This equation includes several (linear and nonlinear) phenomena in the right-hand term: the propagation loss (attenuation coefficient  $\alpha$ ), the high order dispersion (polynomial Taylor expansion  $\beta_m$ ), the nonlinear Kerr effect (governed by the nonlinear parameter  $\gamma$ ), the nonlinear absorption (restricted here to four-photon absorption, with a coefficient  $\alpha_{4PA}$ ), self-steepening, Raman effect, and free carrier induced absorption and dispersion. Based on the effective nonlinearity extracted for silicon germanium [1, 2] and crystalline silicon [8] we assume that the dispersion of  $n_2$  is negligible in the mid-IR. In this equation, the constant values of both the nonlinearity  $n_2$  and the effective area of the waveguide mode  $A_{eff}$  are taken at the central frequency  $\omega_0$  of the pulse. In addition, only the propagation loss measured at the pump wavelength is included considering the very low propagation loss variation reported between 3.5μm and 5μm. The parameters used for self-steepening and Raman are those of crystalline silicon [9]. The high-order dispersion includes  $\beta_m$  values, up to the 8<sup>th</sup> order, to properly reproduce the waveguide mode dispersion between 2.5μm and 5.5μm (see Table S 2).

**Table S 2 Extracted dispersion coefficients at 4μm used in simulations**

$\beta_2$ (ps <sup>2</sup> /m)	$-5.37 \times 10^{-2}$	$\beta_6$ (ps <sup>6</sup> /m)	$3.95 \times 10^{-8}$
$\beta_3$ (ps <sup>3</sup> /m)	$1.99 \times 10^{-3}$	$\beta_7$ (ps <sup>7</sup> /m)	$-1.46 \times 10^{-9}$
$\beta_4$ (ps <sup>4</sup> /m)	$2.71 \times 10^{-5}$	$\beta_8$ (ps <sup>8</sup> /m)	$1.93 \times 10^{-11}$
$\beta_5$ (ps <sup>5</sup> /m)	$-6.62 \times 10^{-7}$	$\beta_9$ (ps <sup>9</sup> /m)	

The impact of free-carriers present in the waveguide with a density  $N_c(z,t)$  is modeled by including both the free-carrier absorption cross-section  $\sigma$  and  $\mu=2k_c k_0/\sigma$  with the dispersion parameter  $k_c$  coming from [1]. Since we rule out linear, two-photon and three-photon absorption in SiGe at 4μm, we assume that free-carriers are generated via four-photon absorption only and recombine within a lifetime  $\tau$ . We model the temporal variation of their density at a given position along the waveguide by the following rate equation:

$$\frac{\partial N_c}{\partial t} = \frac{\alpha_{4PA}}{4\hbar\omega} \left(\frac{|A|^2}{A_{eff}}\right)^4 - \frac{N_c}{\tau}$$

which complements the NLSE to compute the free carrier density at each step. The last term on the right hand side was neglected, since reported values for  $\tau$  in Si based waveguides are much longer than our pulse duration ( $\sim 200$ fs) and shorter than the time period between two subsequent pulses (63MHz repetition rate) [9]. Table S 3 summarizes the numerical values of the parameters used in our simulations.

**Table S3 Numerical values of the parameters (at 4 $\mu$ m) used in the model**

$T_{FWHM}$ (fs)	205	$\alpha$ (dB/cm)	0.38
$P_0$ (W)	75 – 2350	$n_2$ (cm <sup>2</sup> /W)	$2.55 \times 10^{-14}$
L (cm)	7	$\alpha_{APA}$ (cm <sup>5</sup> /GW <sup>3</sup> )	$1.16 \times 10^{-6}$
$A_{eff}$ ( $\mu$ m <sup>2</sup> )	6.25	$\sigma$ (cm <sup>2</sup> )	$1.45 \times 10^{-17} \times (4/1.55)^2$
$\alpha$ (dB/cm)	0.38	$k_c$ (cm <sup>3</sup> )	$-5.0 \times 10^{-21} \times (4/1.55)^2$

A comparison of the experiments and simulations using this model is presented in the main text of the article. Figure 4 shows the spectra at the output of the waveguide for different pump powers. We observe a relatively good agreement between the simulation and the experiment, with slight differences at short (<3 $\mu$ m) and long wavelengths (> 5.5 $\mu$ m). The signal at short wavelengths is slightly stronger in simulations compared with experiments. This can be attributed to the higher propagation loss and the non-negligible three photon absorption around 3 $\mu$ m, which are not included in our model. On the long wavelength side, the intensity of the simulated spectrum is also slightly higher than in the experiment. We attribute this to the fact that the experimental dispersion is not well reproduced by our 8<sup>th</sup> order polynomial near the cut-off wavelength of the waveguide. Note that the small difference between the simulated and experimental pump spectrum is a result of the experimental “pump” spectrum being measured at the output of the waveguide at very low coupled peak power and not directly from the pump laser itself, while the pump spectrum was calculated at the input of the waveguide. Regarding the on-chip supercontinuum power presented in Figure 5, the simulated and experimental results are in good agreement, with a low Root Mean Square deviation value of only 0.37mW (i.e. 4% of the maximum signal).

Supercontinuum in the larger cross-section waveguide 2) has not been simulated since our model does not include wavelength dependence of the effective area, silicon material loss and modal overlap with silicon substrate, which directly affect linear loss towards longer wavelengths. Taking this into account could help reproduce the SC at long wavelengths, especially beyond 7  $\mu$ m.

## References

1. Carletti, L., et al., *Mid-infrared nonlinear optical response of Si-Ge waveguides with ultra-short optical pulses*. Opt Express, 2015. **23**(25): p. 32202-14.
2. Carletti, L., et al., *Nonlinear optical response of low loss silicon germanium waveguides in the mid-infrared*. Opt Express, 2015. **23**(7): p. 8261-71.
3. Bogumilowicz, Y., et al., *SiGe high-temperature growth kinetics in reduced pressure-chemical vapor deposition*. Journal of Crystal Growth, 2005. **274**(1-2): p. 28-37.
4. Hartmann, J.M., et al., *Impact of the H2 bake temperature on the structural properties of tensily strained Si layers on SiGe*. Journal of Crystal Growth, 2008. **310**(10): p. 2493-2502.
5. Hartmann, J.M., et al., *Investigation of the low temperature /high temperature approach to produce Si 0.5 Ge 0.5 and Ge strain relaxed buffers*. ECS Transactions, 2016. **75**(8): p. 579-588.
6. Agrawal, G., *Nonlinear Fiber Optics, Fifth Edition*. 5 edition ed. 2012, Amsterdam: Academic Press. 648.
7. Dudley, J.M. and J.R. Taylor, *Supercontinuum Generation in Optical Fibers*. 1 edition ed. 2010, Cambridge ; New York: Cambridge University Press. 418.
8. Gai, X., et al., *Nonlinear absorption and refraction in crystalline silicon in the mid-infrared*. Laser & Photonics Reviews, 2013. **7**(6): p. 1054-1064.

9. Lin, Q., O.J. Painter, and G.P. Agrawal, *Nonlinear optical phenomena in silicon waveguides: modeling and applications*. Optics Express, 2007. **15**(25): p. 16604-16644.

## Conclusion

In this second chapter, we presented the generation of bright and broadband supercontinua in silicon germanium-on-silicon waveguides. For this purpose, two waveguides were used. The first one was a single-mode waveguide with optimized nonlinearity and the second was a multi-mode waveguide designed to extend supercontinuum up to the mid-infrared absorption limit of silicon.

We first presented the linear and nonlinear characterization of these waveguides in the mid-infrared and we then demonstrated supercontinuum generation across a broad mid-IR wavelength range. We measured the propagation loss in a wavelength range from 3 to 5  $\mu\text{m}$  using low power picosecond pulses (i.e. less than 1 mW power 7.5 ps long pulses). Constant and low loss between 0.2 and 0.3 dB/cm has been measured at wavelengths from 4 to 5  $\mu\text{m}$ . Transmission measurements were then performed using sub-picosecond pulses ( $\sim 200$  fs long pulses) centered around 4  $\mu\text{m}$  wavelength at different pulse power levels. This allowed us to extract low nonlinear loss using a numerical model. Finally, we performed spectra measurements recording bright supercontinua spanning from 2.6 to 6.2  $\mu\text{m}$  in the waveguide with optimized nonlinearity and from 3.0 to 8.3  $\mu\text{m}$  in the multimode waveguide optimized to achieve a large bandwidth.

The propagation loss reported in this work has been the lowest loss reported to date in germanium based waveguides (see Table 2 of the Optica paper). Such a low propagation loss combined with the low nonlinear losses of the waveguide materials enabled us to achieve bright supercontinuum with more than 10 mW on-chip power at the output. This is more than an order of magnitude higher power than that of the previously reported supercontinuum in silicon-on-sapphire waveguides spanning up to 5.5  $\mu\text{m}$  (for similar input power). Dispersion engineering of our waveguides allowed us to achieve supercontinuum spectra extending to the longest wavelength reported to date in any Si-based platform, reaching the c-Si absorption limit at 8.5 $\mu\text{m}$ .

Bright supercontinuum covering the entire mid-IR atmospheric absorption band (4 – 8 $\mu\text{m}$ ) is desired for molecular spectroscopy. However, in practice, fluctuations of the supercontinuum spectra from pulse to pulse severely limit the sensitivity of molecule detection using these sources. Therefore, high coherence of supercontinuum is required for these applications. The next chapter discusses the coherence properties of the mid-infrared supercontinuum that has been presented in this chapter.

## **Chapter 3.**

# **High coherence at $f$ and $2f$ of mid-infrared supercontinuum generation in silicon germanium waveguides**





This chapter discusses the coherence properties as numerically calculated by simulations (see section 1.2.3.2 of chapter 1) for the supercontinuum spectrum that was experimentally demonstrated in chapter 2.

High coherence of a mid-infrared supercontinuum is required for high-sensitivity and ultra-fast molecular spectroscopy. It is also required for applications directly relying on coherence such as coherent anti-Stokes Raman spectroscopy (CARS) and optical coherence tomography (OCT). However, until this work, coherent mid-infrared supercontinuum in the silicon chip-based platform had not been reported, even by simulations. Only recently though, a coherent mid-infrared supercontinuum was demonstrated in silicon-on-sapphire waveguides [98].

We numerically analyze the coherence properties of one of the supercontinuum presented in chapter 2. High coherence is calculated for a mid-infrared supercontinuum generated in a 7 cm long SiGe/Si waveguide pumped with 200fs long input pulses centered at  $4\mu\text{m}$ . To support our findings, and explain why such coherence was preserved, we studied the specific dynamics associated with this supercontinuum generation. We found, in particular, the role played by the engineered dispersion profile and the anomalous dispersion band enclosed by two zero GVD wavelengths.

This chapter corresponds to the article entitled “High coherence at  $f$  and  $2f$  of mid-infrared supercontinuum generation in silicon germanium waveguides” submitted to IEEE JSTQE journal (Journal of Selected Topics in Quantum Electronics) and still under review. The article is organized into four sections, which present the numerical model, the experimental and numerical results and the analysis of the supercontinuum generation dynamics.

# High Coherence at $f$ and $2f$ of Mid-Infrared Supercontinuum Generation in Silicon Germanium Waveguides

Milan Sinobad , Alberto Della Torre, Remi Armand, Barry Luther-Davies, Pan Ma, Stephen Madden, Arnan Mitchell , David J. Moss , Jean-Michel Hartmann, Jean-Marc Fédéli , Christelle Monat, and Christian Grillet

**Abstract**—Absorption spectroscopy based on supercontinuum generation in the mid-infrared is a powerful technique to analyze the chemical composition of samples. Furthermore, phase-coherent supercontinuum sources can enable fast data acquisition with coherent, stable pulses that allow single-shot measurements. We report here a numerical study of the coherence of an octave-spanning mid-infrared supercontinuum source that was experimentally obtained in an air-clad SiGe/Si waveguide. We show that engineering two closely spaced zero-dispersion wavelengths that enclose an anomalous dispersion band centered around a fixed pump wavelength can produce supercontinuum pulses with high spectral density and full coherence at the extreme ends of the spectrum. This work is important for absorption spectroscopy, on-chip optical frequency metrology, and  $f$ -to- $2f$  interferometry applications.

**Index Terms**—Optical waveguides, silicon germanium, silicon photonics, supercontinuum (SC) generation.

## I. INTRODUCTION

**S**UPERCONTINUUM (SC) sources are of great interest because of their high spectral brightness over a large spectral bandwidth. In particular, mid-infrared (mid-IR, 3–20  $\mu\text{m}$ ) sources, due to the strong molecular fingerprint in this spectral region [1], are well suited for environmental and toxic

Manuscript received May 24, 2019; revised August 5, 2019; accepted September 2, 2019. Date of publication September 24, 2019; date of current version October 25, 2019. This work was supported in part by the Agence Nationale de la Recherche (ANR) under Grant ANR-17-CE24-0028 and in part by H2020 European Research Council (ERC) under Grant 648546 GRAPHICS. (*Corresponding author: Milan Sinobad.*)

M. Sinobad, A. D. Torre, R. Armand, C. Monat, and C. Grillet are with Institut des Nanotechnologies de Lyon (INL UMR5270), Université de Lyon 69134 Ecully, France (e-mail: milan.sinobad@ec-lyon.fr; alberto.della-torre@ec-lyon.fr; remi.armand@ec-lyon.fr; christelle.monat@ec-lyon.fr; christian.grillet@ec-lyon.fr).

B. Luther-Davies, P. Ma, and S. Madden are with Laser Physics Centre, Australian National University, Canberra 0100, Australia (e-mail: barry.luther-davies@anu.edu.au; pan.ma@anu.edu.au; stephen.madden@anu.edu.au).

A. Mitchell is with the School of Engineering, RMIT University, Melbourne 3001, Australia (e-mail: arnan.mitchell@rmit.edu.au).

D. J. Moss is with the Centre for Microphotonics, Swinburne University of Technology, Hawthorn 3122, Australia (e-mail: dmoss@swin.edu.au).

J.-M. Hartmann and J.-M. Fédéli are with the CEA-Leti, MINATEC Campus, 38054 Grenoble, France (e-mail: jean-michel.hartmann@cea.fr; jean-marc.fedeli@cea.fr).

Color versions of one or more of the figures in this article are available online at <http://ieeexplore.ieee.org>.

Digital Object Identifier 10.1109/JSTQE.2019.2943358

vapors sensing in atmospheric, security and industrial applications [2]. Broadband integrated sources can achieve sensing with high throughput thanks to the parallel detection of several species [3]. Their integration in a complementary metal-oxide-semiconductor (CMOS) compatible integrated platform would lead to high volume, low cost sensing technology. Mid-IR SC was first demonstrated in fibers [4]–[7], in a chalcogenide based platform [8] and recently in CMOS compatible platforms [9], [10]. Among the different CMOS compatible platforms that have been proposed for mid-IR SC generation, silicon germanium-on-silicon waveguides are very promising thanks to the wide transparency window up to 8.5  $\mu\text{m}$  [11]–[13] and good nonlinear properties [14]–[16], with the recent demonstration of SC generation from 3 to 8.5  $\mu\text{m}$  [17].

The SC bandwidth is maximal when pumping the nonlinear waveguide structure in the anomalous dispersion regime [18]. For many applications however, a wide bandwidth is not the only requirement. High coherence across the spectrum is also needed. Locking of the fundamental and second harmonic of coherent broadband sources spanning more than one octave (termed  $f$ -to- $2f$  self-frequency referencing) has played a major role in the fields of frequency metrology and optical clocks [19]–[21]. Coherent SC sources have also been used for precision spectroscopy, high resolution optical tomography [22], [23] and Raman spectroscopy [24]. In the anomalous dispersion regime, however, the mechanism underlying SC generation is generally dominated by soliton fission triggered by noise-seeded modulation instability leading to shot-to-shot fluctuations and degradation of coherence [18]. To effectively transfer the coherence properties of the pump to the generated SC, several strategies have been used. F. Leo *et al.* demonstrated that coherence could be enforced by a high level of two-photon absorption (TPA). This effectively reduces the soliton number in the waveguide. A high coherence was reported in a 1 cm long silicon-on-insulator waveguide pumped at 1.6  $\mu\text{m}$  with 150 fs pulses [25]. However, this approach typically restricts the SC bandwidth at the output. More frequently, coherence is preserved by using a waveguide only slightly longer than the soliton fission length to alleviate coherence degradation due to modulation instability. Using this approach, A. R. Johnson *et al.* demonstrated coherent SC when pumping silicon-nitride waveguides at 1  $\mu\text{m}$  [26]. Alternatively, extremely short pump pulses can be used, in order to increase the

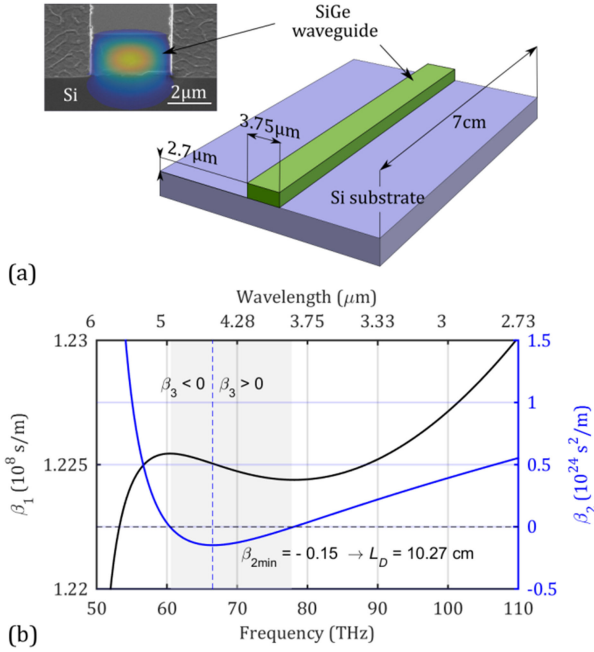


Fig. 1. (a) Waveguide schematics and scanning electron microscope (SEM) image with the superimposed TE fundamental mode electric field profile. (b)  $\beta_1$  (black, left y-scale) and  $\beta_2$  (blue, right y-scale) dispersion curves. The grey area indicates the anomalous dispersion regime. The dispersion length ( $L_D$ ) is calculated for the minimal value of  $\beta_2$  represented by the blue dashed vertical line.

soliton fission length. For instance, N. Singh *et al.* generated a SC with a coherence higher than 90%, on average, by pumping a silicon-on-insulator waveguide with sub-100 fs pulses in the short wave infrared (SWIR). This approach is however constraining from the technological point of view [27]. These strategies were recently used to numerically demonstrate high coherence of the supercontinuum in mid-IR generated from the germanium-on-silicon waveguide [28].

Here, we numerically study the coherence properties of a mid-IR supercontinuum (extending from 2.63 to 6.18  $\mu\text{m}$ ) that was experimentally generated in a 3.75  $\mu\text{m}$   $\times$  2.70  $\mu\text{m}$  cross-section, 7 cm long silicon germanium-on-silicon ( $\text{Si}_{0.6}\text{Ge}_{0.4}/\text{Si}$ ) waveguide pumped by  $\sim 200$  fs pulses at  $\lambda = 4 \mu\text{m}$  [17]. We show that a broad and highly coherent SC can be obtained by pumping the waveguide at a wavelength enclosed in a narrow anomalous dispersion band. Through analysis of the spectrograms and the coherence properties of the SC generated at different locations along the waveguide, we study the dynamics of the underlying mechanism generating the SC in this particular regime. We show that, with this approach, it is possible to achieve a broadband SC with a high degree of coherence irrespectively of the waveguide length and without the need for sub-100 fs pump-pulses or multi-photon absorption.

## II. WAVEGUIDE DESIGN AND NUMERICAL MODEL

Our device consists of a 7 cm long  $\text{Si}_{0.6}\text{Ge}_{0.4}$  on Si (001) air-clad waveguide with a 3.75  $\mu\text{m}$   $\times$  2.70  $\mu\text{m}$  cross-section [see Fig. 1(a)]. We demonstrated in [17] that by pumping such a waveguide with  $\sim 200$  fs pulses at 4  $\mu\text{m}$  wavelength,

TABLE I  
NUMERICAL VALUES OF THE PARAMETERS USED IN THE MODEL

Parameter	Value	Dispersion	Value calc. at $\lambda_0 = 4 \mu\text{m}$ (TE)
$\lambda_0$ ( $\mu\text{m}$ )	4	$\beta$ (1/m)	$5.5 \times 10^6$
$T_{\text{FWHM}}$ (fs)	205	$\beta_1$ (s/m)	$1.22 \times 10^{-8}$
$P_p$ (W)	2350	$\beta_2$ ( $\text{s}^2/\text{m}$ )	$-5.52 \times 10^{-26}$
		$\beta_3$ ( $\text{s}^3/\text{m}$ )	$2.46 \times 10^{-39}$
$A_{\text{eff}}$ ( $\mu\text{m}^2$ )	6.25	$\beta_4$ ( $\text{s}^4/\text{m}$ )	$1.94 \times 10^{-53}$
$L$ (cm)	7	$\beta_5$ ( $\text{s}^5/\text{m}$ )	$-8.26 \times 10^{-68}$
$\alpha$ (dB/cm)	0.38	$\beta_6$ ( $\text{s}^6/\text{m}$ )	$-2.52 \times 10^{-81}$
$n_2$ ( $\text{cm}^2/\text{W}$ )	$2.55 \times 10^{-14}$	$\beta_7$ ( $\text{s}^7/\text{m}$ )	$-1.42 \times 10^{-93}$
$\alpha_{4PA}$ ( $\text{cm}^5/\text{GW}^3$ )	$1.16 \times 10^{-6}$	$\beta_8$ ( $\text{s}^8/\text{m}$ )	$1.02 \times 10^{-106}$
$\sigma$ ( $\text{cm}^2$ )	$1.45 \times 10^{-17} \times (4/1.55)^2$	$\beta_9$ ( $\text{s}^9/\text{m}$ )	$-2.88 \times 10^{-120}$
$k_c$ ( $\text{cm}^3$ )	$-5.0 \times 10^{-21} \times (4/1.55)^2$	$\beta_{10}$ ( $\text{s}^{10}/\text{m}$ )	$3.16 \times 10^{-134}$
$f_R$	0.043		
$\tau_1$ (fs)	12.2		
$\tau_2$ (ps)	3		

we were able to generate high intensity SC signal across a wide bandwidth, with extreme wavelengths (at 2.63  $\mu\text{m}$  and 6.18  $\mu\text{m}$ ) separated by an octave. SC is limited by mode cutoff at long wavelengths ( $\lambda \sim 6 \mu\text{m}$ ) which is induced by the asymmetry of the waveguide with respect to the vertical plane. The first and second order dispersions of the waveguide, calculated by a finite-difference mode solver, are shown in Fig. 1(b) as a function of the optical wavelength. The waveguide dispersion thus exhibits two zero-dispersion wavelengths (ZDW) at 3.84  $\mu\text{m}$  and 4.96  $\mu\text{m}$ , respectively, which enclose an anomalous dispersion band highlighted in grey in Fig. 1(b).

The propagation of short optical pulses in a waveguide can be described by the generalized nonlinear Schrodinger equation (GNLSE) under the slowly varying envelope approximation:

$$\begin{aligned} \frac{\partial A}{\partial z} = & -\frac{\alpha}{2}A + \sum i^{m+1} \frac{\beta_m}{m!} \frac{\partial^m A}{\partial t^m} + i\gamma(\omega_0) \left(1 + \frac{i}{\omega} \frac{\partial}{\partial t}\right) A \\ & \times \int_{-\infty}^t R(t-t') |A|^2 dt' - \frac{\alpha_{4PA}}{2A_{\text{eff}}^3} |A|^6 A \\ & - \frac{\sigma}{2} (1 - i\mu) N_c A \end{aligned} \quad (1)$$

where  $A(z, t)$  is the electric field envelope,  $\alpha$  is the attenuation coefficient,  $\beta_m$  is the  $m$ -th order derivative of the propagation constant with respect to the angular frequency,  $\gamma(\omega_0)$  is the nonlinear parameter at the central frequency of the pulse,  $R(t-t')$  is a function that takes into account Raman contributions,  $\alpha_{4PA}$  is the four-photon absorption coefficient,  $A_{\text{eff}}$  is the effective area at the central frequency of the pulse,  $N_c$  is the free-carrier density in the waveguide,  $\sigma$  is the free-carrier absorption cross-section and  $\mu = 2k_c k_0 / \sigma$  is a dimensionless parameter that encompasses the impact of free-carrier dispersion, with  $k_0$  being the wavenumber and  $k_c$  the free-carrier dispersion parameter [16]. High-order dispersions  $\beta_m$  are included up to  $\beta_{10}$  (see Table I). Here, we consider that the propagation loss is constant and equal to 0.38 dB/cm, as measured at 4  $\mu\text{m}$  [17]. The

nonlinear Raman response function ( $t$ ) is taken equal to that of crystalline silicon [29]. The fractional contribution of the Raman response to the third-order nonlinearity  $f_R$ , the Raman response time  $\tau_1$  and the phonon lifetime  $\tau_2$  are given in Table I.

The temporal variation of the free-carrier density in the waveguide is modeled by the following rate equation:

$$\frac{\partial N_c}{\partial t} = \frac{\alpha_4 P A}{4\hbar\omega} \left( \frac{|A|^2}{A_{eff}} \right)^4 \quad (2)$$

The recombination lifetime is neglected in (2), as the reported value in silicon based waveguides ( $\sim 10$  ns) [30] is (i) much longer than our pulse duration ( $T_{FWHM} = 205$  fs) and (ii) much shorter than the time period between subsequent pulses. The nonlinear parameter and effective area of our waveguide are  $\gamma = 0.63$  (W·m) $^{-1}$  and  $A_{eff} = 6.25$   $\mu\text{m}^2$ , respectively [17]. The GNLS was numerically solved using the split-step Fourier method. The numerical values of the parameters used in the model are summarized in Table I.

The degree of first-order coherence  $g_{12}^{(1)}$  of the generated supercontinuum is calculated from the following formula [18]:

$$g_{12}^{(1)}(\lambda) = \left| \frac{\langle E_1^*(\lambda) E_2(\lambda) \rangle}{\sqrt{\langle |E_1(\lambda)|^2 \rangle \langle |E_2(\lambda)|^2 \rangle}} \right| \quad (3)$$

where the angle brackets denote an ensemble average over forty independently generated pairs of supercontinua  $E_{1,2}(\lambda)$  with random input noise. Noise was modelled by adding one photon per mode (according to our pump repetition rate  $fr = 63$  MHz) with a Gaussian distribution of both amplitude and phase of variance  $2\sigma$  equal to  $h\nu/2$  and  $\pi$ , respectively [31]. A similar approach has been used to model noise in SC generated in silicon-on-insulator [27] and silicon-on-sapphire platforms [10].

### III. RESULTS AND DISCUSSION

#### A. Experimental Supercontinuum Generation and Calculated Coherence

The waveguide was pumped in the Transverse Electrical (TE) polarization by a 200 mW tunable OPA laser (MIROPA-fs, Hotlight Systems) delivering 205 fs pulses centered at 4  $\mu\text{m}$  (75 THz frequency) with a repetition rate of 63 MHz [17].

Fig. 2 (bottom) shows the measured (blue curve) and simulated (black curve) spectra resulting after propagation of a pulse with a 2.35 kW coupled peak power. The experimentally generated SC spans over more than one octave, from 2.63  $\mu\text{m}$  up to 6.18  $\mu\text{m}$ , with a 3.55  $\mu\text{m}$  bandwidth at  $-30$  dB. The on-chip power spectral density at  $\lambda = 5.8$   $\mu\text{m}$  ( $f$ ) is  $-52$  dBm·nm $^{-1}$ . At  $\lambda = 2.9$   $\mu\text{m}$  ( $2f$ ), it is greater than  $-37$  dBm·nm $^{-1}$ .

The overall bandwidth of the simulated SC agrees relatively well with that measured experimentally. One striking difference though is that the signals generated by simulations at both  $f$  and  $2f$  exhibit greater power than the average one ( $-32.6$  dBm) calculated over the  $-30$  dB bandwidth. This lower power spectral density on the long wavelength side for the experimental SC is most likely due to water vapor absorption at around 5.5–6  $\mu\text{m}$  [32], which takes place along the free-space path from the

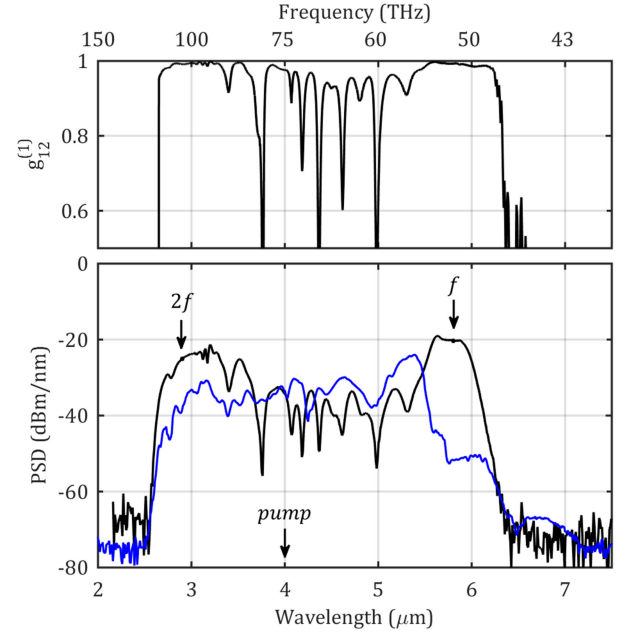


Fig. 2. Calculated coherence at the output of the waveguide (top), experimental (blue) and simulated (black) spectra (bottom) for  $\lambda_p = 4$   $\mu\text{m}$ ,  $T_{FWHM} = 205$  fs and  $P_p = 2.35$  kW. The spectrum is simulated with added noise, i.e. one photon per mode with random phase and amplitude.

chip output to the spectrometer. The lower signal measured at short wavelengths comes from an increase of the measured propagation loss (below  $\lambda = 3.5$   $\mu\text{m}$ ) that is not considered in our simulations. Fig. 2 (top) shows the calculated coherence, which remains high at the extreme parts of the spectrum. The apparent loss of coherence in the central part of the spectrum, where the signal is lower, is due to the low signal to noise ratio.

Fig. 3 shows the evolution of the pulse, as calculated from simulations, in the time domain (a), the spectrum (b) and the coherence (c) as a function of the propagation distance up to 7 cm.

After a few centimeters of propagation along the waveguide, the central part of the spectrum, close to the pump wavelength appears to be depleted relative to the normal dispersion bands towards the high and low wavelengths [Fig. 3(b)]. Full coherence is achieved at the extreme parts of the SC spectrum at all propagation distances [Fig. 3(c)]. Moreover, by choosing the waveguide length slightly shorter ( $\sim 2$  cm), it is possible to maintain high coherence across the entire spectrum without affecting the spectral bandwidth, as the spectrum is already fully broadened [see red line in Fig. 3(c)]. In contrast to the strategies that have been pursued in references [25], [27], the coherence is not degraded here by the use of a pump pulse duration longer than 100 fs nor by the low multi-photon absorption. Finally, we do not observe on Fig. 3(a) the temporal pulse compression that typically governs the dynamics of SC in the anomalous dispersion regime and leads to soliton fission. We investigate the origin of these features in the next section.

#### B. Supercontinuum Generation Dynamics

In this section, we numerically investigate the dynamics of SC generation in our waveguide pumped in an anomalous dispersion



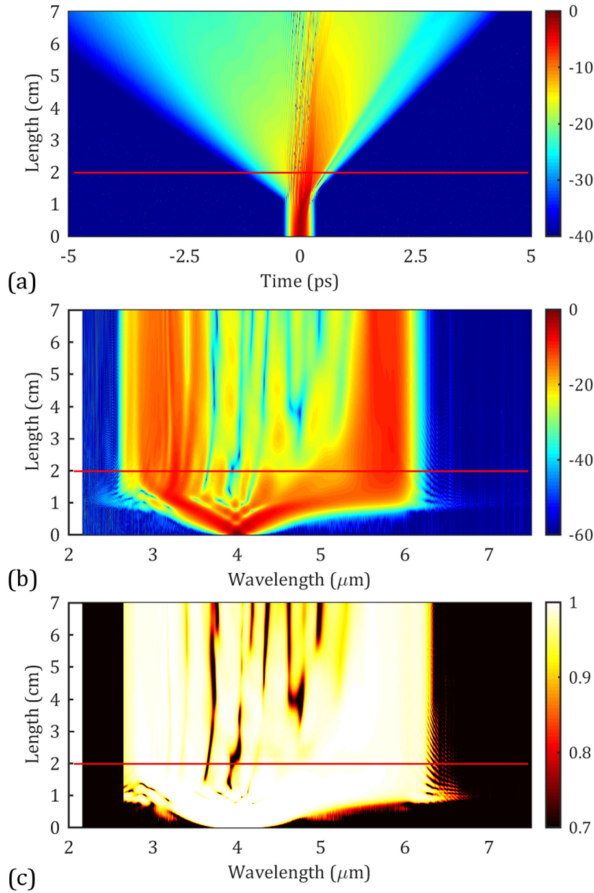


Fig. 3. Evolution of the simulated pulse in the (a) time domain, (b) spectrum, and (c) coherence at different propagation distances for  $\lambda_p = 4 \mu\text{m}$ ,  $T_{\text{FWHM}} = 205 \text{ fs}$ , and  $P_p = 2.35 \text{ kW}$ .

band surrounded by two closely spaced ZDWs (here, at  $3.84$  and  $4.96 \mu\text{m}$ ). The dynamics of SC generation when pumping in a narrow anomalous dispersion band has been explored in optical fibers [33]–[35]. Different explanations have been raised, discussing the interplay of self-phase modulation (SPM) and four-wave mixing (FWM) as well as the formation of solitons, soliton annihilation and the generation of dispersive waves. The bandwidth of the central anomalous dispersion window with respect to the pump characteristics critically governs the mechanisms that drive the SC dynamics. Furthermore, although the potential for pulse recompression was numerically shown in [33], none of these papers explicitly studied the coherence properties of the spectra.

To get more insights into the underlying phenomena that dominate the generation of our mid-IR SC, we simulate the pulse evolution in both the spectral and time-domain at intermediate distances along our waveguide length. Considering our waveguide dispersion and pump characteristics, the soliton fission length given by  $L_{\text{fiss}} = T_0/(\gamma P_0 |\beta_2|)^{1/2}$  is equal to  $L_{\text{fiss}} = 1.38 \text{ cm}$  and the input soliton order is  $N = 20$ . Fig. 4 shows the spectrum, time-domain and spectrogram of the SC signal generated at 8 intermediate steps along the  $7 \text{ cm}$  long waveguide due to a pump pulse with a peak power equal to  $2.35 \text{ kW}$  at  $4 \mu\text{m}$  ( $75 \text{ THz}$  frequency). The spectrogram provides simultaneous information about the temporal and spectral profile

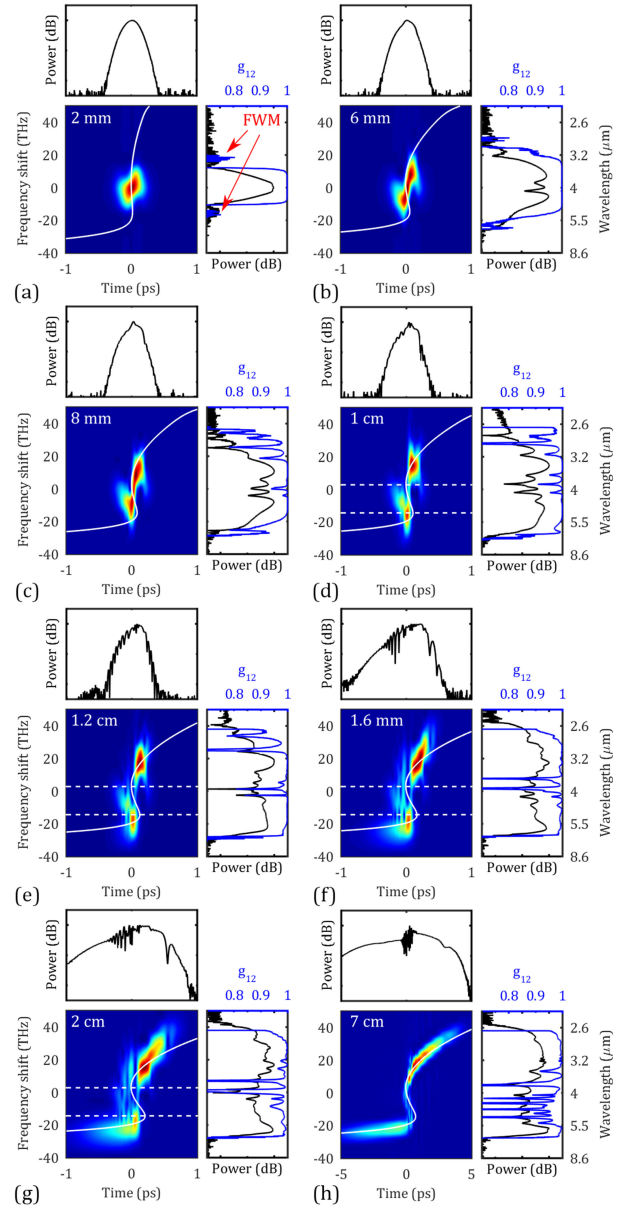


Fig. 4. Calculated spectrogram with superimposed group delay (white curve), pulse in time domain, spectrum (black curve) and coherence (blue curve) at (a)  $2 \text{ mm}$ , (b)  $6 \text{ mm}$ , (c)  $8 \text{ mm}$ , (d)  $1 \text{ cm}$ , (e)  $1.2 \text{ cm}$ , (f)  $1.6 \text{ cm}$ , (g)  $2 \text{ cm}$  and (h)  $7 \text{ cm}$  length. The frequency shift is calculated with respect to the input pump frequency ( $75 \text{ THz}$ ). The white dashed lines in (d) to (g) present the boundaries of the anomalous dispersion band.

of the pulse, and its related chirp. It is mathematically described as:

$$\Sigma(\omega, \tau) = \left| \int_{-\infty}^{\infty} E(t) g(t - \tau) e^{-i\omega t} dt \right|^2 \quad (4)$$

with  $g(t - \tau)$  being a variable-delay Gaussian shape gate function with  $\sim 130 \text{ fs}$  duration [18].

Up to  $0.6 \text{ cm}$  distance propagation, the spectrum shows the typical features of SPM, with 3 lobes that are roughly symmetric around the pump wavelength and a positive linear chirp [see Fig. 4(b)]. The effect of dispersion in the vicinity of the pump wavelength is indeed negligible after this short distance ( $L_D = 27.6 \text{ cm}$  for our  $205 \text{ fs}$  pulses). This is indicated by the

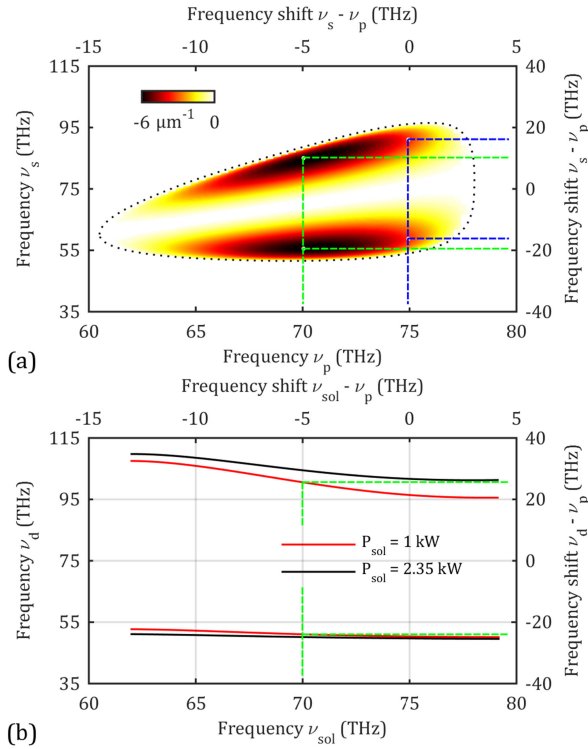


Fig. 5. (a) Linear phase mismatch for degenerate four-wave mixing around the pump frequency  $\nu_p$ . The black dotted line represents the frequencies corresponding to a zero linear phase mismatch. The dashed blue and green lines point out the frequencies with the maximum negative phase mismatch for a pump at 75 and 70 THz frequency ( $\nu_p$ ) respectively. (b) Phase matched frequencies to a soliton of frequency varied across the anomalous dispersion band for 1 kW (red) and 2.35 kW (black) of soliton peak power. The dashed green lines point out the frequencies that are phase matched to a soliton of 1 kW peak power at 70 THz.

group delay, close to zero around the pump, represented by the white solid curve superimposed to the spectrogram. At the same time, some signal appears from noise in frequency bands at  $\pm 16$  THz from the input frequency, corresponding to 3.3 and  $5.1 \mu\text{m}$  wavelengths [see Fig. 4(a) and (b)].

To better clarify the origin of these sidebands, we calculated the spectral dependence of the linear phase mismatch associated with degenerate four-wave mixing (FWM) pumped at the angular frequency  $\omega_p$  and given by the following equation [36], [37]:

$$\Delta\beta = 2\beta(\omega_p) - \beta(\omega_s) - \beta(\omega_i) \quad (5)$$

where  $\omega_s$  and  $\omega_i$  are the angular frequencies of the signal and the idler respectively. The result associated with our waveguide dispersion is plotted on Fig. 5(a) as a function of the FWM pump frequency  $\nu_p$  (bottom axis), and the frequency shift (top axis) with respect to the 75 THz (input) frequency. For  $\nu_p = 75$  THz, this curve exhibits two minimum (negative) linear phase mismatch values equal to  $-3.4 \text{ cm}^{-1}$ . They are reached for symmetric frequencies  $\nu_s$  at  $\pm 16$  THz from the 75 THz pump (blue dashed line). The value of the nonlinear phase mismatch  $2\gamma P_p$ , which counterbalances the linear one, is equal to  $15 \text{ cm}^{-1}$  close to the entrance of the waveguide. Hence, the spontaneous generation of a probe and an idler signal by

degenerate FWM of the pump signal will be more effective at the two frequencies ( $\pm 16$  THz), for which the total (linear and nonlinear) phase mismatch is closer to zero. We therefore attribute the symmetrically positioned side bands observed in the SC spectrum close to the entrance of the waveguide to noise seeded spontaneous FWM. As expected, this signal is not fully coherent ( $g_{12} < 0.8$ ) [see blue curve in Fig. 4(a)] and exhibits a relatively broad bandwidth.

Between 0.8 cm and 1.2 cm along the waveguide length, dispersion starts being substantial (see the negative group delay presented with white curve in Fig. 4(c) and (d) around the pump wavelength). Yet, due to continued SPM and the limited bandwidth of the central anomalous dispersion window, a significant amount of power has been already pushed outside of the anomalous dispersion band [see Fig. 4(d) and (e)]. The depletion of the anomalous dispersion region results in an apparent loss of coherence in the central part of the spectrum, which is however only a consequence of the low signal to noise ratio. From the spectrograms, two high energy pulses appear and split in the spectral (and time-) domain, lying very close to the two ZDWs. The pulse on the low wavelength trailing edge, in particular, strongly overlaps with the normal dispersion regime ( $L = 1$  and 1.2 cm) and seems to undergo some SPM on its own with a positive linear chirp growing between 1.2 and 2 cm, generating, in turn, more side lobes in this part of the spectrum. These new components generated by SPM in a normal dispersion regime are highly coherent, as seen in Fig. 4(f)–(g).

At around 1 cm, some part of the pump energy, which is redshifted by around  $-5$  THz from the input frequency, remains in the middle of the anomalous dispersion band. Subsequent transfer of energy occurs from this band to both sides of the spectrum [Fig. 4(e)–(g)]. The oscillations occurring in the temporal domain at the leading edge of the pulse [for  $L = 1.2$  and 1.6 cm in Fig. 4(e) and (f)], having a period of  $\sim 50$  fs, can be seen as the result of the beating between frequencies with a 20 THz distance. At the low level, the observed energy transfer might be attributed to degenerate FWM between the remaining redshifted signal in the anomalous dispersion band (which could act as a pump) and the tail of the low energy peak at  $\sim -20$  THz (which could act as an idler), leading to the generation of a signal at higher frequencies and to an enhancement of the idler [38]. This interpretation roughly agrees with the frequencies at which the calculated FWM linear phase mismatch is minimum [Fig. 5(a), green dashed lines]. For a pump at 70 THz (i.e.,  $-5$  THz from the input frequency), these correspond to an idler at around  $-20$  THz and a signal at around 10 THz from the input frequency. Indeed, the estimated nonlinear phase mismatch induced by the pump signal in the anomalous band (estimation  $6 \text{ cm}^{-1}$ ) compensates for the maximum negative linear phase mismatch values afforded by the waveguide dispersion ( $-6 \text{ cm}^{-1}$ ), leading to more effective FWM at frequencies corresponding to the minimum (negative) linear phase mismatch.

As an alternative interpretation, the energy transfer around the two ZDWs between 1 cm and 2 cm could be understood as dispersive wave generation seeded by a soliton at  $-5$  THz. The corresponding phase matching condition is given by the

following equation [37]:

$$\beta(\omega_{sol}) + \beta_1(\omega_{sol})(\omega_d - \omega_{sol}) + \frac{1}{2}\gamma P_{sol} - \beta(\omega_d) = 0 \quad (6)$$

where  $\omega_d$  and  $\omega_{sol}$  are the dispersive wave and soliton angular frequencies, respectively, and  $P_{sol}$  is the soliton peak power. Fig. 5(b) plots the frequencies that are phase matched with the soliton as a function of its frequency. As a rough approximation, this calculation considers that the duration of the soliton is that of the pump ( $T_{FWHM} = 205$  fs) and that its peak power is either 1 kW or 2.35 kW. The 1 kW peak power would correspond to a soliton carrying 40% of the input pulse power [estimated from the spectrogram on Fig. 4(d)] which would not experience pulse compression. In this case, dispersive waves are expected to be generated at around  $-24$  and  $+25$  THz from the input frequency (i.e., about  $-20$  and  $+30$  THz from the redshifted signal in the anomalous band). It is difficult to unambiguously attribute the redshifted signal at  $-5$  THz to a soliton. However, this dispersive wave mechanism could explain part of the signal that is transferred spectrally further from the pump than the aforementioned FWM mechanism at 1.6 and 2 cm [Fig. 4(f)–(g)]. In addition, the  $\sim 50$  fs time-domain oscillation at the leading edge of the pulse could be explained by the beating between the  $-5$  THz red-shifted signal and the low energy ( $-24$  THz) dispersive wave.

Considering the relatively broad generated features in the spectrum though, we cannot rule out either of the two mechanisms. We note that the high frequency band is slightly broader, which might be due to the distinct frequencies that are created in this range by each process (10 THz and 25 THz for FWM and dispersive wave, respectively). We therefore conclude that the observed spectrum is most likely the result of the interplay between SPM, FWM and dispersive wave generation. Most importantly, all these processes preserve coherence.

At 2 cm [Fig. 4(g)], following this energy transfer, the two sidebands in the normal regime carry most of the power. Further propagation [Fig. 4(h)] results in the attenuation of the pulse around the pump wavelength due to linear and nonlinear loss and in the temporal separation of the two side bands according to the distinct group delay in these two bands (see white group delay curve in Fig. 4)

From this analysis, we can understand the high degree of coherence obtained for our supercontinuum. Its generation is dominated by mechanisms that all preserve coherence, namely SPM and energy transfer through FWM and/or dispersive wave generation. We stress that, due to the high amount of energy pushed out of the anomalous dispersion window in the early stages of the propagation, the effective soliton number is probably less than 20, therefore limiting the detrimental impact of soliton fission on coherence. As a result of its limited bandwidth, the anomalous dispersion band cannot accommodate the entire spectrally broadened spectrum before soliton fission occurs. We thus do not observe the typical temporal pulse compression leading to soliton fission nor clear evidence of soliton fission in the time domain. Finally, we note that although the absolute bandwidth of the anomalous dispersion region is relatively wide

in our case, i.e., 1160 nm compared to 165 nm in [33], the bandwidth to pump wavelength ratio is comparable, as we pump in the mid-IR region. We thus observe a similar dynamics to that observed for fibers with a narrow anomalous dispersion band in the near-IR [33]. This leads to high coherence over most of the spectrum, in particular at frequencies distanced by one octave.

The high power spectral density and high degree of coherence at the extreme parts of the octave spanning SC makes this spectrum particularly interesting for  $f$ -to- $2f$  interferometry [39]. A  $f$ -to- $2f$  interferometer based technique has been proposed in 1999 by H. R. Telle *et al.* [19] to measure and stabilize the carrier-envelope offset of two-cycle lasers, a fundamental requirement for high-harmonic generation applications [40]. Moreover, measuring the radio-frequency beats that can be generated via  $f$ -to- $2f$  self-frequency referencing using broadband laser sources spanning over one octave can be used to stabilize pulse for high precision spectroscopy and frequency metrology applications. The coherence of dispersive waves at  $f$  and  $2f$  is not affected by the low multi-photon absorption, allowing us to take full advantage of the extremely low nonlinear losses to maximize SC bandwidth and output power. Furthermore, the generated SC covers a great part of the molecular fingerprint region, with potential applications for on-chip spectroscopy.

#### IV. CONCLUSION

We have shown that an on-chip mid-IR octave spanning supercontinuum generated in an anomalous dispersion regime surrounded by two closely spaced ZDWs maintained a high degree of coherence at its extreme parts. The interplay between the different mechanisms driven by this specific dispersion profile ensures that coherence is achieved without requiring high TPA, specific waveguide length, nor being constrained by the use of sub-100 fs input pulses. Since the spectrum covers the molecular fingerprint region, the reported SC is well suited for on-chip sensing applications. Moreover, the high power spectral density and the high coherence of the octave-distanced signals make this supercontinuum source promising for  $f$ -to- $2f$  interferometry, with potential applications for high-precision spectroscopy and frequency metrology.

#### ACKNOWLEDGMENT

We acknowledge the support of the International Associated Laboratory between France and Australia (LIA ALPhFA), and author Christelle Monat acknowledges the support of the Institut Universitaire de France.

#### REFERENCES

- [1] Y.-C. Chang, *Design, Fabrication and Characterization of Mid-Infrared Strip Waveguide for Laser Spectroscopy in Liquid Environments*. Lausanne, Switzerland: EPFL, 2012.
- [2] A. Schliesser, N. Picqué, and T. W. Hänsch, "Mid-infrared frequency combs," *Nature Photon.*, vol. 6, pp. 440–449, 2012.
- [3] H. Pires, M. Baudisch, D. Sanchez, M. Hemmer, and J. Biegert, "Ultrashort pulse generation in the mid-IR," *Prog. Quant. Electron.*, vol. 43, pp. 1–30, 2015.
- [4] Y. Yu *et al.*, "1.8–10  $\mu\text{m}$  mid-infrared supercontinuum generated in a step-index chalcogenide fiber using low peak pump power," *Opt. Lett.*, vol. 40, pp. 1081–4, Mar. 2015.

- [5] T. Cheng *et al.*, "Mid-infrared supercontinuum generation spanning 2.0 to 15.1  $\mu\text{m}$  in a chalcogenide step-index fiber," *Opt. Lett.*, vol. 41, pp. 2117–20, May 2016.
- [6] C. R. Petersen *et al.*, "Increased mid-infrared supercontinuum bandwidth and average power by tapering large-mode-area chalcogenide photonic crystal fibers," *Opt. Express*, vol. 25, pp. 15336–15348, Jun. 2017.
- [7] D. D. Hudson *et al.*, "Toward all-fiber supercontinuum spanning the mid-infrared," *Optica*, vol. 4, p. 1163, 2017.
- [8] Y. Yu *et al.*, "Experimental demonstration of linearly polarized 2–10  $\mu\text{m}$  supercontinuum generation in a chalcogenide rib waveguide," *Opt. Lett.*, vol. 41, pp. 958–61, Mar. 2016.
- [9] N. Singh *et al.*, "Midinfrared supercontinuum generation from 2 to 6  $\mu\text{m}$  in a silicon nanowire," *Optica*, vol. 2, pp. 797–802, 2015.
- [10] N. Nader *et al.*, "Versatile silicon-waveguide supercontinuum for coherent mid-infrared spectroscopy," *APL Photon.*, vol. 3, 2018, Art. no. 036102.
- [11] R. Soref, "Mid-infrared photonics in silicon and germanium," *Nature Photon.*, vol. 4, pp. 495–497, 2010.
- [12] J. M. Ramirez *et al.*, "Low-loss Ge-rich Si<sub>0.2</sub>Ge<sub>0.8</sub> waveguides for mid-infrared photonics," *Opt. Lett.*, vol. 42, pp. 105–108, Jan. 2017.
- [13] J. M. Ramirez *et al.*, "Graded SiGe waveguides with broadband low-loss propagation in the mid infrared," *Opt. Express*, vol. 26, pp. 870–877, Jan. 2018.
- [14] N. K. Hon, R. Soref, and B. Jalali, "The third-order nonlinear optical coefficients of Si, Ge, and Si<sub>1-x</sub>Ge<sub>x</sub> in the midwave and longwave infrared," *J. Appl. Phys.*, vol. 110, pp. 11301–11301, 2011.
- [15] L. Carletti *et al.*, "Nonlinear optical response of low loss silicon germanium waveguides in the mid-infrared," *Opt. Express*, vol. 23, pp. 8261–71, Apr. 2015.
- [16] L. Carletti *et al.*, "Mid-infrared nonlinear optical response of Si-Ge waveguides with ultra-short optical pulses," *Opt. Express*, vol. 23, pp. 32202–14, Dec. 2015.
- [17] M. Sinobad *et al.*, "Mid-infrared octave spanning supercontinuum generation to 8.5  $\mu\text{m}$  in silicon-germanium waveguides," *Optica*, vol. 5, pp. 360–366, Apr. 2018.
- [18] J. M. Dudley, G. Genty, and S. Coen, "Supercontinuum generation in photonic crystal fiber," *Rev. Mod. Phys.*, vol. 78, pp. 1135–1184, Apr. 2006.
- [19] H. R. Telle *et al.*, "Carrier-envelope offset phase control: A novel concept for absolute optical frequency measurement and ultrashort pulse generation," *Appl. Phys. B*, vol. 69, pp. 327–332, 1999.
- [20] R. Holzwarth *et al.*, "Optical frequency synthesizer for precision spectroscopy," *Phys. Rev. Lett.*, vol. 85, p. 2264, 2000.
- [21] T. Udem, R. Holzwarth, and T. W. Hänsch, "Optical frequency metrology," *Nature*, vol. 416, p. 233, Mar. 2002.
- [22] I. Hartl *et al.*, "Ultrahigh-resolution optical coherence tomography using continuum generation in an air-silica microstructure optical fiber," *Opt. Lett.*, vol. 26, pp. 608–610, 2001.
- [23] N. Nishizawa, Y. Chen, P. Hsiung, E. Ippen, and J. Fujimoto, "Real-time, ultrahigh-resolution, optical coherence tomography with an all-fiber, femtosecond fiber laser continuum at 1.5  $\mu\text{m}$ ," *Opt. Lett.*, vol. 4, pp. 2846–2848, 2004.
- [24] H. Kano and H.-O. Hamaguchi, "Characterization of a supercontinuum generated from a photonic crystal fiber and its application to coherent Raman spectroscopy," *Opt. Lett.*, vol. 28, pp. 2360–2362, 2003.
- [25] F. Leo, S. P. Gorza, S. Coen, B. Kuyken, and G. Roelkens, "Coherent supercontinuum generation in a silicon photonic wire in the telecommunication wavelength range," *Opt. Lett.*, vol. 40, pp. 123–6, Jan. 2015.
- [26] A. R. Johnson *et al.*, "Octave-spanning coherent supercontinuum generation in a silicon nitride waveguide," *Opt. Lett.*, vol. 40, pp. 5117–20, Nov. 2015.
- [27] N. Singh *et al.*, "Octave-spanning coherent supercontinuum generation in silicon on insulator from 1.06  $\mu\text{m}$  to beyond 2.4  $\mu\text{m}$ ," *Light Sci. Appl.*, vol. 7, pp. 17131–17138, 2018.
- [28] J. Yuan *et al.*, "Mid-infrared octave-spanning supercontinuum and frequency comb generation in a suspended Germanium-membrane ridge waveguide," *J. Lightw. Technol.*, vol. 35, pp. 2994–3002, Jul. 2017.
- [29] L. A. L. Yin, Q. Lin, and G. P. Agrawal, "Soliton fission and supercontinuum generation in silicon waveguides," *Opt. Lett.*, vol. 32, pp. 391–393, 2007.
- [30] Q. Lin, O. J. Painter, and G. P. Agrawal, "Nonlinear optical phenomena in silicon waveguides: Modeling and applications," *Opt. Express*, vol. 15, pp. 16604–16644, Dec. 2007.
- [31] A. Ruehl *et al.*, "Ultrabroadband coherent supercontinuum frequency comb," *Phys. Rev. A*, vol. 84, Jul. 2011, Art. no. 011806.
- [32] P. Linstrom, *NIST Chemistry WebBook*, NIST Standard Reference Database 69, Boulder, CO, USA: NIST, 1997.
- [33] K. M. Hilligsøe *et al.*, "Supercontinuum generation in a photonic crystal fiber with two zero dispersion wavelengths," *Opt. Express*, vol. 12, pp. 1045–1054, 2004.
- [34] M. H. Frosz, P. Falk, and O. Bang, "The role of the second zero-dispersion wavelength in generation of supercontinua and bright-bright soliton-pairs across the zero-dispersion wavelength," *Opt. Express*, vol. 13, pp. 6181–6192, 2005.
- [35] I. Babushkin *et al.*, "Simple route toward efficient frequency conversion for generation of fully coherent supercontinua in the mid-IR and UV range," *Light Sci. Appl.*, vol. 6, p. e16218, Feb. 2017.
- [36] M. R. Lamont, B. T. Kuhlmey, and M. C. de Sterke, "Multi-order dispersion engineering for optimal four-wave mixing," *Opt. Express*, vol. 16, pp. 7551–7563, Mar. 2008.
- [37] G. P. Agrawal, *Nonlinear Fiber Optics*, 5th ed. Amsterdam, The Netherlands: Academic Press, 2012.
- [38] D. Castello-Lurbe, N. Vermeulen, and E. Silvestre, "Towards an analytical framework for tailoring supercontinuum generation," *Opt. Express*, vol. 24, pp. 26629–26645, Nov. 2016.
- [39] M. Yu, B. Desiatov, Y. Okawachi, A. L. Gaeta, and M. Lončar, "Coherent two-octave-spanning supercontinuum generation in lithium-niobate waveguides," *Opt. Lett.*, vol. 44, pp. 1222–1225, Mar. 2019.
- [40] A. de Bohan, P. Antoine, D. B. Milošević, and B. Piraux, "Phase-dependent harmonic emission with ultrashort laser pulses," *Phys. Rev. Lett.*, vol. 81, p. 1837, 1998.

**Milan Sinobad** received the B.Sc. degree in electrical engineering from Belgrade University, Serbia, in 2012, and the M.Sc. degree in nanoscale engineering from the Université de Lyon, France, in 2014. He is currently working toward the Ph.D. degree in engineering with the RMIT University, Melbourne, Australia. His research interests include silicon photonics, mid-infrared photonics, laser physics, and nonlinear optics.

**Alberto Della Torre** received the B.Sc. degree in engineering physics from the Polytechnic of Milan, in 2015, and the M.Sc. degree in nanoscale engineering from the Université de Lyon, Lyon, France, in 2017. Currently, he is working toward the Ph.D. degree in engineering with the Institut des Nanotechnologies de Lyon (INL), Ecole Centrale de Lyon, Ecully, France. His research interests include nonlinear optics, mid-infrared photonics, silicon photonics, and photonic crystals.

**Remi Armand** received the B.S. degree in electrical engineering from the Ecole Normal Supérieur de Cachan, Cachan, France, in 2015, and the M.S. degree in electrical engineering from the Université Paris-Saclay, Saclay, France, in 2018. He is currently working toward the Ph.D. degree in physics with the Ecole Centrale de Lyon, Ecully, France. His research interests include the design of structure to generate mid-infrared broadband sources, and fundamental study of nonlinear photonics.

**Barry Luther-Davies** received the B.Sc. and Ph.D. degrees in laser physics and nonlinear optics from the University of Southampton, Southampton, U.K., in 1970 and 1974, respectively.

He is an Emeritus Professor of laser physics with the Australian National University (ANU), Canberra, Australia, with experience in the diverse areas of research including lasers, laser-matter interaction physics, photonics, optical materials, and nonlinear optics. He joined the ANU in 1974, where he led a team working on the physics of laser-produced plasmas, until the early 1990s, when the research evolved into studies of laser-materials processing and pulsed laser deposition of thin films. More recently, he has specialized in nonlinear optical materials and devices and photonics with a strong interest in the development of devices for optical signal processing as part of the Australian Research Council's Centre of Excellence for Ultrahigh-Bandwidth Devices for Optical Systems (CUDOS). He has published more than 300 papers in scientific journals, contributed several book chapters and many hundreds of conference papers.

Dr. Luther-Davies is a Fellow of the Optical Society of America and the Australian Academy for Technological Sciences and Engineering. He was awarded the Pawsey Medal of the Australian Academy of Science in 1986 for his contribution to laser-plasma interaction physics and was an ARC Federation Fellow from 2003 to 2008. He serves as an Advisory Editor for Optics Communications.

**Pan Ma**, photograph and biography not available at the time of publication.

**Stephen J. Madden** received the B.Sc. degree in electronic engineering and the Ph.D. degree in integrated optics from Imperial College in London, London, U.K., in 1985 and 1989, respectively.

He is Associate Professor and a Fellow with Laser Physics Centre, Australian National University (ANU), Canberra, Australia. He has spent most of his career in industry. In 1991, he joined the Telstra Research Laboratories, Melbourne, Australia. In 1997, he became the Director of Research at ADC Telecommunications, Minneapolis, MN, USA, before leaving to become VP engineer with the Sparkolor Corporation, Santa Clara, CA, USA, in 2001. More recently, he led a research within CUDOS, a research consortium between seven Australian universities, into photonics devices. He has published more than 200 papers.

**Arnan Mitchell** received the Ph.D. degree in engineering from RMIT University, Melbourne VIC, Australia, in 2000.

He is a Distinguished Professor with the School of Engineering, RMIT University, Bundoora, Australia, and is Director of RMIT Micro Nano Research Facility. He is a highly multidisciplinary researcher working in microchip technologies combining light, sound, fluids, and electronics with applications spanning radar systems for defence, high-speed fiber-optic communications, and point-of-care diagnostic systems for biomedicine. He is enthusiastic about translating technology into the hands of end-users and has dedicated much of his career to building diverse teams and comprehensive micro and nanotechnology infrastructure to enable breakthrough discoveries to achieve real-world impact.

**David J. Moss** (S'83–M'88–SM'09–F'16) received the B.Sc. degree in physics from the University of Waterloo, Waterloo, ON, Canada, and the M.Sc. and Ph.D. degrees in nonlinear optics from the University of Toronto, Toronto, ON, in 1983 and 1988, respectively.

He is the Director of the Centre for Micro-Photonics with the Swinburne University of Technology, Melbourne, Australia, leading research programs in integrated nonlinear nanophotonics, microwave photonics, telecommunications, quantum optics, biophotonics, renewable energy, and other areas. From 1988 to 1992, he was with the National Research Council of Canada, Institute for Microstructural Sciences, Ottawa, Canada, working on III–V optoelectronic devices. From 1992 to 1994, he was a Senior Visiting Scientist with the Hitachi Central Research Laboratories, Tokyo, Japan, working on high-speed optoelectronic devices for 10-Gb/s fiber-optic telecommunications systems. From 1994 to 1998, he was a Senior Research Fellow with the Optical Fiber Technology Centre, University of Sydney, Australia. From 1998 to 2003, he was a Manager with JDS Uniphase, Ottawa, Canada, leading a team developing products for 40-Gb/s telecommunications systems. From 2003 to 2013, he was with the University of Sydney and the Centre for Ultra-High Bandwidth Devices for Optical Systems working on ultrahigh bandwidth optical signal processing, integrated nonlinear nanophotonic circuits, and photonic crystal devices. He has about 600 journal/conference papers including a *Nature*, *Science*, eight *Nature Photonics*, and five *Nature Communications* papers.

Dr. Moss received the 2011 Australian Museum Eureka Science Prize and the Google Australia Award for innovation in computer science. He has been active on many conference committees, including the General Program Chair of OSA Integrated Photonics Research in Vancouver, July 2016, and the General Chair in New Orleans, 2017. He is a Fellow of the IEEE Photonics Society, the Fellow of the Optical Society of America, and the SPIE.

**Jean-Michel Hartmann** received the Ph.D. degree in physics from Université Grenoble Alpes, France, in 1997.

He joined CEA, Leti, Grenoble, France, in 1999, as a SiGeC Epitaxy Research Scientist. He was a Postdoctoral Fellow with the Imperial College, London, U.K. He is currently coordinating group-IV epitaxy activities in Leti's Technological Platform Department. He has the rank of CEA Research Director.

**Jean-Marc Fédéli** received the Electronics Engineer Diploma from INPG Grenoble, Grenoble, France, in 1978.

He was involved in the development of various magnetic memories and magnetic components as Project Leader, Group Leader, and Program Manager with the CEA-LETI, Grenoble, France. For two years, he was Advanced Program Director with the Memscap Company, France, for the development of RF-MEMS, then with the CEA-LETI in 2002 as a Coordinator of silicon photonic projects until 2012. Under a larger research partnership, he works on many technological aspects on photonics on CMOS (Si rib and stripe waveguides, a-Si waveguides, slot waveguides), Si modulators, Ge photodetectors, and InP integrated sources on Si. He has been participating in different European projects such as EPIXFAB for MPW circuit fabrication and has coordinated the FP7 PLAT4M project on Silicon Photonics Platform. Since 2014, he has moved to sensing activities with photonics, and he is currently the Technical Manager of the H2020 MIRPHAB pilot line on liquid and gas systems sensors. His H factor is around 35 with more than 200 publications and 50 patents. He is the author of three book chapters (one on magnetic recording and two on silicon photonics).

**Christelle Monat** (M'08) received the Ph.D. degree in electronic integrated devices from the Ecole Centrale de Lyon, Ecully, France, in 2003.

She was with the École Polytechnique Fédérale de Lausanne, Switzerland, for two years, where she was involved in research on single-photon sources. She joined the Centre for Ultrahigh-bandwidth Devices for Optical Systems (CUDOS), School of Physics, University of Sydney, Australia, in late 2005 and led the research on slow light-enhanced nonlinear optics between 2007 and 2010. Since late 2010, she has been an Associate Professor with the Institut des Nanotechnologies de Lyon, Ecole Centrale de Lyon, and was awarded an ERC consolidator grant on graphene-based nonlinear photonic integrated circuits in 2015. Her current research interests include slow light, photonic crystals, III–V Si hybrid photonics, microlasers, and nonlinear optics in the near- and mid-IR.

**Christian Grillet** received the Ph.D. degree in electronic integrated devices from the Ecole Centrale de Lyon, Ecully, France, in 2003.

In 2004, he joined the Centre for Ultrahigh-bandwidth Devices for Optical Systems (CUDOS), University of Sydney, Sydney, Australia. He then joined Centre national de la recherche scientifique (CNRS), Paris, France, in 2013. He leads the International Associated Laboratory in Photonics between France and Australia (LIA ALPhFA). His research interests include integrated nonlinear optics, mid-infrared integrated optics, photonic crystals, and slow light.

## Conclusion

In this chapter, we numerically analyzed the coherence of an octave-spanning mid-infrared supercontinuum, as was experimentally generated in silicon germanium-on-silicon waveguides. The numerical analysis was conducted on the results associated with the waveguide (referred to as waveguide 1 in Chapter 2) that was designed to operate in a single-mode regime at the 4  $\mu\text{m}$  pump wavelength, and for which we performed extensive linear and nonlinear measurements. To give additional insights into the underlying physics that preserved coherence for this supercontinuum, we provided a detailed analysis of the supercontinuum generation dynamics along the propagation distance.

We reported here a high coherence for the supercontinuum spanning from 2.6 to 6.2  $\mu\text{m}$  in the mid-infrared. The degree of the first-order coherence is larger than 90% across almost the entire spectrum and it is more than 99% at the extreme parts of the spectrum that are separated by an octave. The analysis of the supercontinuum generation dynamics reveals that the high coherence is maintained thanks to the specific dispersion profile, i.e. the 4  $\mu\text{m}$  pump in the anomalous dispersion band is enclosed with two relatively closely spaced zero group velocity dispersion (GVD) wavelengths. The interplay between the different mechanisms driven by this specific dispersion profile ensures that coherence is achieved without requiring high two-photon absorption, specific waveguide length, or being constrained by the use of sub-100 fs input pulses.

The reported supercontinuum covering the molecular fingerprint spectral region thus turns out to be well suited for on-chip sensing application. The high power spectral density and the high coherence of the octave-distanced signals make this spectrum promising for  $f$ -to- $2f$  interferometry, with potential applications for high-precision spectroscopy and frequency metrology.

We note that it has been long acknowledged that a highly coherent supercontinuum, with coherence equal to the unity over the entire spectrum, could be achieved when using waveguides operating in the all-normal dispersion regime. This reemphasizes that dispersion is key to the generated supercontinuum characteristics and the underlying device performance. The next chapter discusses how the dispersion can be shifted from anomalous to all normal using a simple post-fabrication dispersion trimming technique.

## **Chapter 4.**

# **Dispersion trimming for mid-infrared supercontinuum generation in a hybrid chalcogenide/silicon-germanium waveguide**

This chapter discusses dispersion trimming using a simple post-fabrication technique.


The dispersion profile of the fabricated structures can deviate from the nominal parameters defined at the design stage due to fabrication inaccuracies. Dispersion trimming can turn out to be useful when it is required to compensate for the dispersion deviation and/or to optimize the dispersion profile of a fabricated waveguide. The deposition of a chalcogenide cladding on top of our air-clad SiGe/Si waveguides can be used for dispersion trimming owing to the wide mid-infrared transparency of the chalcogenide material and its lower refractive index than that of the silicon germanium alloy.

This chapter shows how the dispersion of a SiGe/Si waveguide (corresponding to the so-called waveguide 1 design of chapter 2) can be shifted from anomalous to all normal when coat the waveguide with a 1.26 $\mu\text{m}$  thick chalcogenide layer. Supercontinua are measured for both the initially air clad and chalcogenide-clad silicon germanium-on-silicon waveguides, showing specific features associated with the two distinct dispersion regimes. In addition, we studied how the dispersion profile of these waveguides can be trimmed by adjusting the chalcogenide top cladding layer thickness. This provides an additional degree of freedom to control the dispersion profile of mid-IR waveguides, at the core of supercontinuum generation.

This chapter corresponds to the article entitled “Dispersion trimming for mid-infrared supercontinuum generation in a hybrid chalcogenide/silicon-germanium waveguide” published in “JOSA B” in early 2019. The article is organized into five sections, which present the device design/fabrication, the experimental results and the numerical analysis of dispersion trimming.



# Dispersion trimming for mid-infrared supercontinuum generation in a hybrid chalcogenide/silicon-germanium waveguide

MILAN SINOBAD,<sup>1,2</sup>  ALBERTO DELLA TORRE,<sup>1,\*</sup> BARRY LUTHER-DAVIS,<sup>3</sup> PAN MA,<sup>3</sup> STEPHEN MADDEN,<sup>3</sup> SUKANTA DEBBARMA,<sup>3</sup> KHU VU,<sup>3</sup> DAVID J. MOSS,<sup>4</sup> ARNAN MITCHELL,<sup>2</sup> JEAN-MICHEL HARTMANN,<sup>5</sup> JEAN-MARC FEDELI,<sup>5</sup> CHRISTELLE MONAT,<sup>1</sup> AND CHRISTIAN GRILLET<sup>1</sup>

<sup>1</sup>Université de Lyon, Institut des Nanotechnologies de Lyon (INL), 69131 Ecully, France

<sup>2</sup>School of Engineering, RMIT University, Melbourne, VIC 3001, Australia

<sup>3</sup>Laser Physics Center, Australian National University, Canberra, ACT 0100, Australia

<sup>4</sup>Centre for Microphotonics, Swinburne University of Technology, Hawthorn, VIC 3122, Australia

<sup>5</sup>Université Grenoble Alpes, CEA-Leti, 38054 Grenoble Cedex 9, France

\*Corresponding author: [alberto.della-torre@ec-lyon.fr](mailto:alberto.della-torre@ec-lyon.fr)

Received 15 October 2018; revised 2 December 2018; accepted 3 December 2018; posted 5 December 2018 (Doc. ID 348366); published 8 January 2019

We report a simple post-process technique that harnesses a hybrid chalcogenide/silicon-germanium system for the control of waveguide dispersion. By adding a chalcogenide top cladding to a SiGe/Si waveguide, we can substantially change the dispersive properties, which underpin the generation of a supercontinuum. In our particular example, we experimentally show that a shift from anomalous to normal dispersion takes place. We numerically study the dispersion dependence on the chalcogenide thickness and show how to use this additional degree of freedom to control the position of the zero dispersion wavelengths and hence the spectral span of the supercontinuum. Finally, we compare our approach with more traditional techniques that use geometry for dispersion tailoring. © 2019 Optical Society of America

<https://doi.org/10.1364/JOSAB.36.000A98>

## 1. INTRODUCTION

Broadband supercontinuum sources can be used advantageously in a wide variety of fields, from high-bit-rate communications and wavelength multiplexing [1] to biophotonics [2]. The mid-infrared (mid-IR) spectral region (covering the 3–20  $\mu\text{m}$  wavelength range) is of great interest because of the large number of potential applications from biomedical imaging and medical and environmental sensors to food quality analysis and security [3–9]. Indeed, many chemical compounds have strong spectral fingerprints in this region due to their resonant frequencies associated with the vibrational and rotational modes of molecules. In this context, on-chip broadband mid-IR light sources, like supercontinua, are key for the development of efficient compact mid-IR spectroscopic platforms.

Mid-IR supercontinuum generation has already been demonstrated using different integrated platforms, e.g., chalcogenide [10], silicon-on-insulator waveguides [11,12], and silicon-on-sapphire waveguides [13,14]. Recently, the (theoretically foreseen) strong nonlinear properties [15], wide transparency window from 3 to 15  $\mu\text{m}$ , and CMOS compatibility of germanium [6,16,17] have generated increasing interest in germanium-based platforms. Generally, SiGe alloys are used

to combine the superior nonlinear properties of germanium with an additional design parameter (the germanium content of the alloy) for a better control of the nonlinear properties of the waveguide (nonlinear index, multiphoton absorption, and dispersion) and to limit the waveguide/substrate lattice mismatch. The first demonstration of nonlinear effects in a SiGe waveguide was reported by Hammani *et al.* in 2014, showing mid-to-near-infrared conversion by four-wave mixing in a graded-index SiGe on a silicon waveguide [18], followed by the demonstration of supercontinuum generation from 1.45 to 2.79  $\mu\text{m}$  on the same platform [19]. Low propagation losses have been reported in graded-index SiGe waveguides [20,21], and a complete characterization of the nonlinear optical response of step-index  $\text{Si}_{0.6}\text{Ge}_{0.4}$  on Si waveguides was performed by Carletti *et al.* in 2015 [22,23]. The latter work eventually led to our recent demonstration of the first supercontinuum generated across more than one octave (from 3 up to 8.5  $\mu\text{m}$ ) in SiGe waveguides [24]. In that work, an air cladding was used to achieve low anomalous dispersion in spite of the low index contrast between the SiGe core and the Si substrate. Controlling the waveguide dispersion is key to governing the nonlinear dynamics and hence the properties



(bandwidth, coherence etc.,) of the generated supercontinuum. Sophisticated waveguide geometries have been proposed to that end. For instance, Bao *et al.* numerically studied a double-slot waveguide to obtain a flat and low dispersion [25] and a notch waveguide enabled Nader *et al.* to tune the zero-dispersion wavelength (ZDW) [14]. In all these demonstrations, however, the dispersive properties are set at the design stage and cannot be adjusted once the device has been fabricated [11–14,24,25]. Hence, they are subject to fabrication inaccuracies, surface contamination, and the presence of defects. Post-process tuning mechanisms are therefore of great interest to adjust or correct *a posteriori* the waveguide dispersion to match the target value.

Here we show that it is possible to fine-tune the dispersion profile *a posteriori* by adding a chalcogenide cladding layer on top of a highly nonlinear SiGe waveguide, introducing a simple post-processing tool to control the supercontinuum dynamics and its properties.

Several approaches have been proposed for post-process tuning of optical properties in optical fibers [26,27] and photonic crystals [28–31]. However, the restricted number of design parameters makes post-process dispersion control of waveguides trickier. In this regard, the addition of a chalcogenide top cladding appears as a simple and elegant tool for post-trimming the dispersion, depending on the actual structure produced by fabrication. Chalcogenide glasses have been used for post-tuning distributed feedback lasers [32], quantum cascade lasers [33], photonic crystal cavities [34–36], and photonic crystal waveguides [37]. Here we report a proof of concept demonstration in which the deposition of a chalcogenide top cladding on nonlinear SiGe/Si waveguides enables us to tune the group velocity dispersion of the fundamental mode. In our example, the group velocity dispersion changes from anomalous to normal at the pump wavelength, enabling us to observe supercontinuum generation from 3.1 up to 5.5  $\mu\text{m}$  in the normal dispersion regime. This demonstrates that the heterogeneous integration of materials can be used as a post-processing technique to tune the waveguide dispersive properties and therefore control supercontinuum generation. We numerically show that the dispersion can be further

adjusted by setting the thickness of the deposited chalcogenide layer within a reasonable 100 nm resolution tolerance. The related effect on dispersion is equivalent to enlarging the waveguide by about 15% but without degrading the waveguide nonlinear response.

## 2. DESIGN AND FABRICATION

A  $3.75 \times 2.7 \mu\text{m}^2$  cross section, 5 cm long  $\text{Si}_{0.6}\text{Ge}_{0.4}$  on a Si waveguide (see [24] for details on the fabrication process) was coated with a 1.26  $\mu\text{m}$  thick layer of a chalcogenide  $\text{Ge}_{11.5}\text{As}_{24}\text{Se}_{64.5}$ , deposited by thermal evaporation [38]. The chalcogenide refractive index is considered constant and equal to 2.6 [39]. The waveguide is operated as a transverse-electric (TE) single-mode structure at the pump wavelength of 4.15  $\mu\text{m}$ . Figure 1(a) shows scanning electron microscope (SEM) and atomic force microscope (AFM) images (top and bottom, respectively) of the waveguide surrounded by the chalcogenide layer. The top parts of Figs. 1(b) and 1(c) show the schematic of the waveguide before and after the deposition of the chalcogenide, respectively, while the corresponding simulated mode profiles (log scale) at 4.15  $\mu\text{m}$  are shown in the bottom parts. Table 1 summarizes the key parameters of the waveguide, with and without the chalcogenide top cladding, simulated by a finite-difference mode solver. Due to the low refractive index difference between the core and top cladding, the effective area of the mode slightly increases by  $\sim 10\%$  when the chalcogenide cladding is added; however, the mode confinement in the core of the waveguide remains unaffected and high ( $\sim 94\%$ ). In principle, this allows us to maintain a high nonlinear efficiency, as dictated by the strong light interaction with the nonlinear SiGe core material.

Even though the influence of the cladding on the linear optical properties of the waveguide was not experimentally investigated, the relatively low mode energy overlap with the chalcogenide top cladding (0.52% at 4.15  $\mu\text{m}$ , see Table 1) suggests that the impact of the chalcogenide surface roughness [Fig. 1(a)] on optical losses is limited. Scattering losses are dominant in high-index contrast waveguides and have less impact in the mid-infrared as they scale as  $\lambda^{-4}$  [7]. Indeed, numerical

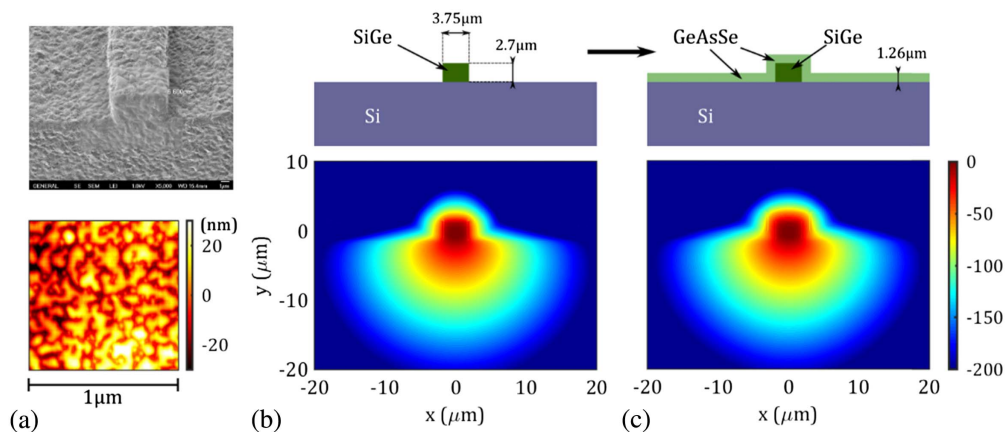


**Fig. 1.** (a) SEM (top) and AFM (bottom) images of the waveguide after the deposition of chalcogenide. Schematic (top) and simulated mode profile at 4.15  $\mu\text{m}$  for the waveguide before (b) the deposition of chalcogenide and for the (c) chalcogenide-clad waveguide. Simulations were performed using Lumerical and are represented with a logarithmic scale.

**Table 1. Cutoff Wavelength, Group Velocity Dispersion, Effective Area, Mode Energy Confinement, and Effective Index at the Pumping Wavelength ( $4.15 \mu\text{m}$ ) of the  $3.75 \times 2.7 \mu\text{m}^2$  Cross-Section Waveguide with an Air-Clad or a  $1.26 \mu\text{m}$  Thick Chalcogenide-Top Cladding**

Parameter	Air Clad	Chalcogenide Clad
Cutoff wavelength ( $\mu\text{m}$ )	6	6.52
GVD (ps/nm/km) at $4.15 \mu\text{m}$	11.6 (anomalous)	-12.1 (normal)
$A_{\text{eff}}$ ( $\mu\text{m}^2$ ) at $4.15 \mu\text{m}$	6.35	6.9
Mode confinement (%) in the SiGe core at $4.15 \mu\text{m}$	94.3	94.4
Mode confinement (%) in the top cladding at $4.15 \mu\text{m}$	0.0032	0.52
Effective index at $4.15 \mu\text{m}$	3.496	3.504

simulations, taking into account the roughness measured by AFM [rms = 15 nm, see Fig. 1(a) bottom] at both the core/chalcogenide cladding and top chalcogenide interfaces, show that the impact of scattering is negligible ( $\sim 0.2$  dB/cm of extra loss).

Figure 2(a) shows the spectral dependence of the effective area and the mode confinement factor in the core of the waveguide with and without the chalcogenide layer. The dispersion profile and the effective index are shown in Fig. 2(b). Considering the initial dimensions of the air-clad waveguide, the related anomalous dispersion at the pump wavelength shifts from anomalous to normal when the chalcogenide cladding is added. At the same time, the waveguide cutoff wavelength, which is characteristic of these vertically asymmetric waveguides [24], is slightly increased from 6 to  $6.52 \mu\text{m}$ .

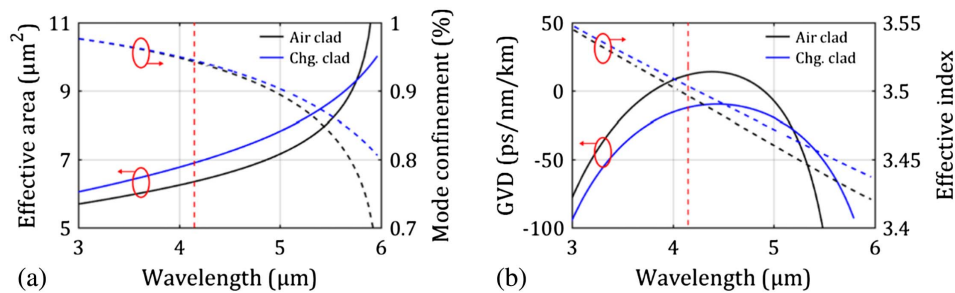


**Fig. 2.** (a) Calculated effective area (continuous lines) and mode confinement (dashed lines) for the air-clad (black) and chalcogenide-clad (blue) waveguide. (b) Calculated group velocity dispersion (continuous lines) and effective area of the mode (dashed lines) for the air-clad (black) and chalcogenide-clad (blue) waveguide. The red dashed line indicates the pump wavelength ( $4.15 \mu\text{m}$ ).

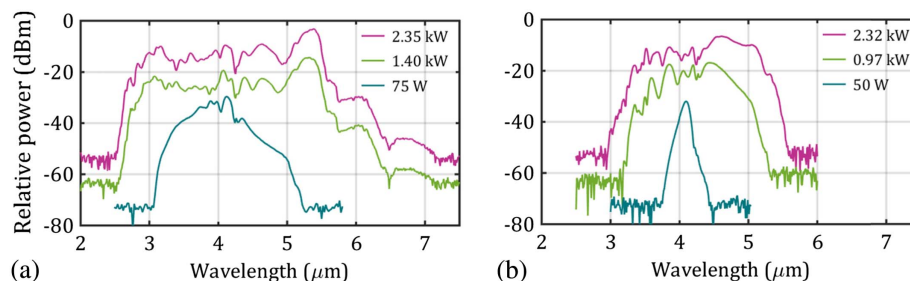


**Fig. 3.** Spectra measured out of the (a) 7 cm long air-cladded and (b) 5 cm long chalcogenide-cladded SiGe/Si waveguide with the same  $3.75 \times 2.7 \mu\text{m}^2$  SiGe core cross-section dimensions for increasing coupled peak power.

### 3. SUPERCONTINUUM GENERATION

We used the same setup, as described in Ref. [24], to couple light into the waveguide and collect the output spectra. The waveguide was pumped at  $4.15 \mu\text{m}$  with  $\sim 200$  fs pulses delivered by a 200 mW tunable OPA laser source (MIROPA-fs, Hotlight Systems) with a repetition rate of 63 MHz. Optical waveplates and polarizers were used to control the power and polarization of the optical pulses, which were coupled to the waveguide with a set of chalcogenide lenses. The coupling loss was assumed to be the same at each facet and equal to those inferred in Ref. [24] ( $-4.9$  dB). The output spectrum was recorded by a liquid-nitrogen-cooled MCT (HgCdTe) photo-detector positioned at the output of the spectrometer. A lock-in detection technique was used to minimize the impact of thermal noise.

Figure 3 shows the experimental output spectra for increasing coupled peak power between 50 and  $2.35$  kW (corresponding to up to 50 mW of laser average power) obtained by pumping an air-clad waveguide [Fig. 3(a)] or a chalcogenide-clad waveguide [Fig. 3(b)], with the same SiGe core cross-section dimensions. The air-clad waveguide is slightly longer (7 cm) than the one with the chalcogenide cladding (5 cm). In both cases, a relatively broad supercontinuum was generated, spanning from  $2.63$  up to  $6.18 \mu\text{m}$  (with a  $-30$  dB bandwidth of  $3.55 \mu\text{m}$ ) and from  $3.1$  to  $5.5 \mu\text{m}$  (with a  $-30$  dB bandwidth of  $2.4 \mu\text{m}$ ) for the air cladding and chalcogenide cladding case, respectively. Some differences can be observed, which illustrate the changes to the dispersion caused by the addition of the chalcogenide top cladding. First, the spectrum is broader for the air-clad case as compared to the chalcogenide-clad case. This is expected for supercontinuum generated in the

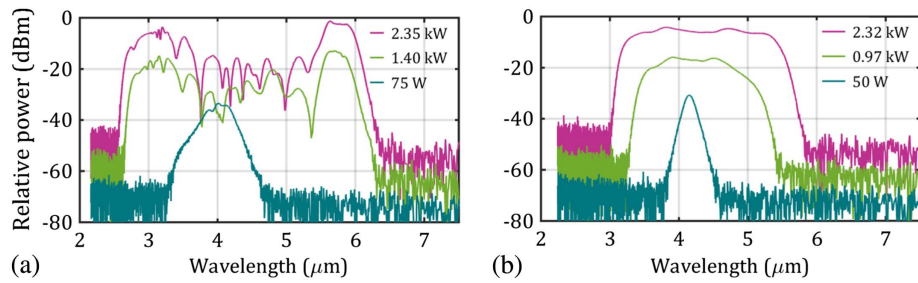


**Fig. 4.** Simulated spectra out of the (a) 7 cm long air-cladded and (b) 5 cm long chalcogenide-cladded waveguide for increasing coupled peak power.

anomalous dispersion rather than in the normal dispersion regime. Second, the supercontinuum amplitude is quite uneven in the long wavelength regime for the air-clad case, while the longer wavelength region of the supercontinuum spectrum generated by the chalcogenide top cladding device appears comparatively more regular.

This contrast in the long wavelength spectral signature is also a characteristic difference between the supercontinuum generation primarily in the anomalous dispersion regime (driven by soliton fission) and the normal dispersion regime (driven by self-phase modulation and optical wave breaking). We stress that the 2 cm difference in waveguide length should not be the cause of the observed differences between the supercontinua, as the spectrum of the air-clad anomalous dispersion case does not evolve much beyond the soliton fission length ( $\sim 1.4$  cm), as was investigated in Ref. [24].

The supercontinuum generation process was simulated for both waveguides by numerically solving the nonlinear Schrödinger equation using the split-step Fourier method (see supplement in the Ref. [24] for more information). The Taylor expansion coefficients of the propagation constant were considered up to the tenth order. As a reasonable approximation, we used the same parameters for the linear loss, the nonlinear effects (Kerr and four photon absorption), the free-carrier absorption and dispersion, self-steepening, and the Raman effects as those used in Ref. [24] for the simulation of the air-clad waveguide pumped at  $4.15 \mu\text{m}$ . Indeed, the chalcogenide compound is transparent deep into the mid-infrared, and its nonlinear contribution was neglected, as only 0.5% of the mode field energy overlaps with the chalcogenide cladding (see Table 1).

The experimental results of Fig. 3 are in good agreement with the simulations shown in Fig. 4; the bandwidth in particular is relatively well reproduced by the simulations. Some of the discrepancies, like the lobes at shorter wavelengths in the measured spectra on Fig. 3(b), are likely due to the coupling of light with higher-order modes and absorption to  $\text{CO}_2$  (around  $4.2 \mu\text{m}$ ) and hydrocarbons (around  $3.2 \mu\text{m}$ ) that are not taken into account in our simulation. These effects indeed equally affect the short wavelength spectral signature for both waveguides.

## 4. RESULTS AND DISCUSSION

### A. Dispersion Tailoring

We have shown experimentally that by adding a chalcogenide layer on top of a SiGe/Si waveguide, a change in the dispersion occurs, shifting, in this particular example, from an anomalous to normal dispersion at the pump wavelength. To expand on our findings, we performed a numerical analysis of the impact of the chalcogenide layer thickness on the group velocity dispersion [see Fig. 5(a)]. As the chalcogenide thickness increases, the overall dispersion gradually decreases, shifting towards normal values when depositing more than 500 nm of chalcogenide. This change is accompanied by a variation in the ZDWs and the flattening of the dispersion profile. The last trend is better observed in Fig. 5(b), which plots the corresponding third-order dispersion ( $\beta_3$ ). The third-order dispersion becomes smaller as the chalcogenide thickness increases, decreasing by more than a half (from  $21.4$  to  $9.8 \times 10^{-10} \text{ ps}^3/\mu\text{m}$ ) from the air-clad case to the  $1.26 \mu\text{m}$  thick chalcogenide-clad case, indicating that a flatter profile

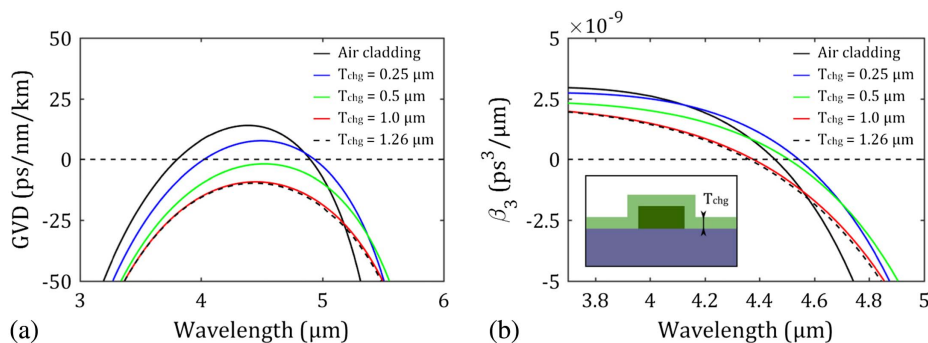


**Fig. 5.** (a) Calculated group velocity dispersion (GVD) for different thicknesses of the chalcogenide layer. (b) Corresponding third-order dispersion. The inset shows a schematic of the SiGe waveguide with chalcogenide cladding.

of the group velocity dispersion is obtained. Moreover, the dispersion profile converges as the chalcogenide thickness approaches 1  $\mu\text{m}$ , in agreement with the confinement of the mode in the waveguide core. As a flat profile of the dispersion is generally targeted for supercontinuum generation, both in the anomalous and in the normal dispersion regime, the possibility of controlling the dispersion profile and the position of the ZDWs by simply changing the thickness of the chalcogenide layer is a convenient post-process dispersion engineering tool. When supercontinuum generation in the anomalous dispersion regime is targeted, the position of the ZDWs determines the spectral location of the dispersive waves, which are located at the extreme parts of the spectrum. Therefore, the dispersive waves and thus the supercontinuum bandwidth and center wavelength can be selectively tuned by changing the thickness of the chalcogenide cladding.

The most common technique to tailor the dispersion profile of a waveguide with a given thickness is to change its width at the design stage. Figure 6 shows the group velocity dispersion of an air-clad 2.7  $\mu\text{m}$  thick SiGe/Si waveguide for different widths. By increasing the width, we observe, similarly to the hybrid case, that the group velocity dispersion decreases, while the ZDWs are pushed toward longer wavelengths. However, the dispersion profile is less sensitive to the change of the waveguide width than to the thickness of the additional chalcogenide layer. For instance, a wide waveguide ( $\sim 25\%$  larger) is needed in order to substantially flatten the dispersion. Increasing the waveguide width could lead to a multi-mode regime and significantly increases the effective area, which may negatively impact the strength of nonlinearities, expressed through the factor  $\gamma = 2\pi n_2 / \lambda A_{\text{eff}}$ , where  $n_2$  is the nonlinear index and  $A_{\text{eff}}$  is the effective area. By contrast, we have shown that the additional chalcogenide layer only moderately affects the effective area (see Table 1).

As a comparison example, the black dashed curve in Fig. 6 shows the dispersion profile of a 3.75  $\mu\text{m}$  wide waveguide with a 250 nm thick chalcogenide top cladding. The dispersion curve is similar to the one of a 4.3  $\mu\text{m}$  wide air-clad waveguide (green curve). The maximum group velocity dispersion shifts from 11.6 ps/nm/km down to 7.53 ps/nm/km by widening the air-clad waveguide and down to 7.67 ps/nm/km by adding the chalcogenide layer, while the ZDWs shift from 3.8 and

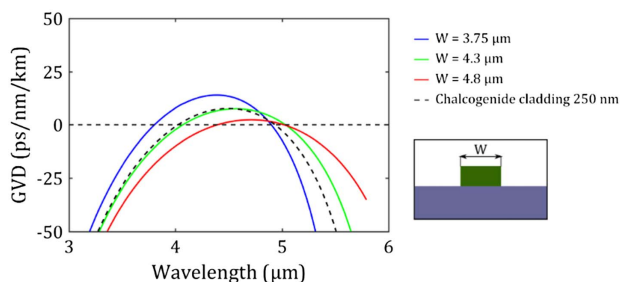


**Fig. 6.** Calculated group velocity dispersion for different waveguide widths (the thickness is fixed to 2.7  $\mu\text{m}$ ) and for a 3.75  $\mu\text{m}$  wide waveguide with 250 nm thick chalcogenide top cladding (dashed black curve). The dashed black line indicates the zero dispersion. The out inset shows a schematic of the air-clad waveguide.

4.89  $\mu\text{m}$  to 4.07 and 5.03  $\mu\text{m}$  and to 4.02 and 4.94  $\mu\text{m}$ , respectively.

While the tuning of the dispersion properties is very similar with the two techniques, the effective area of the mode is lower in the 250 nm thick chalcogenide-clad case (6.77  $\mu\text{m}^2$ , compared to 7.14  $\mu\text{m}^2$  in the 4.3  $\mu\text{m}$  wide air-clad case), leading to a higher  $\gamma$  factor. The undesirable increase in the effective area of the air-clad waveguide is even more severe when targeting normal dispersion for which a waveguide width of more than 5  $\mu\text{m}$  is needed, resulting in a  $\gamma$  factor of less than 0.45  $(\text{Wm})^{-1}$ , compared to  $\gamma = 0.57 (\text{Wm})^{-1}$  for the chalcogenide-clad waveguide. Importantly, we reemphasize that the chalcogenide layer can be added as a post-process, and the thickness of the layer could be chosen to trim the dispersion properties after the fabricated waveguide is characterized. A thickness resolution of the chalcogenide layer around 100 nm is easily achievable.

## B. Outlook

Besides the potential for adjusting the waveguide dispersion by controlling the thickness of a chalcogenide top cladding, the high photosensitivity of chalcogenide glasses [38] can be used to locally change their refractive index, density, and thickness through simply illuminating this material with light energy above their band gap. Exploiting the photosensitivity of these glasses is thus, in principle, an additional tool for post-trimming the properties of individual waveguides not only to relax the fabrication constraints but also to tailor the dispersion along the waveguide and to optimize the design of individual structures for different environments and applications [40]. Finally, although it was not exploited here, chalcogenide glasses possess a third-order optical nonlinearity up to a thousand times higher than silica glasses, [41] minimizing the potential negative impact that an additional top cladding might have on the effective nonlinear parameter.

## 5. CONCLUSION

We presented a simple post-process technique to fine-tune the dispersion profile of a nonlinear SiGe on an Si waveguide through adding a top chalcogenide layer for changing the properties of a chip-based generated supercontinuum. We demonstrated the utility of this approach through the generation of a mid-IR supercontinuum and have compared it with more traditional geometric changes of the waveguide dimensions.

Supercontinuum generation in both the normal and anomalous dispersion regimes requires group velocity dispersion profiles that are as low in magnitude and as flat as possible. Nanowaveguides that are used in integrated platforms can fulfill these strict requirements through design adjustment. They are, however, very sensitive to fabrication inaccuracies, surface roughness, surface contamination, and the presence of defects, resulting in deviations of the final device from the targeted dispersion profile. Therefore, a post-process approach that allows us to trim the group velocity dispersion depending on the actual structure produced by fabrication is a highly attractive complementary tool for optimizing chip-based supercontinuum generation. Finally, the wide transparency window of both the SiGe core and the chalcogenide cladding makes this

platform well suited to extend mid-IR coherent supercontinuum generation toward longer wavelengths, covering a great part of the mid-IR region, with potential applications in biomedical imaging, medical and environmental sensors, food quality analysis, and security.

**Funding.** Agence Nationale de la Recherche (ANR) (ANR-17-CE24-0028); H2020 European Research Council (ERC) (648546).

**Acknowledgments.** We acknowledge the support of the International Associated Laboratory between France and Australia (LIA ALPhFA), and author Christelle Monat acknowledges the support of the Institut Universitaire de France. We thank Aziz Benamrouche for the Atomic Force Microscope measurements of the chalcogenide surface.

## REFERENCES

- A. E. Willner, S. Khaleghi, M. R. Chitgarha, and O. F. Yilmaz, "All-optical signal processing," *J. Lightwave Technol.* **32**, 660–680 (2014).
- H. Tu and S. A. Boppart, "Coherent fiber supercontinuum for biophotonics," *Laser Photon. Rev.* **7**, 628–645 (2013).
- L. Wang and B. Mizaikoff, "Application of multivariate data-analysis techniques to biomedical diagnostics based on mid-infrared spectroscopy," *Anal. Bioanal. Chem.* **391**, 1641–1654 (2008).
- B. Guo, Y. Wang, C. Peng, H. L. Zhang, G. P. Luo, and H. Q. Le, "Laser-based mid-infrared reflectance imaging of biological tissues," *Opt. Express* **12**, 208–219 (2004).
- M. Sieger and B. Mizaikoff, "Toward on-chip mid-infrared sensors," *Anal. Chem.* **88**, 5562–5573 (2016).
- R. Soref, "Mid-infrared photonics in silicon and germanium," *Nat. Photonics* **4**, 495–497 (2010).
- L. Zhang, A. M. Agarwal, L. C. Kimerling, and J. Michel, "Nonlinear group IV photonics based on silicon and germanium: from near-infrared to mid-infrared," *Nanophotonics* **3**, 247–268 (2014).
- H. Lin, Z. Luo, T. Gu, L. C. Kimerling, K. Wada, A. Agarwal, and J. Hu, "Mid-infrared integrated photonics on silicon: a perspective," *Nanophotonics* **7**, 393–420 (2017).
- T. Hu, B. Dong, X. Luo, T. Liow, J. Song, C. Lee, and G. Lo, "Silicon photonic platforms for mid-infrared applications," *Photon. Res.* **5**, 417–430 (2017).
- Y. Yu, X. Gai, P. Ma, K. Vu, Z. Yang, R. Wang, D. Choi, S. Madden, and B. Luther-Davies, "Experimental demonstration of linearly polarized 2–10  $\mu\text{m}$  supercontinuum generation in a chalcogenide rib waveguide," *Opt. Lett.* **41**, 958–961 (2016).
- R. K. W. Lau, M. R. E. Lamont, A. G. Griffith, Y. Okawachi, M. Lipson, and A. L. Gaeta, "Octave-spanning mid-infrared supercontinuum generation in silicon nanowaveguides," *Opt. Lett.* **39**, 4518–4521 (2014).
- R. Kou, T. Hatakeyama, J. Horng, J. Kang, Y. Wang, X. Zhang, and F. Wang, "Mid-IR broadband supercontinuum generation from a suspended silicon waveguide," *Opt. Lett.* **43**, 1387–1390 (2018).
- N. Singh, D. Hudson, Y. Yu, C. Grillet, S. D. Jackson, A. Casas-Bedoya, A. Read, P. Atanackovic, S. G. Duvall, S. Palomba, B. Luther-Davies, S. Madden, D. J. Moss, and B. J. Eggleton, "Midinfrared supercontinuum generation from 2 to 6  $\mu\text{m}$  in a silicon nanowire," *Optica* **2**, 797–802 (2015).
- N. Nader, D. L. Maser, F. C. Cruz, A. Kowligy, H. Timmers, J. Chiles, C. Fredrick, D. A. Westly, S. Woo Nam, R. P. Mirin, J. M. Shainline, and S. Diddams, "Versatile silicon-waveguide supercontinuum for coherent mid-infrared spectroscopy," *APL Photon.* **3**, 036102 (2018).
- N. K. Hon, R. Soref, and B. Jalali, "The third-order nonlinear optical coefficients of Si, Ge, and  $\text{Si}_{1-x}\text{Ge}_x$  in the midwave and longwave infrared," *J. Appl. Phys.* **110**, 011301 (2011).
- G. Z. Mashanovich, C. J. Mitchell, J. Soler Penades, A. Z. Khokhar, C. G. Littlejohns, W. Cao, Z. Qu, S. Stankovic, F. Y. Gardes, T. Ben Masaud, H. M. H. Chong, V. Mittal, G. Senthil Murugan, J. S. Wilkinson, A. C. Peacock, and M. Nedeljkovic, "Germanium mid-infrared photonic devices," *J. Lightwave Technol.* **35**, 624–630 (2017).
- M. Nedeljkovic, J. Soler Penades, V. Mittal, G. Senthil Murugan, A. Z. Khokhar, C. Littlejohns, L. G. Carpenter, C. B. E. Gawith, J. S. Wilkinson, and G. Z. Mashanovich, "Germanium-on-silicon waveguides operating at mid-infrared wavelengths up to 8.5  $\mu\text{m}$ ," *Opt. Express* **25**, 27431–27441 (2017).
- K. Hammani, M. A. Etabib, A. Bogris, A. Kapsalis, D. Syvridis, M. Brun, P. Labeye, S. Nicoletti, and P. Petropoulos, "Towards nonlinear conversion from mid-to near-infrared wavelengths using Silicon Germanium waveguide," *Opt. Express* **22**, 9667–9674 (2014).
- M. A. Etabib, L. Xu, A. Bogris, A. Kapsalis, M. Belal, E. Lorent, P. Labeye, S. Nicoletti, K. Hammani, D. Syvridis, D. P. Shepherd, J. H. V. Price, D. J. Richardson, and P. Petropoulos, "Broadband telecom to mid-infrared supercontinuum generation in a dispersion-engineered silicon germanium waveguide," *Opt. Lett.* **40**, 4118–4121 (2015).
- J. M. Ramirez, V. Vakarín, C. Gilles, J. Frigerio, A. Ballabio, P. Chaisakul, X. Le Roux, C. Alonso-Ramos, G. Maisons, L. Vivien, M. Carras, G. Isella, and D. Marris-Morini, "Low-loss Ge-rich  $\text{Si}_{0.2}\text{Ge}_{0.8}$  waveguides for mid-infrared photonics," *Opt. Lett.* **42**, 105–108 (2017).
- J. M. Ramirez, Q. Liu, V. Vakarín, J. Frigerio, A. Ballabio, X. Le Roux, D. Bouville, L. Vivien, G. Isella, and D. Marris-Morini, "Graded SiGe waveguides with broadband low-loss propagation in the mid infrared," *Opt. Express* **26**, 870–877 (2018).
- L. Carletti, P. Ma, Y. Yu, B. Luther-Davies, D. Hudson, C. Monat, R. Orobtcouk, S. Madden, D. J. Moss, M. Brun, S. Ortiz, P. Labeye, S. Nicoletti, and C. Grillet, "Nonlinear optical response of low loss silicon germanium waveguides in the mid-infrared," *Opt. Express* **23**, 8261–8271 (2015).
- L. Carletti, M. Sinobad, P. Ma, Y. Yu, D. Allieux, R. Orobtcouk, M. Brun, S. Ortiz, P. Labeye, J. M. Hartmann, S. Nicoletti, S. Madden, B. Luther-Davies, D. J. Moss, C. Monat, and C. Grillet, "Mid-infrared nonlinear optical response of Si-Ge waveguides with ultra-short optical pulses," *Opt. Express* **23**, 32202–32214 (2015).
- M. Sinobad, C. Monat, B. Luther-Davies, P. Ma, S. Madden, D. J. Moss, A. Mitchell, D. Allieux, R. Orobtcouk, S. Boutami, J. M. Hartmann, J. M. Fedeli, and C. Grillet, "Mid-infrared octave spanning supercontinuum generation to 8.5  $\mu\text{m}$  in silicon-germanium waveguides," *Optica* **5**, 360–366 (2018).
- C. Bao, Y. Yan, L. Zhang, Y. Yue, N. Ahmed, A. M. Agarwal, L. C. Kimerling, J. Michel, and A. E. Willner, "Increased bandwidth with flattened and low dispersion in a horizontal double-slot silicon waveguide," *J. Opt. Soc. Am. B* **32**, 26–30 (2015).
- F. Lu and W. H. Knox, "Generation, characterization, and application of broadband coherent femtosecond visible pulses in dispersion micromanaged holey fibers," *J. Opt. Soc. Am. B* **23**, 1221–1227 (2006).
- G. Wong, L. Zang, M. S. Kang, and P. St. J. Russell, "Measurement of group-velocity dispersion of Bloch modes in photonic-crystal-fiber rocking filters," *Opt. Lett.* **35**, 3982–3984 (2010).
- J. Pan, Y. Huo, K. Yamanaka, S. Sandhu, L. Scaccabarozzi, R. Timp, M. L. Povinelli, S. Fan, M. M. Fejer, and J. S. Harris, "Aligning micro-cavity resonances in silicon photonic-crystal slabs using laser-pumped thermal tuning," *Appl. Phys. Lett.* **92**, 103114 (2008).
- F. Raineri, C. Cojocar, R. Raj, P. Monnier, and A. Levenson, "Tuning a two-dimensional photonic crystal resonance via optical carrier injection," *Opt. Lett.* **30**, 64–66 (2005).
- C. Grillet, C. Monat, C. L. Smith, M. W. Lee, S. Tomljenovic-Hanic, C. Karnutsch, and B. J. Eggleton, "Reconfigurable photonic crystal circuits," *Laser Photon. Rev.* **4**, 192–204 (2010).
- A. Casas Bedoya, P. Domachuk, C. Grillet, C. Monat, E. C. Mägi, E. Li, and B. J. Eggleton, "Reconfigurable photonic crystal waveguides created by selective liquid infiltration," *Opt. Express* **20**, 11046–11056 (2012).
- T. K. Sudoh, Y. Nakano, and K. Tada, "Wavelength trimming technology for multiple-wavelength distributed-feedback laser arrays by photo-induced refractive index change," *Electron. Lett.* **33**, 216–217 (1997).
- S. Song, S. S. Howard, Z. Liu, A. O. Dirisu, C. F. Gmachl, and C. B. Arnold, "Mode tuning of quantum cascade lasers through optical

- processing of chalcogenide glass claddings," *Appl. Phys. Lett.* **89**, 041115 (2006).
34. M. W. Lee, C. Grillet, S. Tomljenovic-Hanic, E. C. Mägi, D. J. Moss, B. J. Eggleton, X. Gai, S. Madden, D. Choi, D. A. P. Bulla, and B. Luther-Davies, "Photowritten high-Q cavities in two-dimensional chalcogenide glass photonic crystals," *Opt. Lett.* **34**, 3671–3673 (2009).
35. A. Faraon, D. Englund, D. Bulla, B. Luther-Davies, B. J. Eggleton, N. Stoltz, P. Petroff, and J. Vučković, "Local tuning of photonic crystal cavities using chalcogenide glasses," *Appl. Phys. Lett.* **92**, 043123 (2008).
36. M. W. Lee, C. Grillet, C. Monat, E. Mägi, S. Tomljenovic-Hanic, X. Gai, S. Madden, D. Choi, D. Bulla, B. Luther-Davies, and B. J. Eggleton, "Photosensitive and thermal nonlinear effects in chalcogenide photonic crystal cavities," *Opt. Express* **18**, 26695–26703 (2010).
37. M. W. Lee, C. Grillet, C. L. C. Smith, D. J. Moss, B. J. Eggleton, D. Freeman, B. Luther-Davies, S. Madden, A. Rode, Y. Ruan, and Y. Lee, "Photosensitive post tuning of chalcogenide photonic crystal waveguides," *Opt. Express* **15**, 1277–1285 (2007).
38. D. A. P. Bulla, R. P. Wang, A. Prasad, A. V. Rode, S. J. Madden, and B. Luther-Davies, "On the properties and stability of thermally evaporated Ge-As-Se thin films," *Appl. Phys. A* **96**, 615–625 (2009).
39. H. G. Dantanarayana, N. Abdel-Moneim, Z. Tang, L. Sojka, S. Sujecki, D. Furniss, A. B. Seddon, I. Kubat, O. Bang, and T. M. Benson, "Refractive index dispersion of chalcogenide glasses for ultra-high numerical-aperture fiber for mid-infrared supercontinuum generation," *Opt. Mater. Express* **4**, 1444–1455 (2014).
40. Y. Ruan, M. Kim, Y. Lee, B. Luther-Davies, and A. Rode, "Fabrication of high-Q chalcogenide photonic crystal resonators by e-beam lithography," *Appl. Phys. Lett.* **90**, 071102 (2007).
41. S. Dai, Y. Wang, X. Peng, P. Zhang, X. Wang, and Y. Xu, "A review of mid-infrared supercontinuum generation in chalcogenide glass fibers," *Appl. Sci.* **8**, 707 (2018).

## Conclusion

In this chapter, we discussed the dispersion trimming technique performed after the waveguide fabrication and the nonlinear supercontinuum measurements associated with the change in the waveguide dispersion profile (within a post-processing step). This technique can be used to match the dispersion of a fabricated waveguide to an intended design or to optimize the dispersion profile by finely tuning the zero-dispersion wavelengths.

In this particular example, we reported the use of a simple dispersion trimming technique to shift dispersion from anomalous to the all-normal regime. The technique consists of adding a chalcogenide cladding as a post-processing step on the top of a silicon germanium-on-silicon waveguide. We have compared this technique with more traditional techniques relying on geometric changes of the waveguide dimensions and found that waveguides with chalcogenide top cladding have lower effective area and flatter dispersion (i.e. lower  $\beta_3$ ). Finally, we demonstrated the utility of this approach through the generation of mid-infrared supercontinuum. The result reported here is, to our knowledge, the first mid-infrared supercontinuum generation in an all-normal dispersion regime on a silicon-based chip. Consequently, the resulting supercontinuum spectrum is smoother than using a more traditional anomalous dispersion regime.

As a cladding material, we used the selenide glass owing to its wide transparency window to around  $16\mu\text{m}$ . The wide transparency window and well suited refractive index of the chalcogenide cladding make this technique a highly attractive complementary tool for optimizing the dispersion of the on-chip waveguides operating in the mid-infrared.

## Chapter 5.

# Conclusion and perspectives

The purpose of this thesis was to investigate mid-infrared supercontinuum generation on a silicon-based chip. During the course of this work, performed in collaboration between several French and Australian laboratories under the LIA (Laboratoire International Associé) ALPhFA (Associated Laboratory for Photonics between France and Australia) initiative, I have demonstrated the generation of a bright, coherent and octave-spanning mid-infrared supercontinuum in silicon germanium-on-silicon waveguides. This could prove important for on-chip broadband molecular sensing and spectroscopy applications. Such a supercontinuum has the potential to become an essential ingredient for future mid-IR lab-on-a-chip that can be used at the point-of-care. An application such as early cancer diagnosis via exhaled breath analysis could be envisioned in the long-term [89].

Previously reported results in silicon-on-insulator, silicon germanium-on-insulator, and silicon-on-sapphire platforms demonstrated supercontinua limited to 3.7  $\mu\text{m}$  and 5.5  $\mu\text{m}$  that are the onset wavelengths of the absorption in silica and sapphire substrates, respectively. Moreover, the coherence properties of the reported results were not analyzed. The need to generate coherent and broadband supercontinuum light beyond 5.5  $\mu\text{m}$ , to cover atmospheric absorption band from 4 to 8  $\mu\text{m}$ , is calling for the use of alternative mid-infrared material platforms that are compatible with CMOS fabrication processes. The use of germanium, the material initially used in semiconductor electronics, has been proposed. The good performance reached with this platform can be attributed to several factors: a reduced lattice mismatch between the high index  $\text{Si}_{0.6}\text{Ge}_{0.4}$  core material and the Si cladding that provides low loss waveguides as well as a theoretically predicted strong Kerr index, and low multiphoton absorption losses.

To achieve an octave-spanning supercontinuum, both a strong nonlinearity and low dispersion are required. Considering the low index contrast between SiGe and Si, which is around 0.2 for 40% Ge in SiGe, I showed that a low anomalous dispersion regime could be achieved in an air clad waveguide geometry. Due to their asymmetry, the air clad ridge waveguides supported non-degenerate quasi-TE and quasi-TM linearly polarized modes. This reduced the power fluctuation when coupling light into the waveguide and contributed to the higher spectral coherence provided that the polarization noise was reduced. However, the non-symmetric waveguide geometry also induced a mode cutoff at long wavelengths. Achieving a longer cutoff wavelength can be generally obtained with a larger waveguide cross-section. Therefore, there was a tradeoff in achieving strong confinement and single-mode operation versus achieving low loss and long cutoff wavelength. Taking into account these constraints, two sets of waveguides were designed: the first one with a large cross-section with long cutoff wavelength designed to achieve a large bandwidth and the second one with comparatively “small” cross-section designed to operate in the single-mode regime and to achieve stable and coherent supercontinuum.

In the second chapter, I demonstrated a supercontinuum from a dispersion-engineered silicon germanium-on-silicon waveguide covering 1.4 octave in the mid-infrared. The spectrum spanned up to the 8.5  $\mu\text{m}$  wavelength, which is the longest wavelength generated on a silicon chip,



longer than the best previous result reported in the silicon-on-sapphire platform of 5.5  $\mu\text{m}$ . The generated supercontinuum reached the onset of the silicon absorption in the mid-infrared (i.e. where the absorption loss in silicon is larger than 2 dB/cm). Moreover, the supercontinuum spectrum covers the entire atmospheric absorption band from 4 to 8  $\mu\text{m}$ .

The  $\text{Si}_{0.6}\text{Ge}_{0.4}/\text{Si}$  waveguide propagation loss was measured using the cutback method. Thanks to a tight mode confinement and strong overlap of the field intensity in the core, a propagation loss as low as 0.23 dB/cm was achieved. This has been the lowest propagation loss ( $\sim 0.2$  dB/cm) of any Si-based waveguide in the mid-IR to date. In addition, we reported a low four-photon absorption coefficient that was extracted comparing our results with our numerical model. The low propagation loss combined with the low nonlinear loss yielded high on-chip power. More than 10 mW on-chip SC power was generated with  $\sim 50\%$  power conversion efficiency. This result is an improvement of more than an order of magnitude with respect to the previously reported result in silicon germanium-on-silicon platform [143].

A spectrally bright supercontinuum, demonstrated in the second chapter, is desirable for the mid-infrared molecular spectroscopy. In addition to larger bandwidth and high brightness, high spectral coherence is also required for high-sensitivity ultra-fast molecule detection. Indeed, incoherent supercontinuum pulse suffers from spectral fluctuations from pulse to pulse that limits the sensitivity of the detection. I discussed the coherence properties of the mid-infrared supercontinuum generated on our platform, in the subsequent chapter.

In the third chapter, we actually demonstrated the high-coherence of an octave-spanning mid-IR supercontinuum generated in our silicon germanium-on-silicon integrated platform. The coherence property was numerically investigated for the supercontinuum presented in the second chapter, highlighting the usefulness of the achieved result for a lot of applications. To bring additional insights into the origin of this coherence, we reported a detailed analysis of the supercontinuum generation dynamics, demonstrating a new approach that can be used to achieve high coherence without the constraining use of very short pulses and short waveguides. The high coherence of the pump pulse was preserved owing to a specific dispersion profile where an anomalous dispersion regime was surrounded by two closely spaced zero-GVD wavelengths. In short, a significant part of the spectrum is generated in the normal dispersion regime, resulting in an effective reduction of the soliton order and decreasing the impact of modulation instability and other mechanisms that typically degrade coherence. This makes the reported result the first (numerically assessed) coherent mid-IR supercontinuum in this novel type of nonlinear platform – silicon germanium-on-silicon.

The coherence of the supercontinuum has been numerically investigated. In the future, it would be important to experimentally explore the coherence properties of the SC pulses, even though this is a challenging task in the mid-infrared wavelength range. Fully coherent supercontinuum pulses can be recompressed. High coherence can thus be proved by measuring the auto-correlation of the compressed pulse. More often, the coherence is assessed through the interference pattern between two subsequent SC pulses. However, to date, this method has not been reported for SC in the mid-infrared. In the mid-infrared, only the coherence characterization by the relative intensity noise (RIN) measurements has been reported.

The coherence of distinct spectral components has been used as a tool to analyze the supercontinuum generation dynamics. The calculation of the degree of coherence at different

wavelength is indeed useful, as it allows one to distinguish between different spectral features in the supercontinuum and attribute them to either coherent and incoherent processes, e.g. dispersive waves and modulation instability.

The fourth chapter showed how adding a chalcogenide top cladding onto our SiGe/ Si waveguides could be used as a post-fabrication step to trim the waveguide dispersion in the mid-infrared. The selenide glass was used as a top cladding material owing to its wide transparency window to around 16 $\mu\text{m}$ . This dispersion trimming method can be used to optimize the waveguide dispersion profile by fine-tuning of the zero-GVD wavelengths, to compensate for any deviation from the targeted dispersion profile and to shift the dispersion profile of a waveguide, from anomalous to all normal, for instance. This can be useful to achieve a specific dispersion profile as that discussed in the third chapter where the pump is enclosed by two closely spaced zero-GVD wavelengths. The experimental dispersion profile of a fabricated waveguide can deviate from the intended design due to inaccuracies in both modeling and fabrication steps. In this scenario, this technique allows for compensating, as part of a post-fabrication step, the deviations from the targeted dispersion. In chapter 4, as a proof of concept of this capability, we have tuned the dispersion of a SiGe/ Si waveguide from anomalous to all normal dispersion. Dispersion trimming was numerically investigated. The fourth chapter then reported supercontinuum in all normal dispersion that generally maintains the coherence of the sub-picosecond pump as the SC dynamics is dominated by the coherent self-phase modulation processes. Measuring the waveguide dispersion could be useful to experimentally support our numerical results.

The results achieved in this thesis clearly establish the silicon germanium-on-silicon as a relevant platform for mid-infrared silicon photonics. By demonstrating a bright and broadband supercontinuum up to 8.5  $\mu\text{m}$ , we showed the full potential of this platform. The generated supercontinuum is well suited for on-chip sensing applications as it covers the entire atmospheric absorption band from 4 to 8  $\mu\text{m}$ . Moreover, the high coherence of the octave-spanning supercontinuum allows for  $f$ -to- $2f$  interferometry that is required to stabilize the supercontinuum spectrum for frequency metrology on a chip.

As a perspective, we consider exploring alternative material platforms to further improve our supercontinuum properties (in terms of bandwidth, brightness and coherence). Considering the good nonlinear properties of silicon germanium, as demonstrated in this thesis, the germanium-on-silicon germanium platform could be a solution to extend the operation wavelength range beyond 8.5 $\mu\text{m}$  on a CMOS compatible chip. The lattice mismatch between germanium and silicon germanium is less than between germanium and pure silicon. This could potentially reduce the density of threading dislocations at the interface that is required to achieve low loss waveguides in this platform.

In this thesis, a femtosecond laser operating around 4  $\mu\text{m}$  wavelength has been used to generate the supercontinua. Regarding the use of this pump, I identified two challenges for future work. The first challenge is to achieve coherent supercontinuum spanning an octave in the mid-infrared under (less constraining) picosecond pulse excitation. The second challenge is to achieve bright supercontinuum at shorter pump wavelength ( $\lambda < 4\mu\text{m}$ ). These two aspects could contribute to facilitate the assembly of the demonstrated supercontinuum with a more compact pump source, thereby helping the widespread deployment of this broadband light technology.

Shifting anomalous dispersion to longer wavelengths in simple ridge waveguide is generally accompanied by a red-shift of the first zero-dispersion wavelength. This requires a long pump wavelength. Certainly, this will be an issue when exploiting the entire transparency window of the germanium up to 15 $\mu$ m. More advanced designs than a simple ridge waveguide will be required. The other solution might be to exploit a multimode waveguide. In a multimode waveguide, the dispersion of the higher order mode can be designed for near-infrared operation and the dispersion of the fundamental mode for mid-infrared. Provided that the modes are coupled, a short wavelength pump can be used.

Finally, the mid-infrared supercontinuum achieved here has been suggested for molecular detection. Silicon germanium-on-silicon is realized in a CMOS compatible fabrication process allowing for the integration of many photonics components and micro-fluidics on the same chip. This advantage should be exploited to demonstrate the high sensitivity molecule detection scheme using a coherent mid-infrared supercontinuum.

## References

1. Alfano, R.R., *The Supercontinuum Laser Source Fundamentals*. 2006: Springer New York.
2. Steinmeyer, G. and J.S. Skibina, *Entering the mid-infrared*. Nat. Photonics, 2014. **8**(11): p. 814-815.
3. Alfano, R.R. and S.L. Shapiro, *Observation of Self-Phase Modulation and Small-Scale Filaments in Crystals and Glasses*. Physical Review Letters, 1970. **24**(11): p. 592-594.
4. Alfano, R.R. and S.L. Shapiro, *Emission in the Region 4000 to 7000 A Via Four-Photon Coupling in Glass*. Physical Review Letters, 1970. **24**(11): p. 584-587.
5. Ranka, J.K., R.S. Windeler, and A.J. Stentz, *Visible continuum generation in air-silica microstructure optical fibers with anomalous dispersion at 800 nm*. Optics Letters, 2000. **25**(1): p. 25-27.
6. Dudley, J.M. and J.R. Taylor, *Ten years of nonlinear optics in photonic crystal fibre*. Nature Photonics, 2009. **3**: p. 85.
7. Lau, R.K.W., et al., *Octave-spanning mid-infrared supercontinuum generation in silicon nanowaveguides*. Opt. Lett., 2014. **39**(15): p. 4518-4521.
8. Yu, Y., et al., *A broadband, quasi-continuous, mid-infrared supercontinuum generated in a chalcogenide glass waveguide*. Laser & Photonics Reviews, 2014. **8**(5): p. 792-798.
9. Russell, P., *Photonic Crystal Fibers*. Science, 2003. **299**(5605): p. 358-362.
10. Agrawal, G.P., *Nonlinear Fiber Optics, Fifth Edition*. 5 edition ed. 2012, Amsterdam: Academic Press. 648.
11. Udem, T., R. Holzwarth, and T.W. Hänsch, *Optical frequency metrology*. Nature, 2002. **416**: p. 233.
12. Hall, J.L., *Defining and measuring optical frequencies: the optical clock opportunity – and more*. Nobel lecture, 2005.
13. Kuyken, B., et al., *Mid-infrared to telecom-band supercontinuum generation in highly nonlinear silicon-on-insulator wire waveguides*. Opt. Express, 2011. **19**(21): p. 20172-81.
14. Singh, N., et al., *Midinfrared supercontinuum generation from 2 to 6 um in a silicon nanowire*. Optica, 2015. **2**(9): p. 797-802.
15. Yu, Y., et al., *Experimental demonstration of linearly polarized 2-10 mum supercontinuum generation in a chalcogenide rib waveguide*. Opt. Lett., 2016. **41**(5): p. 958-61.
16. Johnson, A.R., et al., *Octave-spanning coherent supercontinuum generation in a silicon nitride waveguide*. Opt. Lett., 2015. **40**(21): p. 5117-20.
17. Yu, Y., et al., *1.8-10 mum mid-infrared supercontinuum generated in a step-index chalcogenide fiber using low peak pump power*. Opt. Lett., 2015. **40**(6): p. 1081-4.
18. Petersen, C.R., et al., *Mid-infrared supercontinuum covering the 1.4–13.3 um molecular fingerprint region using ultra-high NA chalcogenide step-index fibre*. Nat. Photonics, 2014. **8**(11): p. 830-834.
19. Dai, S., et al., *A Review of Mid-Infrared Supercontinuum Generation in Chalcogenide Glass Fibers*. Appl. Sci., 2018. **8**(5): p. 707.
20. Franken, P.A., et al., *Generation of Optical Harmonics*. Physical Review Letters, 1961. **7**(4): p. 118-119.
21. Stolen, R.H., E.P. Ippen, and A.R. Tynes, *Raman Oscillation in Glass Optical Waveguide*. Applied Physics Letters, 1972. **20**(2): p. 62-64.

22. Ippen, E.P. and R.H. Stolen, *Stimulated Brillouin scattering in optical fibers*. Applied Physics Letters, 1972. **21**(11): p. 539-541.
23. Stolen, R.H., *The Early Years of Fiber Nonlinear Optics*. Journal of Lightwave Technology, 2008. **26**(9): p. 1021-1031.
24. Agrawal, G.P., *Nonlinear fiber optics: its history and recent progress [Invited]*. J. Opt. Soc. Am. B, 2011. **28**(12): p. A1-A10.
25. Knight, J.C., et al., *All-silica single-mode optical fiber with photonic crystal cladding*. Optics Letters, 1996. **21**(19): p. 1547-1549.
26. Leuthold, J., C. Koos, and W. Freude, *Nonlinear silicon photonics*. Nat. Photonics, 2010. **4**(8): p. 535-544.
27. Borghi, M., et al., *Nonlinear silicon photonics*. J. Opt., 2017. **19**(9): p. 093002.
28. Spence, D.E., P.N. Kean, and W. Sibbett, *60-fsec pulse generation from a self-mode-locked Ti:sapphire laser*. Optics Letters, 1991. **16**(1): p. 42-44.
29. Sibbett, W., A.A. Lagatsky, and C.T.A. Brown, *The development and application of femtosecond laser systems*. Optics Express, 2012. **20**(7): p. 6989-7001.
30. Dudley, J.M. and G. Genty, *Supercontinuum light*. Physics Today, 2013. **66**(7): p. 29-34.
31. Shen, Y.R., *The principles of nonlinear optics*. 1984, New York: J. Wiley.
32. Boyd, R.W., *Nonlinear Optics, Third Edition*. Vol. 1. 2008: Academic Press/Elsevier.
33. New, G., *Introduction to nonlinear optics*. 2011, Cambridge: Cambridge Univ. Press.
34. Dudley, J.M. and J.R. Taylor, *Supercontinuum generation in optical fibers*. 2010: Cambridge University Press.
35. Couairon, A., et al., *Practitioner's guide to laser pulse propagation models and simulation*. The European Physical Journal Special Topics, 2011. **199**(1): p. 5-76.
36. Lin, Q., O.J. Painter, and G.P. Agrawal, *Nonlinear optical phenomena in silicon waveguides: modeling and applications*. Opt. Express, 2007. **15**(25): p. 16604-16644.
37. Dudley, J.M., G. Genty, and S. Coen, *Supercontinuum generation in photonic crystal fiber*. Rev. Mod. Phys., 2006. **78**(4): p. 1135-1184.
38. Wang, J. and Y. Long, *On-chip silicon photonic signaling and processing: a review*. Science Bulletin, 2018. **63**(19): p. 1267-1310.
39. Sandercock, J.R., *Brillouin-Scattering Measurements on Silicon and Germanium*. Physical Review Letters, 1972. **28**(4): p. 237-240.
40. Palik, E.D., *Handbook of Optical Constants of Solids*. 1998: Elsevier Science.
41. Nedeljkovic, M., R. Soref, and G.Z. Mashanovich, *Free-Carrier Electrorefraction and Electroabsorption Modulation Predictions for Silicon Over the 1–14um Infrared Wavelength Range*. IEEE Photonics Journal, 2011. **3**(6): p. 1171-1180.
42. Nedeljkovic, M., R. Soref, and G.Z. Mashanovich, *Predictions of Free-Carrier Electroabsorption and Electrorefraction in Germanium*. IEEE Photonics Journal, 2015. **7**(3): p. 1-14.
43. Lin, Q., et al., *Dispersion of silicon nonlinearities in the near infrared region*. Appl. Phys. Lett., 2007. **91**(2): p. 21111-21111.
44. Foster, M.A., et al., *Broad-band optical parametric gain on a silicon photonic chip*. Nature, 2006. **441**(7096): p. 960-963.
45. Corcoran, B., et al., *Green light emission in silicon through slow-light enhanced third-harmonic generation in photonic-crystal waveguides*. Nat. Photonics, 2009. **3**(4): p. 206-210.
46. Miyagi, M. and S. Nishida, *Pulse spreading in a single-mode fiber due to third-order dispersion*. Applied Optics, 1979. **18**(5): p. 678-682.
47. Lamont, M.R., B.T. Kuhlmeier, and M.C. de Sterke, *Multi-order dispersion engineering for optimal four-wave mixing*. Opt. Express, 2008. **16**(10): p. 7551-7563.

48. Roy, S., S.K. Bhadra, and G.P. Agrawal, *Dispersive wave generation in supercontinuum process inside nonlinear microstructured fibre*. Current Science, 2011: p. 321-342.
49. Afshar V, S. and T.M. Monro, *A full vectorial model for pulse propagation in emerging waveguides with subwavelength structures part I: Kerr nonlinearity*. Optics Express, 2009. **17**(4): p. 2298-2318.
50. Foster, M.A., K.D. Moll, and A.L. Gaeta, *Optimal waveguide dimensions for nonlinear interactions*. Optics Express, 2004. **12**(13): p. 2880-2887.
51. Lin, Q. and G.P. Agrawal, *Raman response function for silica fibers*. Optics Letters, 2006. **31**(21): p. 3086-3088.
52. Yin, L.a.L., Qiang and Agrawal, Govind P, *Soliton fission and supercontinuum generation in silicon waveguides*. Opt. Lett., 2007. **32**(4): p. 391-3.
53. Boyraz, O. and B. Jalali, *Demonstration of a silicon Raman laser*. Optics Express, 2004. **12**(21): p. 5269-5273.
54. Rong, H., et al., *A continuous-wave Raman silicon laser*. Nature, 2005. **433**(7027): p. 725-728.
55. Rong, H., et al., *An all-silicon Raman laser*. Nature, 2005. **433**: p. 292.
56. Wartak, M.S., *Computational Photonics: An Introduction with MATLAB*. 2013, Cambridge, UK: Cambridge University Press. 468.
57. Akhmediev, N. and M. Karlsson, *Cherenkov radiation emitted by solitons in optical fibers*. Phys. Rev. A, 1995. **51**(3): p. 2602-2607.
58. Erkintalo, M., et al., *Cascaded phase matching and nonlinear symmetry breaking in fiber frequency combs*. Physical review letters, 2012. **109**(22): p. 223904.
59. Castello-Lurbe, D., N. Vermeulen, and E. Silvestre, *Towards an analytical framework for tailoring supercontinuum generation*. Opt. Express, 2016. **24**(23): p. 26629-26645.
60. *60 years of integrated circuits*. Nature Electronics, 2018. **1**(9): p. 483-483.
61. Soref, R., *The Past, Present, and Future of Silicon Photonics*. IEEE J. Sel. Top. Quantum Electron., 2006. **12**(6): p. 1678-1687.
62. Reed, G.T. and A.P. Knights, *Silicon Photonics: An Introduction*. 2004: Wiley.
63. Jalali, B., *Nonlinear optics in the mid-infrared*. Nat. Photonics, 2010. **4**(8): p. 506-508.
64. Soref, R., *Mid-infrared photonics in silicon and germanium*. Nat. Photonics, 2010. **4**(8): p. 495-497.
65. Vivek, S., et al., *Mid-infrared materials and devices on a Si platform for optical sensing*. Sci. Technol. Adv. Mater., 2014. **15**(1): p. 014603.
66. Zhang, L., et al., *Nonlinear group IV photonics based on silicon and germanium: from near-infrared to mid-infrared*. Nanophotonics, 2014. **3**(4-5): p. 247-268.
67. Rademacher, G., et al. *159 Tbit/s C+L Band Transmission over 1045 km 3-Mode Graded-Index Few-Mode Fiber*. in *Optical Fiber Communication Conference Postdeadline Papers*. 2018. San Diego, California: Optical Society of America.
68. Wabnitz, S., *All-optical signal processing*. 2016, [Place of publication not identified]: Springer international.
69. Mashanovich, G.Z., et al., *Silicon photonic waveguides and devices for near-and mid-IR applications*. IEEE J. Sel. Top. Quantum Electron., 2015. **21**(4): p. 8200112.
70. Zhou, Z., B. Yin, and J. Michel, *On-chip light sources for silicon photonics*. Light: Science & Applications, 2015. **4**: p. e358.
71. Cornet, C., Y. Léger, and C. Robert, *Integrated Lasers on Silicon*. 2016: Elsevier Science.
72. Camacho-Aguilera, R.E., et al., *An electrically pumped germanium laser*. Optics Express, 2012. **20**(10): p. 11316-11320.
73. Wirths, S., et al., *Lasing in direct-bandgap GeSn alloy grown on Si*. Nature Photonics, 2015. **9**: p. 88.

74. Song, B., et al., *3D integrated hybrid silicon laser*. Optics Express, 2016. **24**(10): p. 10435-10444.
75. Sun, C., et al., *Single-chip microprocessor that communicates directly using light*. Nature, 2015. **528**(7583): p. 534-538.
76. Milivojevic, B., et al. *Demonstration of optical transmission at bit rates of up to 321.4Gb/s using compact Silicon based modulator and linear BiCMOS MZM driver*. in *2016 Optical Fiber Communications Conference and Exhibition (OFC)*. 2016.
77. Li, F., et al., *Error-free all-optical demultiplexing at 160Gb/s via FWM in a silicon nanowire*. Opt. Express, 2010. **18**(4): p. 3905-3910.
78. Ji, H., et al., *1.28-Tb/s Demultiplexing of an OTDM DPSK Data Signal Using a Silicon Waveguide*. IEEE Photon. Technol. Lett., 2010. **22**(23): p. 1762-1764.
79. Cotter, D., et al., *Nonlinear optics for high-speed digital information processing*. Science, 1999. **286**(5444): p. 1523-1528.
80. Corcoran, B., et al., *Optical signal processing on a silicon chip at 640Gb/s using slow-light*. Opt. Express, 2010. **18**(8): p. 7770-7781.
81. Xiong, C., et al., *Slow-light enhanced correlated photon pair generation in a silicon photonic crystal waveguide*. Opt. Lett., 2011. **36**(17): p. 3413-3415.
82. Yin, L. and G.P. Agrawal, *Impact of two-photon absorption on self-phase modulation in silicon waveguides*. Opt. Lett., 2007. **32**(14): p. 2031-2033.
83. Moss, D.J., et al., *New CMOS-compatible platforms based on silicon nitride and Hydex for nonlinear optics*. Nat. Photonics, 2013. **7**(8): p. 597-607.
84. Grillet, C., et al., *Amorphous silicon nanowires combining high nonlinearity, FOM and optical stability*. Opt. Express, 2012. **20**(20): p. 22609.
85. Van Camp, M.A., et al., *Demonstration of electrooptic modulation at 2165nm using a silicon Mach-Zehnder interferometer*. Optics Express, 2012. **20**(27): p. 28009-28016.
86. Thomson, D.J., et al., *Optical detection and modulation at  $2\mu\text{m}$ - $2.5\mu\text{m}$  in silicon*. Optics Express, 2014. **22**(9): p. 10825-10830.
87. Baets, R., *Silicon Photonics and its Applications in Life Science*, in *2017 European Conference on Integrated Optics*. 2017: Eindhoven, The Netherlands.
88. *Extending opportunities*. Nat. Photonics, 2012. **6**(7): p. 407-407.
89. Haas, J. and B. Mizaikoff, *Advances in Mid-Infrared Spectroscopy for Chemical Analysis*. Annu. Rev. Anal. Chem., 2016. **9**(1): p. 45-68.
90. Subramanian, A.Z., et al., *Silicon and silicon nitride photonic circuits for spectroscopic sensing on-a-chip [Invited]*. Photonics Research, 2015. **3**(5): p. B47-B59.
91. Antipov, S., et al., *High-power mid-infrared femtosecond fiber laser in the water vapor transmission window*. Optica, 2016. **3**(12): p. 1373-1376.
92. Hudson, D.D., et al., *Toward all-fiber supercontinuum spanning the mid-infrared*. Optica, 2017. **4**(10): p. 1163.
93. Delahaye, H., et al., *Generation of 35 kW peak power 80 fs pulses at 2.9 um from a fully fusion-spliced fiber laser*. Optics Letters, 2019. **44**(9): p. 2318-2321.
94. Mizaikoff, B., *Waveguide-enhanced mid-infrared chem/bio sensors*. Chem. Soc. Rev., 2013. **42**(22): p. 8683-99.
95. Kita, D.M., et al., *Are slot and sub-wavelength grating waveguides better than strip waveguides for sensing?* Optica, 2018. **5**(9): p. 1046-1054.
96. Schliesser, A., N. Picqué, and T.W. Hänsch, *Mid-infrared frequency combs*. Nat. Photonics, 2012. **6**(7): p. 440-449.
97. Liu, Q., et al., *Integrated broadband dual-polarization Ge-rich SiGe mid-infrared Fourier-transform spectrometer*. Opt. Lett., 2018. **43**(20): p. 5021-5024.

98. Nader, N., et al., *Versatile silicon-waveguide supercontinuum for coherent mid-infrared spectroscopy*. APL Photonics, 2018. **3**(3): p. 036102.
99. Gmachl, C., et al., *Recent progress in quantum cascade lasers and applications*. Rep. Prog. Phys., 2001. **64**(11): p. 1533.
100. Yao, Y., A.J. Hoffman, and C.F. Gmachl, *Mid-infrared quantum cascade lasers*. Nat. Photonics, 2012. **6**(7): p. 432-439.
101. Faist, J., et al., *Quantum Cascade Laser*. Science, 1994. **264**(5158): p. 553.
102. Ebrahim-Zadeh, M. and I.T. Sorokina, *Mid-infrared coherent sources and applications*. 2008, Dordrecht: Springer.
103. Singh, N., et al., *Mid-IR absorption sensing of heavy water using a silicon-on-sapphire waveguide*. Opt. Lett., 2016. **41**(24): p. 5776-5779.
104. Tu, H. and S.A. Boppart, *Coherent fiber supercontinuum for biophotonics*. Laser Photonics Rev., 2013. **7**(5).
105. Penades, J.S., et al., *Suspended silicon waveguides for long-wave infrared wavelengths*. Opt. Lett., 2018. **43**(4): p. 795-798.
106. Kou, R., et al., *Mid-IR broadband supercontinuum generation from a suspended silicon waveguide*. Opt. Lett., 2018. **43**(6): p. 1387-1390.
107. Ma, P., et al., *Low-loss chalcogenide waveguides for chemical sensing in the mid-infrared*. Opt. Express, 2013. **21**(24): p. 29927-29937.
108. Hon, N.K., R. Soref, and B. Jalali, *The third-order nonlinear optical coefficients of Si, Ge, and Si<sub>1-x</sub>Ge<sub>x</sub> in the midwave and longwave infrared*. J. Appl. Phys., 2011. **110**(1): p. 11301-11301.
109. Chiles, J. and S. Fathpour, *Silicon photonics beyond silicon-on-insulator*. J. Opt., 2017. **19**(5): p. 053001.
110. Hu, T., et al., *Silicon photonic platforms for mid-infrared applications*. Photonics Research, 2017. **5**(5): p. 417--430.
111. Marris-Morini, D., et al., *Germanium-based integrated photonics from near- to mid-infrared applications*. Nanophotonics, 2018. **0**(0).
112. Mashanovich, G.Z., et al., *Germanium mid-infrared photonic devices*. J. Lightw. Technol., 2017. **35**(4).
113. Macfarlane, G.G. and V. Roberts, *Infrared Absorption of Silicon Near the Lattice Edge*. Physical Review, 1955. **98**(6): p. 1865-1866.
114. Macfarlane, G.G. and V. Roberts, *Infrared Absorption of Germanium near the Lattice Edge*. Physical Review, 1955. **97**(6): p. 1714-1716.
115. Braunstein, R., A.R. Moore, and F. Herman, *Intrinsic Optical Absorption in Germanium-Silicon Alloys*. Phys. Rev., 1958. **109**(3): p. 695-710.
116. Salzberg, C.D. and J.J. Villa, *Infrared Refractive Indexes of Silicon Germanium and Modified Selenium Glass\**. Journal of the Optical Society of America, 1957. **47**(3): p. 244-246.
117. Parker, J.H., D.W. Feldman, and M. Ashkin, *Raman Scattering by Silicon and Germanium*. Physical Review, 1967. **155**(3): p. 712-714.
118. Brinkman, W.F., D.E. Haggan, and W.W. Troutman, *A history of the invention of the transistor and where it will lead us*. IEEE Journal of Solid-State Circuits, 1997. **32**(12): p. 1858-1865.
119. Exploratorium, *Everything Matters: Germanium With Ron Hipschman*. 2018.
120. Fard, M.M.P., G. Cowan, and O. Liboiron-Ladouceur, *Responsivity optimization of a high-speed germanium-on-silicon photodetector*. Opt. Express, 2016. **24**(24): p. 27738-27752.
121. Seo, D., et al., *Multiphoton absorption in germanium using pulsed infrared free-electron laser radiation*. Phys. Rev. B, 2011. **83**(19): p. 195203.
122. Bristow, A.D., N. Rotenberg, and H.M.v. Driel, *Two-photon absorption and Kerr coefficients of silicon for 850–2200nm*. Appl. Phys. Lett., 2007. **90**(19): p. 191104.



123. Nedeljkovic, M., et al., *Surface-Grating-Coupled Low-Loss Ge-on-Si Rib Waveguides and Multimode Interferometers*. IEEE Photonics Technology Letters, 2015. **27**(10): p. 1040-1043.
124. Alonso-Ramos, C., et al., *Germanium-on-silicon mid-infrared grating couplers with low-reflectivity inverse taper excitation*. Optics Letters, 2016. **41**(18): p. 4324-4327.
125. Nedeljkovic, M., et al., *Germanium-on-silicon waveguides operating at mid-infrared wavelengths up to 8.5  $\mu\text{m}$* . Opt. Express, 2017. **25**(22): p. 27431-27441.
126. Shen, L., et al., *Two-photon absorption and all-optical modulation in germanium-on-silicon waveguides for the mid-infrared*. Opt. Lett., 2015. **40**(10): p. 2213-6.
127. De Leonardis, F., B. Troia, and V. Passaro, *Mid-IR optical and nonlinear properties of germanium on silicon optical waveguides*. J. Lightw. Technol., 2014. **32**(22): p. 3747-3757.
128. De Leonardis, F., et al., *Modelling of Supercontinuum Generation in the Germanium-on-Silicon Waveguided Platform*. J. Lightw. Technol., 2015. **33**(21): p. 4437-4444.
129. De Leonardis, F., et al., *Investigation of mid-infrared second harmonic generation in strained germanium waveguides*. Opt. Express, 2016. **24**(10): p. 11126-11144.
130. Yuan, J., et al., *Mid-Infrared Octave-Spanning Supercontinuum and Frequency Comb Generation in a Suspended Germanium-Membrane Ridge Waveguide*. J. Lightw. Technol., 2017. **35**(14): p. 2994-3002.
131. Malik, A., et al., *Ge-on-Si and Ge-on-SOI thermo-optic phase shifters for the mid-infrared*. Optics Express, 2014. **22**(23): p. 28479-28488.
132. Radosavljevic, S., B. Kuyken, and G. Roelkens, *Efficient 5.2  $\mu\text{m}$  wavelength fiber-to-chip grating couplers for the Ge-on-Si and Ge-on-SOI mid-infrared waveguide platform*. Opt. Express, 2017. **25**(16): p. 19034--19042.
133. Radosavljevic, S., et al., *Mid-infrared Vernier racetrack resonator tunable filter implemented on a germanium on SOI waveguide platform [Invited]*. Opt. Mater. Express, 2018. **8**(4): p. 824.
134. Chang, Y.-C., et al., *Low-loss germanium strip waveguides on silicon for the mid-infrared*. Optics Letters, 2012. **37**(14): p. 2883-2885.
135. Malik, A., et al., *Germanium-on-Silicon Mid-Infrared Arrayed Waveguide Grating Multiplexers*. IEEE Photonics Technology Letters, 2013. **25**(18): p. 1805-1808.
136. Roelkens, G., et al., *Silicon-based heterogeneous photonic integrated circuits for the mid-infrared*. Optical Materials Express, 2013. **3**(9): p. 1523-1536.
137. Gallacher, K., et al., *Low loss Ge-on-Si waveguides operating in the 8-14 $\mu\text{m}$  atmospheric transmission window*. Optics Express, 2018. **26**(20): p. 25667-25675.
138. Ramirez, J.M., et al., *Low-loss Ge-rich Si<sub>0.2</sub>Ge<sub>0.8</sub> waveguides for mid-infrared photonics*. Opt. Lett., 2017. **42**(1): p. 105-108.
139. Ramirez, J.M., et al., *Graded SiGe waveguides with broadband low-loss propagation in the mid infrared*. Opt. Express, 2018. **26**(2): p. 870-877.
140. Serna, S., et al., *Nonlinear Properties of Ge-rich Si<sub>1-x</sub>Ge<sub>x</sub> Materials with Different Ge Concentrations*. Sci. Rep., 2017. **7**(1): p. 14692.
141. Vakarin, V., et al., *Ultra-wideband Ge-rich silicon germanium integrated Mach-Zehnder interferometer for mid-infrared spectroscopy*. Opt. Lett., 2017. **42**(17): p. 3482-3485.
142. Hammani, K., et al., *Towards nonlinear conversion from mid-to near-infrared wavelengths using Silicon Germanium waveguides*. Opt. Express, 2014. **22**(8): p. 9667-9674.
143. Ettabib, M.A., et al., *Broadband telecom to mid-infrared supercontinuum generation in a dispersion-engineered silicon germanium waveguide*. Opt. Lett., 2015. **40**(17): p. 4118-4121.
144. Ettabib, M.A., et al., *Telecom to Mid-infrared Supercontinuum Generation in a Silicon Germanium Waveguide*. 2015. **1**: p. 7-9.
145. Brun, M., et al., *Low loss SiGe graded index waveguides for mid-IR applications*. Opt. Express, 2014. **22**(1): p. 508-18.

146. Barritault, P., et al., *Mlines characterization of the refractive index profile of SiGe gradient waveguides at 2.15  $\mu\text{m}$* . Opt. Express, 2013. **21**(9): p. 11506-11515.
147. Hammani, K., et al., *Optical properties of silicon germanium waveguides at telecommunication wavelengths*. Opt. Express, 2013. **21**(14): p. 16690-16701.
148. Hammani, K., et al. *Linear and nonlinear properties of SiGe waveguides at telecommunication wavelengths*. in *2013 OSA Optical Fiber Communication Conference*. 2013.
149. Ettabib, M.A., et al., *FWM-based wavelength conversion of 40 Gbaud PSK signals in a silicon germanium waveguide*. Optics Express, 2013. **21**(14): p. 16683-16689.
150. Ettabib, M.A., et al., *Polarization Insensitive Wavelength Conversion in a Low-Birefringence SiGe Waveguide*. IEEE Photon. Technol. Lett. , 2016. **28**(11): p. 1221-1224.
151. Carletti, L., et al., *Nonlinear optical response of low loss silicon germanium waveguides in the mid-infrared*. Opt. Express, 2015. **23**(7): p. 8261-71.
152. Carletti, L., et al., *Mid-infrared nonlinear optical response of Si-Ge waveguides with ultra-short optical pulses*. Opt. Express, 2015. **23**(25): p. 32202-14.
153. Sinobad, M., et al., *Mid-infrared octave spanning supercontinuum generation to 8.5 $\mu\text{m}$  in silicon-germanium waveguides*. Optica, 2018. **5**(4): p. 360-366.
154. Reboud, V., et al., *Germanium based photonic components toward a full silicon/germanium photonic platform*. Prog. Cryst. Growth Charact. Mater., 2017. **63**(2): p. 1-24.
155. Frigerio, J., *Silicon-Germanium Heterostructures for Silicon Photonics Applications*. 2014, Politecnico di Milano.
156. Hsieh, I.-W., et al., *Supercontinuum generation in silicon photonic wires*. Opt. Express, 2007. **15**(23): p. 15242-9.
157. Koonath, P., D.R. Solli, and B. Jalali, *Limiting nature of continuum generation in silicon*. Appl. Phys. Lett., 2008. **93**(9): p. 091114.
158. Singh, N., et al., *Supplementary : Midinfrared supercontinuum generation from 2 to 6  $\mu\text{m}$  in a silicon nanowire*. Optica, 2015. **2**(9): p. 797-802.
159. Chiles, J., et al. *Mid-infrared supercontinuum generation in high-contrast, fusion-bonded silicon membrane waveguides*. in *2017 IEEE Photonics Conference (IPC)*. 2017.
160. Hannaford, P., *Femtosecond Laser Spectroscopy*. 2005: Springer US.
161. Paschotta, R., *Noise of mode-locked lasers (Part I): numerical model*. Appl. Phys. B, 2004. **79**(2): p. 153-162.
162. Paschotta, R., *Noise of mode-locked lasers (Part II): timing jitter and other fluctuations*. Appl. Phys. B, 2004. **79**(2): p. 163-173.
163. Bellini, M. and T.W. Hänsch, *Phase-locked white-light continuum pulses: toward a universal optical frequency-comb synthesizer*. Optics Letters, 2000. **25**(14): p. 1049-1051.
164. Heidt, A.M., *Pulse preserving flat-top supercontinuum generation in all-normal dispersion photonic crystal fiber*. J. Opt. Soc. Am. B, 2010.
165. Heidt, A.M., *Novel coherent supercontinuum light sources based on all-normal dispersion fibers*. 2011.
166. Heidt, A.M., et al., *Limits of coherent supercontinuum generation in normal dispersion fibers*. J. Opt. Soc. Am. B, 2017. **34**(4): p. 764-775.
167. Leo, F., et al., *Coherent supercontinuum generation in a silicon photonic wire in the telecommunication wavelength range*. Opt. Lett., 2015. **40**(1): p. 123-6.
168. Singh, N., et al., *Octave-spanning coherent supercontinuum generation in silicon on insulator from 1.06  $\mu\text{m}$  to beyond 2.4  $\mu\text{m}$* . Light Sci. Appl., 2018. **2018**(7).
169. Saleh, B.E.A. and M.C. Teich, *Fundamentals of photonics*. 2007, Hoboken, N.J.: Wiley-Interscience.
170. Svelto, O., *Principles of Lasers*. 2010: Springer US.

171. Xia, C., et al., *10.5 W Time-Averaged Power Mid-IR Supercontinuum Generation Extending Beyond 4  $\mu\text{m}$  With Direct Pulse Pattern Modulation*. IEEE Journal of Selected Topics in Quantum Electronics, 2009. **15**(2): p. 422-434.
172. Liu, K., et al., *High power mid-infrared supercontinuum generation in a single-mode ZBLAN fiber with up to 21.8 W average output power*. Optics Express, 2014. **22**(20): p. 24384-24391.
173. Yin, K., et al., *15.2 W spectrally flat all-fiber supercontinuum laser source with >1 W power beyond 3.8  $\mu\text{m}$* . Optics Letters, 2017. **42**(12): p. 2334-2337.
174. Yao, C., et al., *High-power mid-infrared supercontinuum laser source using fluorotellurite fiber*. Optica, 2018. **5**(10): p. 1264-1270.
175. Dave, U.D., et al., *Telecom to mid-infrared spanning supercontinuum generation in hydrogenated amorphous silicon waveguides using a Thulium doped fiber laser pump source*. Opt. Express, 2013. **21**(26): p. 32032-32039.
176. Chavez Boggio, J.M., et al., *Dispersion engineered silicon nitride waveguides by geometrical and refractive-index optimization*. J. Opt. Soc. Am. B, 2014. **31**(11): p. 2846-2857.
177. Hammani, K., et al., *Octave Spanning Supercontinuum in Titanium Dioxide Waveguides*. Appl. Sci., 2018. **8**(4): p. 543.
178. Fedeli, J. and S. Nicoletti, *Mid-Infrared (Mid-IR) Silicon-Based Photonics*. Proceedings of the IEEE, 2018. **106**(12): p. 2302-2312.
179. Carletti, L., *Photonique intégrée nonlinéaire sur plate-formes CMOS compatibles pour applications du proche au moyen infrarouge*. 2015, Ecole Centrale de Lyon.